The University of Strathclyde

Department of Physics

Two-photon excited fluorescence and applications in distributed optical fibre temperature sensing

by

Craig John Dalzell

A thesis presented in fulfilment of the requirements for the degree of Doctor of Philosophy in Physics

2011

This thesis is the result of the author's original research. It has been composed by the author and has not been previously submitted for examination which has led to the award of a degree.

Signed: Date:

Acknowledgements

I would like to acknowledge support by a UK Engineering and Physical Science Research Council (EPSRC) post graduate studentship. The use of the OPO laser from the EPSRC's Laser Loan Pool is also gratefully acknowledged.

I would like to thank Dr Ivan Ruddock and Dr Thomas Han for serving as my advisors through this PhD and in the projects which preceded it. Without their generous support and guidance this project would not have been possible.

I would also like to extend my thanks to Dr David Hollis for the loan of the rare-earth glass samples used in Chapter 6 and for his advice both on my practical work and especially on the writing of this thesis.

Grateful acknowledgement also goes out to Ken Grattan, Aiden Arnold and Yu Chen for serving on my examination committee and for taking the time to read this work and to aid me in improving it.

My gratitude also goes out to my colleagues with the University of Strathclyde, especially the technicians within the Department of Physics for their assistance with the practical elements of this investigation.

I would not have been able to complete this PhD without the support of my friends which was always there when it was needed. Special mention must go to three people in particular. Đurđica Crnogorac for graphical assistance and her steadfast and optimistic support whenever I needed it. Kateřina Kulhavá for her endless enthusiasm for my work and for keeping me focused on my goals. Finally, my thanks to Anne Williamson who has always been happy to offer her advice and ideas and whose technical advice was crucial on more than one occasion.

To all these people, to my friends and colleagues unnamed, and especially to my family. Thank you.

Abstract

A new class of distributed optical fibre temperature sensor based on time-correlated two-photon excited fluorescence is presented. Counter-propagating excitation pulses are introduced into a length of optical fibre doped with an optically active material. The overlap point can be scanned through any point within the fibre by introducing a mutual delay between the triggering of the two excitation lasers. Fluorescence is generated at the overlap point, is collected by the fibre and detected as it exits one aperture. Temperature can be calculated by measuring the change in the lifetime of the decay of the fluorescence pulse.

The theoretical framework governing the function of the sensor has been developed and generalised for several common excitation pulse shapes. Unlike many other non-linear optical processes the total quantity of fluorescence generated in the overlap region was found to be independent of the peak power and the duration of the excitation pulses as well as the excitation pulse profile. Therefore femtosecond and picosecond excitation pulses are not required.

Following from the theoretical framework the project developed a novel method of measuring the absolute two-photon absorption cross-section of any fluorescent material and this is used to test potential dopants including ruby and several rare-earth metals, the spectroscopy of some of which are presented for the first time.

Praseodymium was selected as a candidate dopant to construct an operational prototype sensor. Temperature sensitivity is demonstrated using both the fluorescence lifetime and by measuring the intensity ratio of two coupled emission lines.

Table of Contents

Index of Figures

1. Introduction

Sensors based on optical fibres are an increasingly important aspect of the sensing industry as they offer several advantages over their conventional electrical and electronic counterparts such as an increased resilience to electromagnetic interference due to a lack of mobile charge carriers[1]; resistance to corrosive or abrasive atmospheres[2] and the ability to operate within environments experiencing extreme temperatures and/or pressures.[3]

The initial work leading to this project began with the invention of the distributed optical fibre sensor described here by Ruddock and Han[4]. The author was invited to take part in a project the following year to help derive the initial theoretical framework on which the sensor was based.

The success of this project led to a larger scale investigation which resulted in the author's MSci dissertation project and which involved expanding and generalising the theoretical framework governing the measurement of two-photon absorption as well as performing the first attempts to measure the absorption cross-section of potential sensor materials such as ruby. This project also validated the theory that two-photon fluorescence could provide useful data which could be correlated to environmental characteristics such as temperature.

The results of both of these projects formed the foundations of the investigation reported here which aimed to fully develop and generalise the theoretical framework of the distributed optical fibre sensor, test and confirm the capabilities of this novel framework as a tool for the spectroscopic analysis of samples and for use in measuring environmental effects on the sample such as a change in temperature.

In order to construct such a sensor some knowledge of the fluorescent properties of the dopant material should be identified as an ideal dopant will exhibit as high a two-photon absorption cross-section as practical, should have at least one detectable fluorescent emission band which has a lifetime which is both long enough to be easily measured (on the order of several 100 μs) and exhibits a large change as

a function of temperature. From a practical standpoint an ideal dopant is likely to be solid due to the complications of attempting to study fluid filled hollow-core fibres although their use is not entirely ruled out by this study.

As part of the characterisation of the candidate dopants used in this investigation a method of measuring the two-photon absorption cross-section of a sample was developed and operates by comparing the relative fluorescence intensities of a given energy transition under both single-photon and two-photon excitation. The validity of this method is demonstrated by its use on the well known organic dye rhodamine 6G.

The investigation then examines a sample of ruby, which is known to be a useful temperature sensing medium but until this investigation was not extensively studied as a medium for two-photon excitation. Ruby seemed to fulfil many of the ideal dopant candidates although the complications of working with a single crystal fibre are discussed.

Perhaps the most promising class of potential dopants are the rare-earth metals as they are easily available doped in silica glass fibres and some are known to show temperature dependent responses. This investigation therefore embarked on a study of several different rare-earth metals and attempts to identify the most promising of these for use in a prototype sensor.

The final chapter of this thesis describes the construction and operation of the prototype sensor using a praseodymium dopant. The major principles of operation; generation and extraction of two-photon excited fluorescence from the fibre; measurement of the fluorescent spectrum; measurement of the fluorescence lifetime and measurement of the temperature dependence of the dopant are all demonstrated.

2. Background and history

2.1. Introduction

The design of the distributed optical fibre sensor presented within this thesis requires the synthesis of multiple branches of applied physics each of which have their own interesting histories and developments.

The first area is two-photon excited fluorescence in which the multi-photon absorption of light can result in fluorescent emission from a sample which has a wavelength which is typically shorter than the wavelength of the excitation photons. This phenomenon was predicted in the early 20th century and first demonstrated after the invention of the laser in 1960 and has since found extensive use in biochemical analytical methods such as microscopy.

Optical fibres now perform a vital role in the modern global telecommunications network but also perform a substantial and growing role in resilient and compact sensors both for single point use and in distributed networks which can monitor conditions over long ranges yet still extract localised data from small sections. The various designs of optical fibre sensor currently in use shall be discussed and compared to the design studied in this thesis.

Finally the concept of using single-photon excited fluorescence for sensing has a detailed history and has found use in single point optical fibre sensors as well as within other sensing fields. The mechanisms and applications used in this field are presented to give context to the applications for the sensor developed here.

By combining each of these areas a sensor can be developed which exploits the material advantages of an optical fibre and the sensing capabilities of a single-photon fluorescence based sensor with the non-linear optical phenomenon of TPF to create a fully distributed fluorescence based fibre in which data can be sensed from any arbitrarily located point within the fibre (something which cannot currently be achieved with SPF based sensors which are typically single point only).

2.2. Two-photon excited fluorescence

In the simple model of light absorption in an optically active medium a particular ion or molecule may be excited from its ground energy state if an incident photon contains enough energy to bridge the energy gap between the ground state and an upper state. Thus for this single-photon absorption (SPA) the medium will absorb light of selected wavelengths only and will be transparent at other wavelengths.

In 1931, Göppert-Mayer[5] first described the theory that an absorbing medium could be excited by light at wavelengths that it was normally transparent to if it did so by the simultaneous interaction of two photons provided that the sum of the energy contained by these photons was equal to the the gap between energy states. The simplest case of this is the degenerate one which involves absorption of two photons each with double the wavelength of the photon required for SPA as shown in Figure 2.2.1.

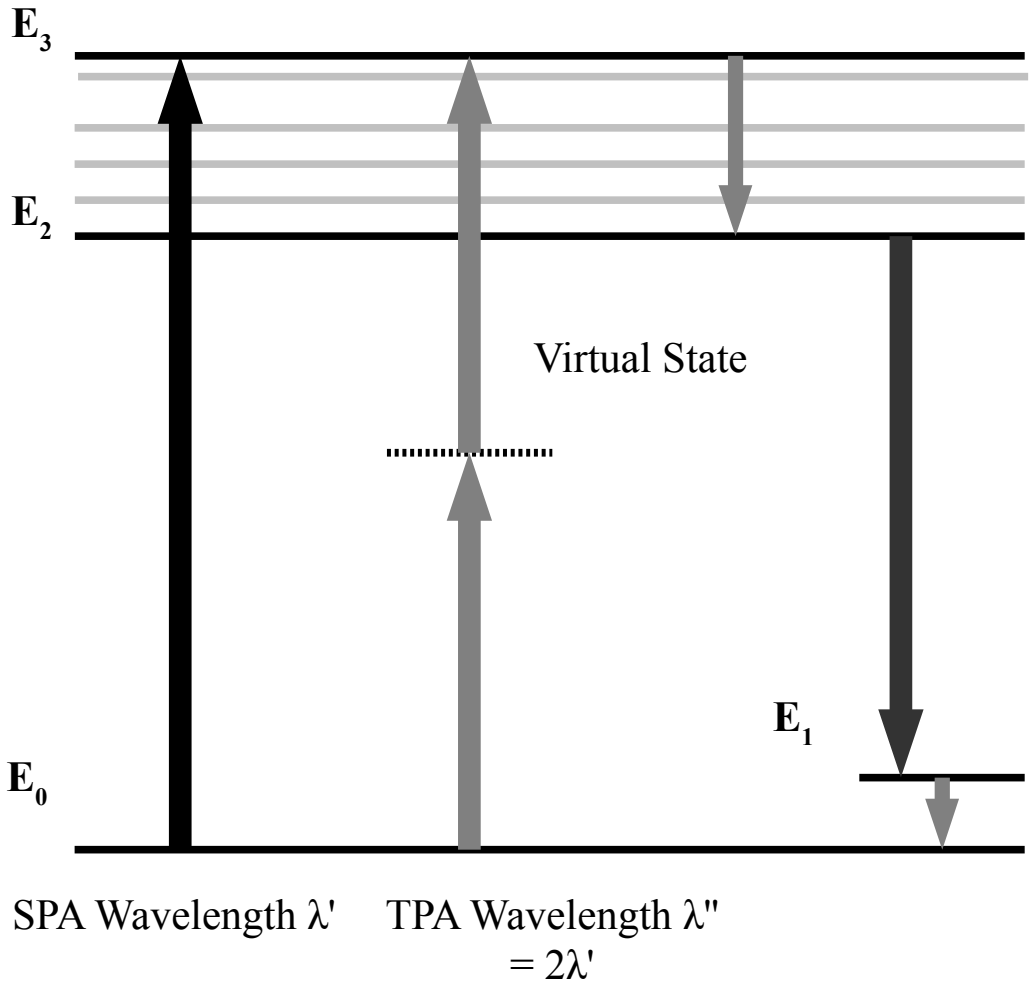

Figure 2.2.1: An optically active medium absorbing light via single-photon absorption (SPA) at wavelength λ' and by two-photon absorption (TPA) at wavelength λ'' where λ'' is twice λ'. The TPA occurs via the short-lived virtual state. Both absorption events may lead to detectable emission either directly or via intermediate decay to lower energy levels.

This two-photon absorption (TPA) does not involve any real intermediate energy states as is the case with excited state up-conversion but it does involve a virtual intermediate step in which the medium is held at a semi-excited state for a short period of time during which the medium can either absorb the second photon or decay back to its ground state. The duration of this virtual state is governed by Heisenberg's Uncertainty Principle and for light with wavelength of approximately 1 μm this gives a lifetime of about 1 femtosecond.[6]

Göppert-Mayer attempted to verify the theory experimentally using incoherent lamps as an excitation source but due to the low intensity of the light source no significant signals were recorded.

The experimental verification came a year after the invention of the laser when Kaiser and Garrett demonstrated the generation of blue fluorescence at 420 nm in CaF_2 doped with Eu^{2+} when excited by the 694 nm emission from a ruby laser.[7]

Over the following years several areas opened up for areas of study involving TPA. One of the first was the exploitation of TPA to measure the duration of increasingly short laser pulses using two-photon excited fluorescence (TPF) and autocorrelation techniques as first demonstrated by Giordmaine.[8]

A short laser pulse is separated into two by a beam splitter and counter propagated through a bath of fluorescent dye, as shown in Figure 2.2.2. below. The pulse wavelength and the absorption characteristics of the dye are selected such that each of the two pulses can excite the dye and cause a streak of emission through the bath. When the pulses are timed to cross each other within the dye the increase of the photon flux within this local region causes an enhancement of the fluorescence produced, especially as TPF is a non-linear process and the resulting fluorescence from any given point is dependent on the square of the exciting photon flux.

This technique can be used to calculate the duration of the pulse by simply measuring the spatial width of the fluorescing region in the bath and correlating with the velocity of light within the medium. A 100 ps pulse, for example, will result in a fluorescing region which is around 3 cm in length. In some cases, pulse shape can also be inferred based on the intensity of the fluorescence along the beam path although this is a more complex issue.[9]

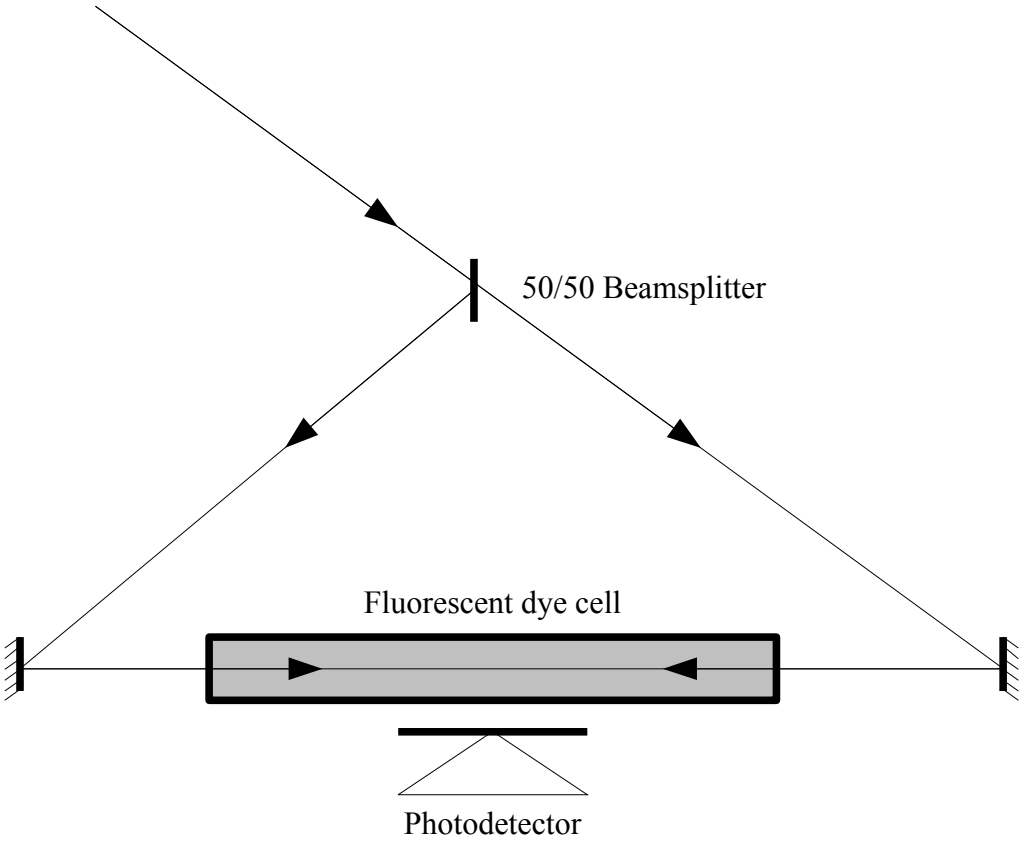

Figure 2.2.2: A TPF auto-correlator. A laser pulse is diverted by the beam splitter and cross-propagated through a solution of TPF dye. A portion of the light is emitted by the dye cell and travels perpendicular to the beam path where it is collected by the photodetector which records the spatial variation of the intensity of the emission across the length of the cell.

Another major application of TPF arrived with the work of Denk et al which led to the invention of the two-photon laser microscope, a schematic of which is shown in Figure 2.2.3.[10][11] Excitation light, usually red or near-IR, is focussed through a biological sample which has been stained with fluorescent dye. The dye is only significantly excited at or near the focus due to the non-linear absorption of the beam. In comparison to a similar single-photon excitation microscope, using this system has been shown to reduce the background signals produced as less light is generated outside of the targeted focus area and the excitation beam used experiences fewer scattering effects due to the longer wavelengths involved. The relatively long wavelengths also reduce photobleaching and other damage to the sample which has made easier the examination of biological processes in still living samples.

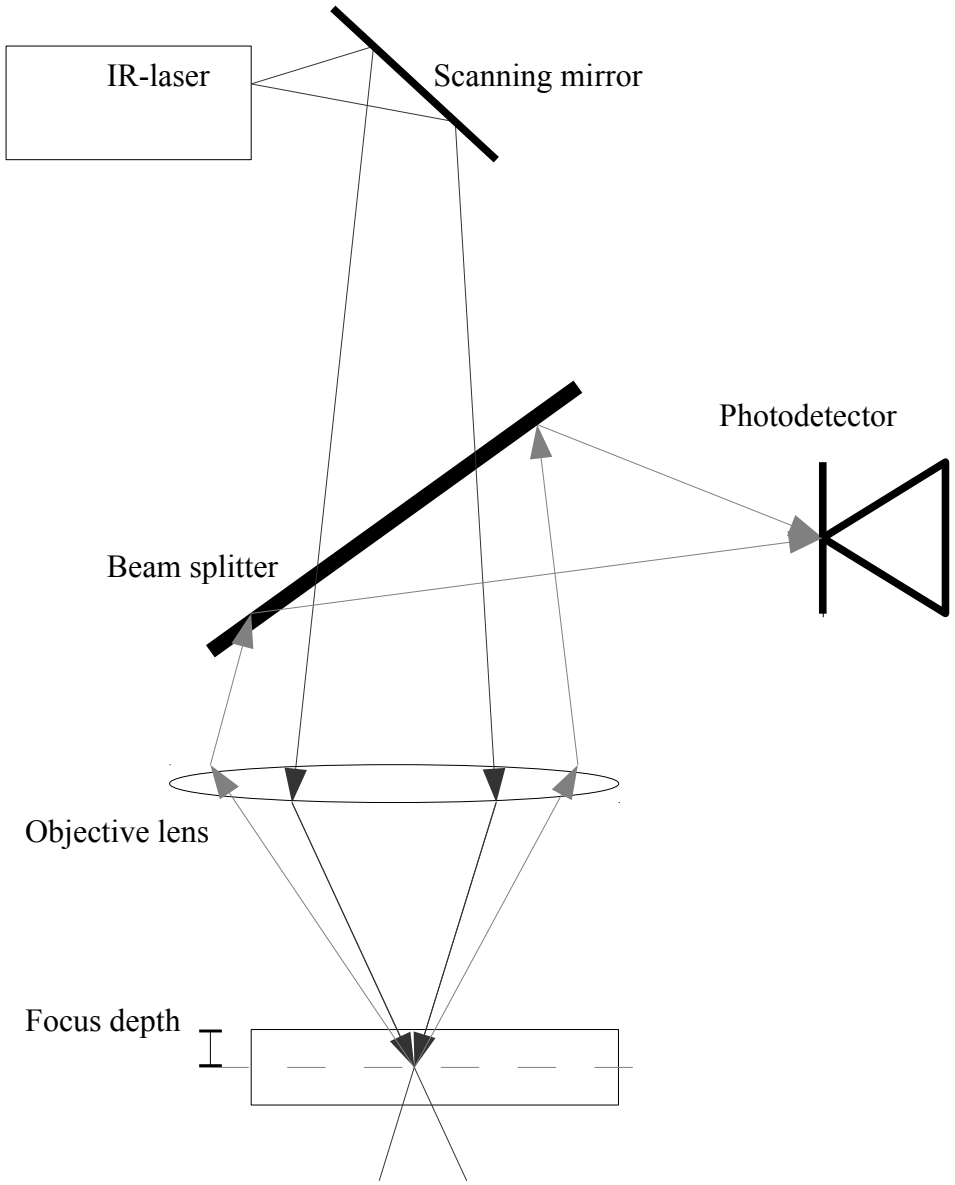

Figure 2.2.3: A schematic of a TPF scanning microscope. Infra-red laser light is guided to and focused onto the test sample. Significant TPF emission is generated only at the focus. A portion of this light (often a visible wavelength) is guided into the detection instrumentation for processing and recording.

2.3. Optical fibre sensors

2.3.1. Historical overview

As with the practical applications multi-photon absorption, optical sensing traces much of it development to the 1960's. In addition to the laser, the invention of low loss optical fibre by Kao[12] in 1966 opened the possibility of multi-kilometer lengths of fibre to be used for optical communications.

Optical fibre sensors (OFS) have become a focus for research in the years since because they open up many new possibilities and innovations which are not possible with traditional electrical sensors. Often, this is due to the inherent advantages that optical media have over the electrical such as their near imperviousness to electrical interference, which is due to the lack of mobile charges in the fibre to conduct current. OFS have also been found to perform well in other harsh environments such as corrosive environments[13], high temperatures[14] or areas of high ionising radiation[15].

Another important advantage of an OFS is that it is relatively simple to multiplex several sensors into a single fibre or into a bundle of fibres and take advantage of the long signal transmission lengths to report data from the sensors to potentially bulky instrumentation far from the signal site. This allows data to be returned from small and difficult to access areas such as drill boreholes or to gather data from distant locations such as along a pipeline to a central location for processing.

2.3.2. Sensor classes and configurations

Optical fibre sensing is currently a rapidly growing research area and has been the subject of considerable invention and innovation in recent years to the point where many different mechanisms for sensing have been developed and discussed in detail.[16] Broadly speaking, optical fibre sensors can be separated into two categories, the extrinsic sensor where light is coupled into and out of the fibre in such a way that it interacts with the environment directly or the intrinsic fibre where the interaction is

within the fibre itself. Further, each of these categories can be split into one of three sub-categories. The first of these is the single point sensor where a long length of passive fibre conducts light to a sensitised tip of some description. After the interrogation the modified light is transmitted back along the fibre to the detection instrumentation.

For the intrinsic sensors, one common example is the single-photon excited fluorescence sensor which uses changes in the emission spectrum of the sensor tip to measure parameters such as changing temperature[17] or chemical concentrations[18]. The details of this sensor will be expanded on in section 2.4. Other intrinsic point sensors include fibres with tips chemically altered so that they bond with and respond to chemicals, such as pharmaceuticals, from the environment.[19]

Extrinsic single point sensors include the extrinsic Fabry-Pérot interferometer[20] which bonds two cleaved fibre ends together in such a way as to leave a small air gap between them. This sensor reflects light preferentially within a small band, the wavelength of which is dependent on the length of the air gap. This results in a sensor which is sensitive to anything which affects this gap length such as pressure[21] or strain[22].

Being only able to make measurements at one location, single point sensors can be too limited for some applications. To broaden their effectiveness it is sometimes possible to either multiplex several discrete sensors in parallel with each other[23] or to construct many single point sensors spaced regularly in one fibre. This is possible with both the intrinsic[24] and extrinsic[25] Fabry-Pérot sensors although with some difficulty. The current industrial growth area for these Quasi-distributed sensors lies in the use of the fibre Bragg grating (FBG) first described by Hill et al[26] in which a periodic refractive index change is written into the fibre at specific points. Each of these gratings reflects a certain range of wavelengths of light dependent on the period of the grating. In a manner similar to the Fabry-Pérot sensors, it is possible to write several gratings into a single length of fibre if each of the gratings reflects a different wavelength range in a process known as wavelength division multiplexing. The individual sensors may then be addressed by using either a broadband light source or a tunable system. Alternatively, assuming the reflectivity of each mirror is

not too high then multiple mirrors each reflecting at the same wavelength may be interrogated separately by monitoring the time of flight between the launch of the excitation pulse and the return of the signals from each mirror in a process known as time division multiplexing (TDM). Of course, both of these systems are not mutually exclusive and a broadband or tunable light source may be used in a hybrid WDM/TDM system.[27] These sensors are most often used to measure temperature and/or strain by monitoring the wavelength shift in the peak of the reflectivity of the grating.[28]

Distributed sensors, in which the entire length of the fibre may be sensitised, form the third major family of optical fibre sensor and can prove to be more effective and flexible than quasi-distributed systems as the latter can often suffer from limitations in the form of the maximum number of sensors which can be multiplexed into a single fibre.[29]

Many distributed sensors prior to this investigation employ interactions between the light pulse travelling down the fibre and the host material of the fibre itself (usually silica) rather than any intentionally integrated structures or dopants and operate by detecting changes in the quantity of light scattered by perturbations within the fibre. Localisation of data so that the position of the cause of any anomaly can be performed by some form of optical time domain reflectometry (OTDR) in which the time of flight between the launch of the excitation pulse and the return of the backscattered signal is measured and thus the range calculated. Alternatively, if both ends of the fibre can be accessed, counter-propagating excitation pulses may be introduced to the fibre and interrogation may take place via forward scattered light.

Early models of sensor employed Rayleigh scattering from microscopic density fluctuations within the fibre[30],[31] and typically detected changes in the polarisation of the backscattered light.

Later designs include sensors employing the inelastic scattering of light due to interactions between photons and the vibrational modes of the atoms within the host fibre in a process known as Raman scattering.[32] The light scattered in this manner typically exhibits a frequency shift in which the photon either gains energy from or loses energy to the vibrational mode which produces two shifted bands

known as the anti-Stokes and Stokes shifted bands respectively. Changes in the frequency and intensity of these bands can be used as an indicator of environmental effects such as temperature.[32]

A third class sensor based on the scattering of light employs the Brillouin scattering effect. This scattering model is similar to Rayleigh scattering in that it involves interactions between photons and density fluctuations within the fibre. Unlike Rayleigh scattering however, Brillouin methods instead take advantage of longitudinal density waves or phonons within the fibre, essentially the light is interacting with sound waves as they propagate through the fibre. These phonons may be generated either by the natural environment of the fibre, in which case the sensor is a spontaneous Brillouin sensor[33], or the phonons may be induced in the fibre by a probe beam in which case it is a stimulated Brillouin sensor.[34]

In either the spontaneous or stimulated case the phonons in the fibre set up a short lived periodic density change within the fibre which causes a small change in the refractive index of the host. In this respect the sensing mechanism is not unlike that of the fibre Bragg grating except that the "mirror" in this arrangement is not fixed in position or time. Changes to the temperature[35] and/or strain[36] imposed on the fibre causes the period of the phonons to change which in turn affects the frequency of the scattered light although as with many other optical sensors the cross-sensitivity of these parameters has long been a cause for concern. Possible de-linking techniques in addition to the use of reference lines have included cross-correlating the Brillouin effects with the effects from Rayleigh scattering to calculate what is known as the Landau–Placzek ratio [37] although this method is limited both in the maximum permissible excitation beam energy and in that detailed knowledge of parameters such as the properties of the fibre host material should be available.

Variations on the Brillouin method have been shown to perform well as a distributed sensor and can be demonstrated to produce results over very long fibre ranges of over 100 km[38], has produced temperature resolutions of less than 0.1 K[39], and spatial resolutions on the mm scale[40] although it is often the case that trade-offs must be made between each of these parameters and maximum performance in one or two of these parameters must come at the expense of the others.

2.4. Fluorescence based sensing

The effect of changing environment on the single photon fluorescence characteristics of materials and the potential for that change to be used for analytical purposes has been demonstrated at least since the latter half of the 19th century[41] in which the intensity of fluorescence from a hydroxyflavone derivative is increased when complexed with aluminium thus serving as a diagnostic for the presence of that metal. Since then many other forms of fluorescence based sensing have been constructed and the applications continue to grow. In all cases this family of sensors relies on measuring changes in the characteristics of the emission of the sensing material. In addition to shifts in fluorescent intensity as in the case above, commonly measured factors include the shift in peak wavelength of the emission lines[42] or by measuring the exponential decay time of the fluorescence[43]

The current most common methods of fluorescence based sensing often use optical fibres to form an intrinsic point sensor where a small section of fibre is doped with the sensing material and is then attached to the end of a long passive fibre through which the excitation light is guided down. A portion of the emitted light from the excited sensor is trapped by the fibre and guided back up to the detection equipment. By this process the sensor can exploit the resistance of optical fibres to harsh environmental effects[15] as well as providing stable and accurate measurements of a variety of common parameters such as temperature[44], strain[45], pressure[46] and other less common ones such as fluid flow rate (via thermal conduction)[47] and magnetic field strength[48] and ionising radiation[49],[50].

As well as the fibre sensing and fluid systems mentioned above, fluorescence based techniques have also found applications in areas such as pressure sensitive paints[51] in which an aerodynamic structure is coated and the fluorescence emitted from whole surface (or a portion thereof) of the structure is imaged remotely to provide a 2 dimensional distributed sensing apparatus.

3. Theory

3.1. Distributed optical fibre sensing

Two photon excited fluorescence (TPF) is generated in an optically active medium, such as a rare earth metal ion, by the near simultaneous absorption of a pair of photons within the medium by means of a short lived virtual energy level[52]. As this technique does not involve a real intermediate level it must be distinguished from excited state upconversion (ESU)[53] and other non-linear "two-photon" absorption methods.

This TPF has been employed in the design of a novel class of continuously distributed sensor which uses counter-propagating laser pulses, confined within a loop of optical fibre, to excite an ionic medium doped into fibre.[54, 55]

Laser pulses are counter-propagated through the fibre such that they meet each other at a point governed by a relative delay time ΔT as shown in Figure 3.1.1 and Figure 3.1.2. Since the TPF process is non-linear and is proportional to the square of the total photon flux at any given position an enhanced burst of fluorescence will be generated at this overlap point in comparison to any TPF arising from the interaction of a single laser pulse with itself and the dopant medium. This TPF pulse will be initially emitted over all directions but a portion of this light, that which is emitted within the acceptance cone of the fibre, will be confined to travel down the length of the fibre where it may be picked up by a detector placed at one or both apertures. The interpretation of the properties of the emission may then be carried out in a similar manner to single-photon fluorescence based sensors.

The sensing medium will be essentially transparent with respect to single photon absorption due to the lack of real energy levels at the excitation photon wavelengths and, ideally, it should also be transparent at the fluorescence wavelength. In addition, two photon absorption is a very weak process compared to equivalent single-photon transitions therefore attenuation of the excitation pulse will be minimal and the absorption of the sensing medium will not act as a limiting factor on the maximum length of the fibre.

Progressively scanning the relative delay time ΔT allows the selection for sensing of any localised point within the fibre and for this point to be scanned along the entire length of the fibre thus achieving a fully distributed fluorescence based sensor.

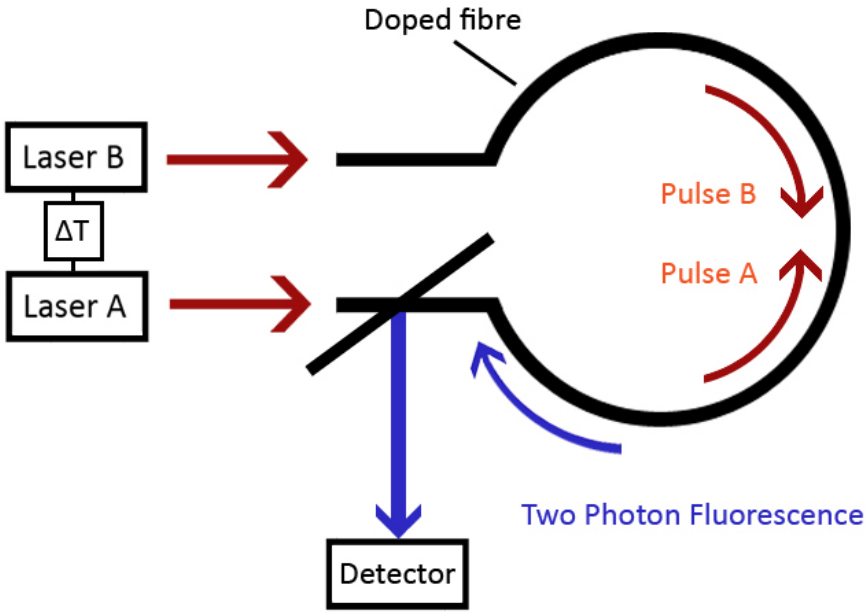

Figure 3.1.1: A schematic diagram of a distributed sensor based on time-correlated TPF in a doped optical fibre. Counter-propagating pulses A and B meet in a location depending on their mutual time delay, ΔT. The TPF generated at their overlap is guided along the fibre and detected.

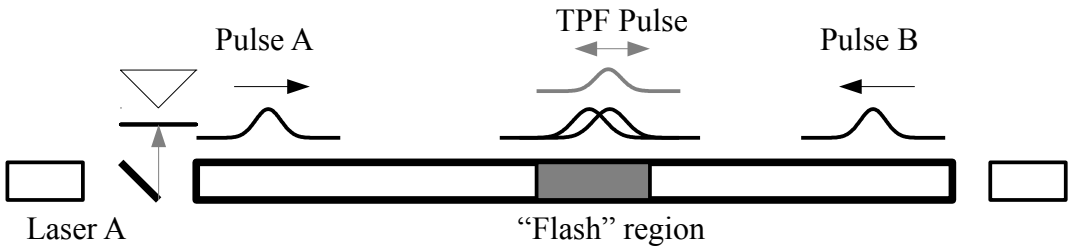

Figure 3.1.2: A side view of the same arrangement showing the similarity of the sensor to an autocorrelation arrangement but with the distinction of the detector place in line with the fibre rather than alongside it.

3.2. Background and general theory

When passively mode-locked lasers were invented in the mid-1960's[56] it became necessary to develop new methods of determining the very short pulse widths generated by these devices as the direct methods such as photodetectors were no longer capable of operating on such short time scales. This problem was solved very quickly, firstly by autocorrelating pulses within a second-harmonic crystal and measuring the frequency doubled light emitted as the pulses are partially overlapped to varying degrees.[57] This technique was surpassed within a year when a method employing TPF was developed.[8] In its simplest form this method uses a triangular arrangement, as shown previously in Figure 2.2.2, where the pulse to be measured is split and cross-propagated through a long sample of a fluorescent medium (often a bath of organic dye in solution). A photodetector is placed perpendicular to the path of the beam through the medium and the intensity of the two-photon fluorescence light emitted as a function of length within the track is measured. This technique provided excellent temporal resolution as it could be related instead to spatial distance (with a 1 ps pulse creating an autocorrelation track of about 0.3 mm long). One downside of this technique was that it did not provide accurate information about pulse shape. Also, the width and intensity profile of the autocorrelation track was not identical to the original pulse which created it so that it could be difficult to reconstruct the shape of the original pulses if they were unknown although in practice if the shape of that pulse was known then a relation between the two could be derived and these relations could be used to aid identification in subsequent experiments.[58]

This method produces effectively the temporally integrated (i.e. the signal measured consists of the light generated over the entire duration of the interaction) and spatially resolved (i.e. the variation of intensity of emission across the length of the cell, thus the shape and width of the emitted pulse, can be measured) profile of the fluorescent emission from the fibre.

The fundamental description of the two-photon excited fibre sensor is in many ways analogous to these autocorrelation descriptions but it does differ in that the detector is positioned viewing along the axis of the fibre therefore the detected

light will be integrated along the correlation region. The system can be said to describe the temporally resolved, spatially integrated equivalent of the auto-correlation arrangement.

Assuming that the duration of the excitation pulses used is much shorter than the fluorescence decay time τ, the amount of light emitted by the sensor may be quantified by first considering the effects of a light pulse of flux n(t) incident on a section of fibre with length dl, with a cross-section A and dopant number density N_1 (i.e. the number of ions per cm^3) then the initial population of ions excited to the upper energy state in this level will be

$$N_2(0) = A\,\delta\,N_1\left[\int_{-\infty}^{\infty} n^2(t)\,dt\right]dl \qquad (1)$$

where δ is the two photon absorption cross section, units cm^4 s ion^{-1} $photon^{-1}$, for the energy levels involved.

This initial population will then decay exponentially as a function of the fluorescence lifetime such that the upper state population at any given time is given by:

$$N_2(t) = N_2(0)e^{\left(\frac{-t}{\tau}\right)} \qquad (2)$$

The rate at which this upper state population decays is therefore given by the differentiation of this upper state population with time such that

$$\frac{dN_2(t)}{dt} = \frac{N_2(0)}{\tau}e^{\left(\frac{-t}{\tau}\right)} \qquad (3)$$

Each decay has a probability governed by η, the quantum efficiency of the material, of emitting a photon with an energy of hυ and this photon has a probability F of being guided from the excitation point to the detector via the body of the fibre as governed by its numerical aperture.

This results in the fluorescence power detected due to emission from an element of the fibre

$$dP(t) = \eta F \frac{d N_2(t)}{dt} dl \tag{4}$$

Thus the detected TPF power emitted from this element by the decay from the upper state population is therefore

$$dP = \frac{\eta F A \delta N_1 h \nu}{\tau} \left[\int_{-\infty}^{\infty} n^2(t) dt \right] e^{-\left(\frac{t}{\tau}\right)} dl \tag{5}$$

If Figure 3.1.2. is considered, the power generated by laser pulse A, that is, the pulse initially moving away from the detector, must account for the time delay generated due to the transit time of the pulse to the section of fibre in question as well as the time delay in the fluorescence light returning down the fibre to the detector. For convenience the origin of time shall be set such that t=0 occurs when the fluorescence light reaches aperture A of the fibre.

The power emitted by a section of fibre excited only by pulse A may be described as

$$dP_A = \frac{\delta N_1 A h \nu}{\tau} \left[\int_{-\infty}^{\infty} n^2(t) dt \right] e^{-\left(\frac{t+T+\Delta T+\left(\frac{2l}{v}\right)}{\tau}\right)} dl \tag{6}$$

where T is the transit time for a light pulse across one pass of the entire length of the fibre, ΔT is the relative delay time between the two excitation pulses, l is the distance from aperture A to the segment of fibre being interrogated at any given moment and v is the speed of light in the fibre. The factor of 2 is required as the excitation pulse must cover a distance l to the interrogation point then the fluorescence light must travel that same distance back to the detector.

Pulse B will always be travelling towards the detector and the detectable fluorescence is travelling in the same direction thus only a single pass within the fibre is considered. Furthermore, the fluorescence from any point in the fibre dP_B will always emerge from the fibre at the same time as the excitation pulse from laser B, that is at t=0. Therefore the fluorescent power emitted by a segment of fibre excited by pulse B will be

$$dP_B = \frac{\delta N_1 A h\nu}{\tau}\left[\int_{-\infty}^{\infty} n_B^2(t)\,dt\right] e^{-\frac{t}{\tau}} e^{-\frac{l}{v\tau}}\,dl \tag{7}$$

The total power emitted by each of these components can be found by integrating with respect to length over the length of the fibre

$$P_A = \frac{1}{2}\delta N_1 A h\nu v\left[\int_{-\infty}^{\infty} n_A^2(t)dt\right] e^{-\left(\frac{t+T+\Delta T}{\tau}\right)}\left(e^{-\frac{2T}{\tau}} - 1\right) \tag{8}$$

$$P_B = \frac{\delta N_1 A h\nu vT}{\tau}\left[\int_{-\infty}^{\infty} n_B^2(t)\,dt\right] e^{\left(\frac{-t}{\tau}\right)} \tag{9}$$

When both of these pulses are present in the fibre at the same time there will be an additional component, ΔP_{TPF}, generated by the cross correlation of the two pulses as they meet. To calculate the total photon flux at any moment in time when the pulses are partially overlapped but offset by a small increment t' such that $n(t) = n_A(t) + n_B(t+t')$ which can be integrated over all values of t to give the area under the two partially overlapped pulses for any given value of t'

$$G(t') = \int_{-\infty}^{\infty} n_A(t)\cdot n_B(t+t')\,dt \tag{10}$$

if t' is defined such that t'=0 represents the maximum overlap of the two pulses.

The total power emitted by the overlap region may then be evaluated by integrating G(t') over all values of t' to find $\Delta P_{TPF}(t)$, the total TPF power of the emitted by the fibre as the result of the cross-correlation of two counter-propagating laser pulses.

$$\Delta P_{TPF}(t) = \frac{2\delta A N_1 h\nu v}{\tau}\left[\int_{-\infty}^{\infty} G(t')\,dt'\right] e^{\frac{-t}{\tau}} \tag{11}$$

where dl, the element of the fibre, is replaced by $v \times dt'$.

A detailed derivation of the physical meaning and the implications of $\int_{-\infty}^{\infty} G(t')\,dt'$ will be outlined in section 3.3.2.

3.3. Calculations including specified pulse shape

3.3.1. Background signals P_A and P_B

With the general expressions for P_A, P_B and ΔP now defined it is possible to further expand them to calculate the fluorescent emission in terms of the known parameters which describe the excitation pulses used, namely the duration of the pulse, the shape of the pulse envelope and the total energy contained within that envelope by way of the total number of photons involved.

In the case where both pulse A and B are of equal duration (i.e. $\Delta t_A = \Delta t_B = \Delta t$), both pulses have a Gaussian profile and the fibre has negligible modal dispersion then the photon flux, n(t), at any given moment is

$$n(t)_{GAUSS} = n_o e^{-\left(\frac{t}{\Delta t}\right)^2} \tag{12}$$

where Δt is the duration covered by one standard deviation. Using this, it can be shown that the total number of photons within the pulse envelope can be found by integrating the instantaneous flux over the entire profile and multiplying by the cross-sectional area of the fibre thus using the standard integration

$$a \cdot \int_{-\infty}^{\infty} e^{-\left(\frac{x^2}{b^2}\right)} dx = a \cdot b \cdot \sqrt{\pi} \tag{13}$$

$$N = A \int_{-\infty}^{\infty} n(t)\, dt = A\, n_o \sqrt{\pi}\, \Delta t = \frac{A\, n_o \sqrt{\pi}\, t_p}{2\sqrt{\ln 2}} \tag{14}$$

where t_P is the FWHM pulse duration and n_o is the peak photon flux of the pulse.

The TPF within the fibre is generated via a non-linear process which is dependent on the square of the instantaneous photon flux $n(t)^2$ therefore the total power of the fluorescence pulse may be found by first integrating $n(t)^2$

$$\int_{-\infty}^{\infty} n(t)^2 dt = n_o^2 \int_{-\infty}^{\infty} e^{-2\left(\frac{t}{\Delta t}\right)^2} dt \tag{15}$$

which, using the same standard integration in equation (13), gives

$$\int_{-\infty}^{\infty} n(t)^2_{GAUSS}\,dt = \frac{\sqrt{\pi}}{\sqrt{2}} n_o^2 \Delta t = \frac{\sqrt{\pi}}{\sqrt{2}} \frac{N^2}{A^2 \pi \Delta t} = \sqrt{\frac{2\ln(2)}{\pi}} \frac{N^2}{A^2 t_p} \tag{16}$$

This can be substituted into equations (8) and (9), the general expressions for P_A and P_B, to give the total TPF power emitted by a length of doped fibre which has been excited by identical Gaussian shaped laser pulses

$$P_A = \frac{K}{2} \frac{\delta N_A^2 N_1 h\nu v}{A t_p} e^{\left(\frac{-t+T+\Delta T}{\tau}\right)} \left(e^{\left(\frac{-2T}{\tau}\right)} - 1\right) \tag{17}$$

$$P_B = K \frac{\delta N_B^2 N_1 h\nu v T}{A t_p \tau} e^{\left(\frac{-t}{\tau}\right)} \tag{18}$$

where K is an energy independent factor depending only on the pulse shape and, following (16), defined as

$$K = \frac{t_p A^2}{N^2} \int_{-\infty}^{\infty} n(t)^2 dt \tag{19}$$

Table 3.3.1.

Pulse Profile	K		n_o
Lorentzian	$\frac{1}{\pi}$	0.318	$\frac{2KN}{A t_p}$
Gaussian	$\sqrt{\frac{2\ln(2)}{\pi}}$	0.664	$\frac{\sqrt{2}KN}{A t_p}$
Hyperbolic Secant	$\frac{1.7627}{3}$	0.588	$\frac{3}{2}\frac{KN}{A t_p}$
Rectangular	1	1.000	$\frac{KN}{A t_p}$
Single-sided exponential	$\frac{\ln(2)}{2}$	0.346	$\frac{2KN}{A t_p}$

Table 3.3.1: Values of pulse shape coefficient K for common pulse profiles.

It has been found that so long as Pulse A and Pulse B have the same profile then the form of the equations for P_A and P_B differ only in the magnitude of this K factor. The values of K are given for several common pulse shapes in Table 3.3.1 above. This K factor may also be used to simplify some expressions such as in equation (14) to restate the peak photon flux of a Gaussian pulse as:

$$n_o = \frac{\sqrt{2}KN}{A t_p} \tag{20}$$

with the other common pulse shapes being re-expressed as in Table 3.3.1.

Table 3.3.2 shows a summary of the components derived above for the Gaussian shaped pulses and for several other common pulse shapes while full derivations of these components may be found in Appendix I.

Table 3.3.2.

Pulse Profile	Photon flux $n(t)$	Pulse duration FWHM, t_p	$\int_{-\infty}^{\infty} n^2(t)dt$	Cross-correlation $G(t')=\int_{-\infty}^{\infty} n_A(t)\cdot n_B(t+t')dt$	$\int_{-\infty}^{\infty} G(t')dt'$	Number of photons $N=A\int_{-\infty}^{\infty} n(t)dt$
Lorentzian	$\frac{n_o}{1+(t/\Delta t)^2}$	$2\Delta t$	$\frac{1}{2}\pi n_o^2 \Delta t$	$\frac{1}{2}\pi n_{oA} n_{oB} \frac{\Delta t}{\left[1+\left(\frac{t'}{2\Delta t}\right)^2\right]}$	$\pi^2 n_{oA} n_{oB} \Delta t$	$\pi A n_o \Delta t$
Single-sided exponential	$n_o \exp-(t/\Delta t)$ $t\geq 0$ 0 $t<0$	$\ln(2)\Delta t$	$\frac{1}{2} n_o^2 \Delta t$	$\frac{1}{2} n_{oA} n_{oB} \Delta t\, e^{-\left(\frac{t'}{\Delta t}\right)}$	$n_{oA} n_{oB} \Delta t^2$	$n_o A \Delta t$
Hyperbolic secant	$n_o \operatorname{sech}^2(t/\Delta t)$	$1.7627\Delta t$	$\frac{4}{3} n_o^2 \Delta t$	$\frac{4}{3} n_{oA} n_{oB} \Delta t \times\left[\frac{3\left(\left(\frac{t'}{\Delta t}\right)\cosh\left(\frac{t'}{\Delta t}\right)-\sinh\left(\frac{t'}{\Delta t}\right)\right)}{\sinh^3\left(\frac{t'}{\Delta t}\right)}\right]$	$4 n_{oA} n_{oB} \Delta t^2$	$2 n_o A \Delta t$
Gaussian	$n_o \exp-(t/\Delta t)^2$	$2\sqrt{\ln(2)}\Delta t$	$\sqrt{\frac{\pi}{2}} n_o^2 \Delta t$	$\sqrt{\frac{\pi}{2}} n_{oA} n_{oB} \Delta t\, e^{-(t'/\Delta t)^2}$	$\pi n_{oA} n_{oB} \Delta t^2$	$\sqrt{\pi} n_o A \Delta t$
Rectangular	n_o $\lvert t\rvert\leq \Delta t/2$ 0 $\lvert t\rvert>\Delta t/2$	Δt	$n_o^2 \Delta t$	$n_{oA} n_{oB} \Delta t\left[1-\lvert t'\rvert/\Delta t\right]$ $\lvert t'\rvert\leq\Delta t$ 0 $\lvert t'\rvert>\Delta t$	$n_{oA} n_{oB} \Delta t^2$	$n_o A \Delta t$

Table 3.3.2: Formulae and values of expressions for common pulse shapes.

3.3.2. The flash signal ΔP

As described in section 3.2, when the cross propagating pulses A and B interact with each other within the fibre the total flux, n(t), at any given moment in space and time is calculated from the cross-correlation of the two pulse envelopes with respect to the local delay, t', between them (where a $t'=0$ indicates the peaks of both pulses are coincident.). The fluorescent flux generated at the point when the two pulses are partially overlapping is given by

$$G(t')=\int_{-\infty}^{\infty} n_A(t)\cdot n_B(t+t')\,dt \tag{10}$$

which takes the product of the flux of pulse A, $n_A(t)$ with the flux of pulse B offset by the local delay t', $n_B(t+t')$ and integrates over all values of t to calculate the area of overlap as demonstrated in Figure 3.3.1 where two pulses each with a t_p of 20 ns are separated by a t' of 25 ns.

The total fluorescent flux emitted by this interaction is then found by calculating these flux areas for all values of t' (i.e. as the pulses transit through each other each other) and integrating all of these areas to find the total fluorescence produced as given by

$$\int_{-\infty}^{\infty} G(t')\,dt' \tag{21}$$

This is shown below in Figure 3.3.2 where the values for G(t') are calculated for several values from $t'=-100$ ns (where the pulses are essentially non-overlapping) through the peak overlap at $t'=0$ ns and out to $t'=+100$ ns where the pulses are again essentially non-overlapping.

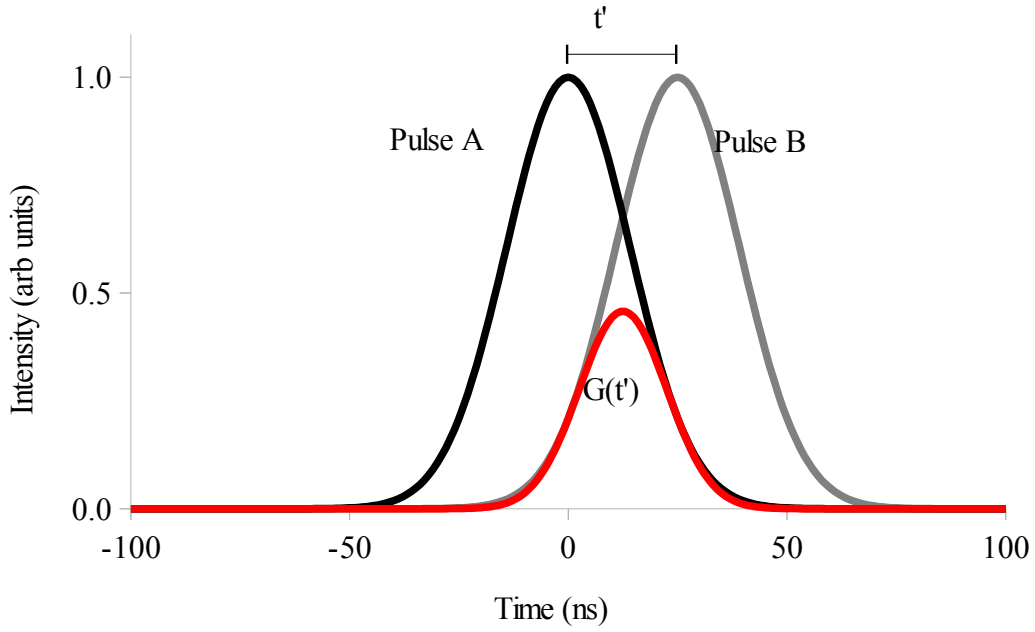

Figure 3.3.1: An illustration of the fluorescence produced by the partial overlapping Gaussian pulses, each with a t_p of 20 ns, separated by a time offset t'.In this example the pulses are separated by $t'=+25$ ns. When $t'=0$ the peaks of the two pulses are co-incident in time and G(t') is at a maximum. The total fluorescence produced as the pulses pass past each other is found by integrating G(t') over all values of t'.

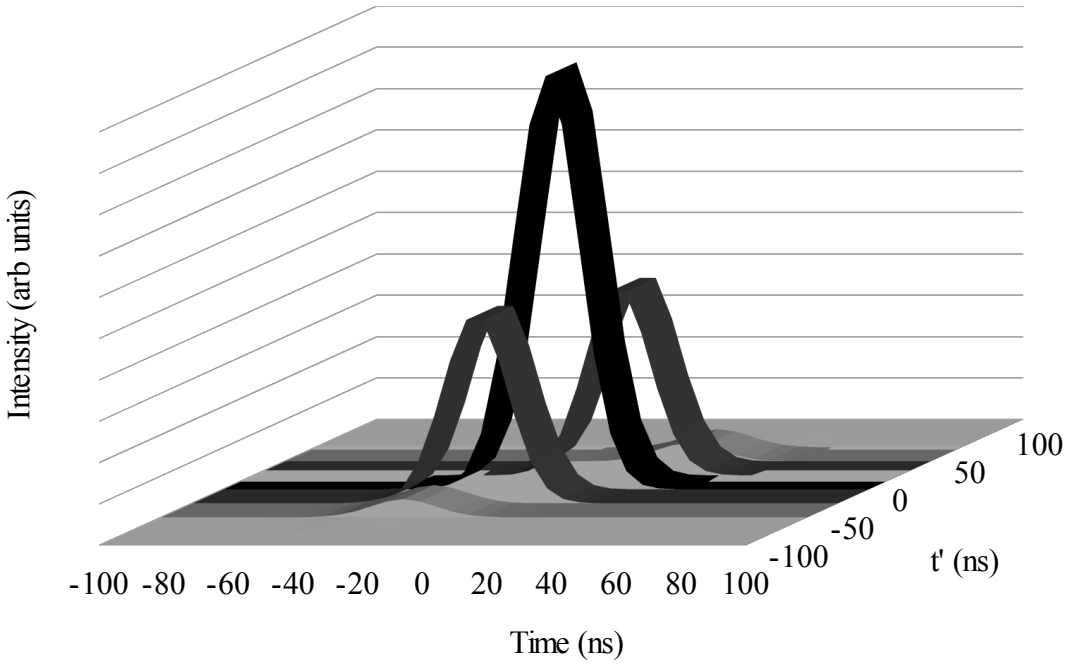

Figure 3.3.2: An illustration of the values of G(t') produced as the pulses translate from a separation of $t'=-100$ to $t'=+100$ ns. The total fluorescence, $\int_{-\infty}^{\infty} G(t')dt'$, is represented by the total volume under the resulting envelope.

In more formal mathematical notation, for the case of two similar Gaussian shaped pulses with equal pulse durations and peak fluxes, as in the example above, the interaction can be evaluated in terms of the total energy in each pulse in a similar manner to the calculations for the background signal.

The expression

$$G(t') = \int_{-\infty}^{\infty} n_A(t) \cdot n_B(t+t')\, dt \tag{10}$$

is expanded to

$$G(t')_{GAUSS} = \int_{-\infty}^{\infty} n_{oA} \cdot n_{oB} e^{\left(\frac{-t}{\Delta t}\right)^2} e^{\left(\frac{-(t+t')}{\Delta t}\right)^2} dt \tag{22}$$

which can be simplified by extracting the n_o and t' terms from the integral to give

$$G(t')_{GAUSS} = n_{oA} \cdot n_{oB} \cdot e^{-\left(\frac{t'}{\Delta t}\right)^2} \int_{-\infty}^{\infty} e^{-\left(\frac{2t^2}{\Delta t^2}\right)} \cdot e^{-\left(\frac{2tt'}{\Delta t^2}\right)} dt \tag{23}$$

to which can be applied the standard integration

$$\int_{-\infty}^{\infty} e^{-a(x^2+b\cdot x)} dx = \sqrt{\frac{\pi}{a}} e^{\frac{1}{4}a\cdot b^2} \tag{24}$$

where $a = \frac{2}{\Delta t^2}$ and $b = t'$ to give

$$G(t')_{GAUSS} = \sqrt{\frac{\pi}{2}} n_{oA} \cdot n_{oB} \cdot \Delta t \cdot e^{-\left(\frac{t'}{2\Delta t}\right)^2} \tag{25}$$

With this expression it is now possible to integrate G(t') over all values of t' to derive the total fluorescent photon flux generated by the Flash region of the fibre.

$$\int_{-\infty}^{\infty} G(t')_{GAUSS}\, dt' = \frac{\sqrt{2}\sqrt{\pi}\sqrt{\pi}}{\sqrt{2}} \cdot n_{oA} \cdot n_{oB} \Delta t^2 = \pi \cdot n_{oA} \cdot n_{oB} \Delta t^2 \tag{26}$$

Recalling equations (14) and (19) the t_P may be substituted in place of Δt and n_o terms may be expanded to give

$$\int_{-\infty}^{\infty} G(t')_{GAUSS}\,dt' = \pi \frac{\sqrt{2}\,K\,N_A}{A\,t_p} \frac{\sqrt{2}\,K\,N_B}{A\,t_p} \frac{t_p^2}{2\sqrt{Ln2}} \tag{27}$$

and expanding K using equation (20) gives

$$\int_{-\infty}^{\infty} G(t')_{GAUSS}\,dt' = \pi \frac{\sqrt{2}\sqrt{Ln2}}{\sqrt{\pi}} \frac{\sqrt{2}\sqrt{Ln2}}{\sqrt{\pi}} \frac{\sqrt{2}\,N_A}{A\,t_p} \frac{\sqrt{2}\,N_B}{A\,t_p} \frac{t_p^2}{4\,Ln2} \tag{28}$$

which simplifies to

$$\int_{-\infty}^{\infty} G(t')_{GAUSS}\,dt' = \frac{N_A\,N_B}{A^2} \tag{29}$$

This can be substituted into (11) to reveal the total fluorescent power emitted by the Flash region of the fibre sensor when excited by Gaussian shaped pulses.

$$\Delta P = \frac{2\delta\,N_A\,N_B\,N_1\,h\,\nu\,v}{A\,\tau} e^{-\left(\frac{t}{\tau}\right)} \tag{30}$$

Note that this means that the total emission power is not dependent on pulse shape, as can also be seen in the equivalent derivations for other common pulse profiles in Appendix I, nor is it dependent on pulse duration. The physical rational for this being that if the excitation pulses are longer (but the energy per pulse is conserved) then more excitable ions are exposed to the overlap region.

3.4. Dispersion/unequal pulse widths

The general form of the derivation for the power emitted by the sensing fibre makes the assumptions that the durations of pulses A and B are identical and that the dispersion for the excitation pulses in the fibre is zero.

In a real fibre however dispersion can become a significant factor, especially over long distances. If the example of a multi-mode fibre is taken then it can be shown that the degree of modal dispersion, in terms of change in pulse duration per unit distance of propagation, $\Delta t/z$ in a multi-mode fibre is given by[59]

$$\frac{\Delta t}{z}=\frac{n_2}{4 c n_1^2}\left(n_1^2-n_2^2\right) \tag{31}$$

Where n_1 is the core refractive index, n_2 is the cladding refractive index and c is the speed of light.

For a typical multi-mode silica fibre n_1 and n_2 may take values of 1.496 and 1.467 respectively[60] which results in a modal dispersion coefficient of 71 ps m^{-1}.

The model can therefore be adapted to remove either or both of the above assumptions by redefining the duration of each pulse such that

$$\zeta_{A,B}=\left(\Delta t_{A,B}+\left(D\cdot l_{A,B}\right)\right) \tag{32}$$

where $\Delta t_{A,B}$ is the initial duration of pulse A or B as it enters the fibre, D is the dispersion coefficient of the fibre, usually measured in ns/km or an equivalent unit and $l_{A,B}$ is the distance that the pulse has travelled down the fibre to the point being interrogated.

Making this substitution into the derivation for Gaussian shaped pulses gives the expression for G(t) dt:

$$G(t')dt=n_{OA}n_{OB}\int e^{-\left(\frac{t}{\zeta_A}^2\right)}e^{-\left(\frac{(t+t')}{\zeta_B}\right)^2}dt \tag{33}$$

which can be expanded to:

$$G(t')dt = n_{oA}\, n_{oB}\, e^{-\left(\frac{t'^2}{\zeta_B^2}\right)} \int e^{-\left[\left(t^2\frac{\left(\zeta_A^2+\zeta_B^2\right)}{\zeta_A^2\zeta_B^2}\right)+\left(t\frac{2t'}{\zeta_B^2}\right)\right]}dt \tag{34}$$

by using the standard integral

$$\int e^{-a\left(x^2+bx\right)}dt = \frac{\sqrt{\pi}}{\sqrt{a}}\, e^{\frac{1}{4}ab^2} \tag{35}$$

and setting

$$a = \frac{\left(\zeta_A^2+\zeta_B^2\right)}{\zeta_A^2\,\zeta_B^2};\; b = \frac{2t'}{\zeta_B^2}\frac{1}{a} = \frac{2t'\zeta_A}{\left(\zeta_A^2+\zeta_B^2\right)} \tag{36}$$

equation (34) can be solved to give

$$G(t')dt = n_{oA}\, n_{oB}\sqrt{\pi}\frac{\zeta_A\,\zeta_B}{\sqrt{\left(\zeta_A^2+\zeta_B^2\right)}}\, e^{-\left(\frac{t'^2}{\zeta_B^2}\left(1-\frac{\zeta_A^2}{\left(\zeta_A^2+\zeta_B^2\right)}\right)\right)} \tag{37}$$

Using the same principles outlined in Section 3.2. G(t) can now be integrated with respect to t' to obtain the total emission generated by the laser pulses at the overlap region of the fibre.

By noting equation (13), the standard integral $a\cdot\int e^{-\left(\frac{x^2}{b^2}\right)}dx = a\cdot k\cdot\sqrt{\pi}$

$$\int_{-\infty}^{\infty} G(t')\,dt' = n_{oA}\, n_{oB}\sqrt{\pi}\frac{\zeta_A\,\zeta_B}{\sqrt{\left(\zeta_A^2+\zeta_B^2\right)}}\int e^{-\left(\frac{t'^2}{\zeta_B^2}\left(1-\frac{\zeta_A^2}{\left(\zeta_A^2+\zeta_B^2\right)}\right)\right)}dt' \tag{38}$$

goes to

$$\int_{-\infty}^{\infty} G(t')\,dt' = n_{oA}\, n_{oB}\,\pi\frac{\zeta_A\,\zeta_B}{\sqrt{\left(\zeta_A^2+\zeta_B^2\right)}}\left[\frac{\zeta_B^2}{\left(1-\frac{\zeta_A^2}{\left(\zeta_A^2+\zeta_B^2\right)}\right)}\right]^{\frac{1}{2}} \tag{39}$$

Equation (20) is converted to reflect the relationship between t_p and Δt, which is then itself converted to the equivalent expression using ζ as shown in equation (32), to give the photon flux for a dispersing Gaussian pulse at a point in the fibre

$$n_{o\,A,B}=\frac{N_{A,B}}{\sqrt{\pi}\,A\,\zeta_{A,B}} \tag{40}$$

This expression is useful to expand $\int_{-\infty}^{\infty} G(t')\,dt'$ to give:

$$\int_{-\infty}^{\infty} G(t')\,dt'=\frac{N_A}{\sqrt{\pi}\,A\,\zeta_A}\frac{N_B}{\sqrt{\pi}\,A\,\zeta_B}\pi\frac{\zeta_A\,\zeta_B}{\sqrt{\left(\zeta_A^2+\zeta_B^2\right)}}\left[\frac{\zeta_B^2}{\left(1-\frac{\zeta_A^2}{\left(\zeta_A^2+\zeta_B^2\right)}\right)}\right]^{\frac{1}{2}}$$

$$\int_{-\infty}^{\infty} G(t')\,dt'=\frac{N_A\,N_B}{A^2}\frac{1}{\sqrt{\left(\zeta_A^2+\zeta_B^2\right)}}\left[\frac{\zeta_B^2}{\left(1-\frac{\zeta_A^2}{\left(\zeta_A^2+\zeta_B^2\right)}\right)}\right]^{\frac{1}{2}}$$

$$\int_{-\infty}^{\infty} G(t')\,dt'=\frac{N_A\,N_B}{A^2}\left[\frac{\zeta_B^2}{\left(\zeta_A^2+\zeta_B^2\right)\left(1-\frac{\zeta_A^2}{\left(\zeta_A^2+\zeta_B^2\right)}\right)}\right]^{\frac{1}{2}}=\frac{N_A\,N_B}{A^2}\left[\frac{\zeta_B^2}{\left(\left(\zeta_A^2+\zeta_B^2\right)-\frac{\zeta_A^2\left(\zeta_A^2+\zeta_B^2\right)}{\left(\zeta_A^2+\zeta_B^2\right)}\right)}\right]^{\frac{1}{2}}$$

$$\int_{-\infty}^{\infty} G(t')\,dt'=\frac{N_A\,N_B}{A^2}\left(\frac{\zeta_B^2}{\zeta_A^2+\zeta_B^2-\zeta_A^2}\right)=\frac{N_A\,N_B}{A^2}\left(\frac{\zeta_B^2}{\zeta_B^2}\right)$$

$$\int_{-\infty}^{\infty} G(t')\,dt'=\frac{N_A\,N_B}{A^2} \tag{41}$$

Which is identical to equation (29) therefore it can be seen that even in the presence of dispersion and making no assumption about the initial duration of either laser pulse the resulting output fluorescence pulse from ΔP is independent of pulse duration and depends only on the total energy contained in the pulses.

It should be noted however that dispersion will impact the effective spatial resolution of the sensor as illustrated in Figure 3.4.1 where a sensor with initial pulse durations of 1 ns and a fibre with zero dispersion produces a spatial resolution of 0.2 m throughout whereas a similar sensor employing a fibre with a dispersion factor

of

2 ps/m will see a maximum resolution of 0.6 m close to the ends of the fibre and a minimum resolution of 0.8 m at the centre of the fibre. (Both examples simulate a fibre with a core refractive index of 1.50).

In the numerical example for equation (31) a multi-mode fibre with a dispersion coefficient of 71 ps m^{-1} was described. If such a fibre were to be used in a 1 km distributed fibre sensor similar to the one above the spatial resolution of that sensor is shown in Figure 3.4.2. The resolution starts at 14.4 m when the overlap region is near either of the apertures of the fibre and is 267 m at the centre of the fibre. This highlights the importance of carefully selecting optical fibres to minimise the effects of dispersion and indicates that a single-mode fibre is likely to be a better candidate for use in a prototype sensor. Significant research has taken place for use in the telecommunications industry in reducing dispersion within single-mode fibres to a minimum and, in certain cases, eliminating it almost entirely[61] and the results of that research are valid for use in optical fibre sensors as well.

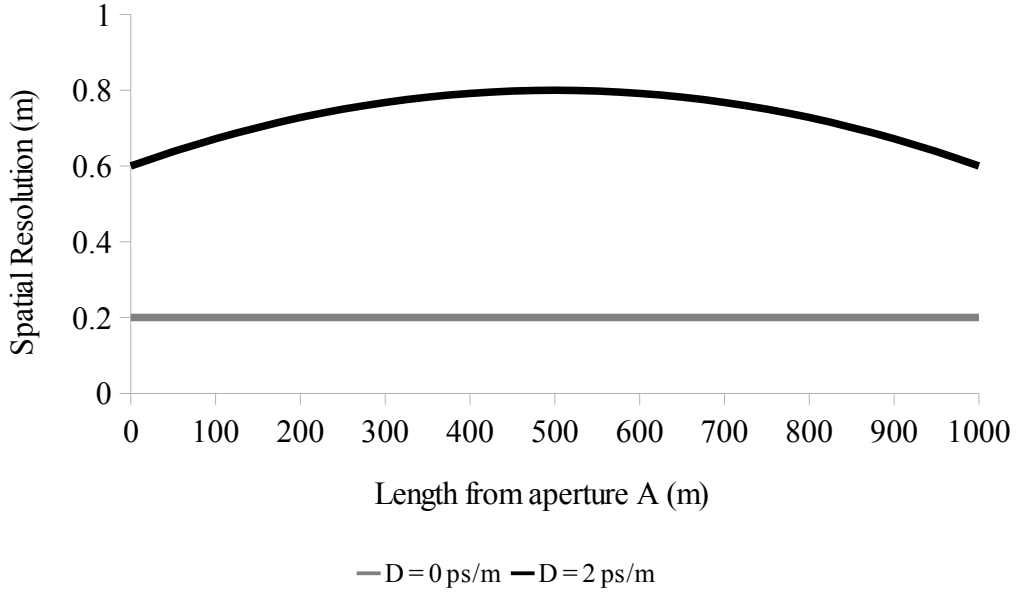

Figure 3.4.1: The spatial resolution of the fibre sensor as a function of the location of the overlap region with respect to aperture A. 1 ns pulses travelling through the fibre (with a core refractive index of 1.50) indicated by the grey line experience no dispersion and the sensor has an effective spatial resolution of 0.2 m throughout its length. Similar pulses travelling through the fibre indicated by the black line experience a dispersion of 2 ps m^{-1} thus the sensor has a variable spatial resolution of between 0.6 m and 0.8 m with the lowest performance occurring at the centre of the fibre.

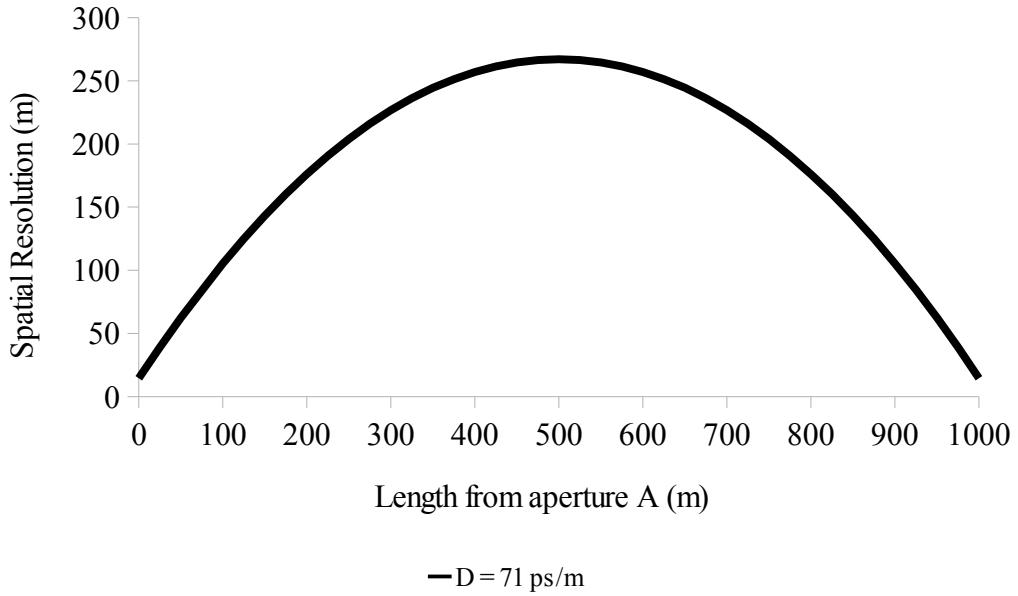

Figure 3.4.2: The spatial resolution of a distributed sensor constructed using a multi-mode fibre with a dispersion coefficient of 71 ps m^{-1}. The resolution is 14.4 m at the apertures and 267 m at the centre of the fibre.

3.6. Simulations

As stated earlier, the primary difference between the description of the proposed two-photon excited fibre sensor and the description of previous autocorrelation arrangements is that the latter is temporally integrated and spatially resolved whereas the former is temporally resolved but spatially integrated. As such the instantaneous intensity of the fluorescent emission from the proposed fibre sensor exhibits a distinct profile as it evolves with time.

To simulate this emission profile the fibre is considered to be excited by degenerate two-photon excitation using counter propagating pulses which have identical intensities and pulse profiles. Thus the total emission can be easily separated into its three components P_A, P_B and ΔP where these are given by equations (17) , (18) and (30) respectively. Since the excitation pulses have the same duration, profile and peak intensity the magnitude of the P_A and P_B should be identical.

Considering P_A only, the excitation pulse travels away from the detector (which is spliced into the fibre near the A aperture) and produces fluorescence throughout the length of the fibre and in all directions. The fluorescence is confined to the fibre only within two cones and only the cone which emits in the direction counter to the propagation fluorescence reaches the detector. As the detector is positioned against the aperture of the fibre (i.e. $l = 0$) the emission is detected immediately.

The excitation pulse which produces P_B however lies at the other end of the fibre and the fluorescence generated, of which only the co-propagating cone is detectable must be delayed by the transit time T before exiting the fibre and being detected.

The enhanced “flash” fluorescence generated at the crossing point of the two pulses must also be delayed by the transit time T and will first emerge from the fibre alongside pulse B and P_B. It may seem that if the flash is generated at the mid-point of the fibre then the emission should perhaps emerge at $t = T/2$ (assuming $\Delta T = 0$) but it must be remembered that pulse B must still travel to the crossing point before ΔP may be generated.

Figure 3.6.1 below demonstrates this simulation for a 10 m silica fibre excited by 10 ns Gaussian pulses such that fluorescence with a decay time of approximately 100 μs is generated.

In this simulation t=0 is defined as the point where the P_B and ΔP components are first detected. A core refractive index of 1.50 means that the transit time T for this fibre is 50 ns so that in this first instance P_A is detected starting from -50 ns.

If the pulse delay time ΔT is adjusted so that pulse A triggers 25 ns after pulse B then the crossing point is moved away from the centre of the fibre to a point 2.5 m towards the A aperture. Figure 3.6.2 shows the result of this shift, P_B and ΔP are still set to emerge at t=0 ns and P_A is seen to emerge only 25 ns before this.

By way of contrast, if the detector is moved to view the side of the fibre, as it would in an autocorrelation arrangement it would record a profile similar to the schematic in Figure 3.6.3 which shows the spatially resolved, temporally integrated version of both of the simulations described above. While a background fluorescence signal would be observed throughout the fibre due to the summation of P_A and P_B a bright region would be noted in the fibre due to the presence of ΔP. This flash region, which in this example is approximately 2 m wide, is shifted towards the A aperture by the effect of the delay time ΔT.

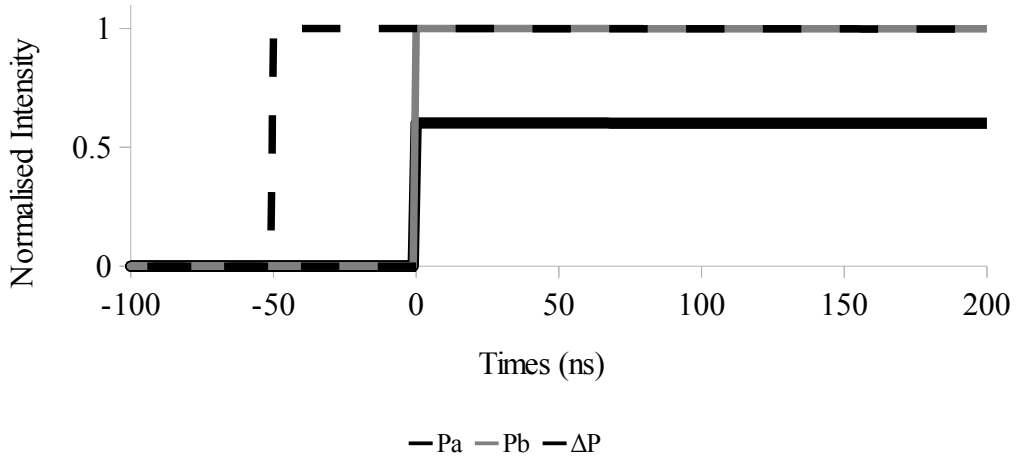

Figure 3.6.1: The simulated emission profile of the fibre sensor. (black dashed line) the fluorescence from P_A is detected from the moment that the pulse passes the detector at t = -50ns. (grey solid line) P_B emerges at t = 0 after travelling the entire length of the fibre and has an intensity similar to that of P_A. (black solid line) ΔP is also detected as it emerges at t = 0 and in this example has a magnitude of approximately 66% that of P_A. As the decay lifetime is significantly longer (≈100μs) than the transit time only minimal decay is observed on this time scale.

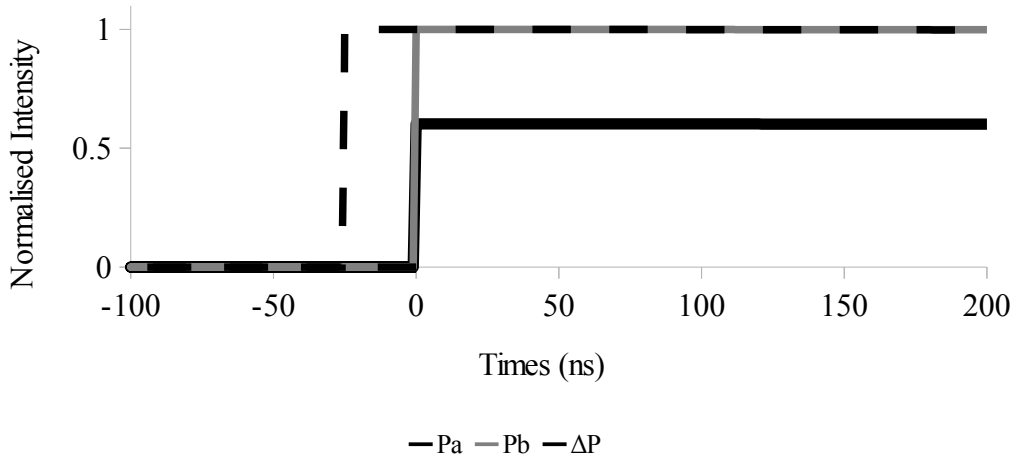

Figure 3.6.2: The simulation of the same fibre with the excitation pulses delayed so that pulse A emits 25ns after pulse B. The crossing point is centred 2.5m away from the A aperture.

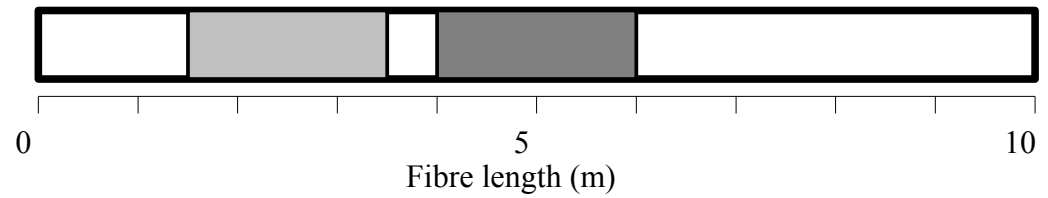

Figure 3.6.3: The position and width of the crossing region in relation to the 10m fibre with (dark grey) ΔT = 0ns as in Figure 3.6.1 and (light grey) ΔT = -25ns as in Figure 3.6.2.

In the case where the TPF fibre sensor must be excited by degenerate laser pulses the limits of detectability of the signal from ΔP are likely to be driven by the contrast ratio between the signal and background light as defined by

$$\text{Contrast ratio} = \frac{P_A + P_B + \Delta P}{P_A + P_B} \tag{42}$$

In the above example of 10 ns pulses travelling through a 10 m fibre with a core refractive index of 1.50 the contrast ratio is approximately 1.33. If the pulse durations are held constant at 10 ns and the fibre length increased, as in the example shown below in Figure 3.6.4, the contrast ratio will asymptote towards a value of 1.00 as the overlap region becomes much smaller in relation to the total fibre length. In this example it may become difficult to resolve the overlap signal at fibre lengths above 100 m without employing signal extraction techniques such as recording and subtracting off the background components of the signal or by reducing or eliminating the background signal.

Possible methods for improving the contrast ratio include simply increasing the pulse durations as this will reduce the background signals while leaving the total overlap emission unchanged (as ΔP is independent of pulse duration) although this will obviously impact the spatial resolution of the sensor.

A method to remove the background signals altogether may be possible by changing the excitation methods to a non-degenerate excitation as shown in Figure 3.6.5. The wavelengths of the two excitation lasers are chosen such that two photons from laser A or two photons from laser B cannot absorb in the medium but a combination of an A and a B photon (as can only occur within the overlap region) can. Thus the background signals P_A and P_B should be completely eliminated while the overlap signal ΔP should remain as intense as it would be in the degenerate case (assuming that the total energy contained within the two pulses is constant).

This method more than any other shows the greatest capacity for solving the background signal problem though as shall be seen in the experimental chapters it requires some careful planning with regard to the dopant material to be used in the fibre. While this method of excitation has been known, at least in principle, since the

earliest application of the two-photon microscope[62] its use in experimental research seems limited with only a few examples appearing in the literature.[63],[64]

If, due to the complexities of the chosen dopant material, true non degenerate two-photon absorption is not possible then a compromise setup may be able to be arranged whereby the laser A wavelength is non-resonant (i.e. not absorbing) and the laser B wavelength is partially or fully resonant as shown in Figure 3.6.5. The energies contained within each pulse could then be arranged such that N_A is much greater than N_B. This would mean that the background component P_A would be non-existent, P_B would be present but much weaker than in the degenerate case (as P_B is proportional to the square of N_B) and ΔP would remain the same as in the degenerate case (again assuming that the total energies involved were constant).

Finally, the K factor may be used to reduce the effective background by careful selection of the pulse profiles used. This factor relates to the fraction of the total energy of the excitation pulse which is contained within the limits of the FWHM, that is, the portion of the pulse with the highest flux. Due to the non-linear nature of the two-photon excitation, photons which reside in the outer wings of the pulse play a greatly reduced role in generating fluorescence. Careful selection of the excitation pulses with a view of minimising K will therefore reduce the generated background light. As an example, from the pulses derived in Table 3.3.1, the rectangular pulse (which contains all of its photons within the FWHM) will generate 50% more background light than a pair of Gaussian pulses and more than 300% more background than the Lorentzian pair.

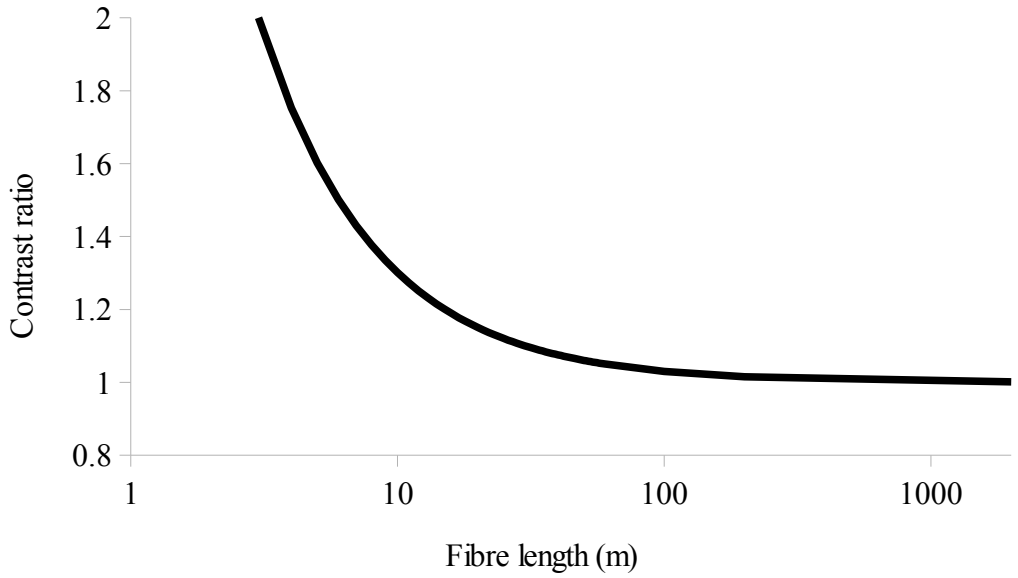

Figure 3.6.4: The change in the contrast ratio of the fibre with fibre length. Excitation pulses are 10 ns in duration which in a fibre with a core refractive index of 1.50 results in an overlap region approximately 2 m in length.

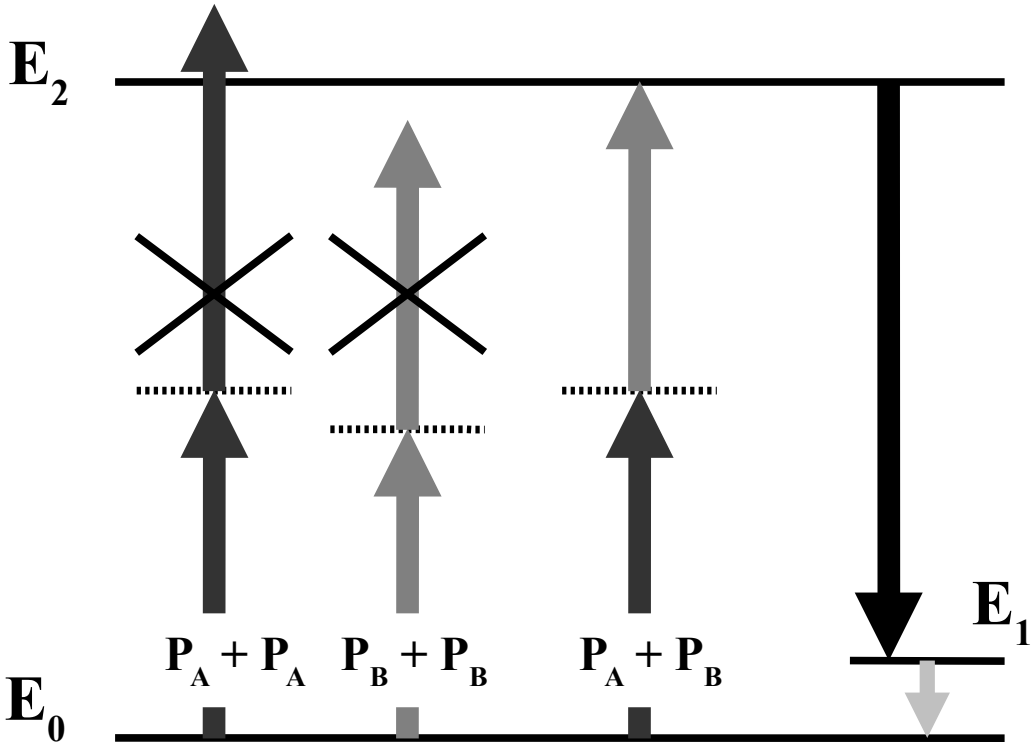

Figure 3.6.5: Non-degenerate two-photon absorption. The wavelengths of the two excitation lasers are chosen such that two photons from laser A or two photons from laser B cannot absorb in the medium but a combination of an A and a B photon (as can only occur within the overlap region) can.

3.7. Conclusion

It can be seen in equation (30) that the total TPF power emitted by the overlap region, ΔP, is completely independent of pulse duration (t_p) and pulse profile. The explanation for this lies in the geometry of the system. The intensity of the excitation light is inversely proportional to the pulse duration but the number of ions which can be illuminated by the overlap region is directly proportional to the length of the cross-correlation of the pulses within the fibre which is in turn directly proportional to the pulse duration. These two effects exactly cancel with each other such that the output TPF power is proportional only on the total energy contained within the excitation pulses. This means that despite being reliant on a non-linear optical process the generation of two-photon fluorescence within the flash region need not require the complex picosecond and femtosecond pulse sources which have been characteristic of typical non-linear optical studies prior to this one.

This discovery opens the possibility of the development of a practical optical fibre sensor employing relatively inexpensive and compact and portable systems based on modulated diode lasers. The system also has the potential for excellent spatial resolution as it is determined solely by the width of the flash region thus, for a silica glass fibre, resolutions of up to 2 → 200 cm may be obtained from the 0.1 → 10 ns pulses delivered by typical laser diode systems. The limits to this resolution will ultimately be set by dispersion of the pulses as they travel through a real optical fibre but it can be seen that in many practical applications this effect remains relatively small.

An important parameter not yet discussed in detail is the two-photon absorption cross-section, δ. By measuring the δ of potential sensor dopants, among other parameters, their viability for use in a distributed temperature sensor can be assessed. A new method for measuring this parameter will be presented and tested in the following chapter.

4. The TPF absorption cross-section

4.1. Introduction

When examining potential dopant materials for their viability as a sensing medium it is important to be able to calculate ahead of time the likely quantity of fluorescence which will be available for sensing purposes and the likely laser power required to excite the medium with sufficient intensity as it may be found that an otherwise ideal candidate simply does not absorb enough light to be effective. Therefore one of the important parameters to consider when investigating the two-photon spectroscopic properties of optically active materials is the two-photon absorption cross-section, usually denoted as either δ[65] as it is in this investigation or as σ_2.[66] Analogous to the single-photon absorption cross section but weak enough that the usual method of measuring the absorption directly by monitoring the extinction of a laser beam passing through it is difficult though it has been demonstrated at least once.[67]

Several other methods of measuring the TPA cross-section exist in the literature the most widely used of which is the z-scan method first described by Sheik-Bahae et al[68] where the sample to be measured is placed near to the focal point of a focussed laser beam. The change in transmittance as the sample is moved towards and through the focal point is measured and, as the non-linear absorption is dependent on photon flux and thus inversely dependent on beam area, the cross-section may be derived. The advantage of this method compared to some other methods is that is dependent only on the absorption characteristics of the sample thus it can be used with samples which have little or no fluorescent emission although the method is limited in that the photon flux must be kept below the damage threshold of the sample which may be difficult near the focal point of the beam especially if pulsed lasers are used.[69]

Fluorescence based methods for calculating the two-photon absorption cross section include one developed by Xu and Webb and involves comparing the intensity of the TPF emission as a function of the input excitation energy to that of another

sample which has a known value of δ.[70]

The disadvantage of this method, aside from requiring a reference sample with known properties, is that certain parameters which can differ between samples such as the absolute quantum efficiency must be measured, a process which can be complicated.[71]

The method used in this investigation is similar to the one used by Xu and Webb but instead of comparing the fluorescent emission of the target sample with a reference sample the method presented here compares the two-photon emission from the sample with the single photon emission intensity resulting from the same emission transition in the same sample. One immediate advantage of this method are that it can be used without a reference sample thus it provides a more direct measurement of δ.

4.2. Calculating δ, the absorption cross section

The calculation of δ, the two-photon absorption cross section may be performed by considering the fluorescent power output of a thin sample of doped material excited by single- and two-photon absorption.

The peak upper state population within any segment of the fibre, $N_2(0,z)$, is determined by the degree of absorption that the excitation pulse has undergone before reaching that segment.

The general form of Beer's Law states that the absorption of light as it passes through a medium is given by:

$$\frac{I}{I_0} = e^{-A'l} \tag{43}$$

where I is the intensity of the light as it exits the medium, I_0 is the intensity of the incident light as it enters the medium, l is the thickness of the medium and A' is the absorbance of the medium.

In the case of single-photon absorption, A' is related to both the single-photon absorption cross-section and the concentration of the medium such that Beer's Law becomes:

$$\frac{I}{I_0} = e^{-\sigma N_1 l} \tag{44}$$

In the two-photon absorption case the absorption of the medium is non-linear and thus dependent on the square of the incident photon flux, n_0 so that the 2nd order Beer's Law becomes:

$$\frac{I}{I_0} = e^{-\delta \int n''^2(t)dt N_1 l} \tag{45}$$

This spatial variation of the excitation intensity leads to the modification of equation (1) such that:

For SPA

$$N_2'(0,z) = \sigma N_1 \int n'(t)dt\, e^{-\sigma N_1 l} \tag{46}$$

and for TPA

$$N_2''(0,z) = \delta N_1 \int n''^2(t)dt\, e^{-\delta \int n''^2(t)dt N_1 l} \tag{47}$$

but the vast difference in the comparative magnitudes of the single- and two-photon absorption cross-sections mean that for most reasonable samples the amount of excitation light absorbed by TPA is negligible, as illustrated in Figure 4.2.1 and Figure 4.2.2 below. Therefore the two-photon excitation pulse can be considered to be unchanged as it passes through the sample and the spatial variation term may be dropped such that

$$N_2''(0,z) = \delta N_1 \int n''^2(t)dt \tag{48}$$

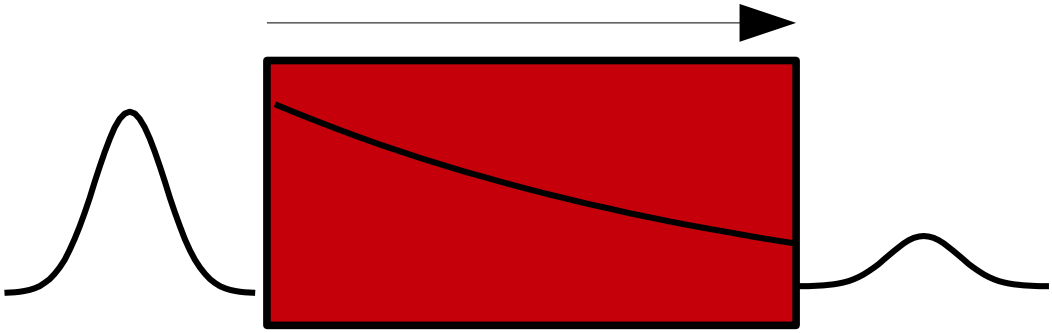

Figure 4.2.1: A Gaussian pulse transmitted through one optical length of a material while undergoing single-photon absorption. The peak intensity of the pulse is reduced by a factor of e^{-1}.

Figure 4.2.2: A similar pulse transmitting through the same thickness of material but this time undergoing two-photon absorption. The relatively low absorption cross-section in comparison to the SPA means that the pulse is essentially unchanged once it exits the sample.

The total fluorescence power emitted as a function of both space and time over a fibre of length L may be found by combining the spatial variation above with the temporal variation found earlier and integrating across the length of the fibre such that

$$P(t,z)=\frac{\eta F A h\nu}{\tau}e^{-\frac{t}{\tau}}\int_0^L N_2(0,z)dz \tag{49}$$

where η is the quantum efficiency of the fluorescent emission, A is the cross-sectional area of the sample excited by the beam, τ is the lifetime of the decay of the fluorescence, F is the collection efficiency of the emitted light.

For single-photon excited fluorescence is therefore

$$P'(t,z)=\frac{\eta F A h\nu}{\tau}e^{-\frac{t}{\tau}}\sigma N_1\left[\int n'(t)dt\right]\int_0^L e^{-\sigma N_1 l}dz \tag{50}$$

$$P'(t)=\frac{\eta F A h\nu}{\tau}e^{-\frac{t}{\tau}}\sigma N_1\left[\int n'(t)dt\right]\frac{1}{\sigma N_1}\left[1-e^{-\sigma N_1 L}\right] \tag{51}$$

$$P'(t)=\frac{\eta F A h\nu}{\tau}e^{-\frac{t}{\tau}}\left[\int n'(t)dt\right]\left[1-e^{-\sigma N_1 L}\right] \tag{52}$$

As the two-photon absorption is relatively negligible the total TPF emitted is simple:

$$P''(t)=\frac{\eta F A h\nu}{\tau}e^{-\frac{t}{\tau}}\left[\int n''(t)^2dt\right]\delta N_1 L \tag{53}$$

This gives the final expression for the two-photon absorption cross-section:

$$\delta=\frac{P''(t)}{P'(t)}\frac{\int n'(t)dt}{\int n''^2 dt}\frac{\left[1-e^{-\sigma N_1 L}\right]}{N_1 L} \tag{54}$$

It can be seen that if the experimental geometry is identical in both single- and two-photon cases and that the same excitation and emission pathways are addressed then both the quantum efficiency and collection efficiency terms cancel.

This expression for δ can be converted into easily measurable parameters by solving the integrated terms, as detailed in Table 3.3.2. and converting N, the

number of photons per excitation pulse into E, the energy per pulse and, for convenience, the excitation pulse is described in terms of wavelength λ.

$$\delta = \frac{P''(t)}{P'(t)} \frac{E'}{E''^2} \left(\frac{A'' t_p''}{K} \right) \left(\frac{h\lambda'}{\lambda''^2} \right) \frac{\left[1 - e^{-\sigma N_1 L}\right]}{N_1 L} \tag{55}$$

In practice, one of the largest sources of uncertainty in measuring δ is in an accurate estimation of the dopant density. We can eliminate this in samples which have a low enough single-photon absorption that, as in the two-photon absorption case, the excitation pulse remains essentially unchanged by its passage through the sample. In such "optically thin" samples the exponential term may be expanded by using the approximation $e^a = 1 + a + \frac{a^2}{2!} + \frac{a^3}{3!} + \ldots$ taken to the second term to give

$$\delta = \frac{P''(t)}{P'(t)} \frac{E'}{E''^2} \left(\frac{A'' t_p''}{K} \right) \left(\frac{hc\lambda'}{\lambda''^2} \right) \sigma \tag{56}$$

Typical values for δ can vary by several orders of magnitude depending on the material but will generally fall around 1 GM or 1×10^{-50} cm^4 s ion^{-1} $photon^{-1}$ with organic dyes designed for two-photon microscopy or 3D data storage tending to take higher values[65][72] than rare-earth[65] or transition metals[73]

4.3. Experimental Procedure

The derivations for the calculation of absorption cross-sections described in Section 4.1. is new and therefore required experimental validation by applying it to a substance with a known single- and two-absorption cross-section.

Rhodamine 6G (R6G) was chosen as it was readily available and its absorption cross-section is both known to be reasonably high and can be measured using nanosecond pulses from a 1064 nm laser[74] similar to the one proposed for this work. The ability to make up a solution with a controlled value of the dopant number density, N_1 was also considered highly advantageous as it would allow validation of the approximations made across equations (43) and (49).

Rhodamine 6G, shown below in Figure 4.1.1, is an organic dye and is a

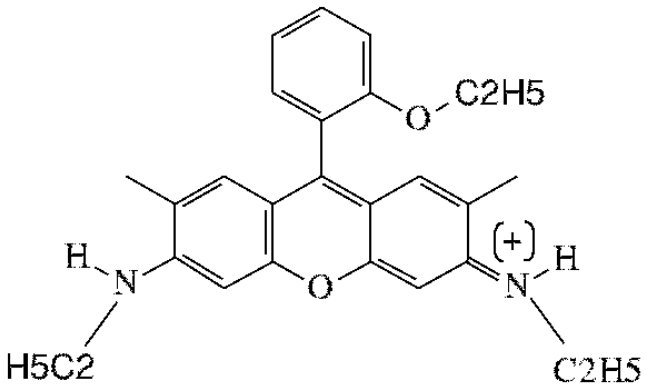

Figure 4.1.1: The molecular structure of Rhodamine 6G

member of the rhodamine sub-group of the class of xanthanine derived dyes and readily dissolves in a variety of solutes including water and ethanol although the former is rarely used as it can cause the dye to form aggregates which hamper fluorescence[75]. When dissolved in ethanol, R6G is known to have a peak absorption of around 530 nm and a peak emission of 590 nm.[76] This makes it an excellent test sample as it could be easily excited via SPA using a Nd:YAG laser operating through a frequency doubling crystal to produce 532 nm output and via TPA using the fundamental output of the same laser so as not to disturb the geometry of the experiment. This would permit the comparison of excitation modes required to calculate the two-photon absorption cross-section with precision and without requiring detailed knowledge of difficult to measure quantities such as the number density of the sample and quantum efficiency at a given temperature.

As mentioned above, both the σ_{532nm}[77],[78] and δ_{1064nm}[65] for R6G have previously been measured as 4.58×10^{-16} cm^2 molecule^{-1} and 5.5×10^{-50} cm^4 s molecule^{-1} photon^{-1} respectively. A previous attempt[67] by the author to measure δ_{1064nm} using a method similar to the one outlined here gave an estimate approximately 2 orders magnitude higher than these values.

The source of this overestimation was identified as being caused by the cuvette used for the measurements exceeding the maximum permissible length, L_{MAX}, to still be considered a thin sample as the thickness of sample through which not less than 90% of the original incident laser energy is transmitted and is calculated, by

rearrangement of the single-photon Beer's Law, as:

$$L_{MAX} = \frac{-\ln(0.90)}{\sigma N_1} \tag{57}$$

This resulted in the sample becoming optically saturated during the single-photon excitation phase thus the underestimation of the amount of fluorescence generated by SPF and a low value of P'(t) which, as can be seen by (49), inflated the apparent value of the two-photon absorption cross section.

For the cuvette used, which was 3mm thick, the maximum permissible concentration was calculated as $4x10^{-7}$ mol.

A solution of R6G was made by dissolving the crystals in ethanol to a concentration of approximately10^{-8} mol. Some uncertainty in the concentration may be present as it has been noted[79] that the methyl groups attached to the main body may (as in the case presented by Hammond[78]) or may not be present on the structure of the molecule which may introduce an error in the estimate of the molar weight upon which the concentration is based by up to 6%. The presence or absence of these methyl groups however should not significantly affect the absorption or emission characteristics as the optically active component of this class of dyes lies in the C=C-C=C structures known as conjugated bonds.[80]

The excitation source was a Continuum Minilight Nd:YAG laser which normally emitted 6 ns pulses at 1064 nm with a maximum output of 25 mJ per pulse but, through the addition of a second harmonic crystal, could also emit 532 nm with a maximum output of 9 mJ per pulse. In both cases the laser could operate at a maximum of 15 Hz. This was targeted onto the sample with the aid of a HeNe laser co-aligned onto the path of the Nd:YAG located using marks burned onto exposed photographic paper as shown in Figure 4.3.2.

Beam energy was measured using a thermopile which was capable of withstanding the high peak powers of the laser when it was operating at maximum output. The output of the thermopile was cross calibrated with a photodiode using the lower powered HeNe laser and a cw Nd:YAG laser.

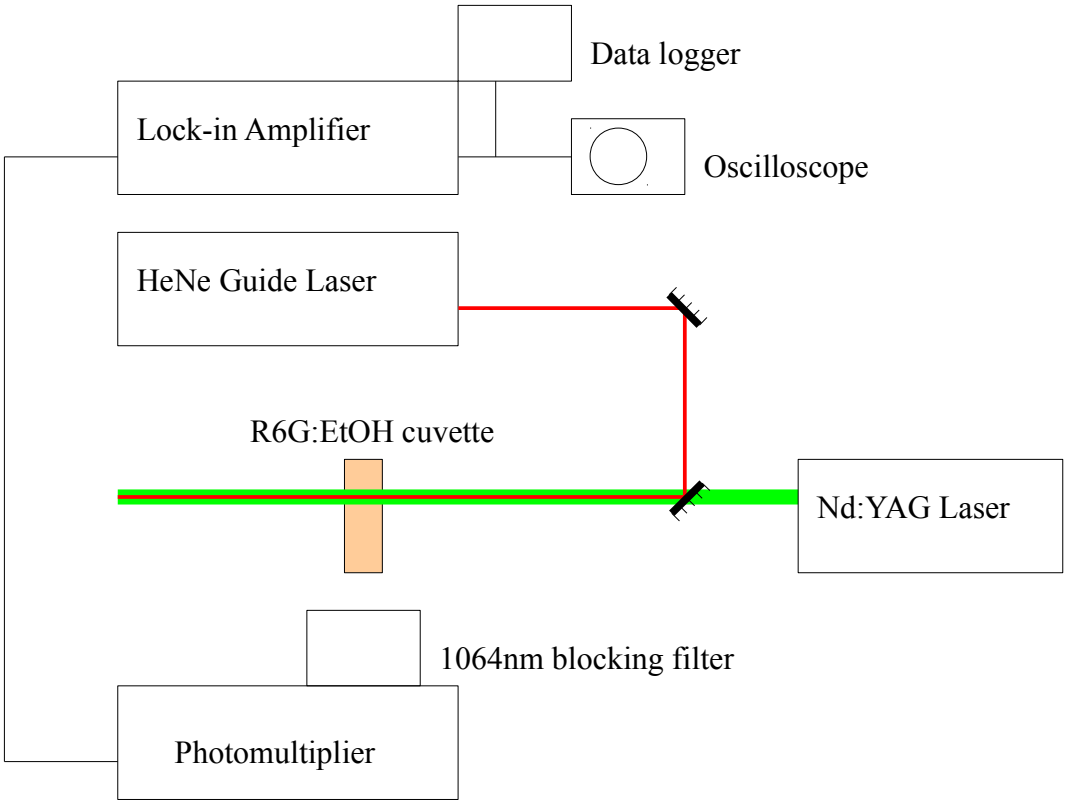

Figure 4.3.2: Experimental arrangement for the detection of TPF from Rhodamine 6G.

The importance of ensuring against saturation effects can be seen in Equation (49) as they would cause an artificially low measurement of P'(t) (the relatively weak effects of two-photon absorption mean that saturation will appear in the SPA experiments long before they could with TPA) which would, in turn, inflate the estimate of δ.

The first can be checked by calculating the maximum permissible photon flux for the sample

$$\left(\frac{E'}{A}\right) = \frac{hc}{\sigma \lambda'} \tag{58}$$

for SPA and

$$\left(\frac{E''}{A}\right)^2 = \frac{\tau}{\delta}\left(\frac{hc}{\lambda''}\right)^2 \tag{59}$$

for TPA.

This yields values of around 0.8 mJ cm^{-2} for the SPA case and 1 kJ cm^{-2} for the TPA case.

In addition the optical saturation caused by an excessive path length, electrical saturation of the photomultiplier also had to be considered and avoided. In most cases the electrical saturation issue could be addressed by adjusting the gain voltage across the PM but in this case there was a requirement to avoid this in order to simplify the comparison on the SPF P'(t) and the TPF P''(t).

The electrical saturation was a little harder to distinguish but could be avoided by adhering to the manufacturers guidelines for the use of the photomultiplier, namely that the current through the PM should be kept below 1 mA. The terminator attached to the PM was, in this case, a low noise 50 Ω termination which implies that electrical saturation starts to take effect when P'(t) is greater than approximately 50 mV which was, coincidently, around the same point that the optical saturation started to manifest.

Both optical and electrical saturation effects could therefore be minimised

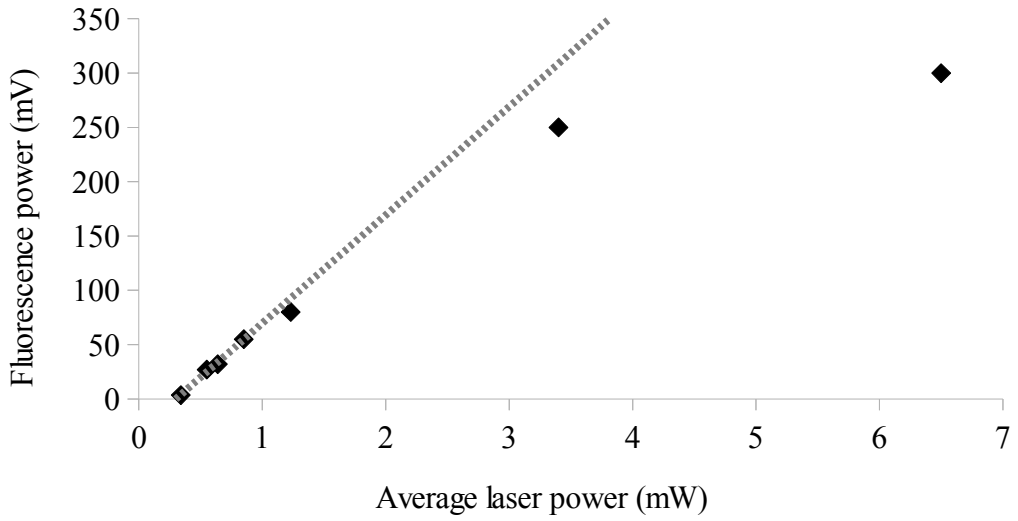

Figure 4.3.1: The optical saturation threshold for P'(t) in R6G. The dashed line represents an ideal plot without saturation.

simultaneously by keeping the average incident laser power below about about 1 mW or 7 μJ per pulse as verified by Figure 4.3.1 in which the SPF emission is plotted in relation to the excitation energy as the dye crosses into the saturation region.

4.4. Experimental Results

After several attempts to optimise the fluorescence output and minimise saturation effects, the electrical component of which was only finally eliminated by placing an ND filter which reduced transmitted light by 2.17×10^{-6} at 532 nm over the PM aperture during the SPF measurements.

The results discovered are summarised below in Table 4.4.1. Included in the estimates for E' and E" are the losses due to Fresnel reflection from the air/glass and glass/ethanol boundaries of the cuvette, such that 95.8% of the laser power incident on the cuvette is available to be absorbed by the R6G.

The uncertainty in the concentration was difficult to quantify due to the uncertainty in the exact chemical structure of the dye as mentioned by Drexage[66] the contribution of this potential uncertainty was neglected from the calculations.

The temporal profile the laser spot was observed using a high speed laser diode and was found to approximate a Gaussian distribution thus a K factor of 0.664

was used as the pulse shape co-efficient.

Applying the values above to equation (49) yields a value of the two-photon absorption cross-section of Rhodamine 6G of 4.4×10^{-50} cm^4 s $molecule^{-1}$ $photon^{-1}$ or 4.4 GM. This value has a margin of uncertainty attached to it of approximately 60%.

Applying the same data to the full form equation (43) gives a value which is essentially identical to the above value. It is thus shown that so long as the conditions for the approximation are valid then equation (49) returns accurate results and the requirement for precise knowledge of the dopant density of a particular sample is greatly lessened. It is therefore possible to use this method even in cases where the dopant density is unknown or not practical to measure. It is sufficient to ensure only that the sample used absorbs less than 10% of the incident excitation light at the SPA wavelength chosen.

Table 4.4.1. Calculation of δ in R6G			
Parameter	Value	Unit	% Uncertainty
P'(t)	8.1	mV	27
P”(t)	4.3	mV	22
E'	1.2	mJ/pulse	27
E”	24	mJ/pulse	2
A”	0.049	cm^2	10
t_p”	6	ns	17
λ'	532	nm	<1
λ”	1064	nm	<1
σ_{532nm}	4.58×10^{-16}	cm^2 $molecule^{-1}$	10
N_1	6.02×10^{12}	molecule cm^{-3}	*
K	0.664	[dimensionless]	n/a
Nd	2.17×10^{-6}	[dimensionless]	2

* *Difficult to quantify. See main text.*

Table 4.4.1: The table of data used for the calculation of the two-photon absorption cross-section of rhodamine 6G.

4.5. Conclusion

A novel method for measuring the two-photon absorption cross-section in a fluorescent medium has been developed and presented. Advantages over other methods include fewer technical challenges as the geometry of the experimental arrangement is not changed between measurements, no need for previously measured reference samples and no requirement for difficult measurements such as the absolute quantum efficiency of the sample.

While the experimental results for δ_{1064nm} for R6G agree closely with the values obtained for nanosecond excitation by Bradley[74] the relatively high uncertainty value at this stage may be a cause for concern. The principle source of uncertainty was from the shot-to-shot variation in laser pulses, especially when trying to measure the extremely low fluorescence signals generated by P”(t).

It should be noted however that even this rough method has yielded results from an organic dye which has a relatively low cross-section compared to other known dyes which can take values many hundreds or thousands of times higher and it has done so using nanosecond scale excitation and a minimum of signal processing.

With this result is is now possible to examine the two-photon absorption cross-section in unknown samples which may be of use for temperature sensing such as the ruby which will be examined in the next chapter.

5. Ruby

5.1. Introduction

For more than fifty years ruby (Cr^{3+}:Sapphire) has been of great importance to the fields of optoelectronics and optical sensing. Not only was ruby the first optical wavelength laser to be demonstrated[81] but it has also had its fluorescence characteristics extensively studied especially for the sensing of pressure, temperature and strain by detecting the emission from the R-lines at approximately 694.3 nm and measuring changes in their spectral shift[82], relative intensities[83] and changes in the fluorescence decay time.[84] The effect that temperature has on the absorption spectrum is also well known and has been studied even as far back as the early 20th century.[85]

Ruby has also had its single-photon absorption spectrum and absorption cross-section spectrum studied in detail in the visible light spectral region (first by Maiman[86], although Cronemeyer[87] found that Maiman had erroneously switched the labelling of the ordinary and extraordinary birefringent axes.). Despite this historical importance however the two-photon absorption properties had not, until this investigation, been studied in any great detail.

Figure 5.1.1 shows a schematic of the energy level structure of ruby and its absorption and emission pathways. In the visible region and under a single-photon regime light is absorbed and excites a Cr^{3+} ion to either the $^4T_1$ and $^4T_2$ lines (single photon absorption peaks at around 400 nm and 550 nm respectively). It may then relax by non-radiative means to the meta-stable ^2E state which produces two well known fluorescence lines known as the R-lines at 694.3nm for R_1 and 692.2 nm for R_2 as is illustrated below in Figure 5.1.1.

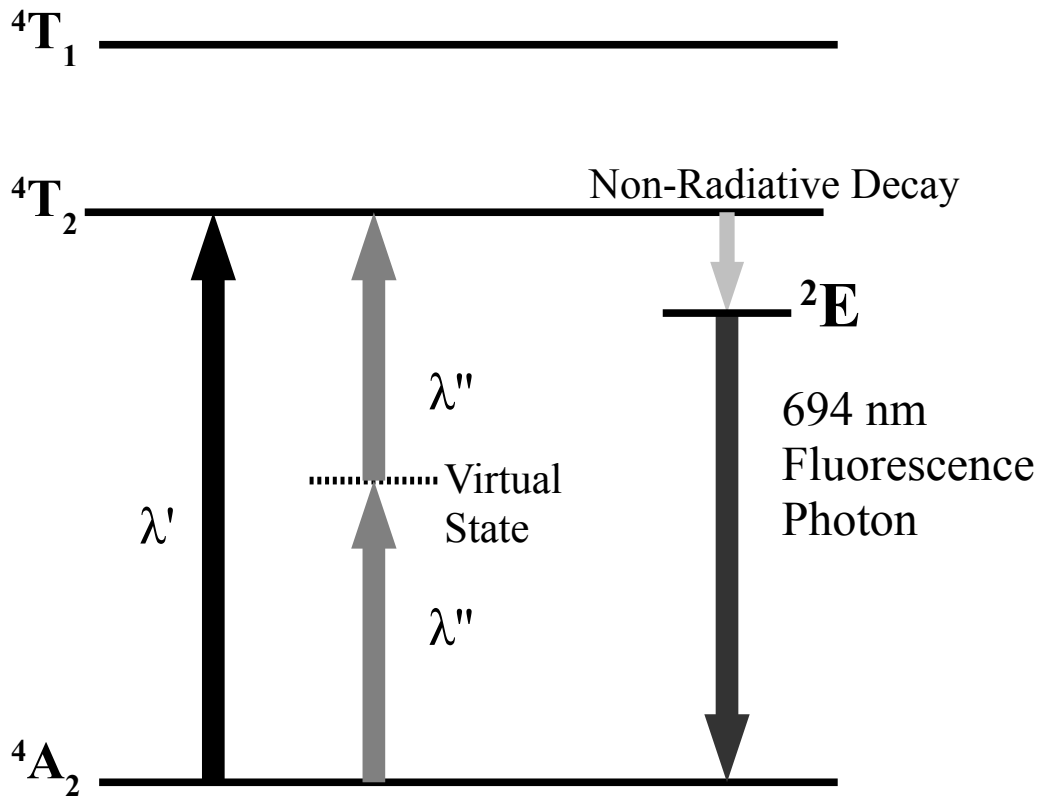

Figure 5.1.1: Simplified energy level diagram for ruby showing both single photon absorption (SPA) and two-photon absorption (TPA) leading to fluorescence via the R-lines and 694 nm

Despite this proven track record and the historical significance of ruby as a fluorescent medium investigations are not as well developed as many organic compounds such as rhodamine 6G or even as much as some of the rare-earth metals detailed later in this thesis. During the precursors to this investigation, which included a preliminary study of two-photon fluorescence in ruby[77], the only independent study of TPF in ruby was published although it focused only on reporting the observation of the fluorescence and made little mention of any quantifiable details of the emission properties beyond confirming a non-linear dependence on excitation power.[88]

This investigation was therefore able to design several experiments to measure the absolute two-photon absorption cross-section of ruby first at a single wavelength then over the NIR spectral range and the polarisation dependence of the absorption over this range. The temperature dependence of the fluorescence decay time constant was also measured under two-photon excitation and was compared to

the temperature response under single photon excitation both by experiment here and by comparison with existing literature.

5.2. Determining birefringent axes and dopant density of ruby.

While the basic experimental arrangement for the measurement of δ in ruby was basically similar to the arrangement used for R6G, some modifications were made. First, ruby exhibits a birefringent index so that the 1 mm thick sample used had to be aligned such that the plane polarised laser beam was parallel to either the ordinary (o-) or extraordinary (e-) axis. First, a set of two rotatable polarisers were placed in the path of a low power HeNe laser such that the beam was totally extinguished. The ruby sample was then placed within a rotatable mount and set between the two polarisers. It can be shown that the ruby will distort the polarisation axis of the beam such that total extinction is prevented in all cases except when the beam is parallel with one of the optic axes of the crystal.[89] It is then possible to positively identify each of these axes as either o-axis or e-axis by checking the single-photon absorption cross-section of the sample for each of these axes since the value of the single-photon absorption cross-section, according to Cronemeyer[87], for σ_o at 532 nm = 1.60×10^{-19} cm^{-2} ion^{-1} and σ_e = 0.60×10^{-19} cm^{-2} ion^{-1}.

A cw Nd:YAG was used to measure the transmission; hence α, the absorption co-efficient of the sample at 532 nm for both axes. For the 0.11 cm crystal sample and including a factor of 0.856 to account for Fresnel reflection $\alpha_{\perp}$ and $\alpha_{//}$ were 1.98 and 1.67 cm^{-1} respectively (within an uncertainly margin of 5%)

This allowed the dopant density of Cr^{3+} ions in the crystal to be measured using

$$N_i = \frac{\alpha}{\sigma} \tag{60}$$

which gave a result of $(1.48\pm0.06)\times10^{19}$ ion cm^{-3}.

The L_{MAX} for ruby was therefore implied to be approximately 0.5 mm which is somewhat lower than the thickness of the sample used. While polishing the sample down below L_{MAX} was considered this would have made the sample much more difficult to handle and properly align so it was decided that it would be easier to

ensure that the minimum photon flux was used to acquire the fluorescence signal and that saturation would be checked for by examining the input laser power versus output fluorescence power in a similar manner to that displayed in Figure 4.3.1.

Figure 5.2.1 shows the results of a test to find the optical saturation threshold in the 0.11 cm sample of ruby. Even with the laser operating at maximum output energy (approximately 120 mJ / pulse) the fluorescence signal showed no sign of optical saturation. Electrical saturation was monitored by the same process as in the previous chapter.

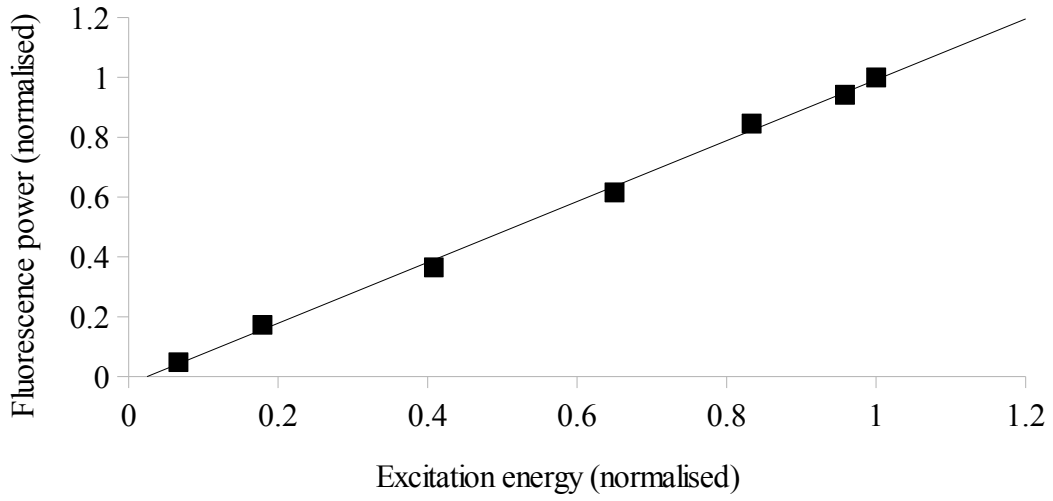

Figure 5.2.1: The linear dependence of SPF in ruby on the excitation power of the Nd:YAG laser. Even near maximum power the data follow the ideal line suggesting limited saturation.

5.3. Single-photon excitation - initial detection of emission

Exciting the ruby sample with 532 nm light produces strong enough fluorescence to be easily seen by eye and by the CCD camera normally used to help align the laser beams. The relatively long fluorescence decay time of several milliseconds allowed this camera to capture an image of the sample at the moment of excitation and shortly afterwards as can be seen in Figure 5.3.1.

To confirm that the emission was indeed characteristic of the 694nm R-line the emission spectrum was recorded using a prism spectrometer capable of a spectral resolution of approximately 0.1 nm. This spectrum, shown in Figure 5.3.2 was also compared to the transmission spectrum of the ruby line filter which would be used later to block scattered laser light.

The results of this scan show both the sharp peak centred around 694 nm (the individual R-lines themselves could not be resolved) and the two Stokes and anti-Stokes shifted side-bands whose distinctive shape is characteristic of ruby and compares well to known spectra in the literature.[90]

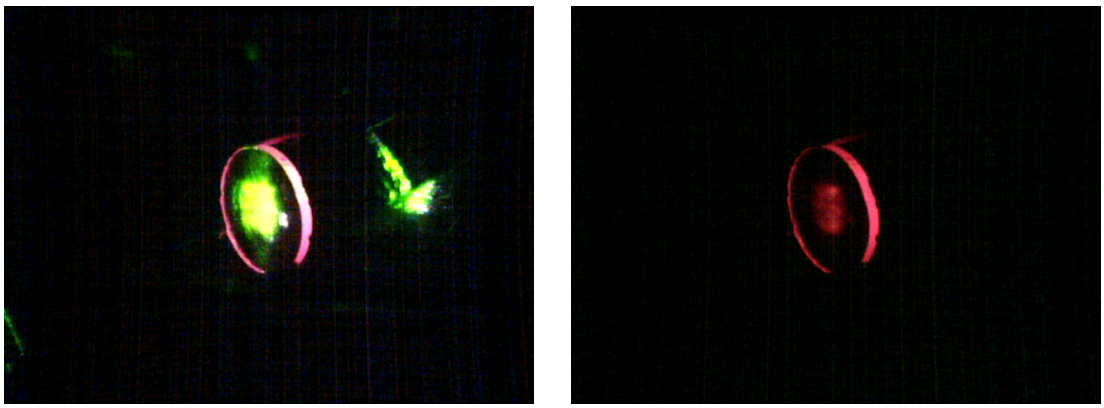

Figure 5.3.1: (left) The ruby sample under 532nm single photon excitation. (right) The 694nm emission from the R-lines after the excitation pulse.

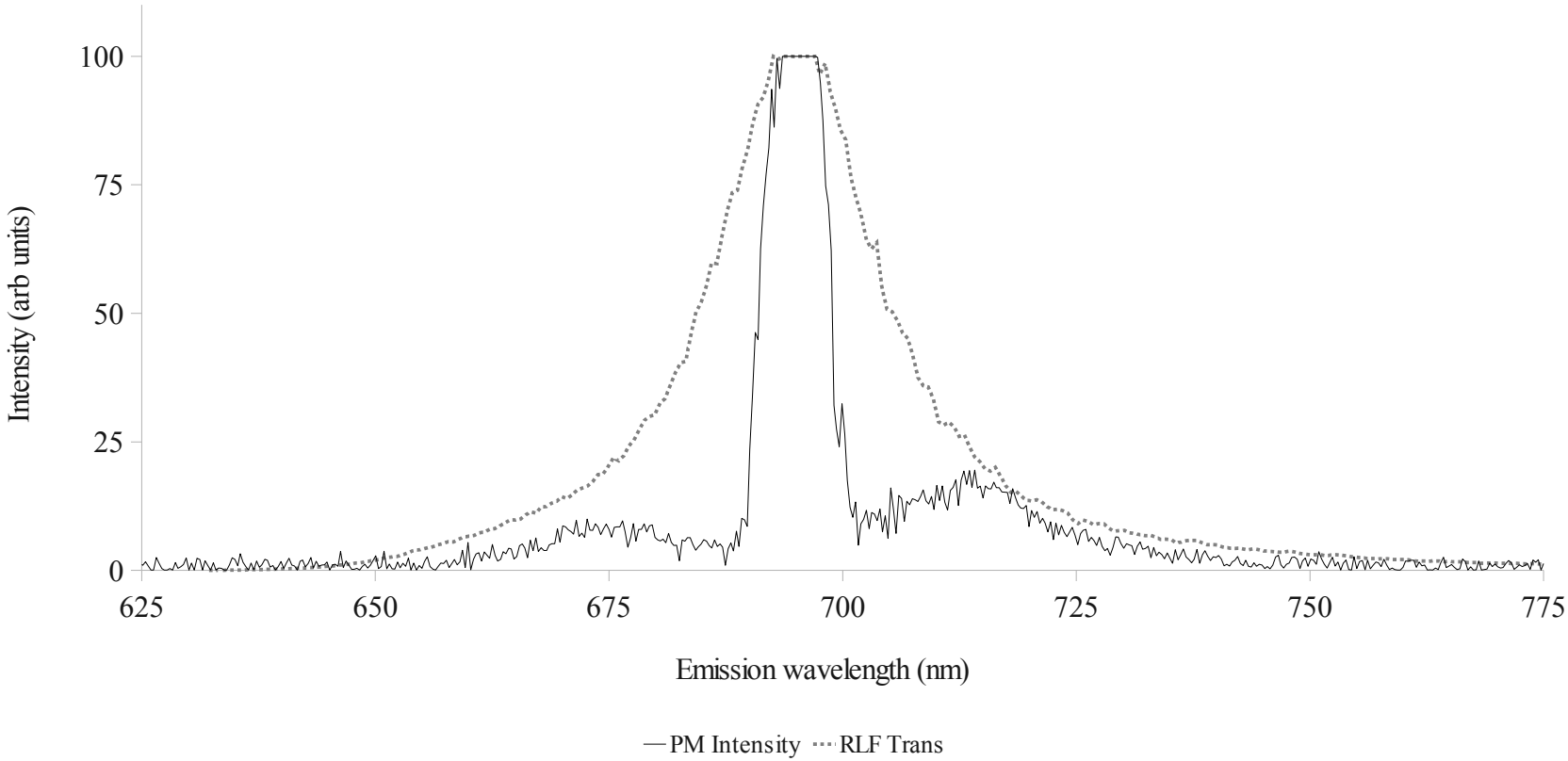

Figure 5.3.2: (solid line) The emission spectrum of ruby under 532nm single photon excitation. On this scale the peak would have a value of approximately 160 units. (dashed line) The transmission of the ruby line filter (RLF) showing that it is capable of transmitting essentially all of the R-line light.

5.4. The effect of temperature on emission

While the response of the emission spectrum to elevated temperatures has already been well studied in detail[90] this effect was tested again to verify the results and to gain a better first-hand experience with handling the sample and to find the limits, if any, to the detection of fluorescence.

The sample of ruby was secured in a stainless steel jig and mounted within a cylindrical oven such that the beam from the 532 nm cw Nd:YAG laser could pass through oven and sample as shown in Figure 5.4.1. The fluorescence light was recovered by mounting the high resolution prism spectrometer slightly off the beam axis so that it could still draw a direct line-of-sight to the sample without being dazzled by too much laser light. The IP28A photomultiplier was secured to the spectrometer by a screw on mount to minimise background signal.

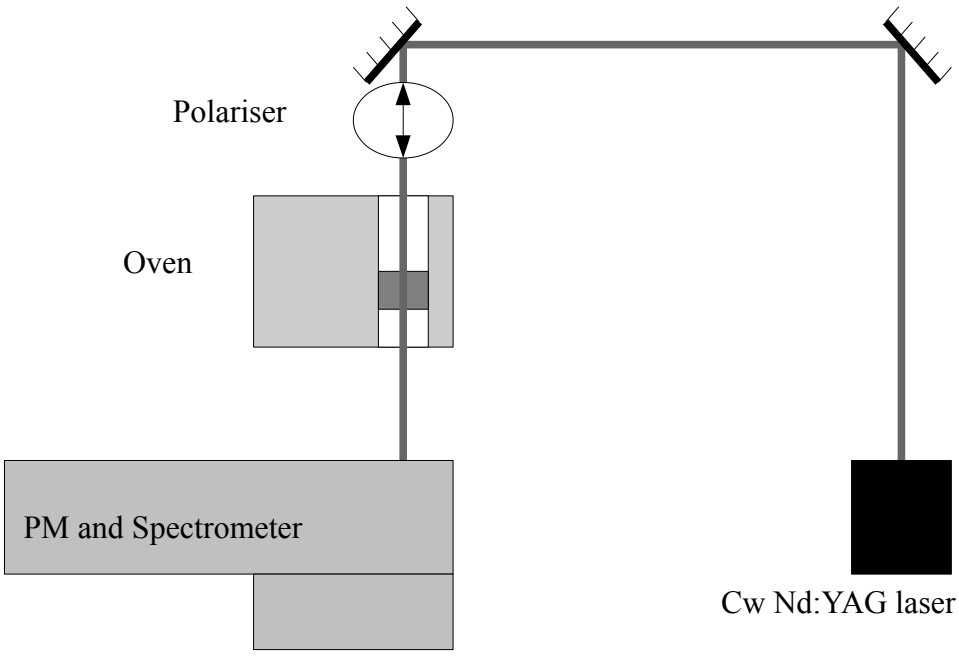

Figure 5.4.1: The experimental arrangement for high temperature experiments on ruby using a cw Nd:YAG laser.

The oven's temperature was raised in increments of about 100 ºC and left to stabilise at each temperature over the course of one hour to avoid transient thermal stress induced components.

While ruby has been shown to perform well at temperatures of up to 1500 ºC[91] and does not melt until a little over 2000 ºC the oven used here was never operated above 1200 ºC. As shown in Figure 5.4.2, fluorescence was detected only up to temperatures of around 400 ºC. This is mainly attributed to the low collection ratio due to the distance that the sample was sited away from the photomultiplier (approximately 30 cm and without any collection optics) and the low throughput of the spectrometer. Nonetheless this was more than sufficient to measure the changes in the emission spectrum and to observe the transfer of light from the R-lines into the phonon side-bands.

Another important parameter is the quantum efficiency however measuring the absolute quantum efficiency (i.e. the ratio of the number of output fluorescence photons emitted per photon absorbed) of a luminescent material is known to be a difficult task involving placing the sample within an integrating sphere so that all of the emitted light may be accurately sampled.[92] For the purposes of this investigation however it was decided that measuring the relative quantum fluorescence would be sufficient.

Figure 5.4.2 shows the thermal response of the emission spectrum. In general the R-lines show a marked reduction as temperature increases as the extra thermally induced phonons transfer energy into the two side-bands. These side-bands are increased and broadened in consequence. Above around 200 ºC, as shown in Figure 5.4.3, the energy contained in the side-bands reaches its peak and ruby shifts away from emitting energy by radiative means as the quantum efficiency begins to drop. Saturation while measuring the R-line component at temperatures below 150 ºC mean that interpreting the change in emission with temperature in this range is less certain although by comparing the width of the R-line peak with the very slight rise in the integrated area of the R-line component suggests that the spectral broadening apparent at higher temperatures is only marginal at temperatures below 150 ºC.

Overall the response of the total emission of the ruby has been found to be

consistent with prior investigation[84] measured under similar circumstances and lends confidence to the techniques used here.

The relative quantum efficiency of the ruby sample could be calculated by taking the product of the fluorescent intensity and the transmission of the sample as they change with temperature and compensating for any change in the incident beam energy at each temperature setting. If the transmission of the sample and the incident energy stay stable yet the fluorescence drops then that indicates a drop in quantum efficiency as fewer fluorescence photons are produced for each unit of photons absorbed.

The final graph, Figure 5.4.4, confirms that the quantum efficiency of the ruby sample is flat or very slightly rising until 300 ^{o}C where it begins to drop exponentially up to the limits of detection. Both this high temperature drop[83],[84] and the low temperature rise from cryogenic temperatures up to 300 ^{o}C[89],[93] have been previously documented although the reason for the transition seems so far unexplained.

In conclusion to this section. It was been shown that the SPF characteristics of the ruby sample used in this investigation showed a measurable response to temperature and did so in a way consistent with previous, independent experiments carried out under similar conditions.

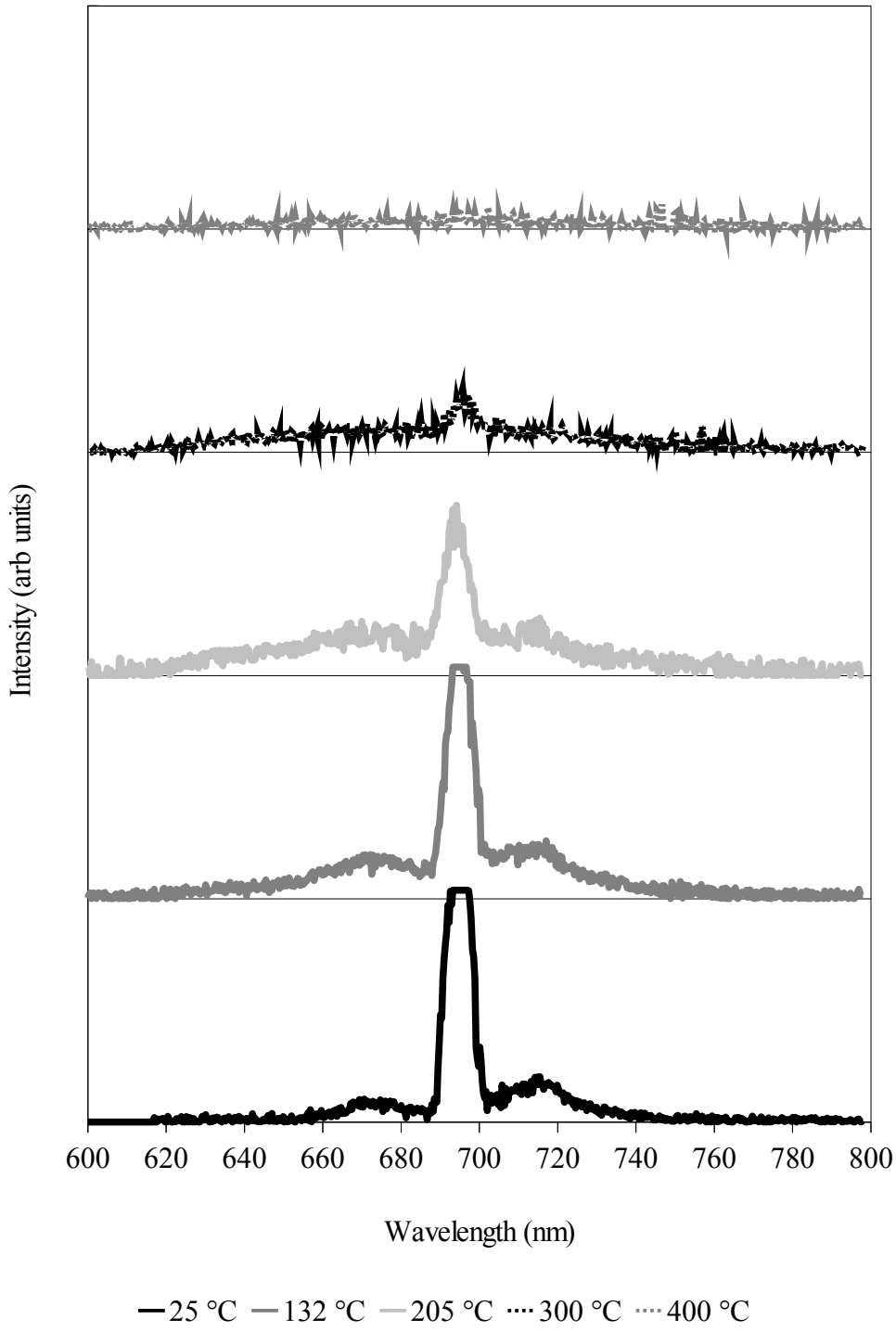

Figure 5.4.2: The change in the emission spectrum of ruby under elevated temperatures. In general the R-lines will decrease in intensity with temperature whereas the phonon assisted side-bands broaden and increase in intensity for a time until a reduction in the quantum efficiency depresses the overall signal.

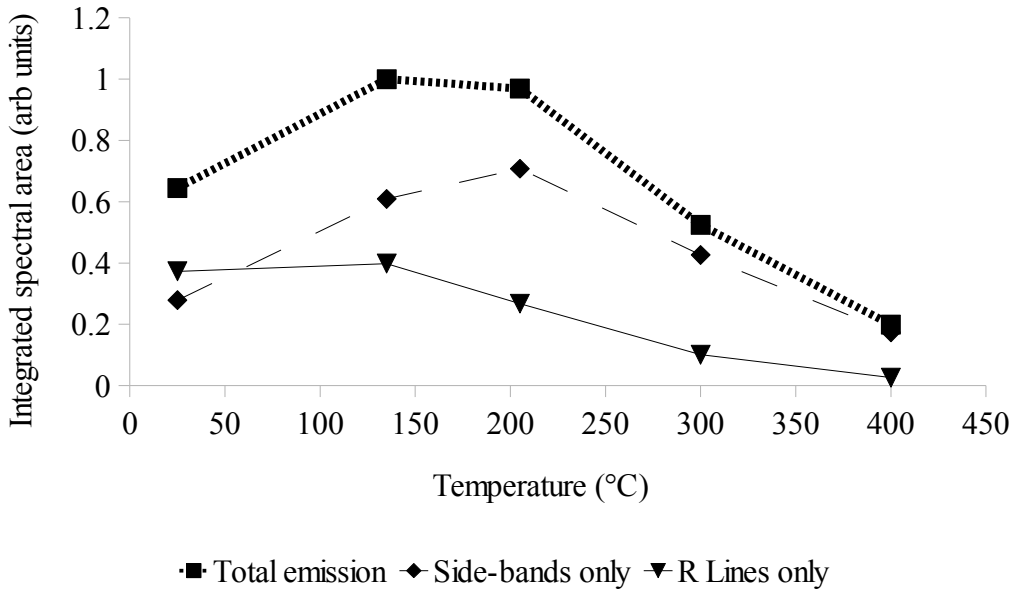

Figure 5.4.3: The change in the total emission of ruby with temperature and the components contributed separately by the R-lines and the side-bands.

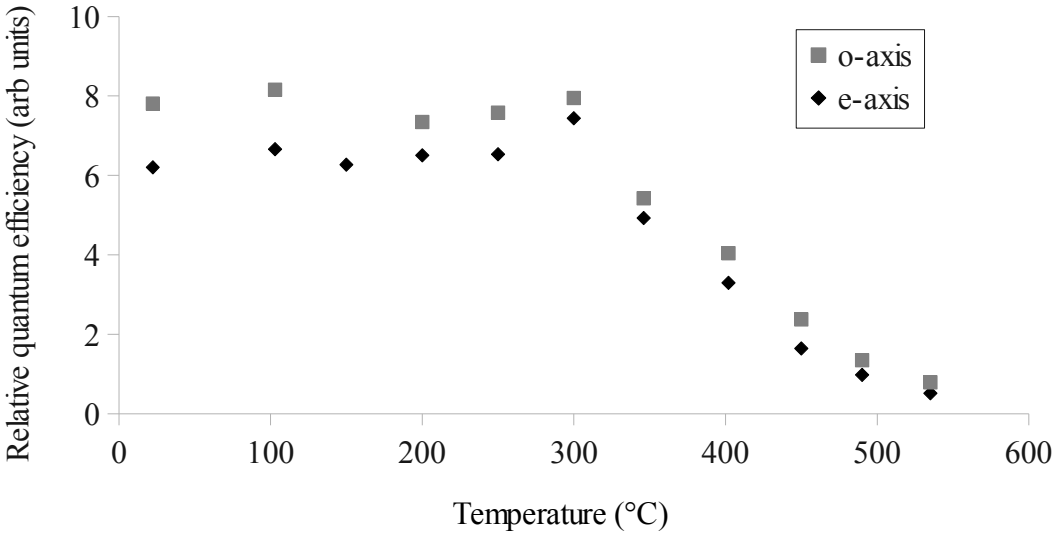

Figure 5.4.4: The effect of elevated temperature on the quantum efficiency of 532 nm SPF. The change in quantum efficiency is flat or slightly rising from room temperature until 300 °C and descends rapidly at higher temperatures. The signal dropped below reliable detectability at around 530 °C.

5.5. Two-photon excitation – Detection and calculation of δ

In section 5.2.2. the single-photon excitation of ruby was demonstrated. As with the Rhodamine 6G the absolute value of the two-photon absorption cross-section was calculated by comparing the output fluorescence given when exciting with 532 nm with the fluorescence emitted due to 1064 nm two-photon excitation. This was calculated for each of the two birefringent axes. The experimental setup was similar to that outlined in Figure (R6G) although in lieu of the lower σ value for the ruby the 50 Ω connector was replaced with a variable impedance box. This unit could be set to any value up to several MΩ, although at impedances higher than about 55 kΩ the electrical falloff time began to approach the fluorescent decay time constant. The minimum temporal resolution of any signal detection was measured by detecting a portion of the scattered excitation laser light (pulse width 5ns) and measuring the half maximum width of the signal and is shown in Figure 5.5.1. It can be seen that the lower performance of the impedance box at 50 Ω is offset by the flexibility gained by it's variable tuning.

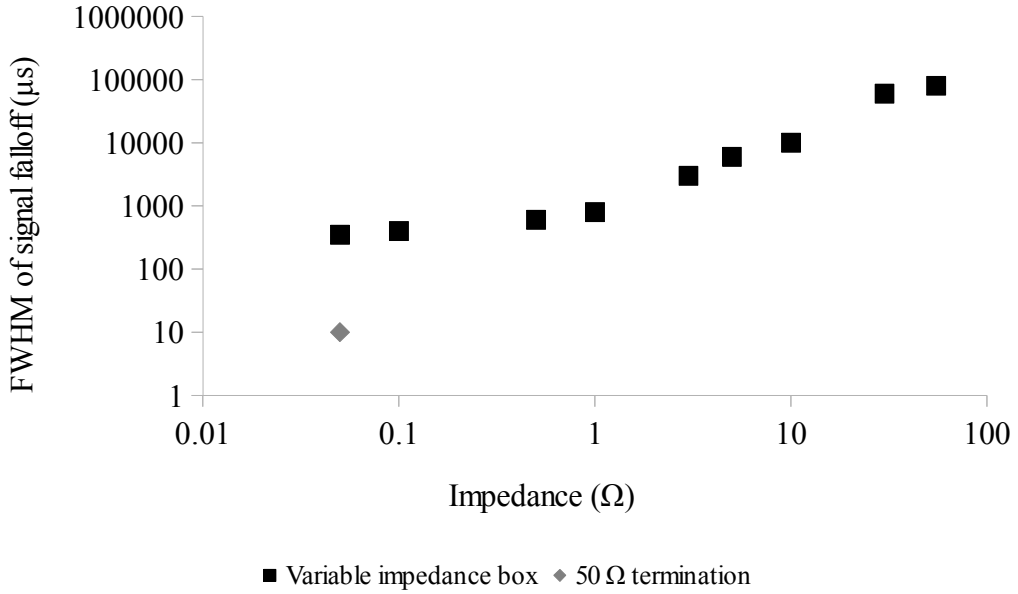

Figure 5.5.1: The half maximum width of the detected signal falloff due to the 50 Ω termination (diamond) and the variable impedance box (squares)

Table 5.5.1. Calculation of δ in ruby			
Parameter	Value	Unit	% Uncertainty
$P'(t)_o$	45.4	mV	5
$P'(t)_e$	75.2	mV	3
$P''(t)_o$	12.6	mV	7
$P''(t)_e$	13.0	mV	6
E'	9.2	μJ/pulse	22
E"	23.9	mJ/pulse	6
A"	0.049	cm^2	10
t_p"	6	ns	17
λ'	532×10^{-7}	cm	<1
λ"	1064×10^{-7}	cm	<1
$\sigma_{//}$	0.6×10^{-19}	cm^2 ion^{-1}	
$\sigma_{\perp}$	1.6×10^{-19}	cm^2 ion^{-1}	
N_1	1.19×10^{19}	ion cm^{-3}	6
K	0.664	[dimensionless]	n/a
Nd	2.46×10^{-4}	[dimensionless]	2

Table 5.5.1. gives the results of the experiment to measure the two-photon absorption cross-section of ruby when excited by 532 nm SPA and 1064 nm TPA and gives a value over the two birefringent axes of $\delta_o = 4.53\times10^{-54}$ cm^4 s ion^{-1} $photon^{-1}$ and $\delta_e = 2.73\times10^{-54}$ cm^4 s ion^{-1} $photon^{-1}$. A margin of uncertainty of approximately 44% is attached to these values stemming mostly from uncertainties in the absolute quantities with the shot-to-shot variation of the laser when used for the SPA experiments being particularly poor. This was due in part to difficulty in measuring the average laser power when the laser was operating near its minimum output settings although the main source of uncertainty was due to the second-harmonic process used to convert the fundamental 1064 nm laser beam to 532 nm as the variation of the intensity of the second-harmonic beam will be proportional to the square of the variation in the fundamental.

If verified this result lies among the lowest recorded values of δ for the materials in the current literature record and certainly lies well below the known values for various organic dyes[94],[95][96] although it should be noted that 532 nm is not the most effective wavelength for ruby to absorb via SPA nor should it be assumed to be so for 1064 nm via the TPA process. The logical extension of this study was to use a tunable laser source to investigation the two-photon absorption and excitation spectra for ruby.

5.6. The two-photon excitation and absorption spectra of ruby

In order to measure the single and two photon absorption spectra of the ruby sample the Nd:YAG laser was replaced with a Continuum Powerlite Nd:YAG laser with the Panther EX Optical Parametric Oscillator attached as shown in Figure 5.6.1. The laser produced 1064 nm light in 10 ns pulses with a repetition rate of 10Hz. This was partially converted to 532 nm via second-harmonic generation then, by combining the 1064 nm photons and the 532 nm photons in a sum-frequency generation step to 355 nm. This 355 nm beam was then passed through a Beta-Barium Borate (BBO) crystal which converted the beam into two complementary beams each with a wavelength dependent on the angle at which the 355 nm beam is incident on the crystal. The first beam (known as the "signal") can, in this case, be tuned between 400 nm and 700 nm while the other (known as the "idler") can be tuned between 700 nm and approximately 2600 nm with an average power output on the order of up to 300 mW (30 mJ per pulse) as shown in Figure 5.6.2. Dichroic mirrors and filters were used to select which beam was most appropriate to the given experiment.

Similar to the experiments in Chapter 4, the average beam power (hence the average energy per pulse) was measured by a thermopile (which had been cross-calibrated against a photodiode power meter) while the output fluorescence was filtered by a ruby line filter and, in the SPF case, a neutral density filter to limit saturation effects.

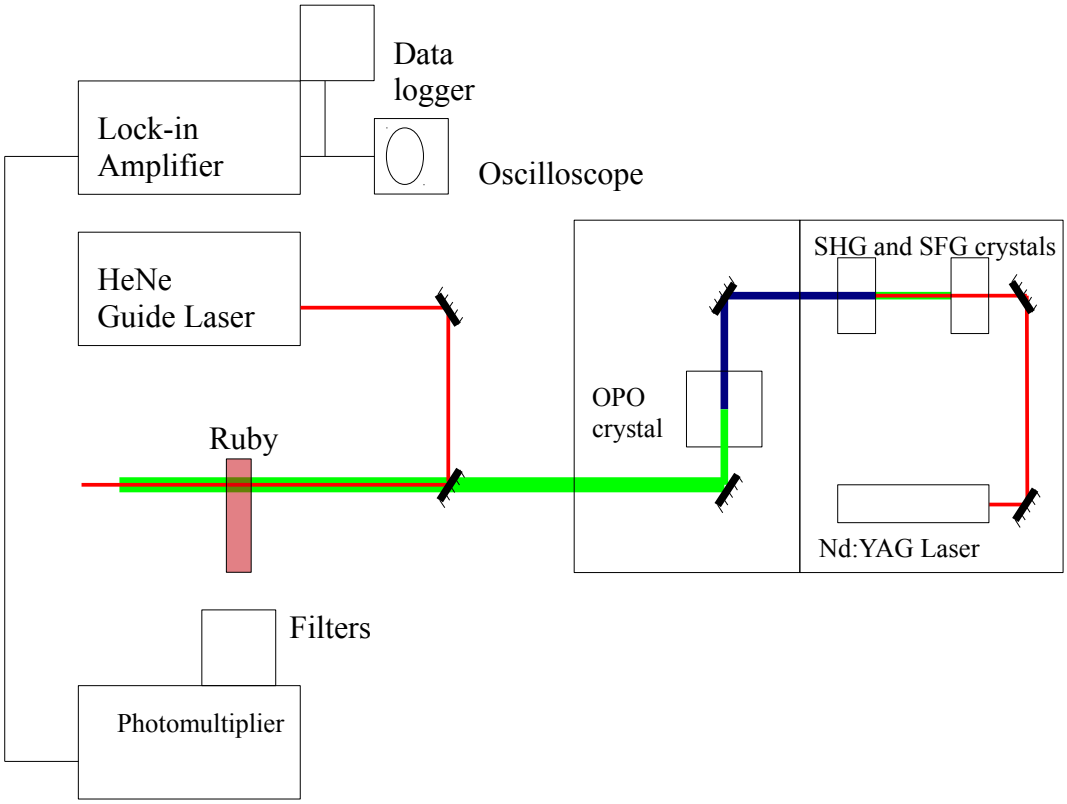

Figure 5.6.1: The experimental arrangement for measuring the SPF and TPF spectra of ruby. The 1064 nm emission from the laser was converted to 532 nm light by second harmonic generation then to 355 nm light by sum-frequency generation of the 1064 nm and 532 nm photons. The 355 nm light was then downconverted by the OPO into the tunable signal and idler beams.

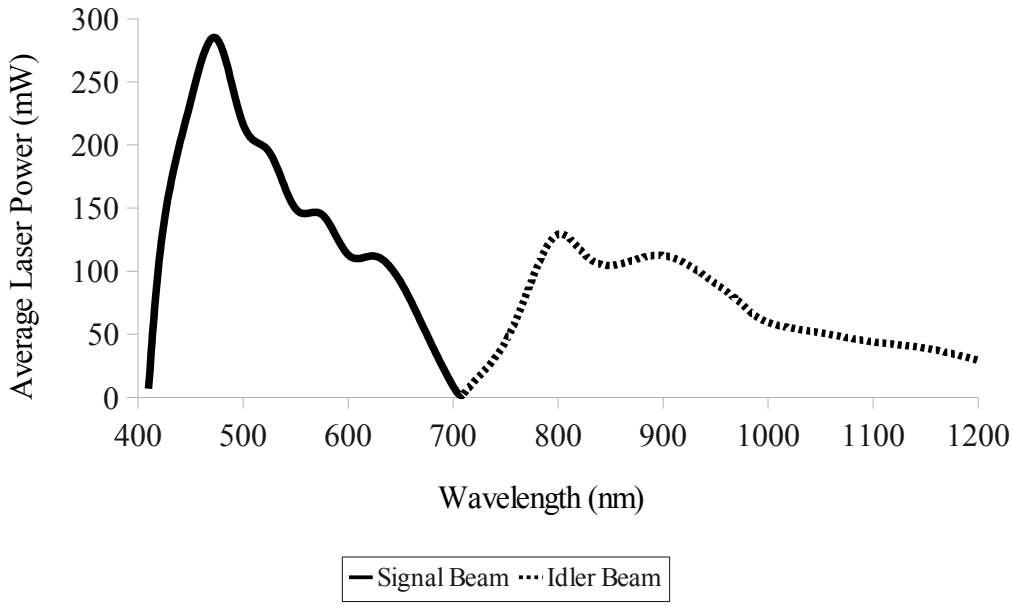

Figure 5.6.2: The typical operating output power of the OPO laser over the range most often used in this investigation.

The single- and two-photon excitation spectra were measured by reading the signal off an oscilloscope at a short, fixed time after the initial detection (t=+0.5 ms) in order to eliminate the effects of any remaining scattered laser light and to avoid the uncertainty involved in identifying the peak emission.

The excitation spectra could be converted to absorption spectra by normalising the excitation spectrum against the incident photon flux at each wavelength in the SPF regime and against the square of the photon flux in the TPF regime. These photon fluxes were calculated via the average power measurements and a conversion taking into account photon energy and pulse shape such that for a Gaussian pulse the photon flux, n_o is:

$$n_o = \frac{\sqrt{2}\,K\,E\,\lambda}{h\,c\,A\,t_p} \tag{61}$$

Where K is the pulse shape coefficient detailed in Chapter 2, E is the beam energy per pulse, λ is the wavelength of the excitation pulse, A is the cross-sectional beam area and t_p is the pulse duration.

The spectra were also normalised against the quantum efficiency of the ruby emission[86] although this had only a limited effect on the final result (i.e. below the margin of uncertainty of the experiment). It is assumed that the quantum efficiency of a radiative transition is essentially independent of excitation path thus is the same for both SPA and TPA at equivalent wavelengths.

At the short end of the two-photon excitation spectra the TPF signal was superimposed on a large background (compared to the very weak TPF signals).

A routine check, the results of which are shown below in Figure 5.6.5, to confirm the source of an excitation path is to check the dependence of the fluorescent intensity as a function of input excitation power

$$P \propto E^n \tag{62}$$

where P, the fluorescent power is proportional to E, the excitation energy, to the power of n, the number of photons absorbed per excitation.

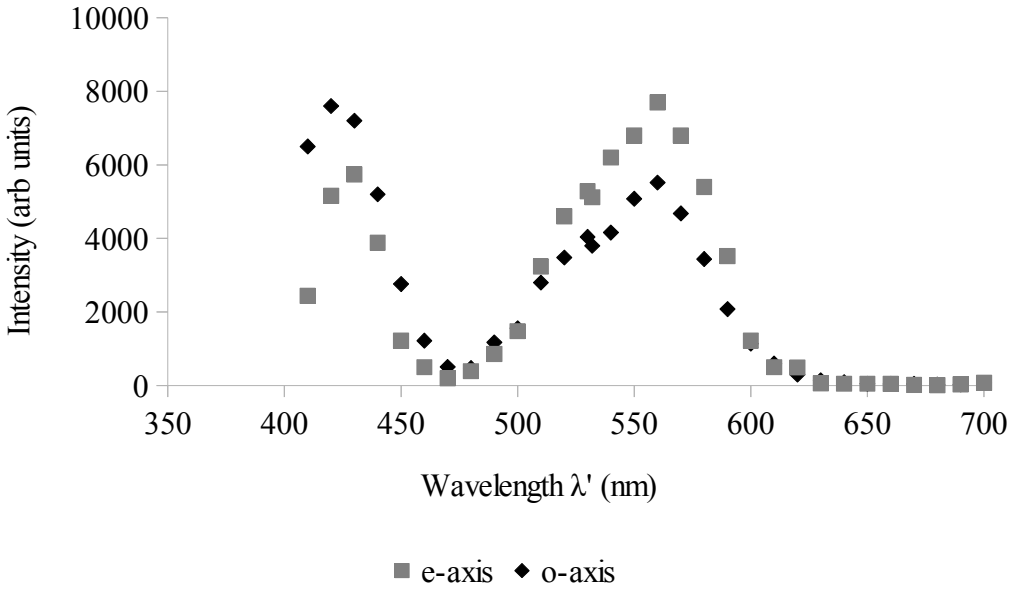

Figure 5.6.3: The single-photon excitation spectra of ruby for both extra-ordinary axis (grey squares) the ordinary axis (black diamonds).

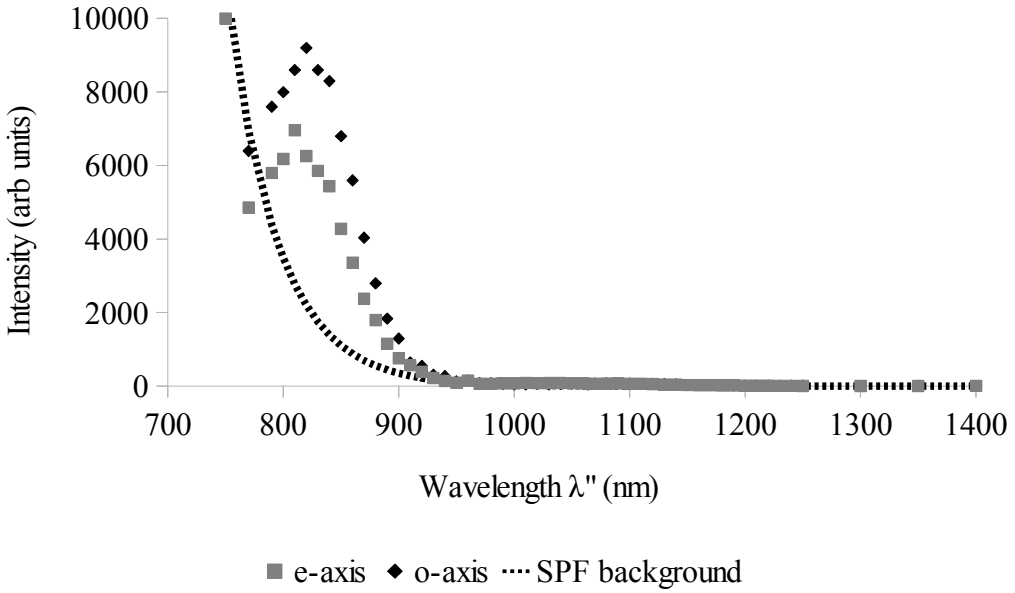

Figure 5.6.4: The two-photon excitation spectrum of ruby for the extra-ordinary axis (grey squares) and the ordinary axis (black diamonds). On this scale the second peak at 1100nm is not easy to view but still lies well above the signal/noise threshold. The large, roughly exponential rise in signal towards 700nm is probably thermally assisted SPA onto the R-line.

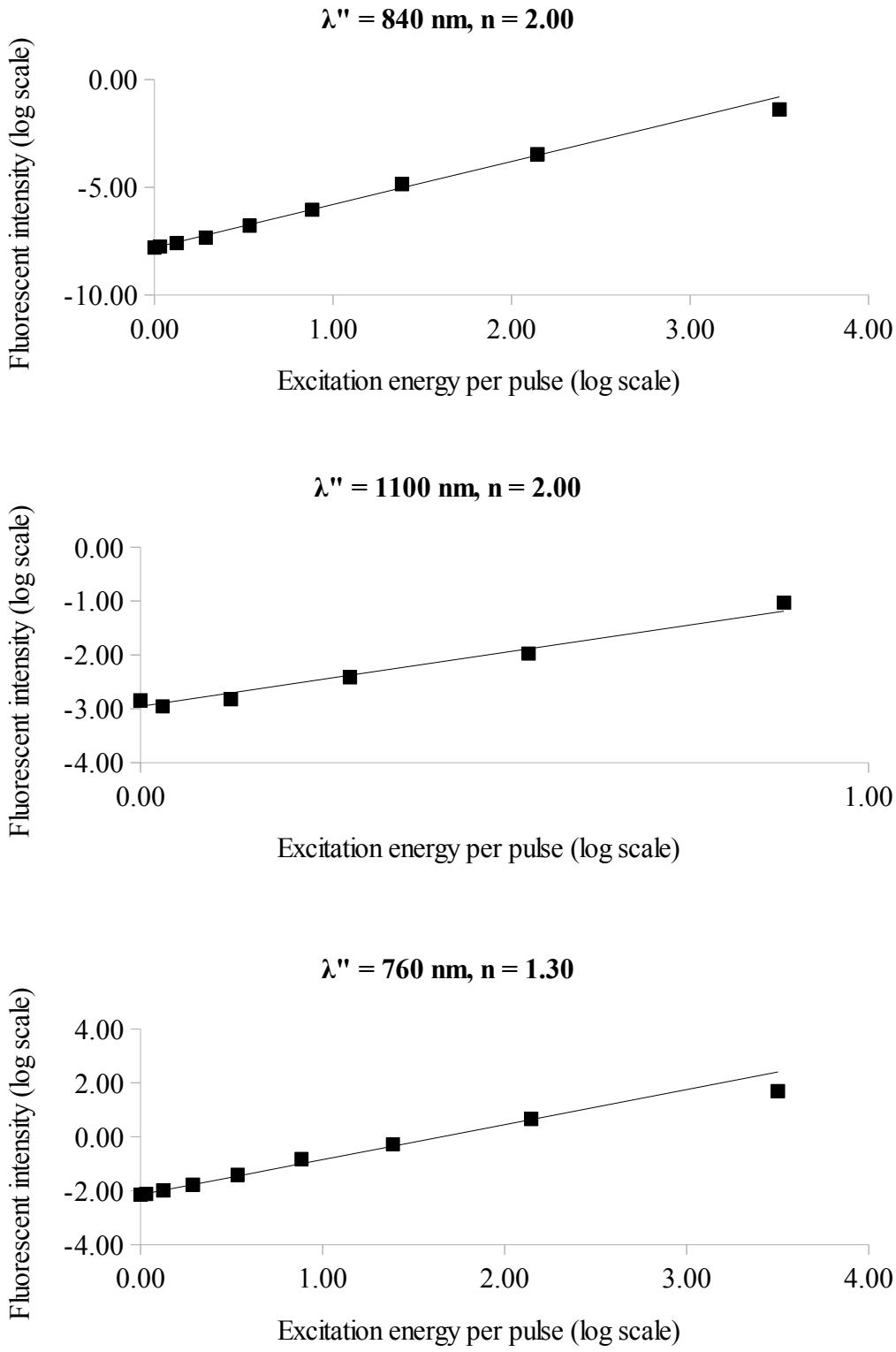

Figure 5.6.5: The TPF intensity vs excitation power. (upper two graphs) Data taken near the two peaks λ" = 840 nm and λ" = 1100 nm. n values of 2.00 indicate a two-photon excitation. (lower graph) Data taken at 760 nm. n = 1.30 indicates that the excitation at this point is dominated by a single-photon process.

The results show that the intensities of the two emission peaks at 840 nm and 1100 nm both show a squared dependence on input excitation energy indicating that they both involve two-photon excitation processes. The intensity variation sampled at 760 nm however shows a dependence of only 1.30 indicating that the exponentially shaped rising curve is likely a single-photon process with a small component of the light at that wavelength coming from the edge of the 860 nm peak. While the origins of this signal are currently unknown it is thought that a combination of phonon assisted absorption onto the R-lines and/or stray transmission through the edge of the 694 nm ruby line filter may be a factor.

It may be of note that this effect does not seem to have been observed in the previous ruby-based TPF experiment which although it measured the power dependence at 800 nm[88] and reported a value of n = 2.05 where, according to Figure 5.6.4, the background should contribute a significant fraction of the output emission especially at low excitation powers.

The single-photon excitation spectrum was normalised against the photon flux (calculated from Figure 5.6.2) and the quantum yield (taken from Maiman) at each wavelength to produce the single-photon absorption spectrum shown in Figure 5.6.7.

The two-photon excitation spectrum was normalised using a similar method, normalising against the square of the photon flux and the quantum yield at the appropriate wavelength with the assumption that the quantum yield for a degenerate two-photon transition is identical to the quantum yield at the equivalent single-photon wavelength. The background signal was easily subtracted by fitting an exponential curve to it.

This resulted in the generation of the the two-photon absorption spectrum of ruby shown in Figure 5.6.6. As can be seen, the main features of the spectrum, the two peaks at 840 nm and 1100 nm are similar to the features of the single-photon spectrum as is the ordering of the preference of the birefringent axes which shows stronger absorption on the o-axis at 840 nm and stronger absorption on the e-axis at 100 nm.

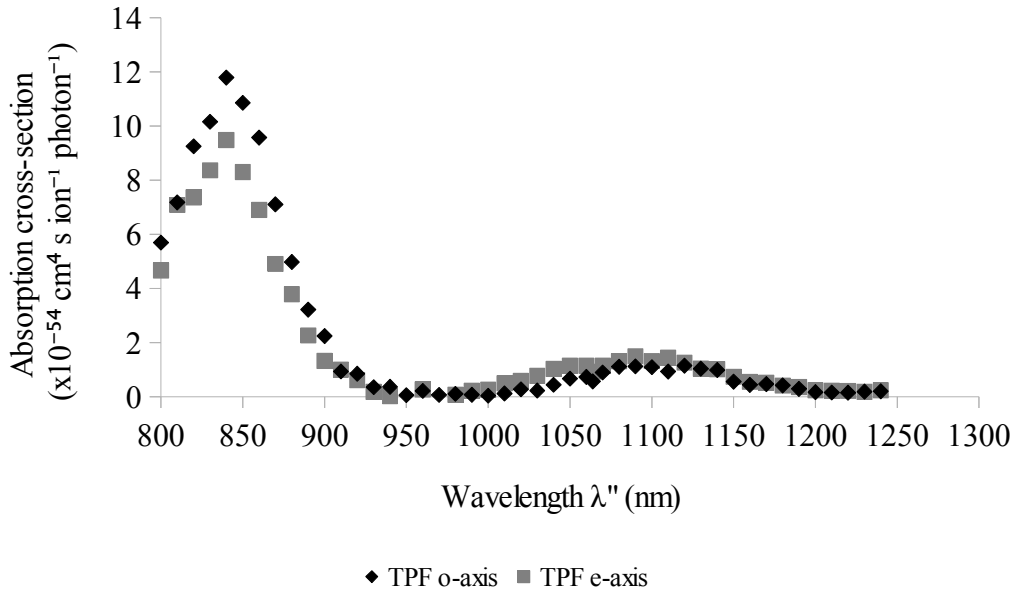

Figure 5.6.6: The two photon absorption spectra for ruby at room temperature showing the peak absorption to the $^4T_1$ band at 840 nm and the peak absorption to the $^4T_2$ band at 1100 nm.

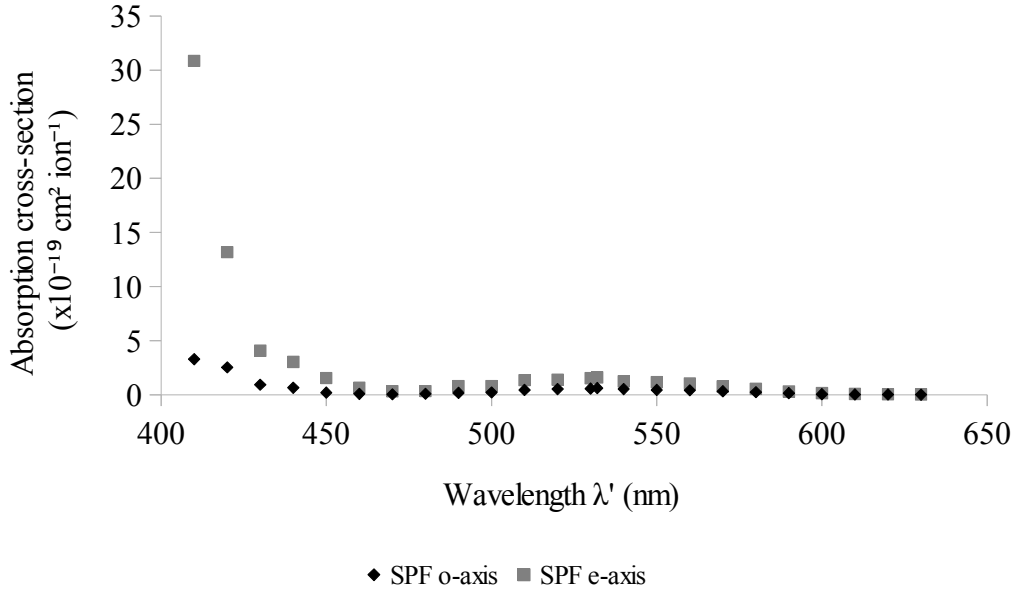

Figure 5.6.7: The single photon absorption spectra for ruby at room temperature. The peak of the $^4T_1$ band at 395 nm could not be conclusively observed due to the upper limits of the laser tuning range.

The overall uncertainty in the precision is about ±40% which comes from a ±20% random uncertainty due to shot-to-shot variation from the laser and the remainder from the absolute uncertainty in some of the parameters such as A", t_p", E" and E'. In general, the two-photon spectra are similar to the single photon ones showing two unequal peaks with the ordinary axis absorption dominating the shorter $^4T_1$ peak and the extraordinary axis absorption becoming greater in the longer $^4T_2$ peak. The position of the $^4T_2$ peak in the two-photon spectrum, λ"=1100 nm agrees well with the predicted position based on two times the single-photon peaks at λ'=550 nm. The shorter peak at λ"=840 nm however shows a significant red shift of about 30 nm from the expected 2x405 nm. It is possible that the competing phonon-assisted process interacts in some way to cause the peak to roll over early.

5.7. τ, the fluorescence decay time constant and response to temperature.

The aim of this experiment was to successfully measure the decay time constant of the ruby emission and correlate the change in decay time with temperature. As stated previously, the effect of temperature on this constant has been well studied in ruby for single-photon excitation[84],[89] and it has proven to have potential as an effective temperature sensor. If this effect could be replicated here then the secondary goal was to repeat the same experiment under two photon excitation.

The experimental arrangement was similar to that used in Figure 5.4.1. except a small rig was constructed to mount the ruby sample on a copper tray, as shown in Figure 5.7.1, which was heated using two soldering irons connected via a feedback loop to a thermocouple to control and stabilise the temperature up to 400 °C.

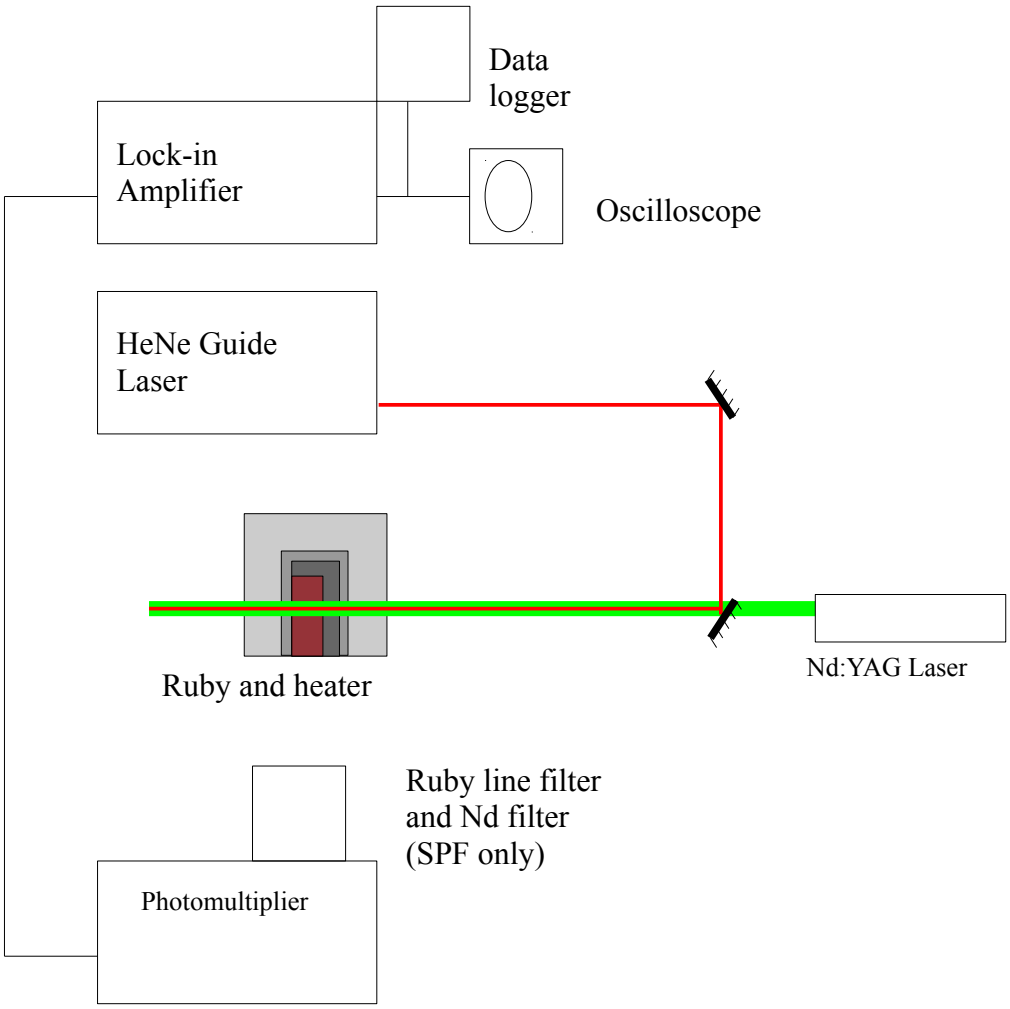

Figure 5.7.1: Schematic of the experimental layout for the effect of temperature on the fluorescent decay time.

The decay time was recorded by passing the signal through a 55 kΩ impedance to the oscilloscope from which a value near the peak intensity (though offset by approximately +0.5 ms to avoid uncertainty in the true peak) and the time taken for the intensity to drop by half was read. This was then converted to a value of τ by noting that for an exponentially decaying signal

$$\tau = \frac{t_{1/2}}{\ln(2)} \tag{63}$$

The ruby was excited with 532 nm pulses from the Continuum Minilite Nd:YAG laser for single-photon excitation and 1064 nm pulses for two-photon excitation. Good thermal contact between the ruby and the heating element was ensured by pressing the ruby against the wall of the element with brass shims. Some thermally conductive paste was tested but it was found to degrade significantly at temperatures above around 200 °C so was discarded. The element and sample were covered with a slotted ceramic cylinder such as to limit convective and radiative losses in a way that still allowed laser light into the chamber and fluorescent light out.

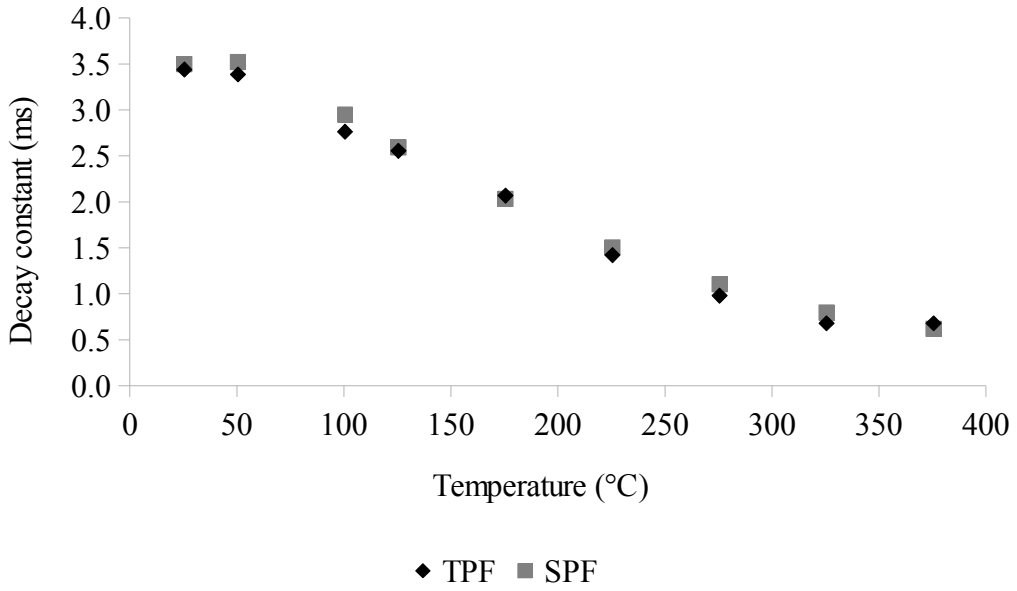

Figure 5.7.2: The fluorescence decay time constant of ruby under single-photon excitation (grey squares) and two-photon excitation (black diamonds). Emission characteristics are shown to be independent of excitation path.

The results in Figure 5.7.2 show the change in decay time with temperature which stays roughly flat at approximately 3.5 ms until a temperature of about 50 ^{o}C is reached before dropping steadily to a value a little above 0.6 ms at 375 ^{o}C. The data show a good correlation with the results of previous studies over a similar range of temperatures[84],[91] and seem to be reasonably independent of excitation path. That is, the characteristics of the emission are similar whether single-photon or two-photon excitation is used. This will have significant implications for the selection of potential dopants for sensor purposes as it implies that any and all existing spectroscopic work performed on dopants in the single-photon regime may be reliably used to predict the behaviour of a potential two-photon sensor.

As a potential improvement for future study it can be seen in Figure 5.6.6 that 1064 nm is not the optimal wavelength for exciting ruby (830 nm has a value for δ which is approximately an order of magnitude greater than the value at 1064 nm) but even at this optimal wavelength the value for delta is on the order of 1 mGM which is far below the values usually found in the literature, especially in the organic dyes where values of $10^{1} - 10^{3}$ GM[87],[85] are commonplace and values up to 230 000 GM have been reported.[82] Since this measurement was performed lower values of delta, on the order of 10^{-56} cm^{4} s ion^{-1} photon^{-1} have been reported in liquid argon.[97]

5.9. Implications for fibre geometries

While ruby has several advantages over silica as a material for a distributed fibre sensor, notably its comparative hardness and high melting point, As a potential dopant for a full scale distributed optical fibre sensor it would not be the first choice for many applications as it's principal excitation and emission pathway is a 3-level optical system thus the fluorescence light would be subject to self-absorption in the fibre. Any absorbed and re-emitted light would record the temperature of the fibre at the re-absorption point rather than at the point intended thus the temperature readings would become progressively scrambled as fibre length is increased. To avoid this the fibre length must be limited to no longer than approximately one optical path length of the dopant, given by:

$$L_{MAX} = \frac{1}{\sigma N_1} \tag{64}$$

where N_1 is the dopant density and σ is the single-photon absorption cross-section of the dopant at the emission wavelength. For the ruby sample studied in this chapter ($N_1 \approx 1.19 \times 10^{19}$ ion cm^{-3}), this is approximately 0.75×10^{-20} cm^2 [81] which gives a maximum acceptable fibre length of 11 cm. For a dopant concentration of 10% of the concentration of the sample used here this maximum length will be therefore be around 1 m as shown in Figure 5.9.1.

Apart from the issues with the dopant, another significant disadvantage inherent to single-crystal fibres lies in the construction of the fibre itself. Whereas silica fibres typically consist of separate core and cladding layers a single crystal fibre in its simplest form would consist only of a single core layer. The core diameter would likely be large enough to permit multi-mode propagation of the excitation pulses. These single-crystal fibres would therefore exhibit significant modal dispersion which would severely compromise the spatial resolution of the sensor although, as was shown in the previous chapter, it would not directly reduce the total amount of TPF generated by the overlapping counter-propagating pulses as ΔP is independent of pulse duration even in the presence of dispersion.

The degree of modal dispersion, in terms of change in pulse duration per unit distance of propagation, $\Delta t/z$ in a multi-mode fibre is given by[98]

$$\frac{\Delta t}{z}=\frac{n_2}{4 c n_1^2}\left(n_1^2-n_2^2\right) \tag{65}$$

where n_1 is the fibre refractive index which for the sapphire used here is 1.77, n_2 is the air refractive index of 1.00 which gives a pulse broadening coefficient of 0.6 ns m^{-1} which would be ruinous for even a 10 m long fibre.

This problem could be solved by bonding a cladding layer onto the fibre but in the high temperature applications likely to require a sensor the cladding would have to have virtually identical thermal conductivity to the core layer so as to avoid affecting the data and there may be engineering issues with the stability of the bonds at high temperatures or with issues involving differential thermal expansions between the layers.

An alternative solution may be to take advantage of the link between refractive index and dopant density. During the production of doped single-crystal fibres by the laser heated miniature pedestal growth technique, gradient index characteristics can be created due to the evaporation of dopant from the melt surface inducing a radial variation to the dopant concentration. This phenomenon has been observed in Ti^{3+}:Al_2O_3 and Cr^{3+}:$Gd_3Sc_2Al_3O_{12}$ (Cr:GSAG) fibres[99] and similar phenomena should be present in various other combinations of dopant and host including ruby (Cr^{3+}:Al_2O_3) which also exhibits a positive change in refractive index with dopant density. The samples mentioned above exhibited a parabolic graded index along their optic axis but regardless of the exact shape of the graded index profile it will have the same function as a separate cladding layer and help to confine and guide the light within the fibre, as shown in Figure 5.9.2, which will dramatically reduce the dispersion of the fibre as well as reducing the effective cross-sectional area of the fibre which will, in turn, increase the production of TPF.

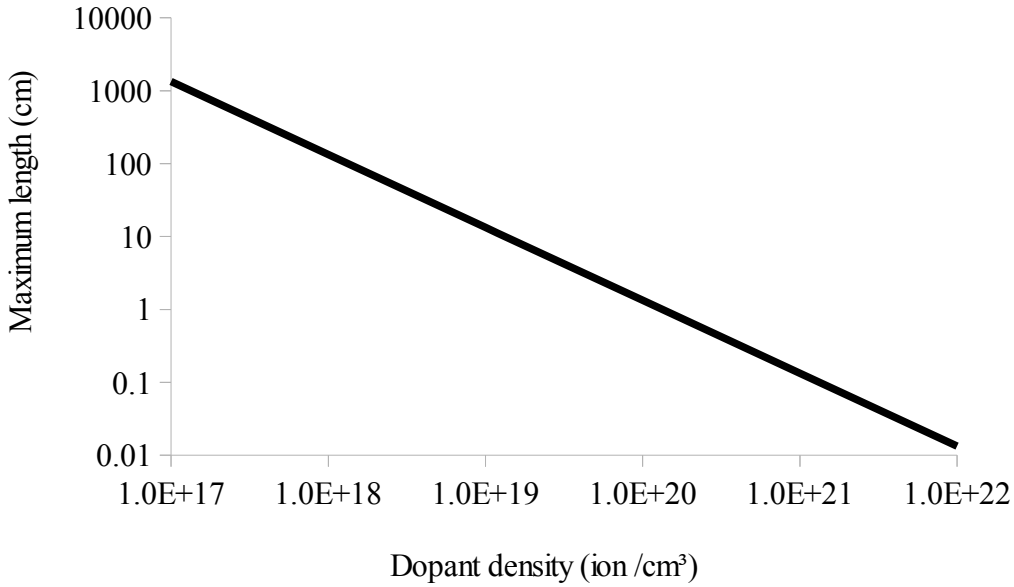

Figure 5.9.1: The maximum length for a ruby-based single-crystal fibre as a function of dopant density.

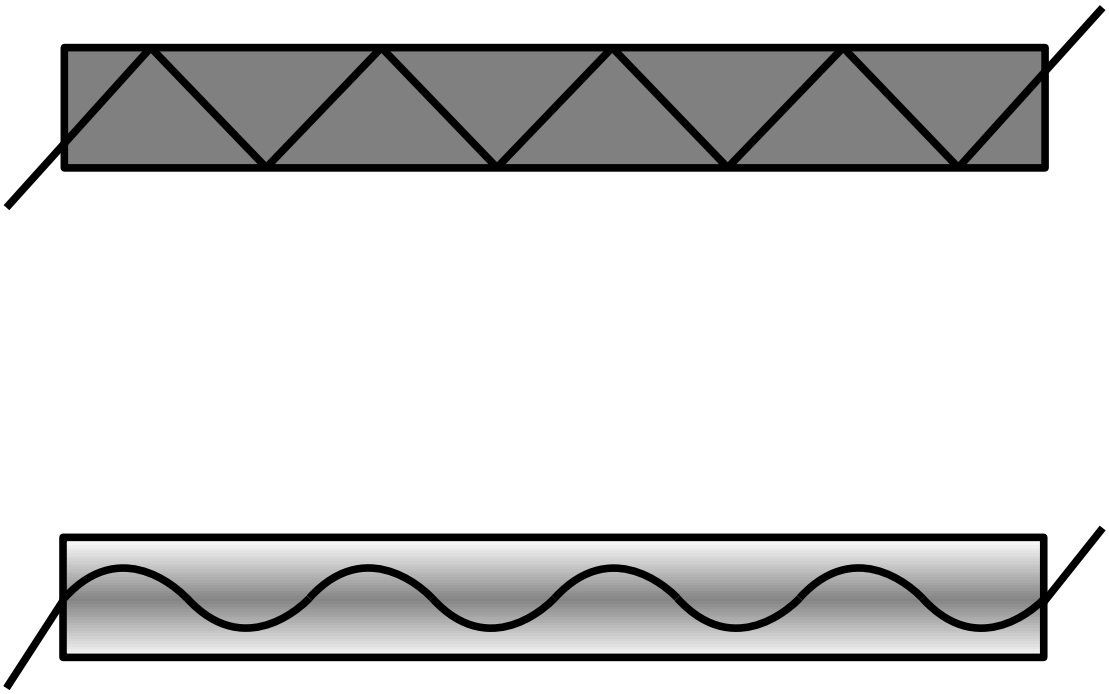

Figure 5.9.2: (top) An illustration showing the path of a ray of light travelling through an unclad single-crystal fibre with a uniform dopant profile. (bottom) The path of a ray of light travelling through a similar fibre with a graded refractive index profile. The light is confined to a smaller effective cross-sectional area of the fibre.

5.10. Conclusions

This chapter has reported the the successful detection of two-photon fluorescence in ruby and the calculation of the degenerate two-photon absorption spectrum in terms of the absolute absorption cross-section. The method for calculating the absorption cross-section has proven sensitive to the very low values of δ found in ruby in spite of the relatively long laser pulses used.

The ability to use the decay time constant of ruby as a temperature sensor has been confirmed for SPF and successfully demonstrated for TPF. Crucially, the response in the TPF case was shown to be similar to the SPF case which would prove to greatly simplify the search for suitable dopants for a practical sensor as the temperature characterisation could be tested, at least initially, using SPF.

Due to the complications of working with crystal fibres; the low two-photon absorption cross-section and, most importantly, the self-absorption of the fluorescence by the sample ruby was found not to be an ideal material for a potential distributed fibre sensor in most applications. Therefore the investigation in the following chapter will extend the techniques used here to a selection of rare-earth metal doped glasses, most of which had not been studied extensively using TPF prior to this body of research.

Through this investigation dopants which could be used as potential temperature sensors in silica fibres would be identified.

6. Rare earth metal doped glasses.

6.1. Introduction

While a single-crystal ruby fibre may be useful in some specialised applications it is likely that a more conventional silicon glass fibre will be sufficient and advantageous in most ordinary temperature sensing environments. This fibre should be doped with an optically active material which has as high a two-photon absorption cross-section as possible and is as sensitive to the desired measurand as possible. The lanthanides, or rare-earth metals, are particularly worthy of consideration as while they do not typically exhibit the extremely high two-photon absorption cross-sections as some organic dyes they have been shown to be reliable sensor dopants for single-photon fluorescence based experiments. The energy level structures of the trivalent lanthanide ions have been studied in detail in previous years and in particular in investigations by Dieke and Crosswhite[100] the results of which are reprinted from their summary in Figure 6.1.1 which was used to help identify the absorption, excitation and emission transitions found during this investigation.

As will be seen throughout this chapter however the two-photon spectroscopic characteristics of many of these are relatively poorly studied in comparison with their single-photon or even their excited-state conversion characteristics both of which have been the subject of extensive research for many decades.

With this lack of basic data it was decided that the principal objective of this chapter of the investigation should cover a broad spectroscopic analysis of as many potential dopant materials as possible in both the single- and two-photon regime. While knowledge of the absolute magnitude of the two-photon absorption cross-section is not strictly necessary to construct a TPF based sensor, so long as fluorescence can be detected, it is advantageous to know both for knowledge's sake (as many of these values had not been published prior to this investigation) and to better predict the capabilities of a potential dopant.

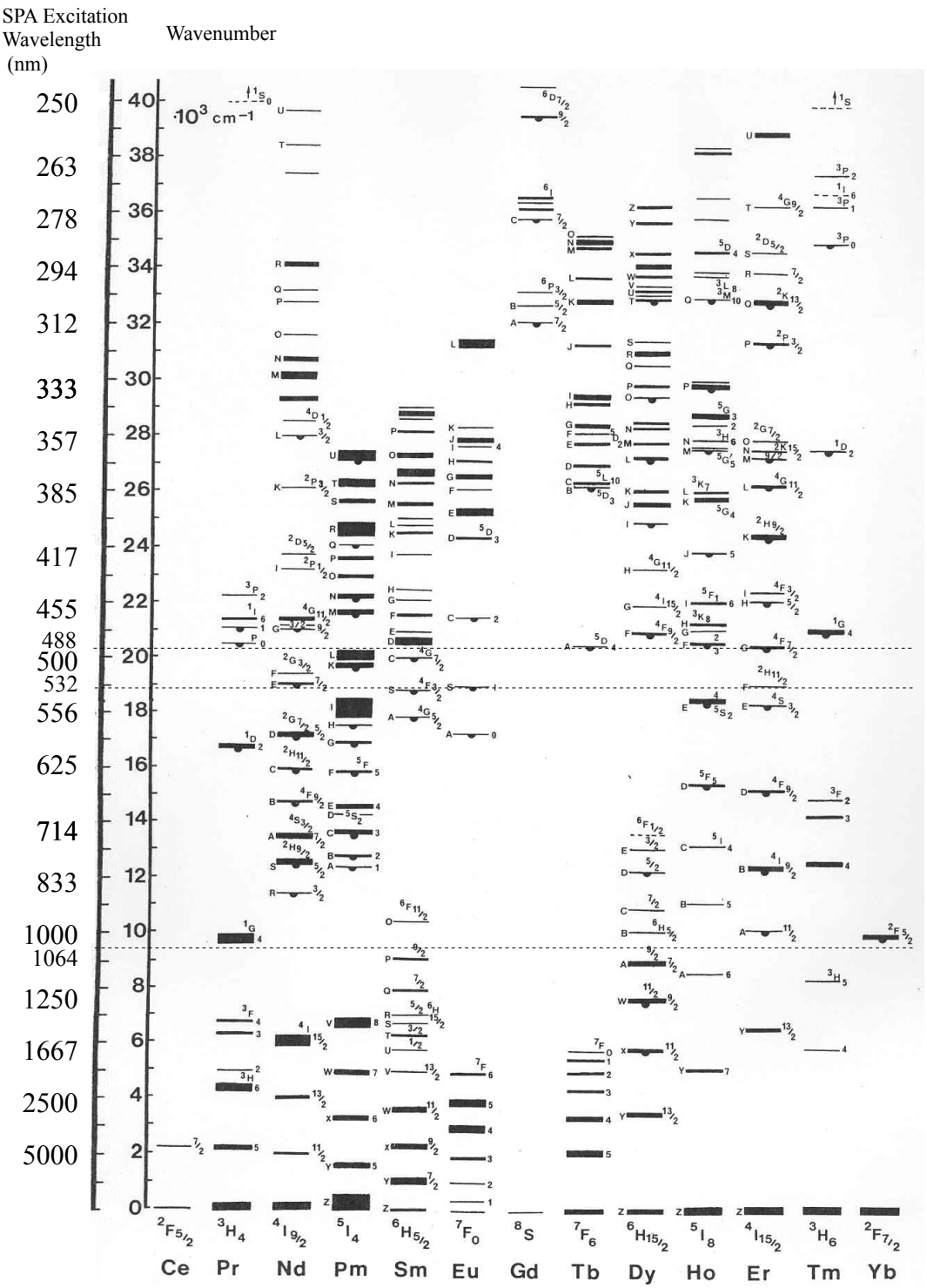

Figure 6.1.1: The energy levels of the trivalent rare-earth ions. Reprinted from Dieke and Crosswhite[100] and modified to include the required SPA excitation wavelength to excite to each energy level from the ground state. Hanging semi-circles indicate a level capable of radiative emission. Dashed lines indicate the three important excitation wavelengths of the 488 nm of an argon ion laser and the 532 nm and 1064 nm of the Nd:YAG laser.

6.1.1. Preparation of samples

The samples obtained for study in this investigation were a series of rare-earth doped fluoride glasses, principally ZBLAN and ZBLALi based, kindly loaned by Dr David Hollis then of the University of the West of Scotland and produced by him. All of the samples were supplied subject to availability and were not made specifically for this project.

Most of the glasses are based on a molar composition of 50 parts ZrF_4, 20 parts BaF_2, 20 parts NaF, 4.5 parts LaF_3, and 5.5 parts AlF_3 or on a slight variation of such. The extra rare-earth dopant was added, typically in the form of XF_3, to a concentration between 0.5 mol % and 2.0 mol % depending on the dopant.

Fabrication of these glasses started by weighing out the fluorides in a dry nitrogen atmosphere inside a sealed glove box before mixing them by shaking inside a plastic container. The mixed powers were transferred to a platinum crucible and lowered into a furnace beneath the glove box. The power was melted by slowly raising the temperature to 1000ºC at which the temperature was maintained for a period of one hour. The melt was then transferred to a brass mould heated to 300ºC which was placed inside an oven to anneal at a temperature of between 250ºC and 300ºC for 30 minutes to remove any stress which may have built up in the glass. After annealing, the glass was slowly cooled at a rate of around 1ºC per minute to room temperature.

Finally the glass sample was polished with jeweller's rouge (finely powdered iron(III) oxide) under the dry nitrogen atmosphere then cleaned with alcohol and acetone.[101]

6.2. Experimental procedure

6.2.1. Measuring the excitation and emission spectra.

The emission and excitation spectra for all of the rare-earth doped glasses tested here were measured using a similar setup to the one used to measure the spectra of ruby in chapter 5.

When the laser was set up for signal or idler emission there was always a small component of the other beam present as well as 355 nm light from the seed laser. These were filtered using either a 700 nm long pass filter (to block the signal beam and 355 nm beam) or a 700 nm short pass filter combined with a 400nm long pass filter (to block the idler and 355 nm seed light respectively). It was especially critical to do this for the TPF experiments where even a small fraction of light leading to SPA would confuse the data.

As with the ruby excitation spectra, all excitation and emission spectra covered here had a resolution of about 7 nm, limited by the spectrometer which was selected for its small size.

6.2.2. Measuring the decay time constant

Given the limitations of measuring τ that were found when studying the ruby an improved system was devised whereby the signal was processed by a Stanford Research Systems SR250 gated boxcar integrator before being recorded and displayed by a PC. A boxcar integrator is capable of isolating large amounts of random noise from a weak but slowly varying periodic signal by sampling a small section or window in such a way that the effects of any random noise on that window are averaged out over the course of a few cycles. The window is then time shifted along the signal by a small amount and the averaging process repeated. By scanning the window across an entire period the signal may then be recovered.[102] The boxcar integrator's driving program included a feature which could estimate the decay time of a recovered exponential decay but it was, in this case, found to be somewhat unreliable in cases which involved multiple exponential decays and/or prominent rise times or where the signal intensity was too low therefore exponential curves were fitted manually using the least squares method.

6.3. Thulium

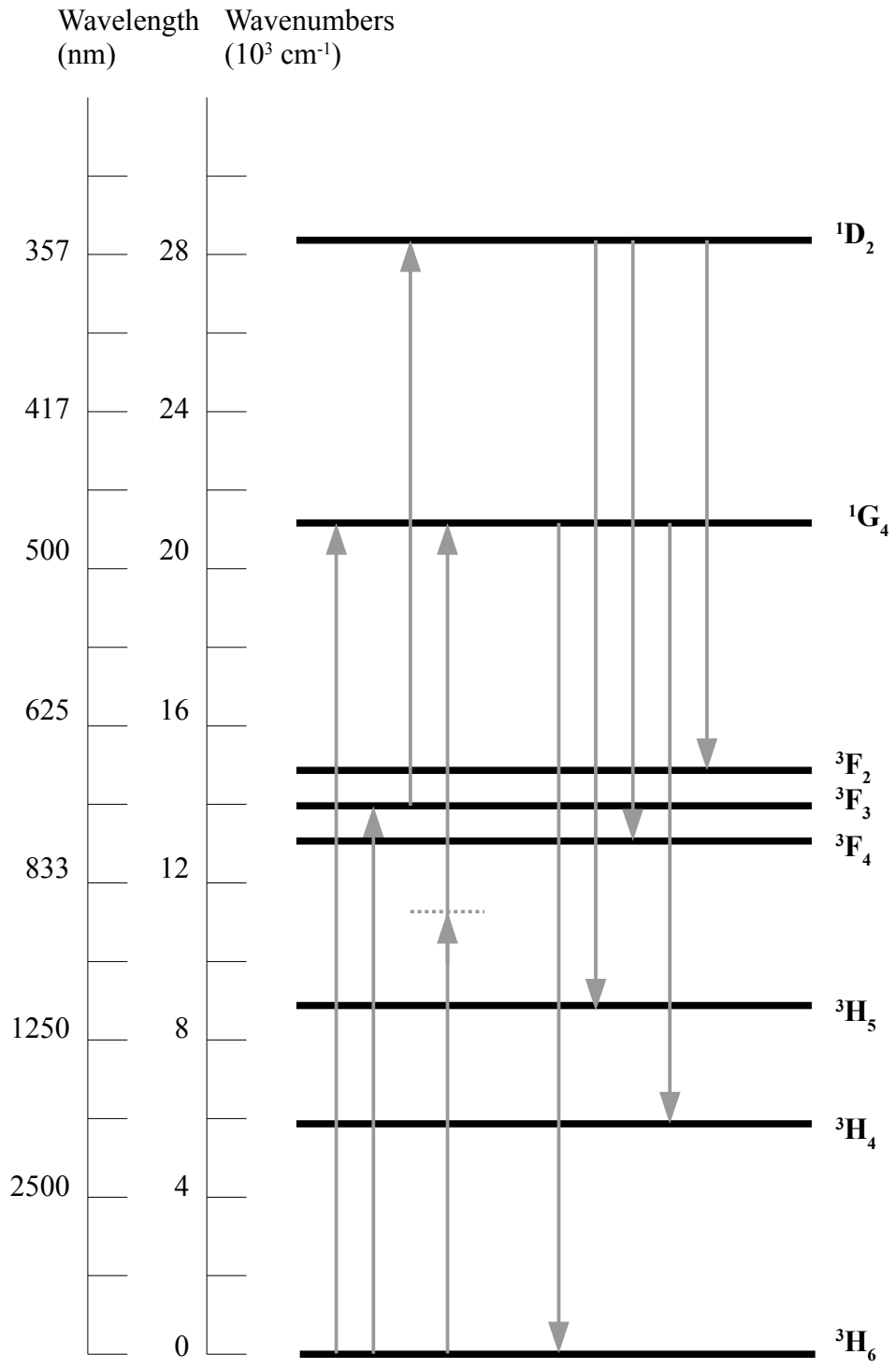

Figure 6.3.1: A simplified energy level diagram for Tm^{3+} showing some of the excitation and emission transitions discussed in this section.

6.3.1. Excitation and emission spectra

The thulium sample used was a ZBLAN glass doped with 0.5 mol weight % TmF_3 giving a Tm^{3+} dopant density of $(3.9 \pm 0.4) \times 10^{20}$ ion cm^{-3}. According to Dieke and Crosswhite[100] there are two energy levels of interest in the visible light region, the $^1D_2$ level excitable by 360 nm SPA and the $^1G_4$ excitable by 470 nm SPA as shown above in Figure 6.3.2. Of these, only the lower one was accessible via SPA from the OPO laser. The upper level was also projected to be difficult to access via degenerate TPA as the $^3F_{2,3,4}$ levels would coincide with the 720 nm excitation required.

The single photon excitation spectrum using the OPO signal beam is recorded in Figure 6.3.2 and Figure 6.3.3. They show the $^3H_6 \rightarrow {}^1G_4$ transition at 467 nm and an unidentified excitation line at 448 nm. The 467 nm excitation resulted in the emission spectrum shown in Figure 6.3.4 which shows several prominent lines. The 470 nm $^1G_4 \rightarrow {}^3H_6$ transition, the 650 nm $^1G_4 \rightarrow {}^3H_4$ transition and the 790 nm $^3H_4 \rightarrow {}^3H_6$ transition are identified. Also observed were relatively faint lines at 540 nm due to $^1D_2 \rightarrow {}^3H_5$ and the 720 nm $^1G_4 \rightarrow {}^3H_5$ transition, shown more clearly in Figure 6.3.5. It is likely that an excited state upconversion is responsible for the excitation of the $^1D_2$ level, possibly via the $^3H_4$ level.

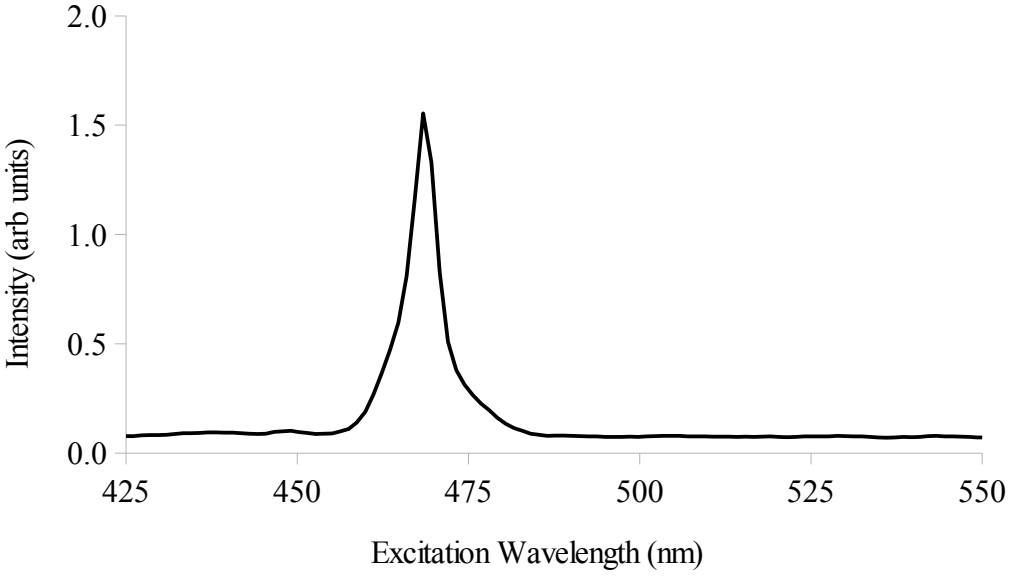

Figure 6.3.2: Excitation of the $^1G_4$ level by SPA resulting in 630 nm emission.

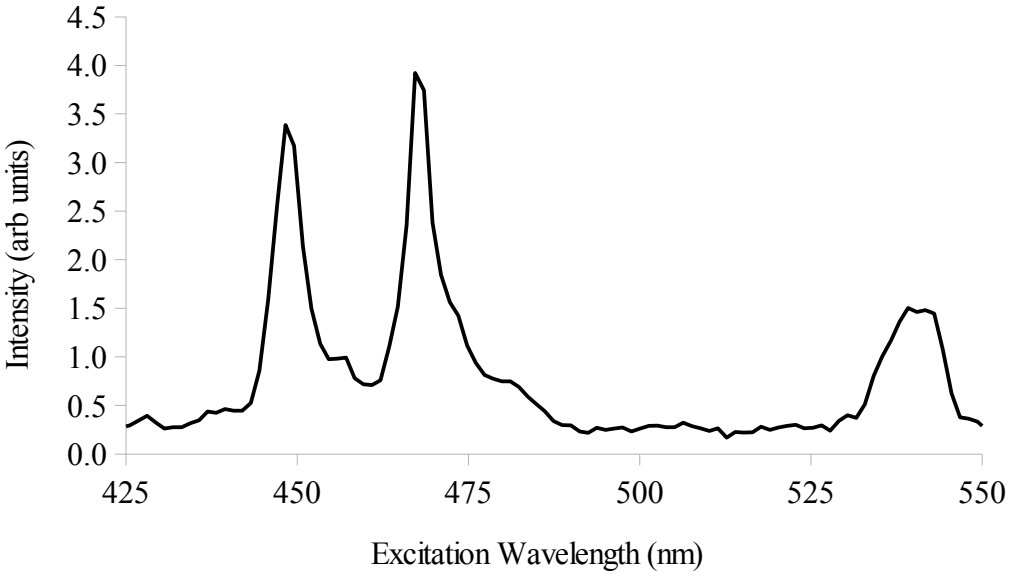

Figure 6.3.3: The single-photon excitation spectrum of the Tm:ZBLAN sample resulting in 540 nm emission. Note the greatly enhanced excitation line at 448 nm.

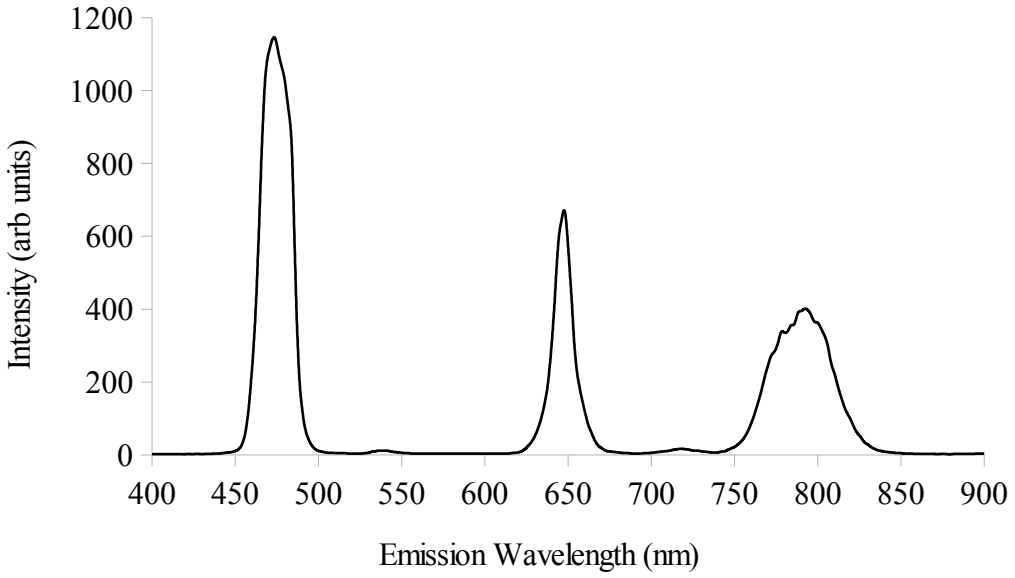

Figure 6.3.4: The emission spectrum associated with 467 nm single-photon excitation. The two weak emission lines at 540 nm and 720 nm are magnified below in Figure 6.3.5.

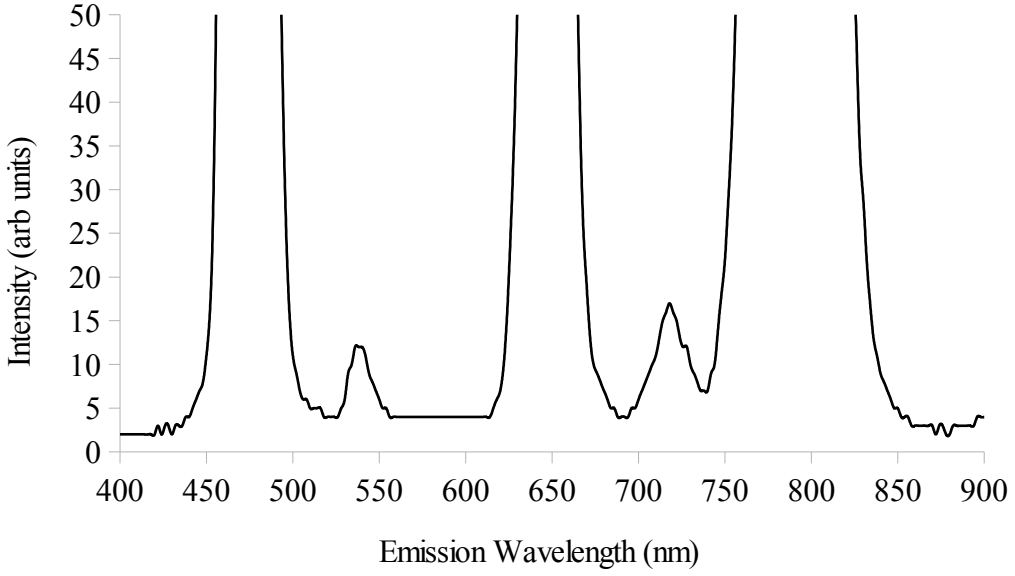

Figure 6.3.5: A rescaled version of Figure 6.3.4 to better show the $^1D_2 \rightarrow {}^3H_5$ transition at 540 nm and the $^1G_4 \rightarrow {}^3H_4$ transition at 720 nm.

Running an excitation spectrum for the 630 nm emission line allowed the scanning of the excited state upconversion band near 800 nm. While not examined completely thoroughly within the scope of this investigation the extent of this band was studied briefly as part of the preparations for the two-photon spectroscopy.

Figure 6.3.6 shows the ESU excitation spectrum which was found to consist of at least three overlapping lines the strongest of which is centred around 795 nm. This spectrum was recorded using settings similar to the single photon spectrum albeit without the neutral density filter covering the photomultiplier hence while the ESU absorption strength is several orders of magnitude less than the primary SPA lines it is still many orders of magnitude stronger than expected for true TPA in a rare-earth metal.

The emission spectrum resulting from 795 nm excitation is recorded in Figure 6.3.7 and shows a broad, heavily saturated (at this scale) band around the laser line, presumably broadened due to resonance with the absorption band. The band has lower level side-bands on either side and shows evidence of three weak peaks at 520 nm, 610 nm and 700 nm.

Two multi-photon excitation lines were observed in the thulium sample at 900 nm and 972 nm. The excitation spectrum in Figure 6.3.8 shows both of these as well as a rising signal towards the short wavelength end of the recorded spectrum. This latter signal was due to the extreme edge of the ESU band mentioned previously and serves to highlight the difference in peak fluorescence strength between the two excitation pathways. The emission spectrum for the two excitation lines, shown in Figure 6.3.9, found only one line at 545 nm in both cases. If the source of this emission line is the same one observed in Figure 6.9.10 then it is difficult to trace the source of the excitation pathway using only two-photon absorption.

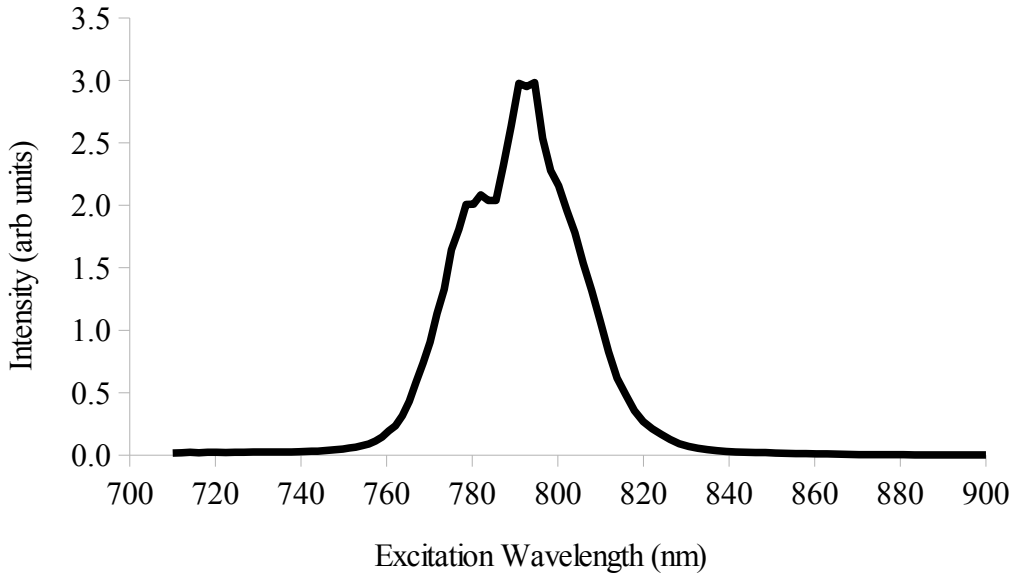

Figure 6.3.6: The excitation spectrum for 630nm emission. The strongest of the three peaks is centred around 795 nm.

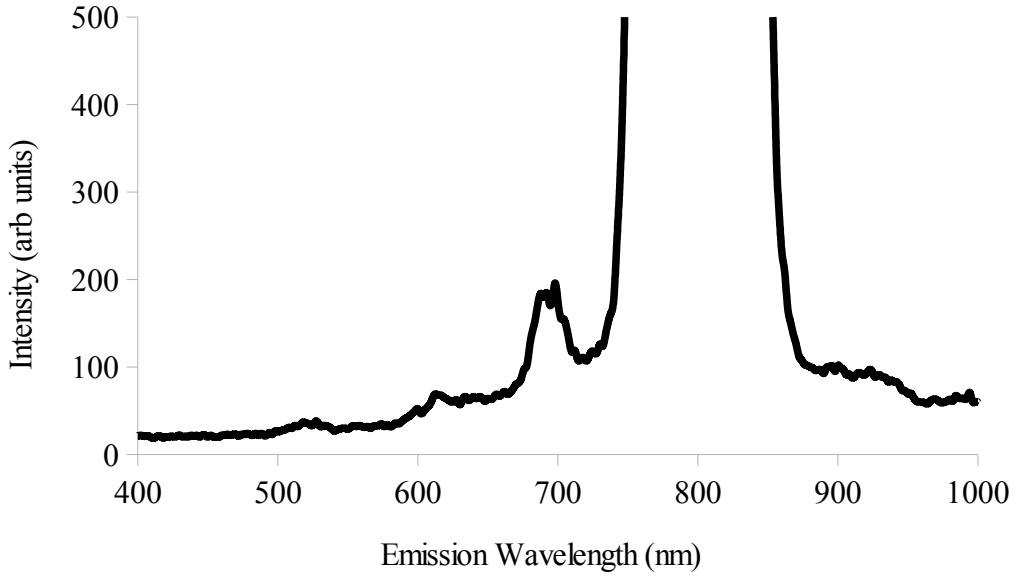

Figure 6.3.7: The emission spectrum of the thulium sample under 795 nm excitation. Notable peaks are centred around 520 nm, 610 nm and 700 nm. The broad, saturated band around 795 nm is a combination of the scattered laser and resonant absorption of the ESU band.

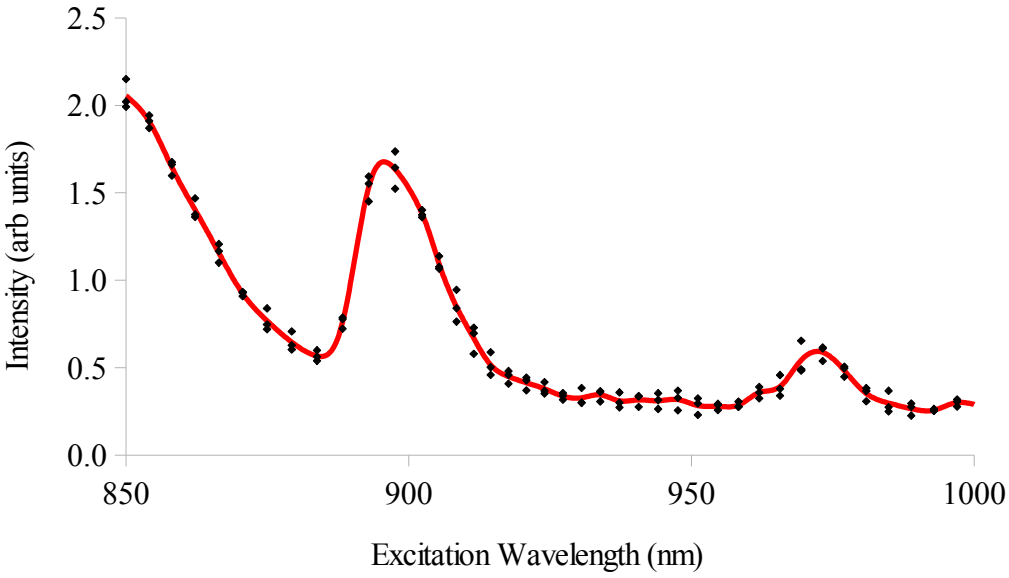

Figure 6.3.8: The two-photon excitation spectrum for 545 nm emission from the Tm^{3+}:ZBLAN sample. The rising signal near 850 nm is the remnant of the ESU side-band. Two TPF peaks were observed near 900 nm and 972 nm

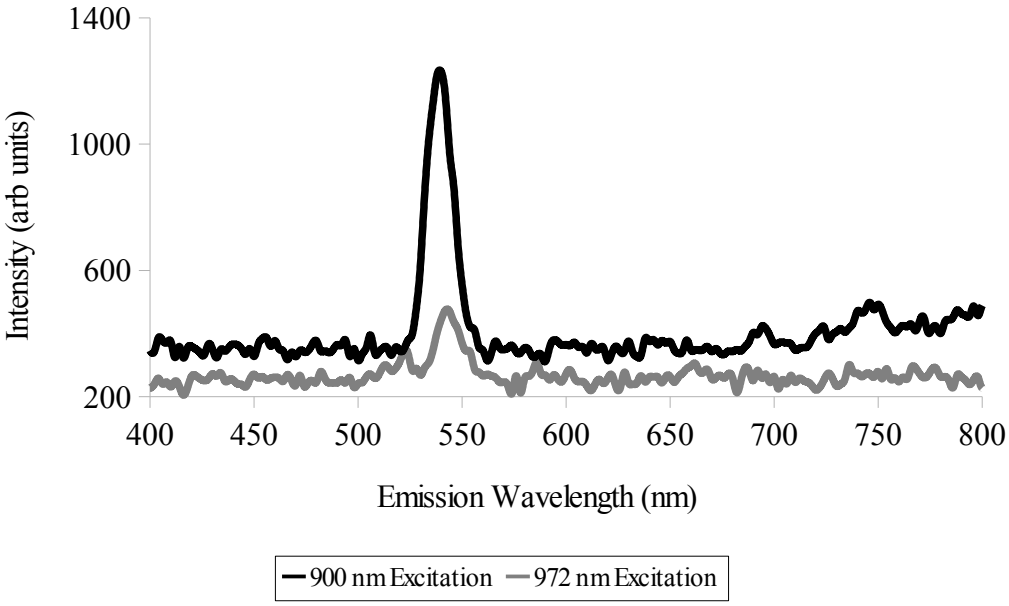

Figure 6.3.9: The two-photon emission spectrum for the Tm^{3+}:ZBLAN sample for each of the two observed excitation line. Only one line, peaking at 545 nm, was observed.

6.3.2. The decay time constant

The decay time constant in thulium was measured at room temperature across several of the recorded emission wavelengths.

The 540 nm emission line was excited by 448 nm and 467 nm SPA and by 900 nm and 970 nm TPA and in most of these cases found a single exponential decay with a decay time constant of approximately 40 μs as shown in Figure 6.3.10.

A notable exception was found in the 970 nm excitation which seems to exhibit a much larger decay time, approximately 129 μs. It is difficult to be conclusive about this measurement however as the signal strength was rather lower then the other excitation lines and the effects of drift in the laser power over the measurement period further reduced the contrast.

Figure 6.3.11 shows the decay characteristics of some of the other emission lines found in the 467nm SPF spectrum such as the 470 nm emission due to the $^1G_4 \rightarrow {}^3H_6$ transition which has a lifetime of 112 μs, The 650 nm emission due to the $^1G_4 \rightarrow {}^3H_4$ transition which was found to have lifetime of 96 μs and the 790 nm $^3H_4 \rightarrow {}^3H_6$ transition which has a lifetime of 116 μs.

6.3.3. Conclusion

As with the previous samples thulium shows some characteristics of a potentially useful dopant for sensor purposes including an energy level structure with reasonably favourable spacing for degenerate TPF. Many questions were unanswered however including, most importantly, the response of the decay time with temperature. Further study of this dopant will be required if a thulium based sensor is to be considered.

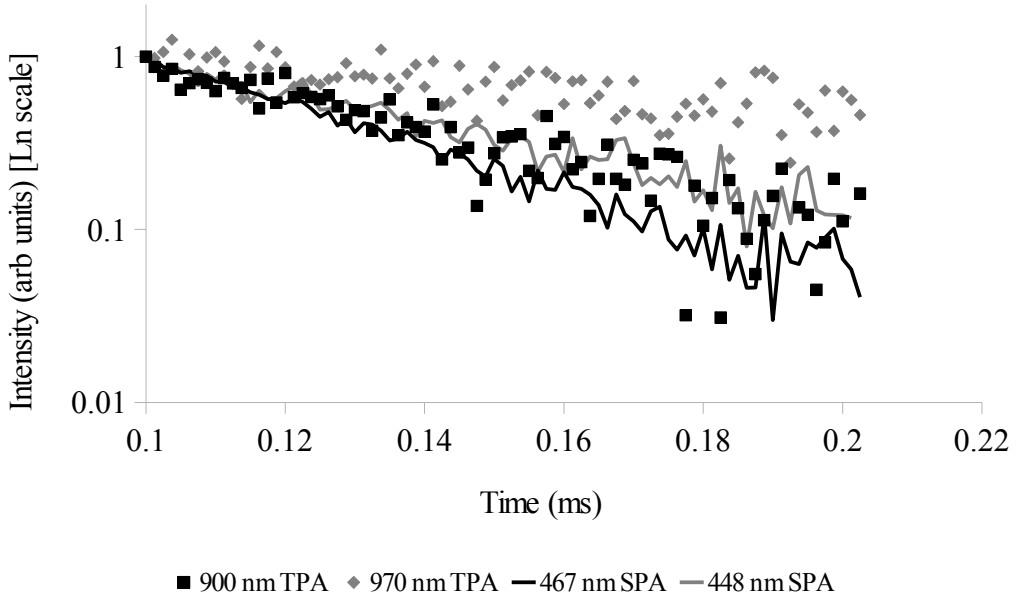

Figure 6.3.10: The normalised room temperature fluorescence decay of the 540 nm emission line. (Solid grey line) 448 nm SPA has a decay time constant of 48 μs, (Solid black line) 467 nm SPA has a decay time constant of 34 μs. (Open diamonds) 900 nm TPA also resulted in a decay time constant of 48 μs. (Closed squares) 970 nm TPA recorded a decay time constant of 129 μs.

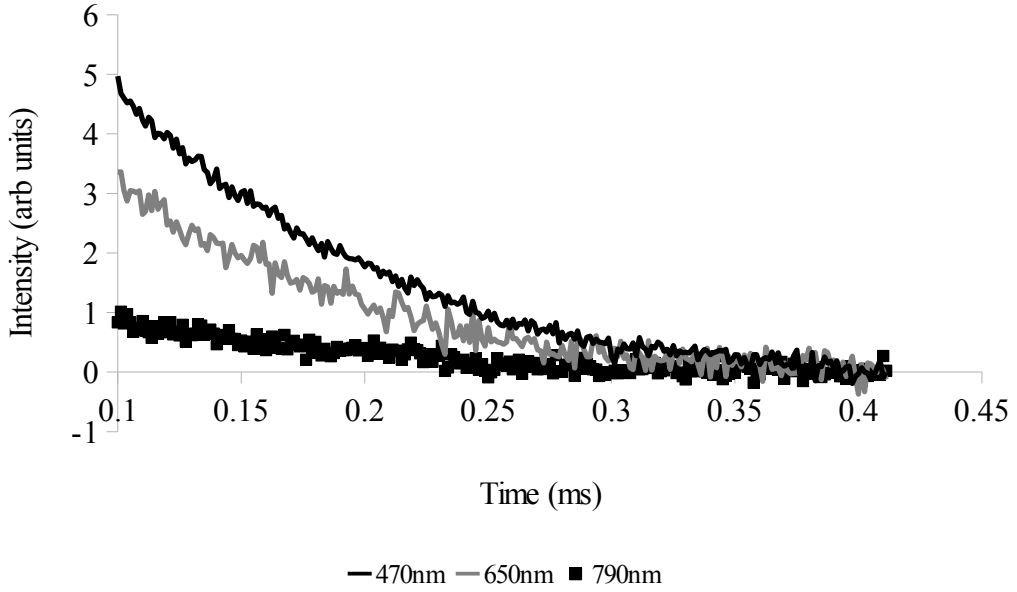

Figure 6.3.11: In addition to 540 nm, exciting Tm^{3+} by 467 nm SPA results in several other emission lines. The 470 nm emission due to the $^1G_4 \rightarrow {}^3H_6$ transition has a lifetime of 112 μs, The 650 nm emission due to the $^1G_4 \rightarrow {}^3H_4$ transition has a lifetime of 96 μs and the 790 nm $^3H_4 \rightarrow {}^3H_6$ transition has a lifetime of 116 μs.

6.4. Gadolinium

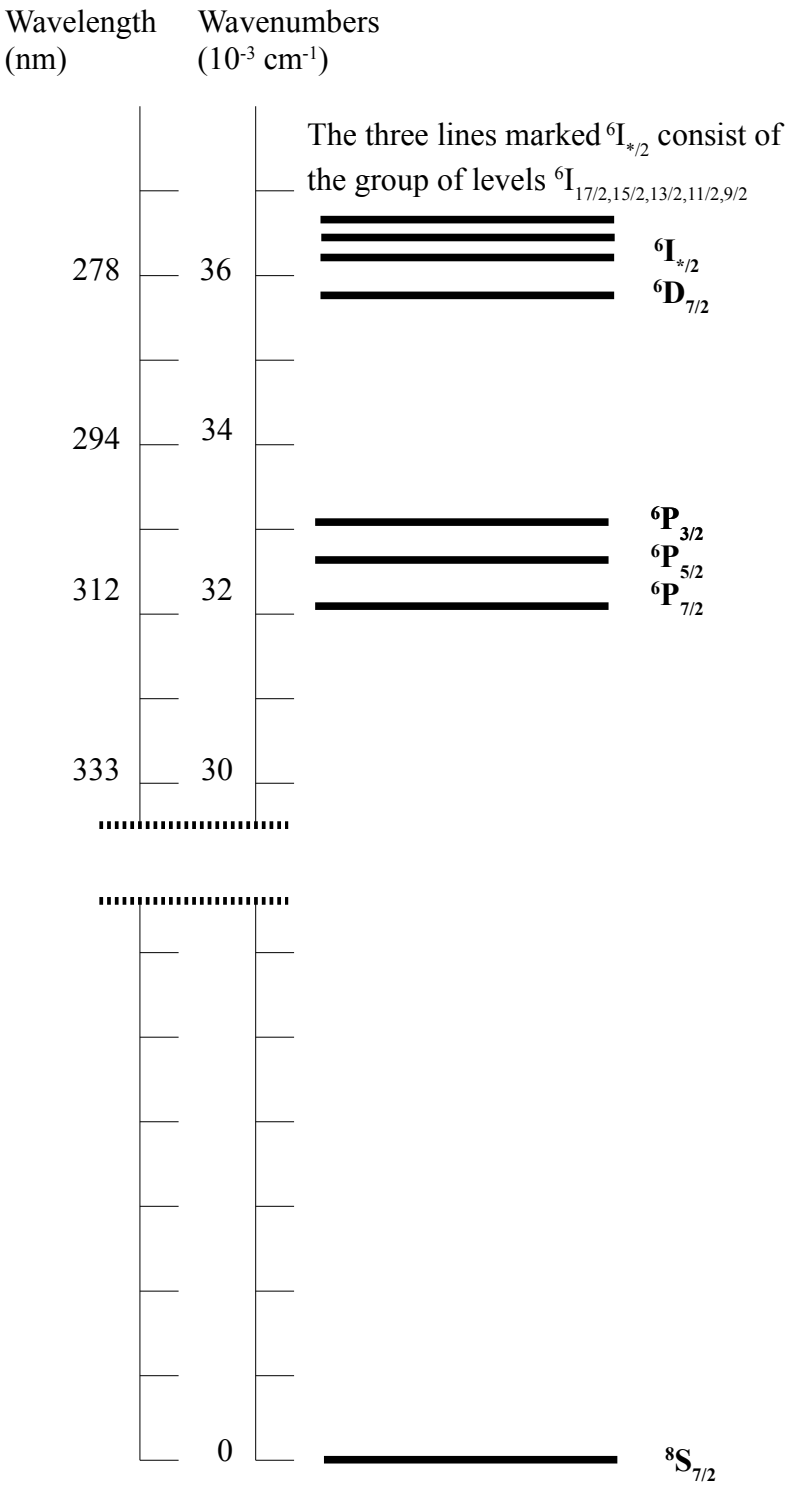

Figure 6.4.1: A simplified energy level diagram for Gd^{3+}. There are no energy levels between the ground state and the $^6P_{7/2}$ level at 32 230 cm^{-1}.

Gadolinium is unusual among the rare-earth metals in that it has an extremely large energy gap between the ground state and the first energy level (around 32 230 cm^{-1} or the equivalent of a single-photon absorption at approximately 310 nm) as shown in Figure 6.4.1 above.[100],[103]

For this reason the excitation and emission characteristics could only be measured in the two-photon regime and a calculation of the absorption cross-section would not be possible. The two-photon absorption of gadolinium appears to be well studied in comparison to the other rare-earths[103],[104],[105] so comparison of the results found here were easier to make than with more sparsely studied dopants.

The sample tested here was a 1% mol weight GdF_3 doped ZBLALi with a Gd dopant density of 1.8×10^{20} ion cm^{-3}.

6.4.1. Results

The two-photon absorption spectrum has already been studied in a CsNaGdCI crystal[14] and describes multiple well separated absorbing lines between 490nm and 625nm. The ZBLALi sample tested here did not show any detectable evidence of these lines but did show the more intense excitation band peaking at 470 nm (the equivalent of a 42 500cm^{-1} transition) shown in Figure 6.4.2. This excitation produced detectable emission in one broad band between 275nm and the UV cut-off at 245 nm as shown in Figure 6.4.3.

As the excitation laser was unable to access the absorption band via single-photon absorption calculation of the absorption cross-section was not possible. It was also not possible to measure the decay time constant as the low detected intensity of the fluorescence resulted in a poor signal-to-noise ratio.

6.4.2. Conclusion

The large energy gap found in gadolinium gives an extremely high degree of flexibility for the investigation of non-degenerate two-photon excitation although the short excitation frequencies required may not be as convenient as the infra-red laser wavelengths used other dopants. Further study may determine if the emission band shows any useful response to temperature or other sensing parameters.

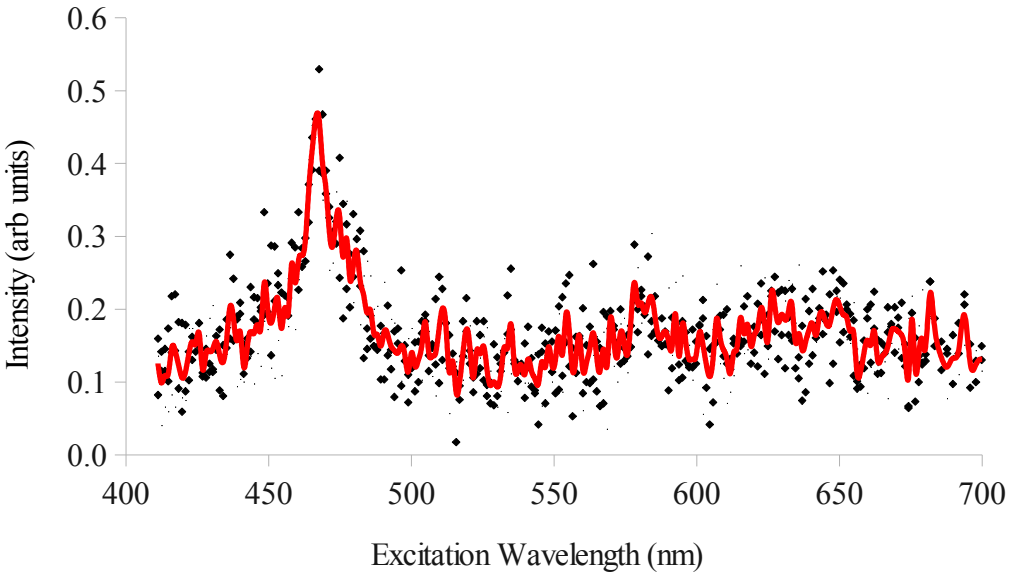

Figure 6.4.2: The two-photon excitation spectrum for 260 nm emission in Gd^{3+}:ZBLALi. One prominent peak was noted at 470 nm.

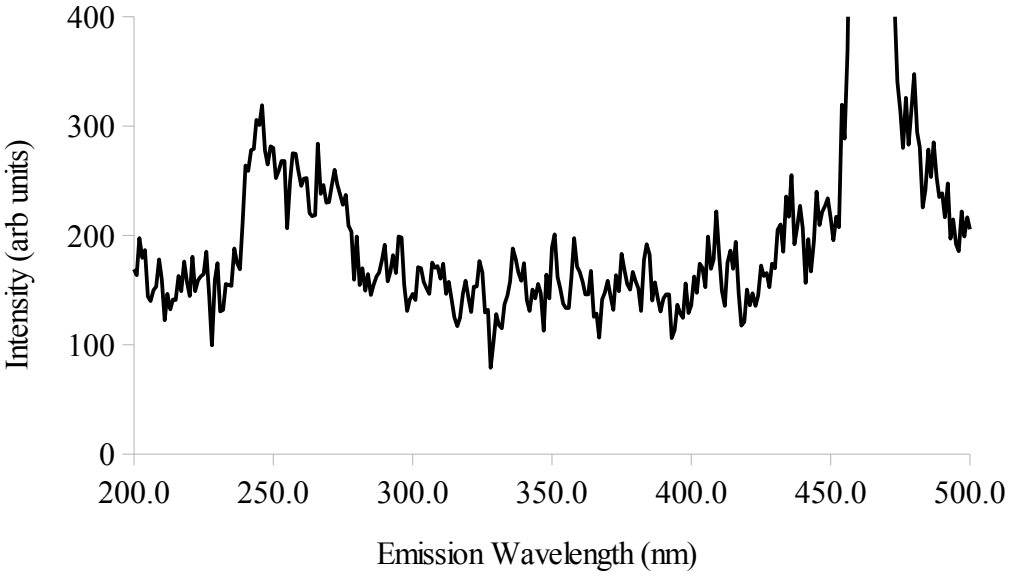

Figure 6.4.3: The emission spectrum for 470 nm TPA in Gd^{3+}:ZBLALi. One emission band was recorded centred around 260 nm.

6.5. Samarium

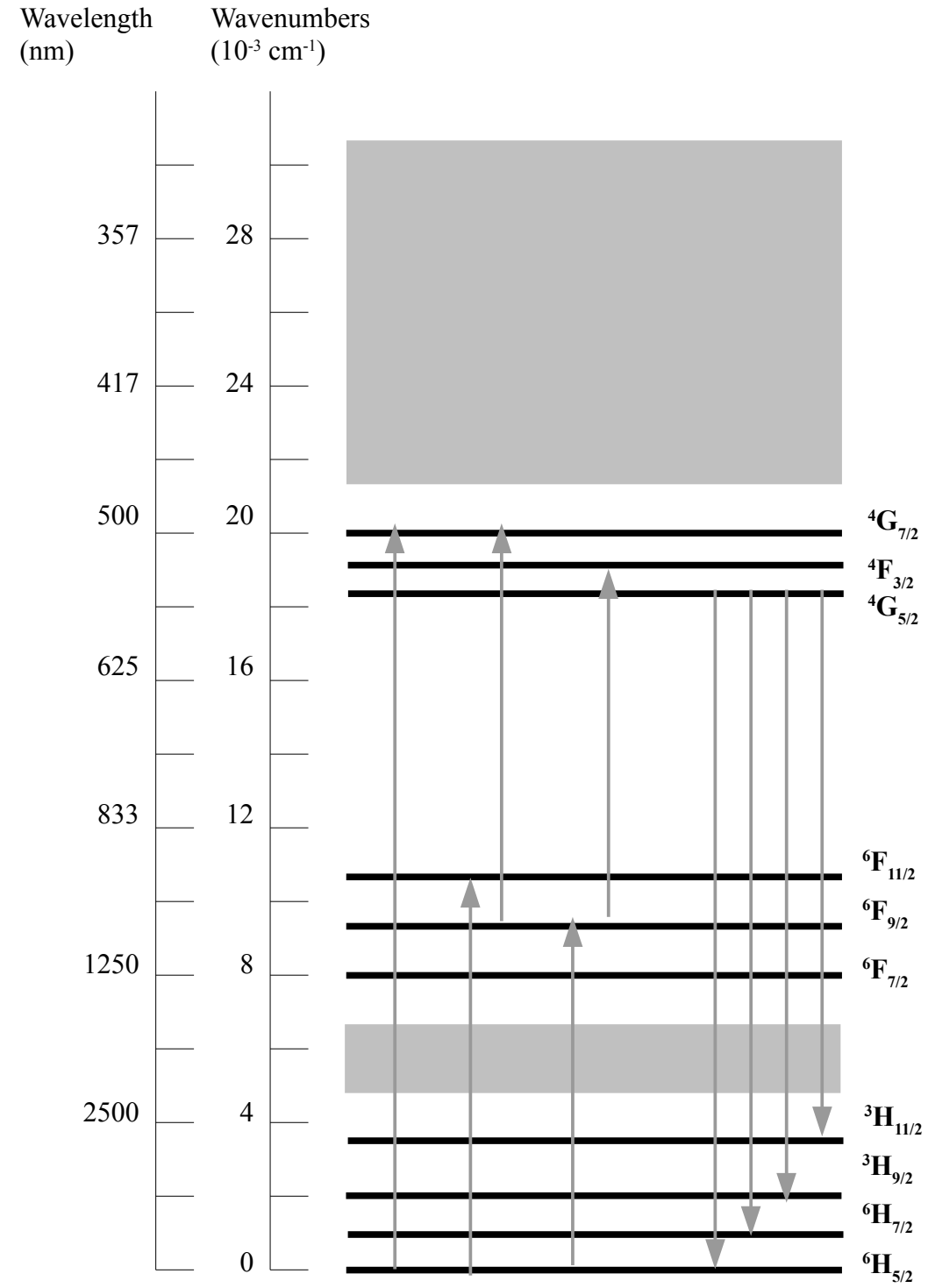

Figure 6.5.1: A simplified energy level for Sm^{3+}. The lower grey box between 5 000 cm^{-1} and 6 500 cm^{-1} represents a group of closely separated levels made up of (in order of lowest to greatest energy) $^6F_{5/2}$, $^6H_{15/2}$, $^6F_{3/2}$, $^6F_{1/2}$, and $^6H_{13/2}$. The upper grey box represents another band of closely separated levels not strongly identified by Dieke.[100]

Samarium was regarded as another promising candidate for TPF as its energy level structure, shown in Figure 6.5.1, is made up of two manifolds of closely clustered lines with a substantial gap between them which ranges from 10 000cm^{-1} to 17 000 cm^{-1} (approximately 1000nm to 590nm). The close spacing of the lines in the manifold however were thought to ultimately limit the dopants potential for non-degenerate two-photon excitation as it was difficult to find any pairs of wavelengths which could combine to excite the upper manifold without each beam also being able to excite by non-degenerate TPA.

The sample examined here was a 1% mol weight Sm^{3+}:ZBLAN with a dopant concentration of 6.8×10^{20} ion cm^{-3}.

6.5.1. Results

In the initial test of the ZBLAN sample was excited via SPA at 467 nm and produced an emission spectrum in the visible region, shown in Figure 6.5.2, with several strong peaks at 565 nm, 595 nm, 645 nm and 705 nm. This matches well the results found by Annapurna et al for Sm^{3+} in $ZnCl_2$ – $BaCl_2$ – LiCl glass which shows emission peaks at 564 nm, 602 nm, 644 nm and 703 nm.[106]

The single-photon excitation for the 645 nm line was also recorded (Figure 6.5.3). Unlike the spectrum reported by Annapurna however only one peak at 467 nm was observed (although this peak exhibits two adjacent structures which may either be sub-peaks or phonon assisted side-bands).

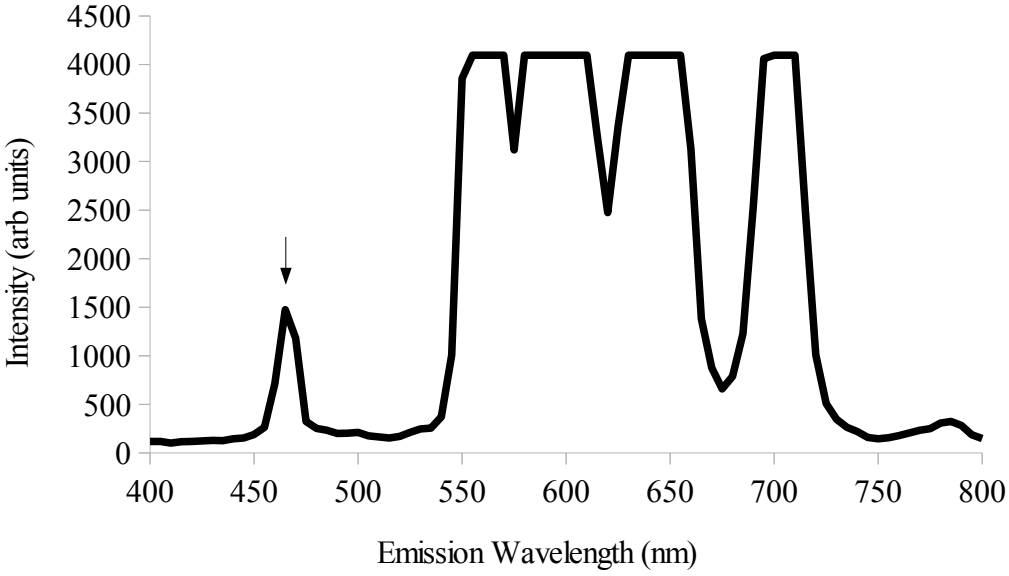

Figure 6.5.2: The emission spectrum recorded for Sm^{3+}:ZBLAN under 466nm SPA. The relative intensities of the peaks were not recorded due to sensor saturation. The laser line is marked by the arrow.

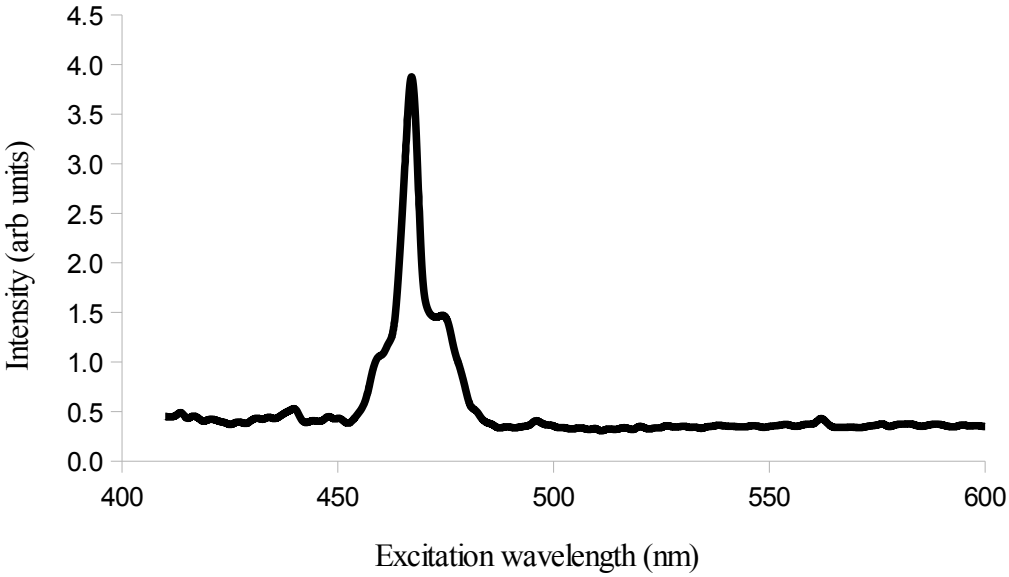

Figure 6.5.3: The single-photon excitation spectrum for 650nm emission in the Sm^{3+}:ZBLAN sample. Only one major peak at 480 nm with two sub-peaks or side-bands was observed.

While no evidence of TPF was found in Sm^{3+} for wavelengths greater than 700nm (despite results from other works such as those by Thorne et al[107]) there was a ESU line found at 945 nm, shown in Figure 6.3.4 and also observed by Thorne et al, which corresponds to excitation to the upper energy levels via the $^6F_{11/2}$ energy level. The emission spectrum from this ESU excitation, shown in Figure 6.3.5, closely matches that of the single-photon excitation strongly suggesting that the emission pathways are similar. Another weak ESU line was observed at 1110nm which corresponds to excitation from $^6H_{1/2} \rightarrow {}^6F_{9/2}$ then from $^6F_{9/2} \rightarrow {}^4G_{5/2}$ though no emission spectrum was recorded for this excitation.

As no TPF could be found in the sample the characteristics of the emission such as the decay lifetimes were not examined. However, they are expected to be similar to those found by Annapurna et al[106] who observed lifetimes of around 480 μs for 602nm emission at room temperature.

6.5.2. Conclusions

With no immediate signs of being able to detect TPF in Sm^{3+} this sample was discarded from the list of potential fibre dopants for the scope of this investigation. It is clear however from the literature that TPF is possible and given that the emission spectrum is easily detectable Sm^{3+} would be a good candidate for a follow-up study if one was to take place in the future.

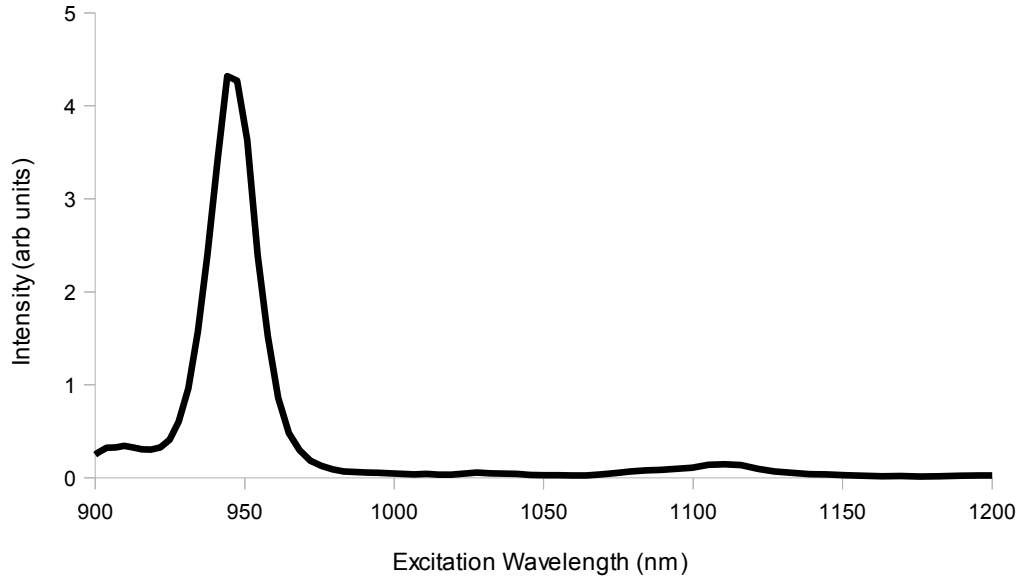

Figure 6.5.4: The ESU excitation spectrum for 650 nm emission in Sm^{3+}:ZBLAN. Two peaks are visible corresponding to excitation via $^6F_{11/2}$ at 945 nm and $^6F_{9/2}$ at 1110 nm.

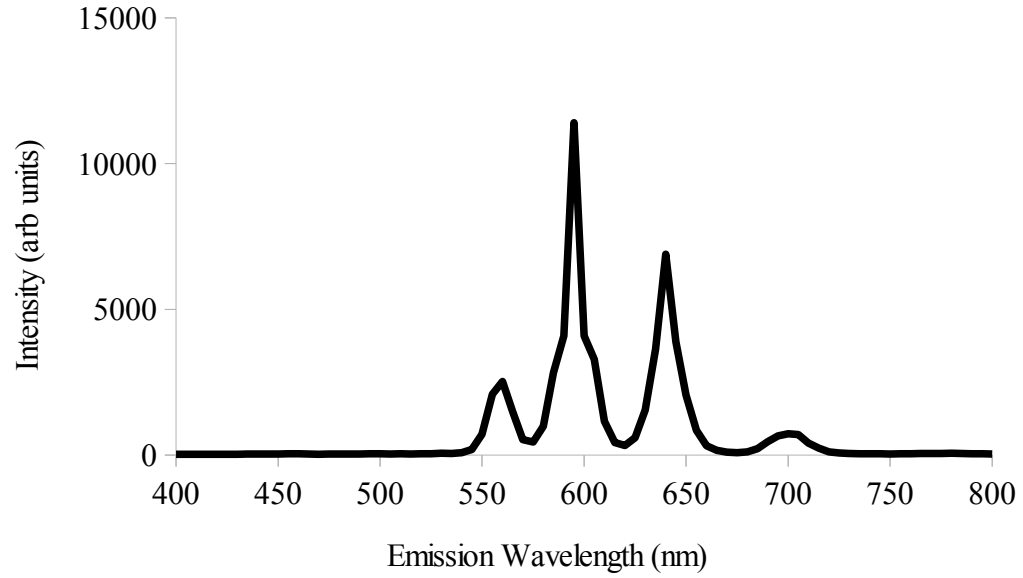

Figure 6.5.5: The emission spectrum resulting from 945nm ESU in Sm^{3+}:ZBLALi. The relative intensities of the peaks match closely those found by SPA by Annapurna et al[106]

6.6. Dysprosium

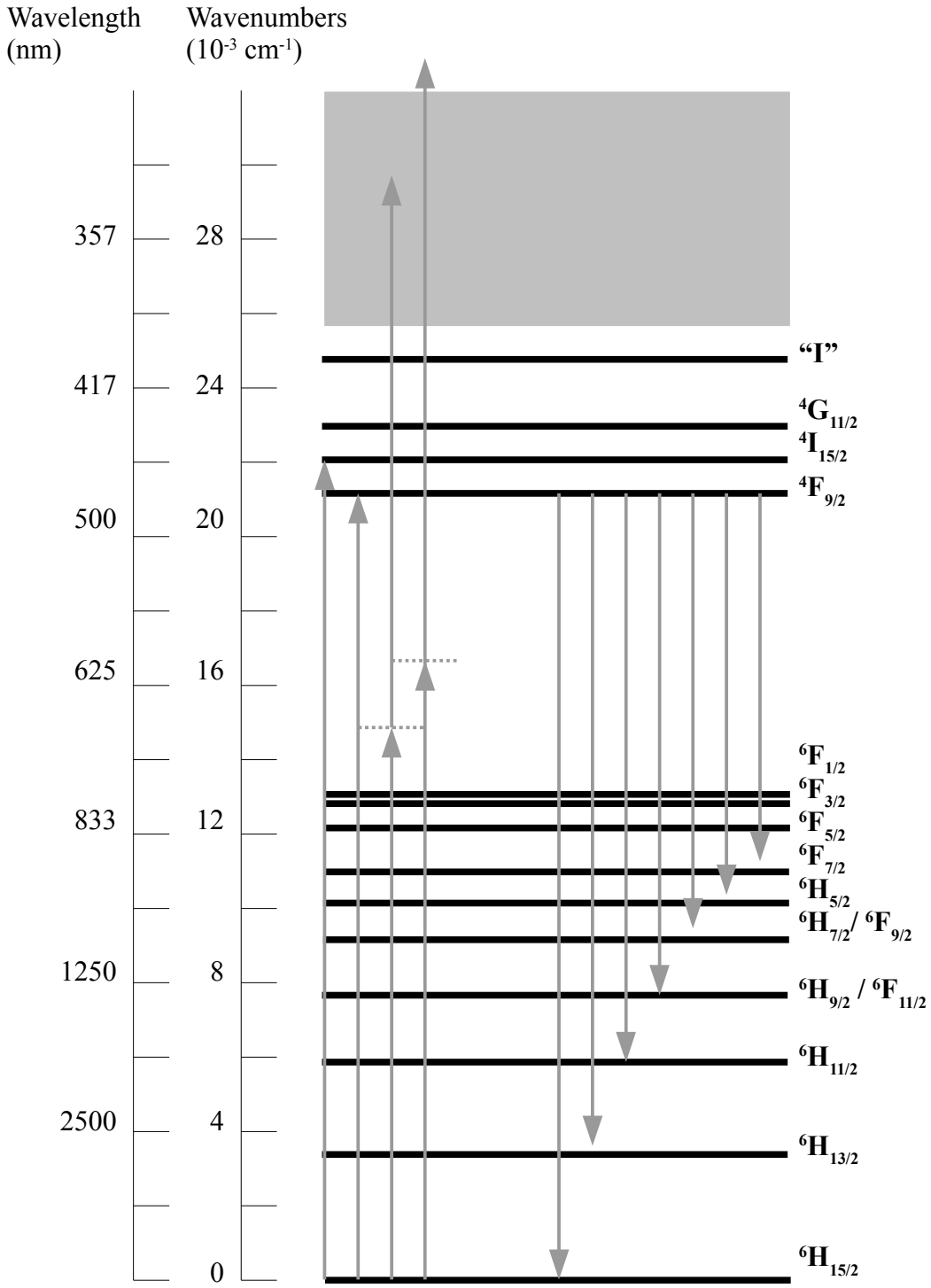

Figure 6.6.1: A simplified energy level diagram for Dy^{3+} and the transitions investigated in this section. The grey box represents levels excitable by photon energies above 25 500 cm^{-1} (The equivalent of a 390nm single photon excitation).

6.6.1. The single-photon absorption cross-section spectrum

The final rare-earth metal reported in this chapter is dysprosium which as a candidate seemed to possess a favourable energy level structure, shown in Figure 6.6.1, as it consists generally of two broad manifolds with a convenient large gap between the $^6F_{1/2}$ at about 13 500 cm^{-1} (an SPA equivalent of 740 nm) and the $^4F_{9/2}$ level at 21 000 cm^{-1} (an SPA equivalent of 475 nm).[100]

The sample used in this study was a ZBLAN glass doped with DyF_3 to a concentration of 1.0 mol wt %, thus giving a Dy^{3+} dopant density of 5.3×10^{20} ion cm^{-3} which allowed a calculation of the single-photon absorption cross-section for the sample over a spectrum ranging across the visible spectrum as shown in Figure 6.6.2. The results gathered correspond well with results gained in other studies of similar glasses.[108] The spectrum shows multiple peaks but they are difficult to identify until after the curving background signal is subtracted off as in Figure 6.6.3 where the majority of the lines identified by Dieke between 350 nm and 900 nm. These include transitions from the $^6H_{15/2}$ ground state to: $^4I_{15/2}$ at 450 nm, $^4F_{9/2}$ at 475 nm, $^6F_{1/2}$ at 740 nm, $^6F_{3/2}$ at 770 nm, the largest peak $^6F_{5/2}$ at 830 nm and $^6F_{7/2}$ at 890 nm in addition to a peak at 490 nm (approx. 26 000 cm^{-1}) which is marked but not identified by Dieke and referred to by Piramidowicz at al[108] as a “group of highly mixed states”. One identified line, the $^4G_{11/2}$ line, which should lie around 430 nm, is visible in the study by Piramidowicz although it is weak compared to adjacent lines.

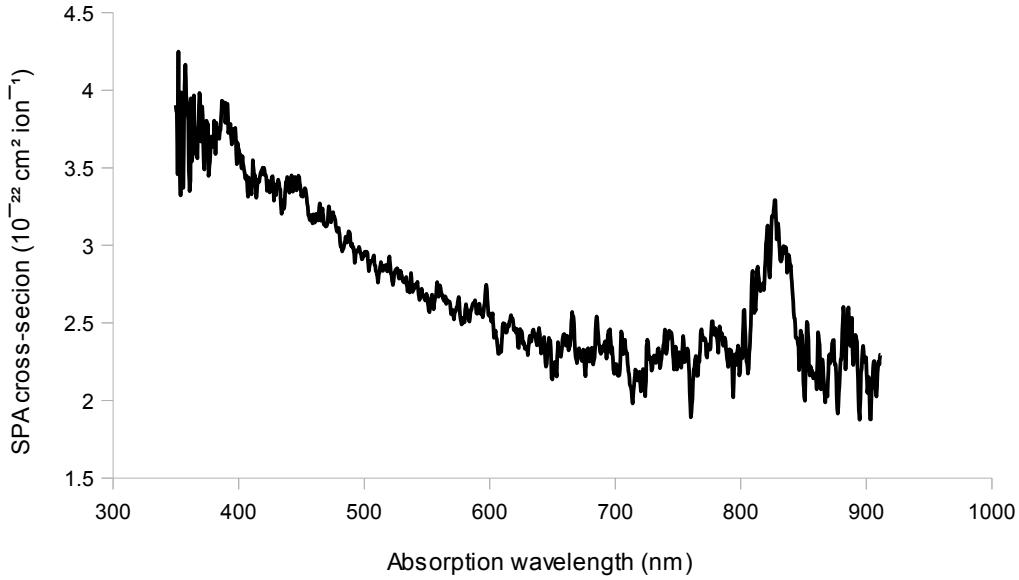

Figure 6.6.2: The single-photon absorption spectrum of the Dy^{3+}:ZBLAN. The absorption lines are partially obscured by the exponential-like background curve.

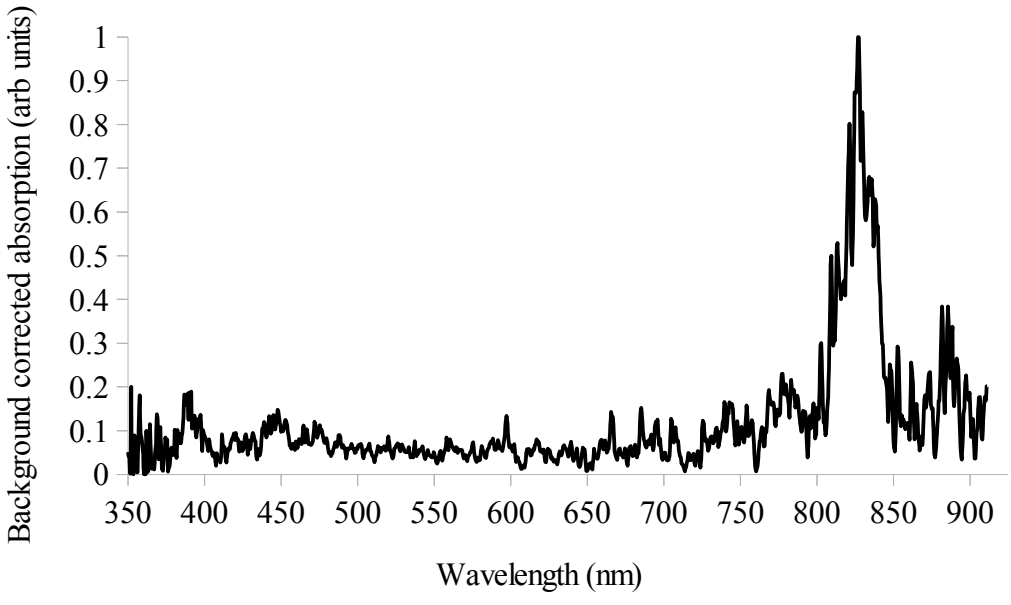

Figure 6.6.3: The absorption spectrum normalised and with the rising background signal removed. Identified absorption lines include transitions from the $^6H_{15/2}$ ground state to: $^4I_{15/2}$ at 450 nm, $^4F_{9/2}$ at 475 nm, $^6F_{1/2}$ at 740 nm, $^6F_{3/2}$ at 770 nm, the largest peak $^6F_{5/2}$ at 830 nm and $^6F_{7/2}$ at 890 nm.

6.6.2. The excitation and emission spectra

The emission spectrum for Dy^{3+} looks reasonably complex and consists predominantly of emission from the $^4F_{9/2}$ energy level, the lowest level in the upper manifold, into the various levels of the lower manifold. Observed first by 420 nm SPF then later by 650 nm and 532 nm TPF and shown in Figure 6.6.4 were emission lines due to transitions from the $^4F_{9/2}$ level which include the 480 nm emission from this transition to the ground state $^6H_{15/2}$; 570 nm emission due to transition to $^6H_{13/2}$; 655 nm to $^6H_{11/2}$; 750 nm to $^6H_{9/2}$/ $^6F_{11/2}$; 840 nm to $^6H_{7/2}$/ $^6F_{9/2}$; 905 nm to $^6H_{5/2}$ and 965 nm to $^6F_{7/2}$.

Examining the strongest emission line, and also the shortest wavelength transition (excluding those terminating to the ground state) the 570 nm $^4F_{9/2} \rightarrow {}^6H_{13/2}$ transition gave the measurement of the single-photon excitation spectrum shown in Figure 6.6.5 which clearly shows the two lowest energy excitation events into the upper manifold. The two lines are identified as the $^4F_{9/2}$ energy level peaking at 465 nm and the $^4I_{15/2}$ level peaking at a little lower than 450 nm. A rising signal as the laser approached the upper limit of its range at 410 nm may be indicative of absorption onto an unnamed level at around 25 000 cm^{-1} (denoted "I" on the Dieke diagram). As with the absorption spectrum, no evidence was found of the $^4G_{11/2}$ line at 430 nm.

Attempts to measure the two-photon excitation spectrum were less than unambiguous as it seems that the large range of the upper manifold and the comparative density of lines results in a near continuous excitation over the full range of the energy gap between the two groups. Furthermore the already low signal strength was partially masked by a semi-periodic source of electrical noise.

One two-photon excitation peak was obtained centred on 640 nm and which may result in excitation to one of the unnamed energy levels at around 31 250 cm^{-1} (possibly the level denoted "R" on the Dieke diagram). Several lines capable of ESU exists between the absorbing line and the primary emission line of $^4F_{9/2}$ (notably the one denoted "O" by Dieke) which explains the short wavelength emission lines seen in the TPF emission spectra in Figure 6.6.4 such as at 270 nm and 350 nm.

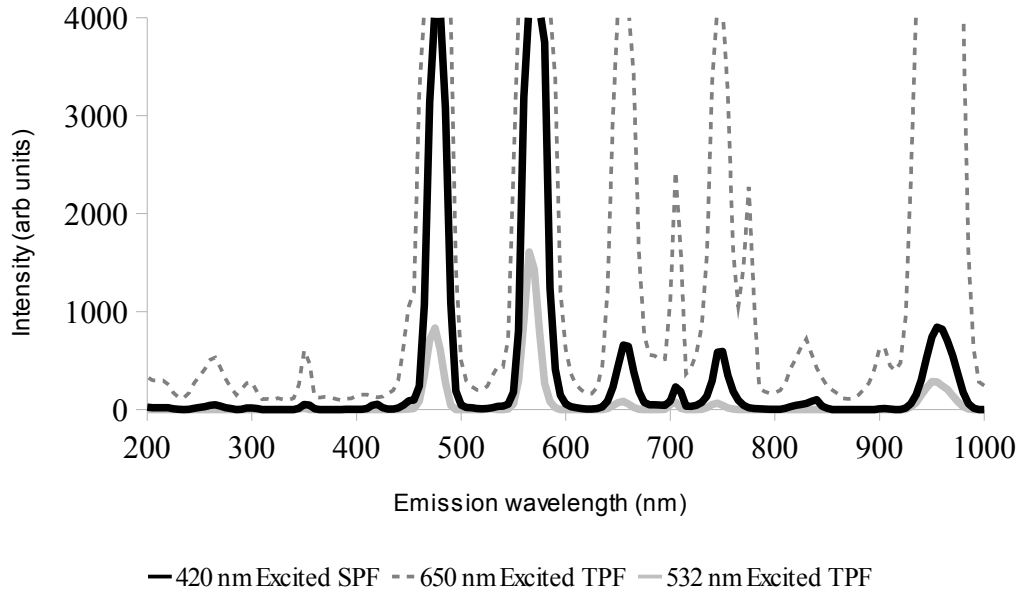

Figure 6.6.4: Several emission spectra for Dy^{3+}:ZBLAN excited by (black solid line) 420 nm SPA, (grey dashed line) 650 nm TPA and (grey solid line) 532 nm excited TPA. Relative peak intensities between the single-photon and two-photon spectra are not to scale.

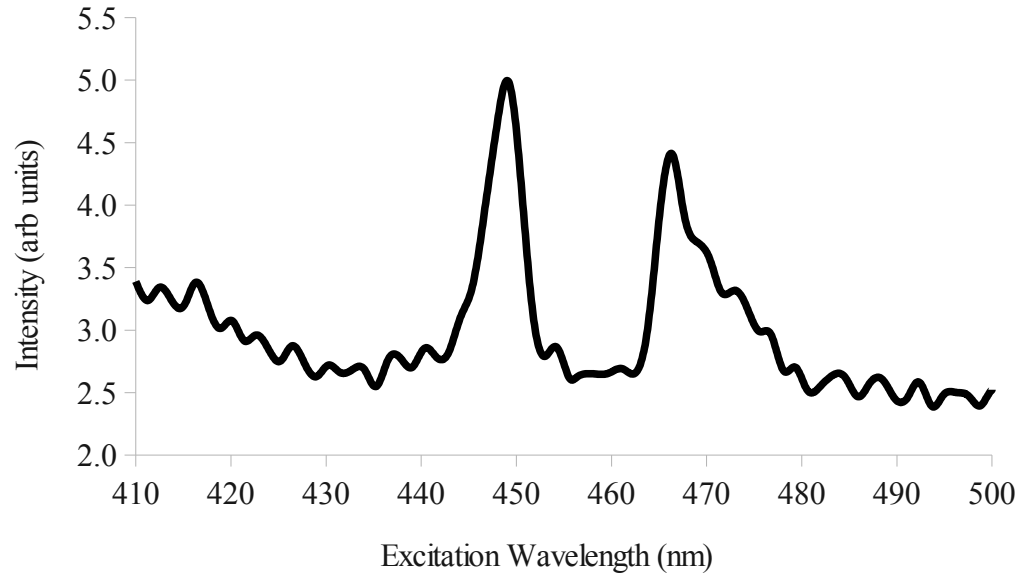

Figure 6.6.5: The single-photon excitation spectrum for Dy^{3+}:ZBLAN emitting at 570 nm. The $^4I_{15/2}$ at 450nm, $^4F_{9/2}$ at 470 nm were the only two lines which could be identified.

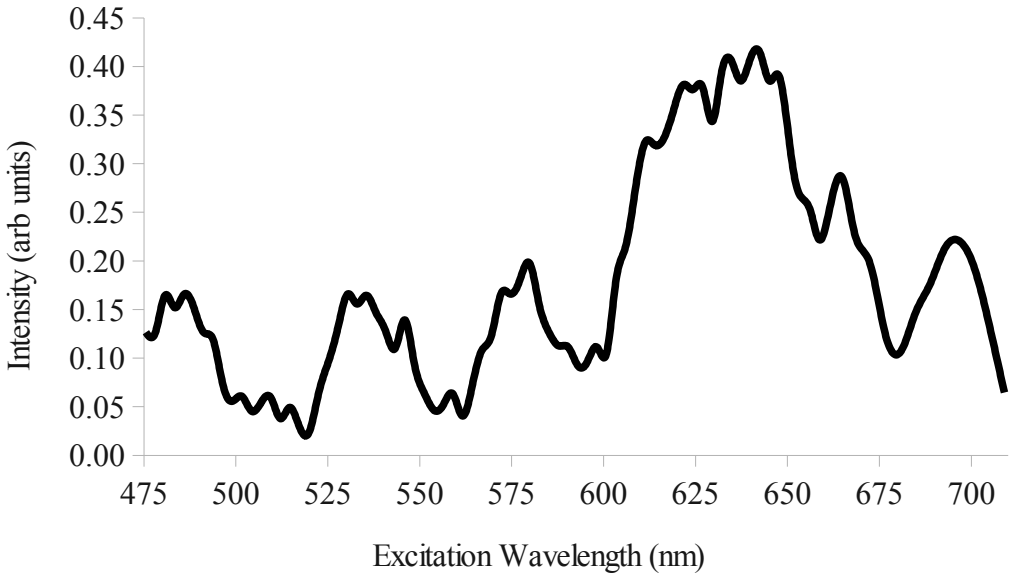

Figure 6.6.6: The two-photon excitation spectrum for Dy^{3+}:ZBLAN emitting at 570 nm. The small peaks with a magnitude of approximately 0.15 were found to be caused by electrical noise. The primary peaks at 640 nm results in absorption to a sub-group of energy levels centred at 31 000 cm^{-1}.

6.6.3. Conclusion

Single- and two-photon excited fluorescence were observed in the Dy^{3+}:ZBLAN sample with relative ease compared to some of the other candidates which may be suggestive of a fairly high absorption cross-section. Additionally, many of the strong fluorescence lines terminate at energy levels above the ground state which, as seen previously, greatly enhances the viability of the candidate for distributed sensing purposes.

As a candidate for non-degenerate TPF however dysprosium suffers from a similar limitation as samarium. The extremely broad upper manifold of levels means that virtually any excitation below 18 000 cm^{-1} (555 nm) will absorb via degenerate TPA so a matched pair with no self-excitation on either beam is likely to be difficult to arrange. This said, a sensor with half the background signal compared to a degenerate system may be of some advantage should dysprosium prove to have useful sensing characteristics.

6.7. Holmium

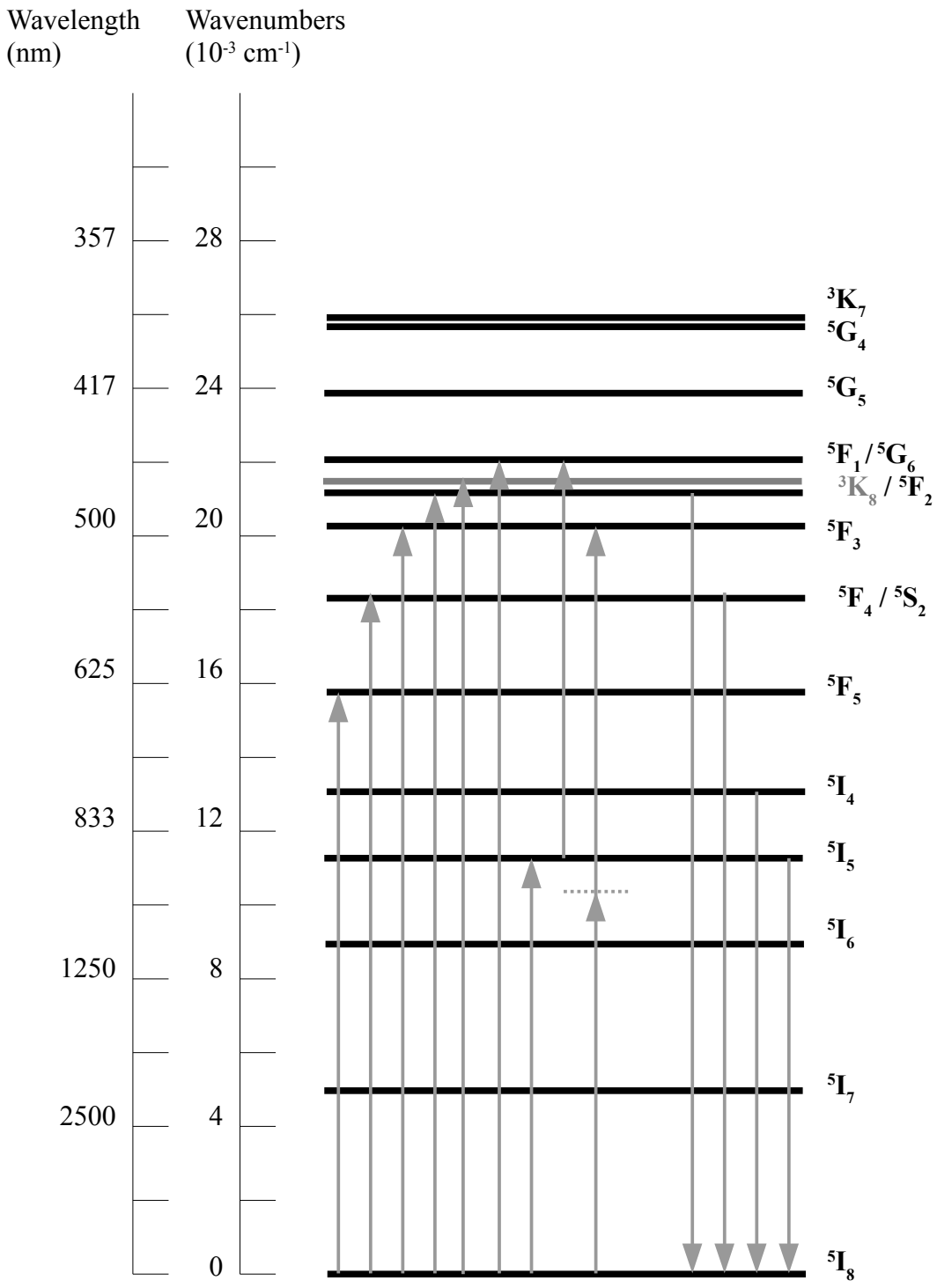

Figure 6.7.1: An energy level diagram for Ho^{3+} with the transitions explored in this section.

At first glance holmium does not seem to present the same opportunities for two-photon excitation as many other rare-earth dopants as the energy levels are much more evenly spaced and lack large gaps which could be easily exploited for two-photon excitation without competing excited state upconversions as can be seen in the energy level diagram in Figure 6.7.1. It has, however, seen some study of its non-linear optical properties recently although with more regard to the excited state upconversion characteristics than the TPF.[109],[110]

The sample used was a ZBLALi glass doped with 2% mol weight HoF_3 giving a Ho^{3+} dopant density of 5.3×10^{20} ion cm^{-3} which allowed the measurement and calculation of the single-photon absorption cross-section spectrum shown in Figure 6.7.2 which compares very well with a previously published study of Ho^{3+} doped in a lead based glass ceramic[110] apart from the rising background signal towards the short wavelength end that was observed in the ceramic.

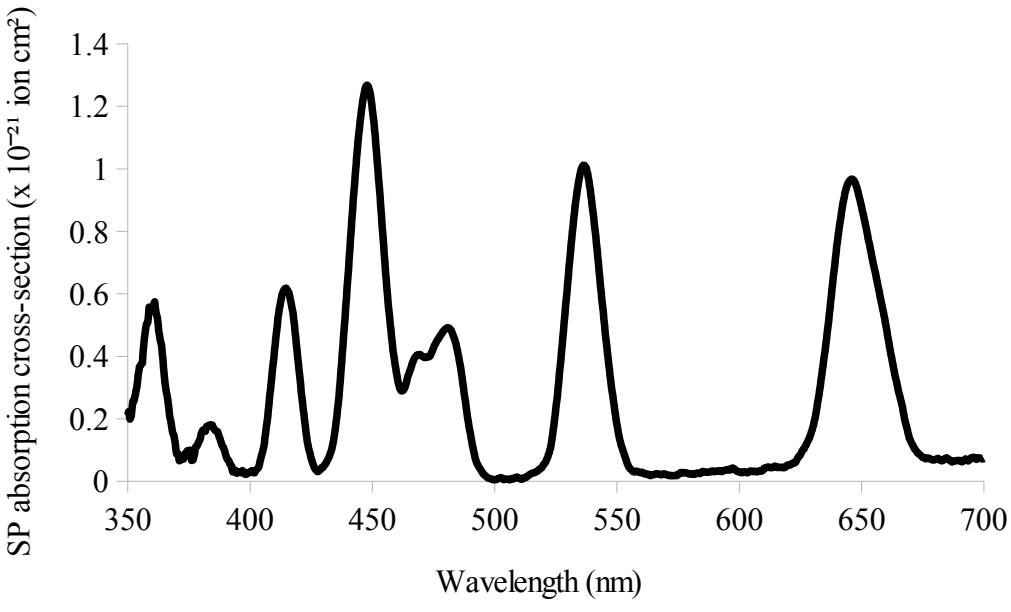

Figure 6.7.2: The single-photon absorption cross section spectrum of Ho^{3+}:ZBLALi. Notable transitions identified are $^5I_8 \rightarrow {}^5F_5$ at 650 nm, $^5I_8 \rightarrow {}^5S_2$ at 540nm and $^5I_8 \rightarrow {}^4F_3$ at 490 nm. Absorption lines due to the $^5I_8 \rightarrow {}^5I_j$ group at wavelengths >700 nm were not observed due to limitations of the sensitivity of the PMT.

6.7.1. The excitation and emission spectra

The single-photon emission spectrum in holmium is clearly defined in both of the studies referenced previously and was used to guide the measurement of the excitation spectra. The single-photon excitation spectrum was measured by monitoring first the $^5F_5 \rightarrow {}^5I_8$ emission at 650 nm and then the $^5I_4 \rightarrow {}^5I_8$ emission at 750 nm. The resulting scans of the excitation spectra, shown in Figure 6.7.3, show in both cases at least four strong lines representing absorption from the ground state to the $^5F_3$, $^5F_2$, $^3K_8$ and $^5F_1$ levels at 485 nm, 471 nm, 459 nm and 451 nm respectively. An additional line is apparent on both spectra, centred around 477 nm but the source of it is not clear from the Dieke Diagram.

Also visible in this SPA scan were two relatively weak excitations (some 40 times less intense than the main peaks) at 540 nm and 650 nm which also lead to 650 nm and 750 nm emission, although, as can be seen in Figure 6.7.4 the intensities of these two emission lines are highly dependent on excitation wavelength with the 750 nm emission being the more favourable of the two under 540 nm excitation and the 650 nm emission being favourable under 650 nm SPA.

ESU resulting in 750 nm emission was also observed at an excitation wavelength of 900 nm and appears to take the path from $^5I_8$ to $^3F_1$ via $^5I_5$. This result stands in slight contrast to the previous ESU study by Gouveia-Neto [110] who claimed to observe the same excitation pathway at 850 nm. While that study excited the sample using a fixed wavelength diode laser and it is possible that they were observing the edge of an absorption line which peaked nearer to 900 nm. Figure 6.7.2 shows that the there is almost no excitation that far away from the peak. It is possible that the difference in hosts plays a significant effect as it may be that the excitation band was blue-shifted with respect to this result just enough for significant signal to be excited by 850 nm. Certainly lack of laser power cannot explain the difference as the published study used a 70 mW cw diode laser whereas in this study the OPO was operating at an average of 200 mW at 850 nm.

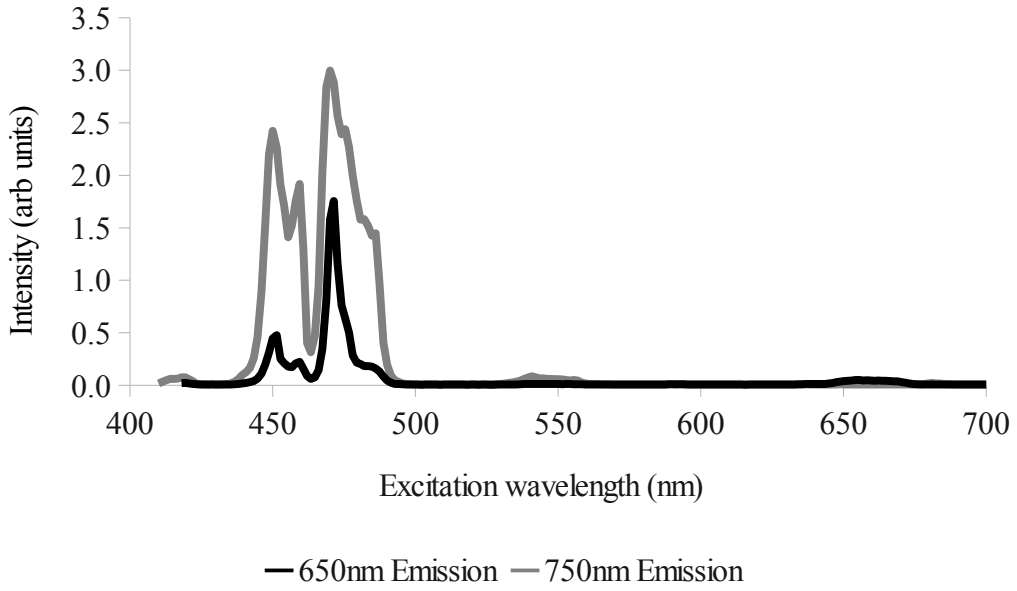

Figure 6.7.3: The single-photon excitation spectra for Ho^{3+}:ZBLALi emitting at 650nm (black line) and 750nm (grey line). The excitation group reveals absorption onto the $^5F_{3,2,1}$ levels between 440 nm and 480 nm and the $^3K_8$ line at 459 nm. Figure 6.7.4 below shows the same graph rescaled to show the weak excitation lines at 540 nm and 660 nm.

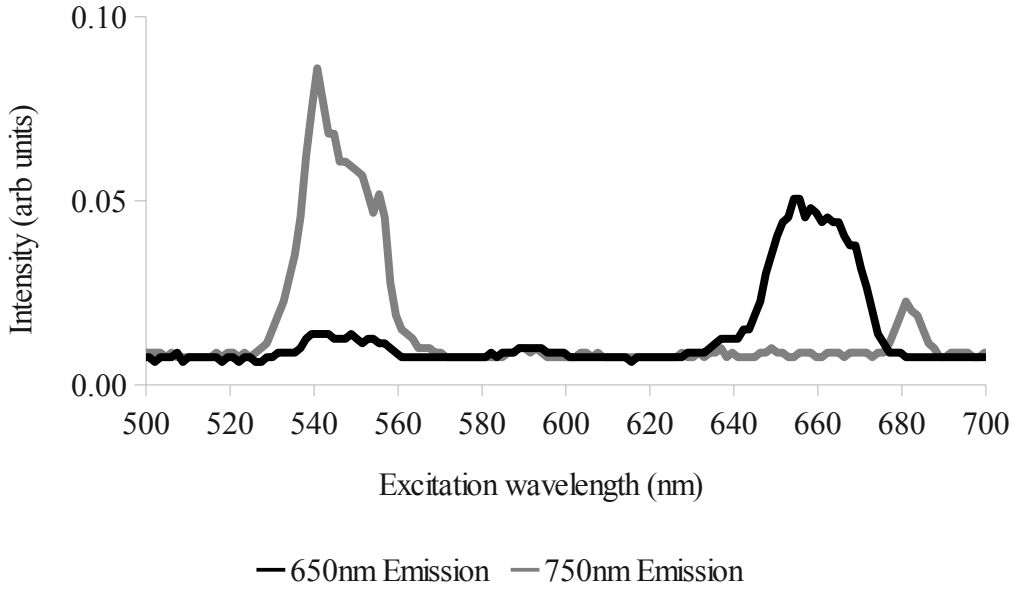

Figure 6.7.4: The single-photon excitation spectra for Ho^{3+}:ZBLALi for 650nm and 750nm emission showing excitation onto the $^5F_4/^5S_2$ band at 540nm and the $^5F_5$ line at 660nm. The scale used here is the same as that of Figure 6.7.3 thus showing the relatively weak excitation of these lines compare to the higher levels.

The emission spectrum for the holmium sample was measured after exciting by several wavelengths. For SPA the sample was excited at 480 nm, the peak of the excitation spectrum in Figure 6.7.3, and 532 nm. The sample was also found to excite by 900 nm ESU as shown in Figure 6.7.5.

All three cases, shown in Figure 6.7.6, consistently produce three prominent lines at 540 nm, originating from the $^4S_2$ and $^5F_4$ levels, 650 nm, from the $^5I_4$ level, and 750 nm, from the $^5I_5$ level. All emission lines seem to terminate at the ground $^5I_8$ level which immediately presents a significant drawback to using holmium as a dopant in a potential distributed fibre. If the principal emission lines terminate to the ground state and those emission transition are also significantly absorbing, as is suggested by Figure 6.7.3 which shows the absorption cross-section for these transitions to be around an order of magnitude greater than that of ruby, then the self-absorption of the fluorescence light will distort the temperature dependent data from the sensing region. This has the effect of severely limiting the range of the fibre sensor to no more than one absorption length which, at the dopant concentration used in this test sample, would be only a few centimetres.

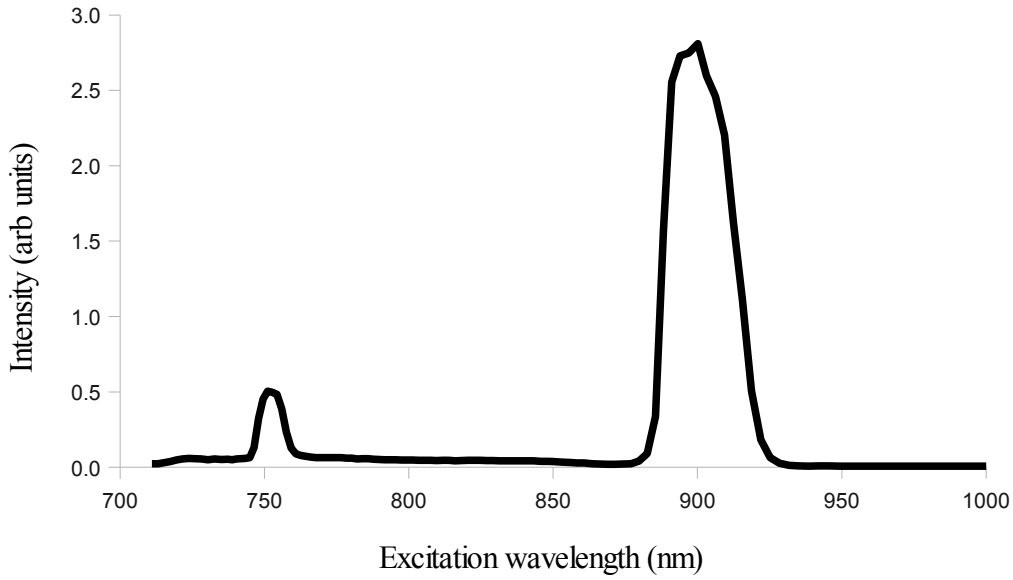

Figure 6.7.5: The ESU excitation spectrum for the Ho^{3+}:ZBLALi sample emitting at 750 nm (stray emission is observed here). One main peak was observed centred around 900 nm.

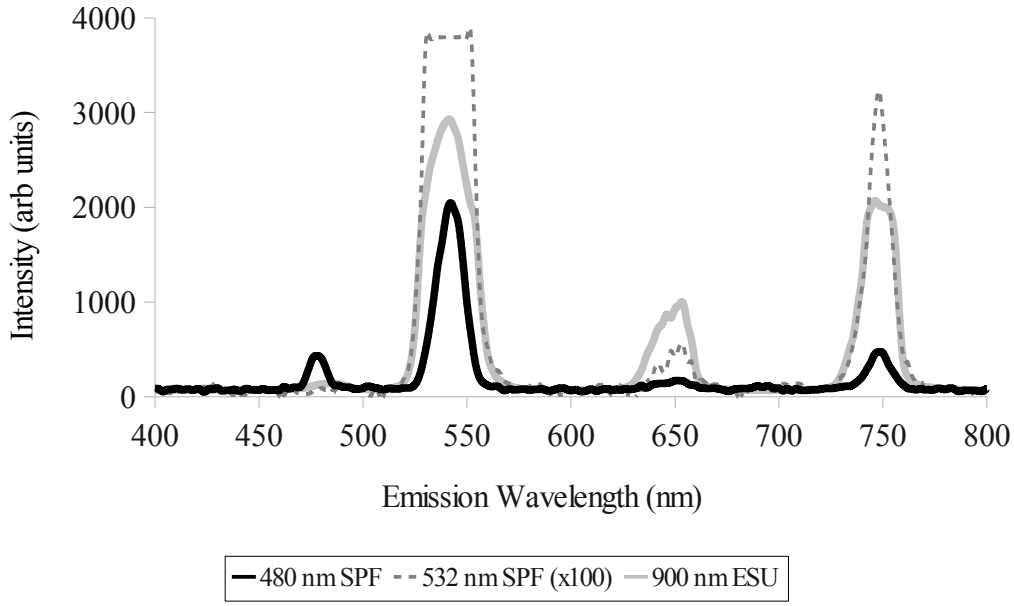

Figure 6.7.6: The emission spectra for the Ho^{3+}:ZBLALi sample under 480 nm single-photon excitation (solid black line), 532 nm single-photon excitation (dashed grey line) and 900 nm excited-state up-conversion

Table 6.7.1. Calculation of δ in Ho^{3+}:ZBLALi			
Parameter	Value	Unit	% Uncertainty
P'(t)	0.18	mV	5
P”(t)	700	mV	5
E'	1.38	mJ/pulse	3
E”	6.82	mJ/pulse	1
A”	0.253	cm^2	10
t_p”	10	ns	17
λ'	485	nm	<1
λ”	960	nm	<1
σ_{486nm}	4.04×10^{-22}	cm^2 ion^{-1}	
N_1	5.3×10^{20}	ion cm^{-3}	1
K	0.664	[dimensionless]	n/a
Nd	2.46×10^{-4}	[dimensionless]	2

Table 6.7.1: The data table used for the calculation of the two-photon excitation cross-section of Ho^{3+}.

6.7.2. TPF and the two-photon excitation cross-section

In addition to ESU, true two-photon excitation was also observed in the holmium sample but was extremely weak compared to some of the other candidate dopants. A small excitation line was recorded at 960 nm just beyond the edge of the ESU line, see Figure 6.7.7. This excitation, which is the degenerate two-photon excitation equivalent of the 480 nm $^5I_8 \rightarrow {}^5F_3$ single-photon transition, produced a faint but detectable trace of the $^4S_2 / {}^5F_4 \rightarrow {}^5I_8$ 540 nm emission line. Even with multiple averaged runs and adjustments to improve the sensitivity Figure 6.7.8 was the best that could be produced given the limits of the instrumentation and the time allowed. It is possible that a small trace of the 750nm line is also visible in this figure but it is not so easily resolved.

The 540 nm emission line was however strong enough to permit an estimate of the two-photon excitation cross section using estimates of the single-photon absorption cross section taken from the absorption spectrum measured for Figure 6.7.3 and combined with the estimations for the dopant concentration.

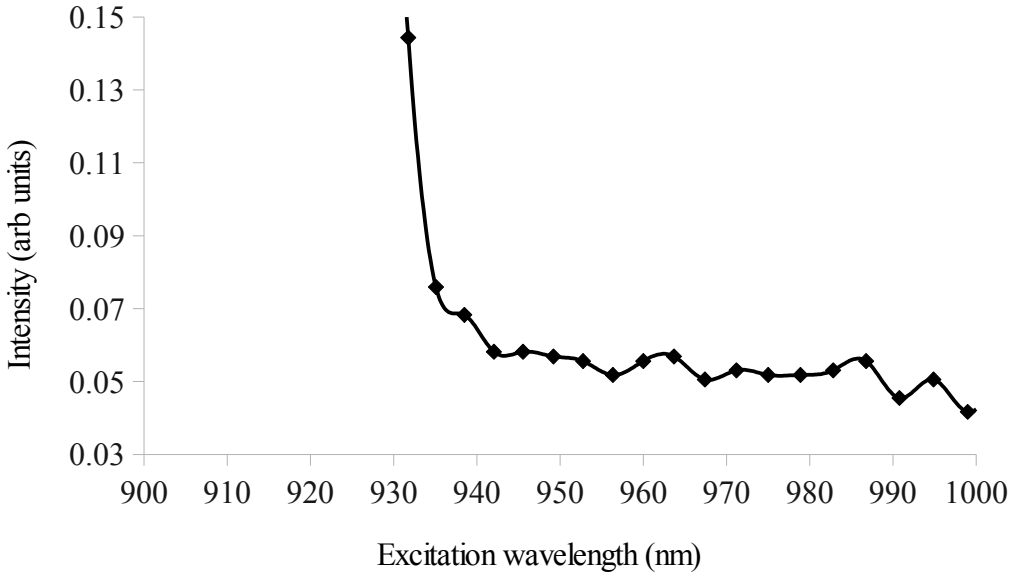

Figure 6.7.7: The two-photon excitation spectrum for 540 nm emission in the holmium sample. For comparison of relative intensities, the peak of the 900 nm ESU in Figure 6.7.2 (the rising edge of which is visible at <940 nm) would be approximately 27 units on this scale.

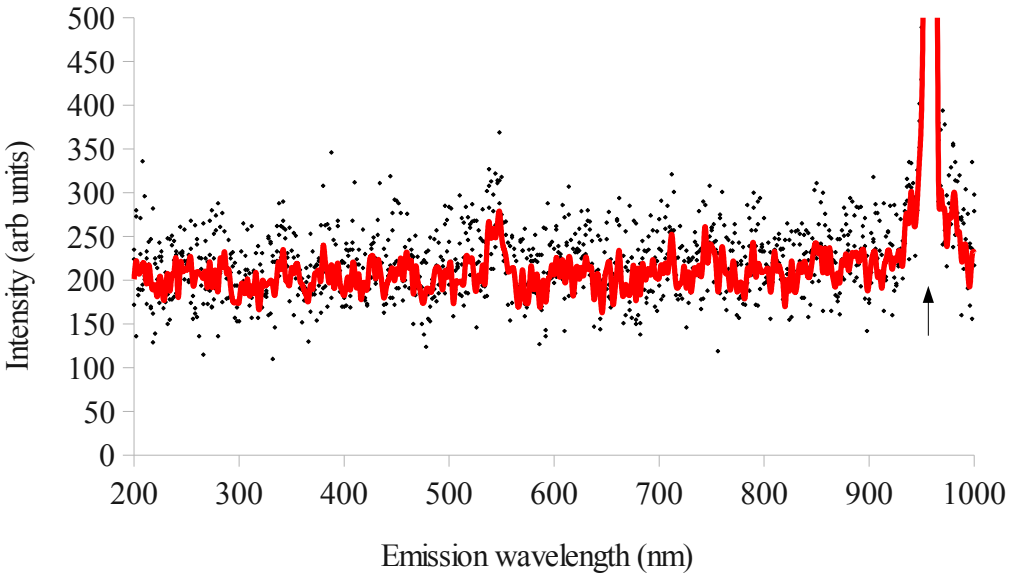

Figure 6.7.8: The two-photon emission spectrum for the Ho^{3+}:ZBLALi sample excited at 960 nm. Only the $^4S_2/^5F_4 \rightarrow {}^5I_8$ transition at 540 nm was observed clearly although a possible trace of the 750 nm $^5I_5 \rightarrow {}^5I_8$ transition may also be present. The laser line at 960 nm is indicated by an arrow.

Table 6.7.1. results in an estimate for the two-photon absorption cross-section of Ho^{3+}:ZBLALi due to 960 nm excitation of $(3.0 \pm 0.6) \times 10^{-55}$ cm^4 s ion^{-1} $photon^{-1}$ which is significantly lower even than the ruby studied here.

The previous study by Gouveia-Neto[110] also reported an excitation event at a similar wavelength, in this case 980 nm, but ascribed this excitation to a phonon-assisted excited state upconversion in which two or three phonons are absorbed to excite the ion to the $^5I_5$ level (i.e. the level involved in the 900 nm ESU transition) and that a further 980 nm excitation brings the system to slightly above the $^5F_2$ level so that a further phonon or two must be emitted to compensate for the extra energy mismatch. It is not immediately apparent from either or both results which mechanism is the one most likely to be dominant though a true two-photon transition has the advantage of being the simpler system, not requiring the involvement of additional phonons. It may be possible to construct an experiment to distinguish the two mechanisms such as by cooling the sample until the phonons are effectively "frozen out". In this case a system dominated by phonon-assisted ESU would no longer absorb at this wavelength whereas one dominated by true TPA would. Another

possible experiment would be to distinguish the processes by measuring the lifetime of the intermediate step by way of using a pump-probe setup where two excitation pulses strike the sample first simultaneously and then by way of an increasing mutual delay until a drop in emission is recorded. The virtual energy level involved in true TPA is extremely short, around 1 fs, therefore the pump pulse and probe pulse must be absorbed by the target ion virtually simultaneously and any mutual delay introduced to the pulses will reduce the excitation intensity. The lifetime of the real energy level involved in ESU on the other hand will be much longer and consequently a relatively large delay may be introduced between the two excitation pulses before a drop in emission is observed.

6.7.3. The fluorescence decay time constant

While the signal from emission due to the multi-photon excitation was too weak to reliably measure any decay times they were measured from the comparatively strong SPF lines using 480 nm excitation.

The decay of emission from the $^5S_2 \rightarrow {}^5I_8$ transition gave rise to the 540 nm emission line, which can be seen in Figure 6.7.9, exhibits a predominantly single exponential decay despite the presence of two separate though closed spaced energy levels and at room temperature has a fluorescence decay constant of 110 μs.

It does however show a fairly long rise time of about 5 μs which may suggest that much of the energy descending from the $^4F_2$ level transfers to the $^5F_4$ level for a time before exciting to the $^4S_2$ from which it can transfer to $^5I_8$ ground state radiatively.

The 650 nm emission profile from the $^5F_5 \rightarrow {}^5I_8$ transition, shown in Figure 6.7.10, is significantly more complex with at least two exponential components measured. The short decay component was measured at 30 μs and the longer one at 80 μs.

Finally, Figure 6.7.11 shows the decay profile of the 750 nm emission due to the $^5I_4 \rightarrow {}^5I_8$ transition was similar to that of the 540 nm emission with a single exponential component with a fluorescence decay time of 100 μs and a rise time of 9 μs.

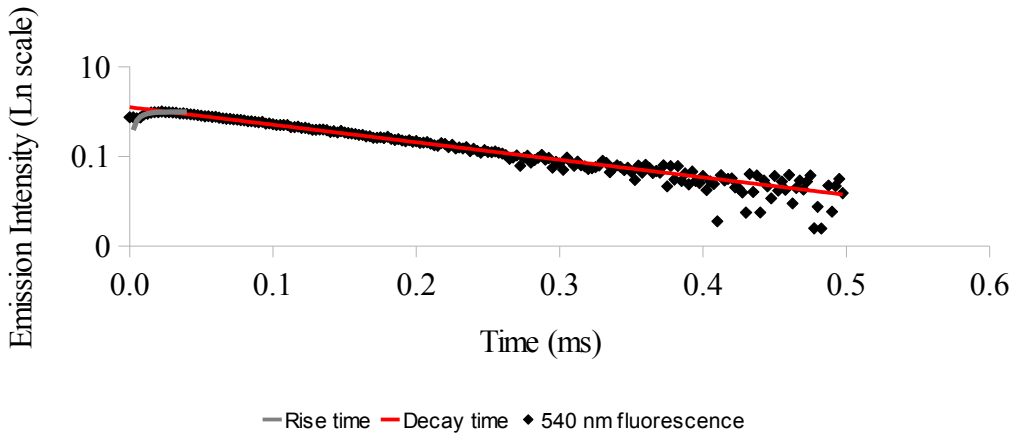

Figure 6.7.9: (diamonds) The decay profile for 540nm SPF with a best fit of (red line) the decay and (grey line) the exponential rise.

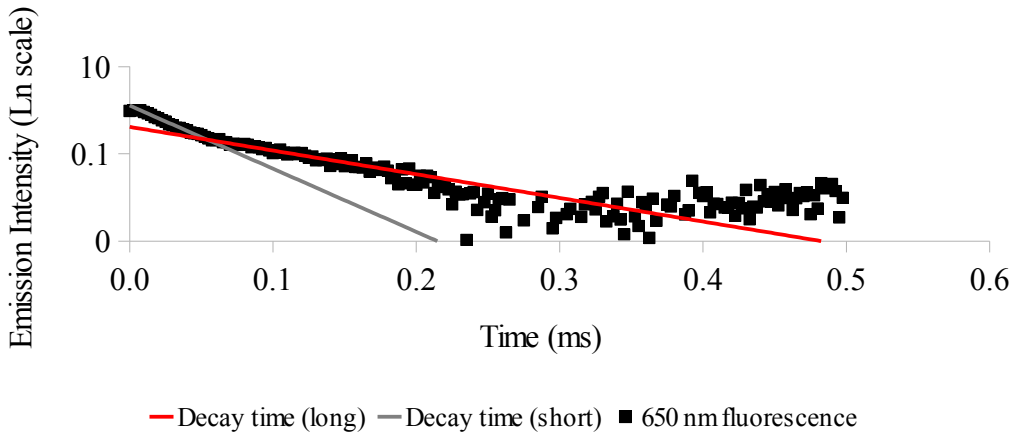

Figure 6.7.10: (squares) The emission profile for 650nm SPF with the first short component (grey line) and long component (red line) of the fluorescent decay.

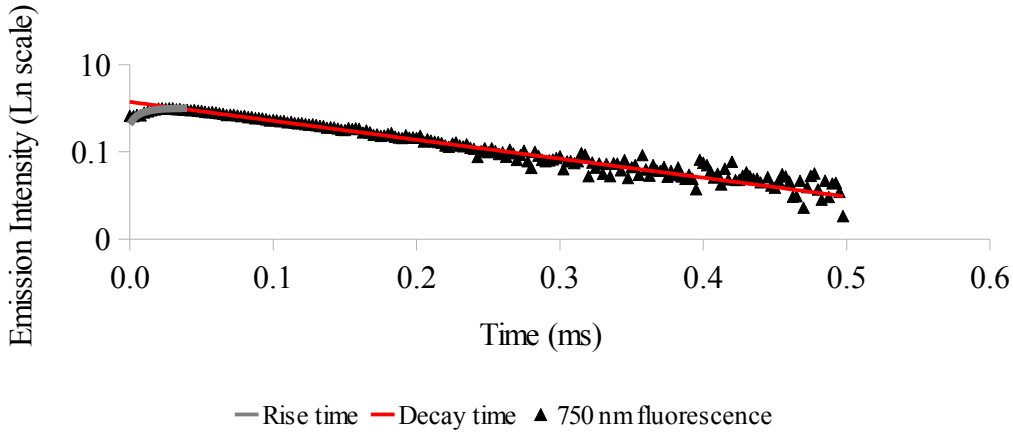

Figure 6.7.11: (triangles)The emission profile for 750nm SPF showing (red line) a single exponential decay and (grey line) a rise time comparable to that of the 540nm emission.

6.7.4. Conclusion

The single-photon and excited-state upconversion excitation and emission spectra have been successfully obtained in Ho^{3+}:ZBLALi compared with similar studies of holmium in other hosts. Two-photon fluorescence was observed and the low value of the excitation cross-section obtained serves to illustrate the sensitivity of the methods used here to derive it. The room temperature decay characteristics of three prominent emission lines were also successfully measured and found to be long enough for easy detection.

Unfortunately holmium does not present as a favourable dopant for the purposes of distributed fibre sensing as, if the TPF transition is confirmed, it shows an extremely low absorption cross-section with respect to the other, more favourable dopants studied in this chapter. Furthermore, the small and regular spacing of the absorption lines would present a challenge should any attempt at non-degenerate excitation be made.

Finally, and most seriously, all of the prominent emission lines terminate directly to the ground state which presents the same problem of self-absorption found in ruby but without the inherent material advantages found in the single crystal fibre. This would severely limit the maximum range of a prospective distributed fibre sensor to only a few centimetres at a dopant concentration of 2 mol wt. % and the prospect of extending the range by reducing the dopant concentration will be limited by the low two-photon absorption cross section.

6.8. Terbium

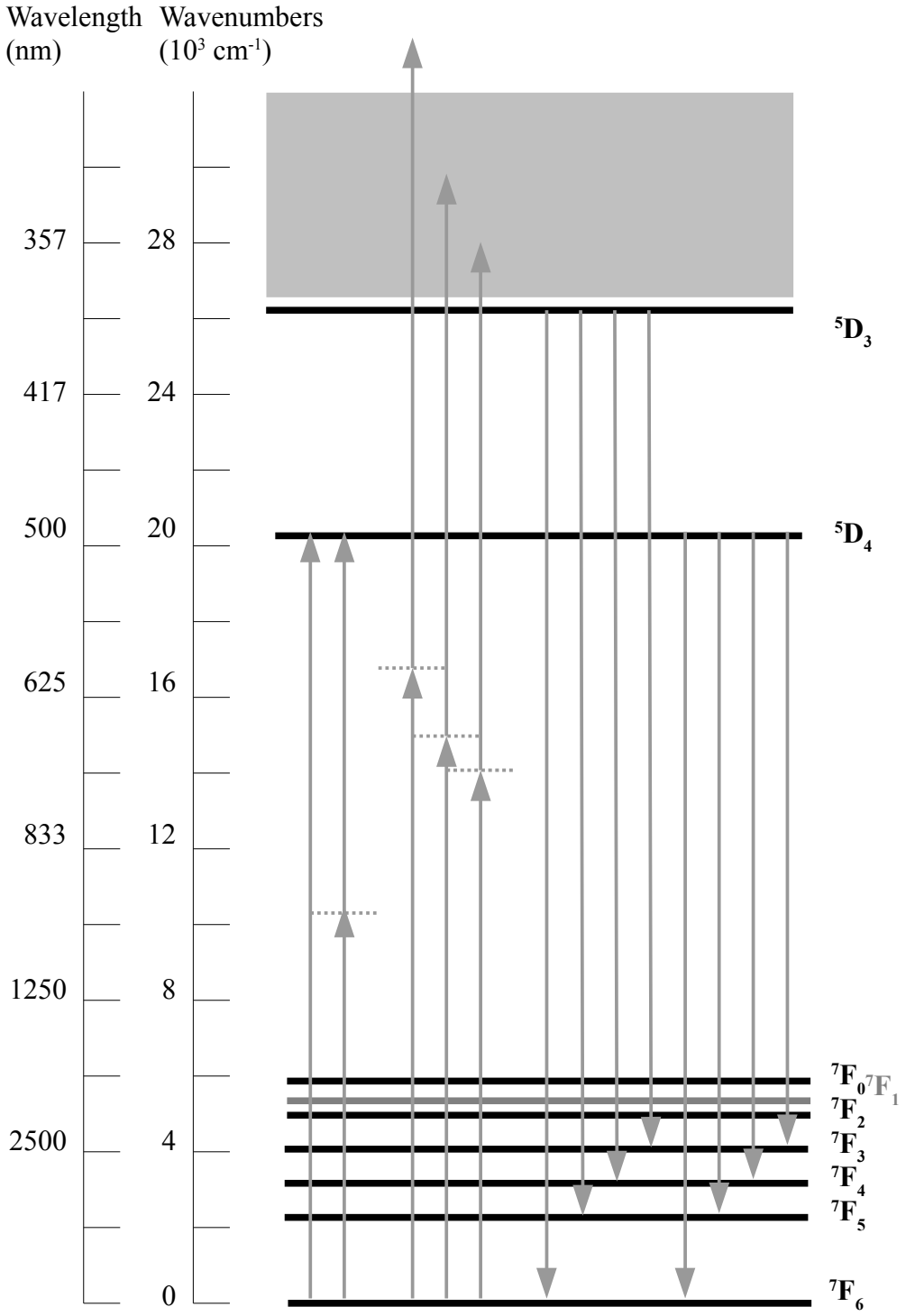

Figure 6.8.1: A simplified energy level diagram for Tb^{3+}. The grey region above 26 500 cm^{-1} (SPA wavelengths shorter than 377 nm) represents a region of many closely spaced levels, not all of which were given full designations by Dieke et al.

6.8.1. Excitation and emission

The second sample examined here was a ZBLAN glass doped with 1 mol weight % Tb_2O_3 (terbium dopant density, $N_1 = 3.4 \times 10^{20}$ ion cm^{-3}) shown in Figure 6.8.2. According to the energy level diagram measured by Dieke and Crosswhite[100] (A simplified version of which is shown above in Figure 6.8.1) it seemed likely that only one energy level, the $^5D_4$ level at about 20 000 cm^{-1} from the ground state, could be reached with both a single-photon and a two-photon excitation due to the OPO's upper limit of 410 nm. It was thought possible that the upper manifold of levels starting from $^5D_3$ (excitable via ~ 385 nm SPA[111]) could be reached by TPA.

The emission spectrum from the $^5D_4$ level has been published several times[112],[113] and describes a series of lines into the $^7F_{6\rightarrow0}$ levels with strong, easily detectable components at 485 nm, 550 nm, 590 nm, 625 nm and 655 nm (for the $^7F_{6\rightarrow2}$ lines respectively).

Figure 6.8.3 below shows the result of exciting the Tb:ZBLAN sample by 485 nm SPA and shows good agreement with the literature over the $^5D_4 \rightarrow {}^7F_{5,4,3}$ lines. The 485 nm resonant emission $^5D_4 \rightarrow {}^7F_6$ line may be partially visible at the extreme edge of the data run but it was intentionally not measured fully to avoid dazzling the photomultiplier with scattered laser light.

The single photon excitation spectrum for the $^7F_6 \rightarrow {}^5D_4$ is shown in Figure 6.8.4 displaying a peak at 482 nm. This predicted that the degenerate two-photon excitation peak for the same transition should be found at around 960 nm.

Figure 6.8.2: The excitation (left) and subsequent emission (right) from the Tb:ZBLAN sample.

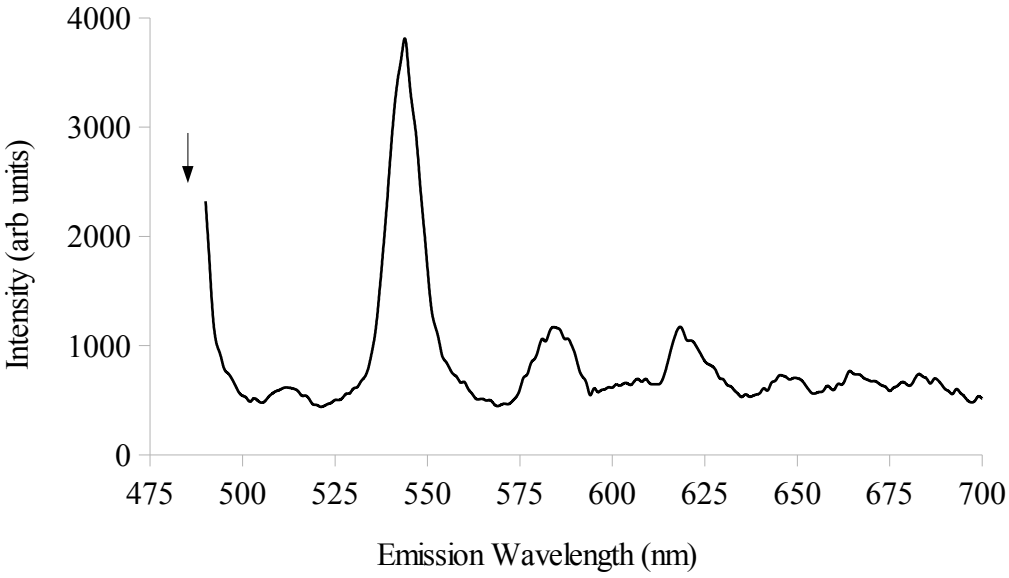

Figure 6.8.3: The emission spectrum of Tb:ZBLAN under 485nm SPA. The peaks visible are associated with the $^5D_4 \rightarrow {}^7F_{5,4,3}$ transitions. The 485nm $^5D_4 \rightarrow {}^7F_6$ transition was not directly observed due to the proximity of the laser line, the wavelength of which is marked by the arrow.

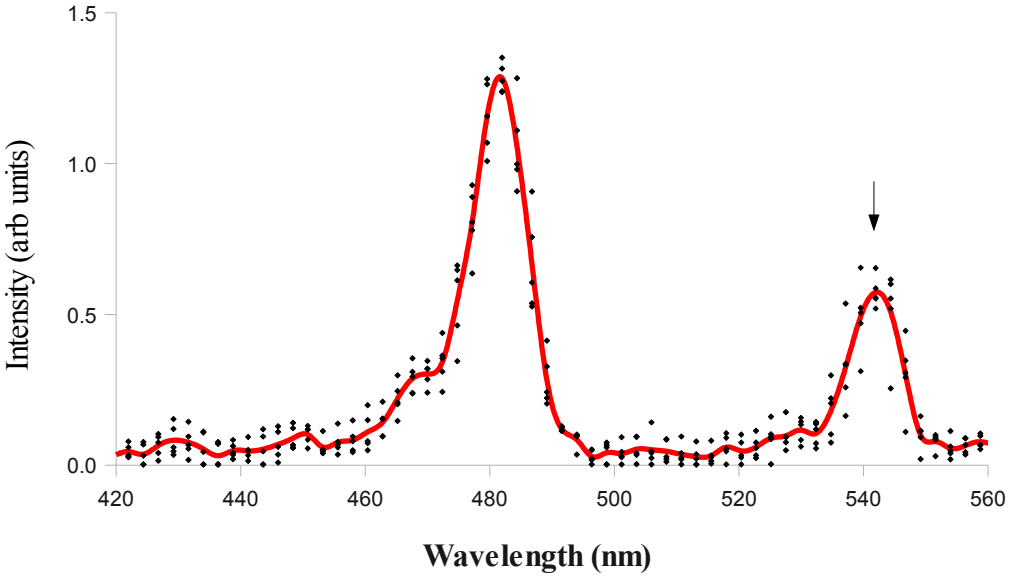

Figure 6.8.4: The single-photon excitation spectrum for the 543nm emission line. the peak of the excitation of the $^7F_6 \rightarrow {}^5D_4$ transition level was measured at 482nm. The laser line and resonant excitation of the $^5D_4$ level are marked with an arrow.

The two photon emission from Tb^{3+} was found to be substantially harder to detect than those found in Pr^{3+} thus the excitation and emission spectra were consequently less detailed.

The two-photon excitation spectrum, shown in Figure 6.8.5, agrees well with the single-photon equivalent showing a single peak corresponding to the $^5D_4$ level at 982nm (2 x 491nm).

Two-photon excited emission, shown in Figure 6.8.6, could only be detected from one transition, identified as $^5D_4 \rightarrow {}^7F_5$. The dearth of the other lines is ascribed to the low signal strength as it is known in the literature that the $^5D_4 \rightarrow {}^7F_5$ is by far the strongest of the emission lines in that manifold.[111],[112],[113]

Another small emission line has been observed at around 520nm in both the SPF and TPF spectra. This has been observed in Tb^{3+} doped in tellurite[113] based glasses but not in organic chelates[112] or soda glass.[111] It is possible therefore that the ZBLAN host used here is responsible.

As stated above, the excitation laser could not be tuned to wavelengths shorter than 410nm so the upper manifold of lines, starting with $^5D_3$ could not be examined via SPA. It was, however possible to excite these levels using TPA, an investigation made easier by the lack of real energy levels in the 380 – 1500nm region (apart from $^5D_4$).

The existing single-photon studies into the two-photon excitation spectrum of Tb^{3+} or even into the single-photon UV excitation spectra are relatively sparse[100],[111],[114] and those which specifically mention two-photon excitation either focus on the emission spectrum and excitation at a single wavelength[115] or the Tb^{3+} ions are bound into an organic chelate or other complex which acts to significantly enhance the absorption process.[116],[117]

With this in mind, the two-photon excitation spectrum of the Tb^{3+} sample is presented in Figure 6.8.7 and shows a partial line near 710nm, which corresponds to the $^7F_6 \rightarrow {}^5D_3$ transition, and two lines at 610nm and 635nm. The latter two lines belong to the UV upper manifold of levels but it is not possible here to reliably identify the individual energy levels responsibly for them.

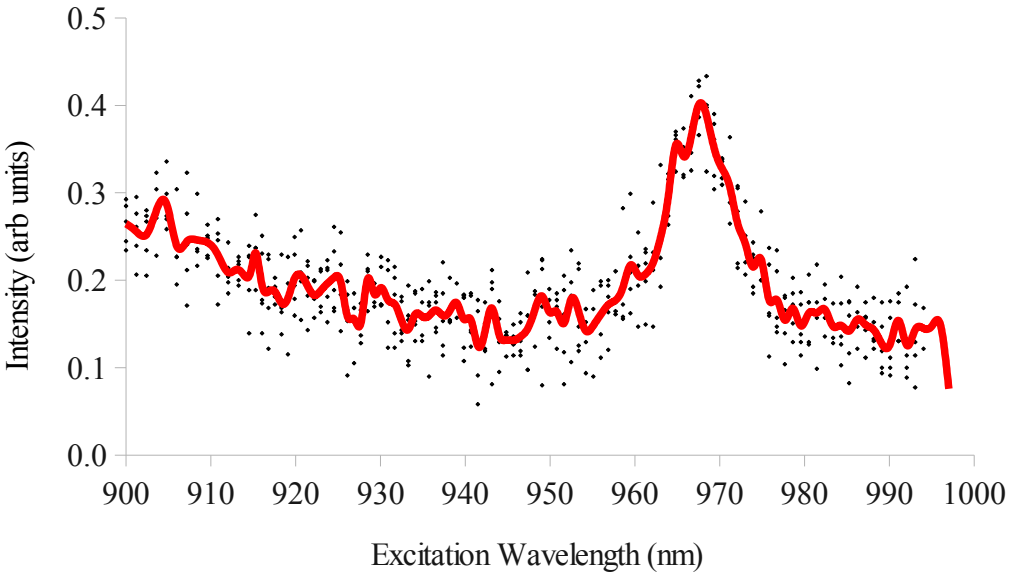

Figure 6.8.5: The two-photon excitation spectrum of the 545 nm emission from the $^5D_4$ level of Tb:ZBLAN. The centre of the peak is at 968 nm, a little longer than that predicted from the single photon spectrum.

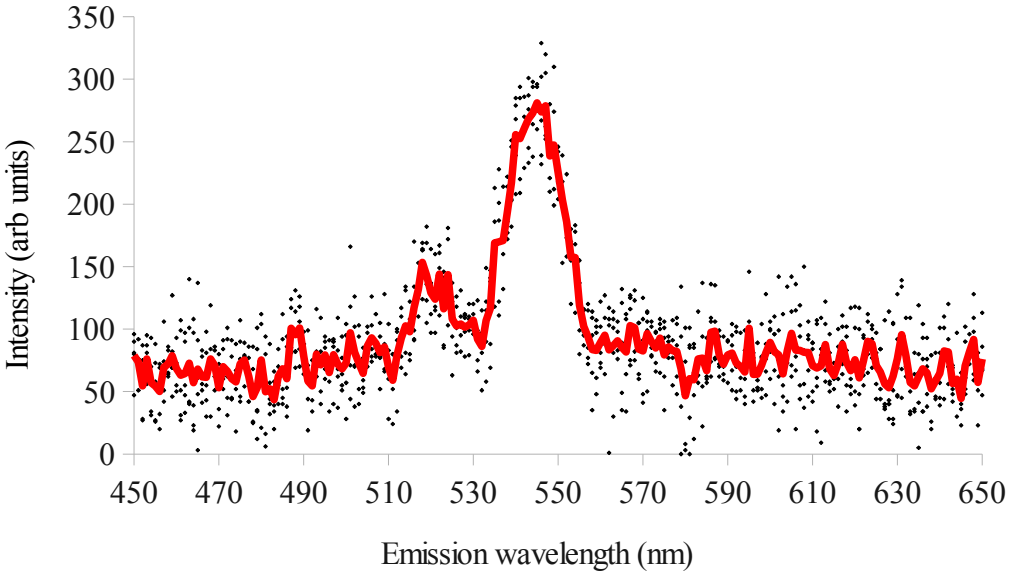

Figure 6.8.6: The emission spectrum associated with the two photon excitation at 968 nm above. Only the 545 nm line was readily detectable in this experiment.

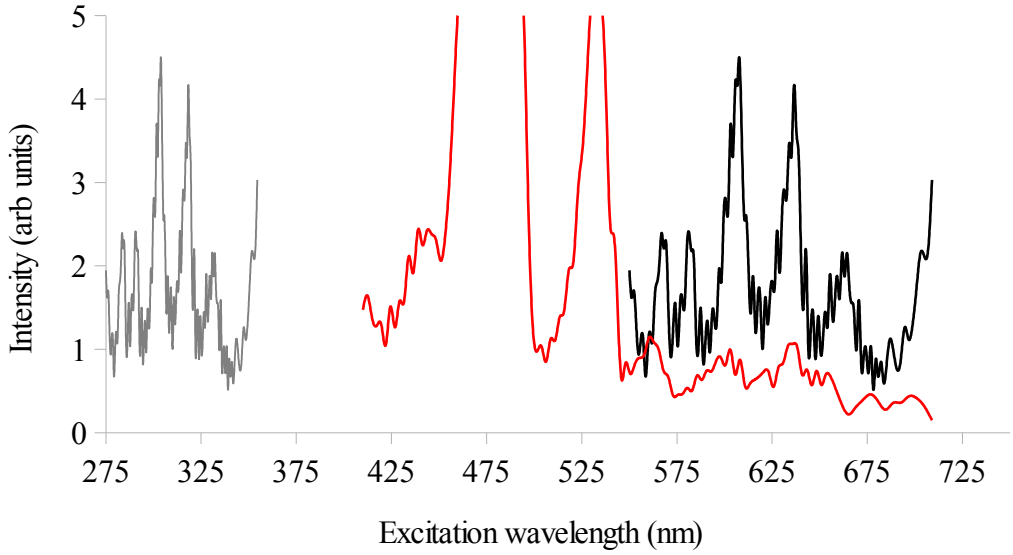

Figure 6.8.7: (red line) The single-photon excitation spectrum of the $^7F_6 \rightarrow {}^5D_4$ transition at 480 nm leading to 540 nm emission to the $^7F_5$ level. (black line) This emission transition is also reached via the $^5D_3$ level and others in the upper manifold by two-photon excitation at 610 nm, 635 nm and close to 710 nm. (grey line) The predicted single-photon excitation wavelengths assuming a degenerate excitation (i.e. $\lambda'' = 2\lambda'$)

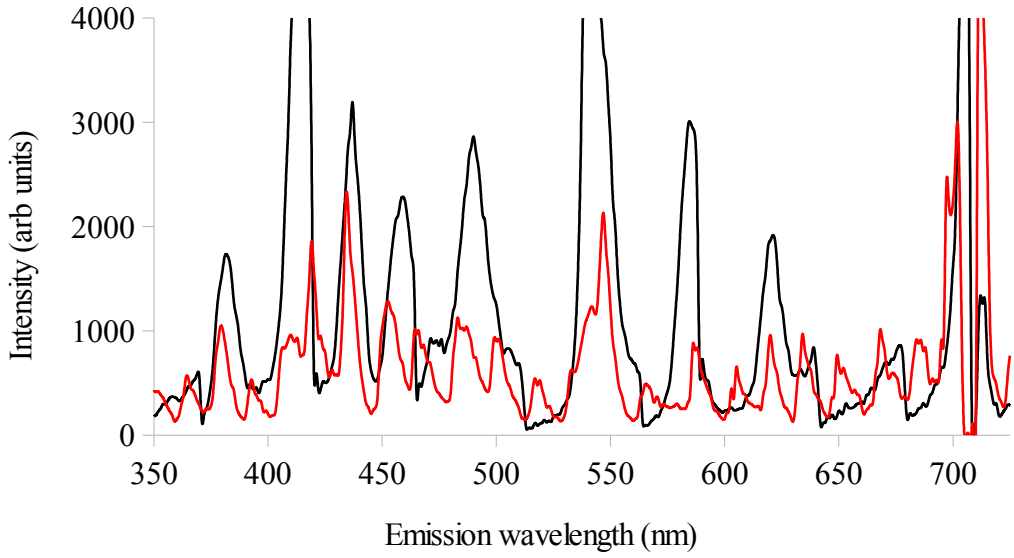

Figure 6.8.8: The extended two-photon excited emission spectrum for Tb:ZBLAN by excitation at 710 nm. In addition to emission from the $^5D_4$ level, the lines of which match those found in Figure 6.8.3, The lines due to emission from $^5D_3$ are also clearly visible. The red line shows the relative intensity of these lines while the excitation laser is unfocussed. The black line shows the effect of focussing the beam onto the sample, increasing the photon flux.

Excitation at 710 nm produces the emission spectrum shown in Figure 6.8.8. This spectrum was recorded first using the beam from the OPO unfocussed by any additional optics (Beam area at sample $A_1 = 0.785$ cm^2) and then again after an additional focussing lens was inserted (Beam area $A_2 = 0.101$ cm^2). The increased photon flux generated by reducing the beam area caused an increase of the measured fluorescence. This lends extra support to the probability that the excitation path involves more than one photon per transition.

The emission spectrum due to 710 nm excitation shows the same $^5D_4$ emission lines observed in the previous single and two-photon excited spectra found in Figure 6.8.4 and Figure 6.8.6 (as well as the previously avoided 490nm $^5D_4 \rightarrow {}^7F_6$ transition). Also observed were a new set of lines at 383 nm, 415 nm, 437 nm and 460 nm. These lines correspond well to the known spectrum[111] associated with transitions from the $^5D_3$ level down to the lower manifold of ^7F_j levels. Two lines, the 444 nm $^5D_3 \rightarrow {}^7F_4$ transition and the 474nm $^5D_3 \rightarrow {}^7F_2$ transition were not clearly resolved possibly due to the relatively low 7nm resolution of the experiment and the low relative intensity of those lines compared to those adjacent to them.

An attempt was made to observe TPF by non-degenerate excitation. Due to the principles of operation of the OPO laser exposing the sample to both the signal and idler beam simultaneously would always result in the energy equivalent of a 355nm excitation (which, according to Figure 6.8.7 should be absorbing) regardless of the tuning of the individual wavelengths. This experiment proved problematic as the two beams were not exactly aligned with each other so the combined flux at the partial overlap of the beams was low. For this reason, focusing the beams was not possible as it reduced the area of overlap even further. In addition, the broad upper energy level manifold meant that it was difficult to find a signal wavelength which did not cause at least some excitation by degenerate TPA.

Ultimately the experiment produced some evidence on enhanced TPF when excited by both 600 nm signal light and 868 nm idler light (wavelengths chosen for maximum energy output and minimum single-beam degenerate TPA) compared to that observed by 600nm excitation alone. It was not possible, within the scope of this attempt, to rule out other influences such as changes in the beam powers due to

switching of the filters used to isolate individual beams.

6.8.2. The two-photon excitation cross-section

As it was not possible to access the upper energy level manifold with SPA the two-photon excitation cross-section could only be calculated for transitions emitting from the $^5D_4$ level. This happened to be convenient as it also meant that changes in the quantum efficiency and other hard to measure factors were likely to be negligible over such a small excitation band (as with all of these calculations, the quantum efficiency for the SPA and TPA transitions at the same energy-equivalent wavelength are assumed to be identical).

Table 6.8.1. Calculation of δ in Tb^{3+}:ZBLAN			
Parameter	Value	Unit	% Uncertainty
P'(t)	4.86	mV	7
P”(t)	4.3	mV	4
E'	1.44	mJ/pulse	3
E”	7.11	mJ/pulse	2
A”	0.101	cm^2	10
t_p”	10	ns	17
λ'	482	nm	<1
λ”	968	nm	<1
σ_{482nm}	1.45×10^{-22}	cm^2 ion^{-1}	
N_1	3.4×10^{20}	ion cm^{-3}	1
K	0.664	[dimensionless]	n/a
Nd	2.46×10^{-4}	[dimensionless]	2

Table 6.8.1: Data table for the calculation of the two-photon excitation cross-section of Tb^{3+}:ZBLAN.

Table 6.8.1. provides the data gathered to calculate the excitation cross-section of the terbium It was not possible to directly measure the single-photon absorption cross-section adequately enough to provide a value precise enough for the calculation so the value used is derived from recent work on Tb^{3+} in borosilicate glass[118] which gives a maximum single-photon excitation cross-section of 1.45×10^{-22} cm^2 ion^{-1} at 482 nm.

This gives an estimate for the peak two-photon absorption cross-section at 968 nm of $(1.4\pm0.3)\times10^{-53}$ cm^4 s ion^{-1} $photon^{-1}$ or 1.4 mGM. While comparative estimates for the value of δ in Tb^{3+} in a glass host were not available after a reasonable search of the literature it has been studied bound into organic complexes which have higher values of δ and act to transfer energy across to the Tb^{3+} ions. Some of the "enhanced" values of δ have been recorded as low as 0.4 GM at 503 nm[119] and as high as 26 GM at 705 nm.[117]

6.8.3. The fluorescence decay time constant

As it was possible to measure both the SPF and TPF from a well defined transition in the terbium sample it was possible to investigate its potential as a temperature sensor dopant by measuring the response of the fluorescence decay time of the 545 nm $^5D_4 \rightarrow {}^7F_6$ transition under both 485 nm SPA and 970 nm TPA.

Unfortunately the TPA signals proved to be of too low an intensity and too noisy to reliably detect. Some data for the SPA transition was recorded, and is shown in Figure 6.8.9. This experiment recorded a room temperature decay time of (3.3±0.1) ms and shows little significant change (no greater than +250 ns/^oC) over a temperature range up to almost 400^oC. This agrees well with recent results found by Yamashita and Ohishi for similar dopant concentrations of Tb^{3+} in borosilicate glasses.[116]

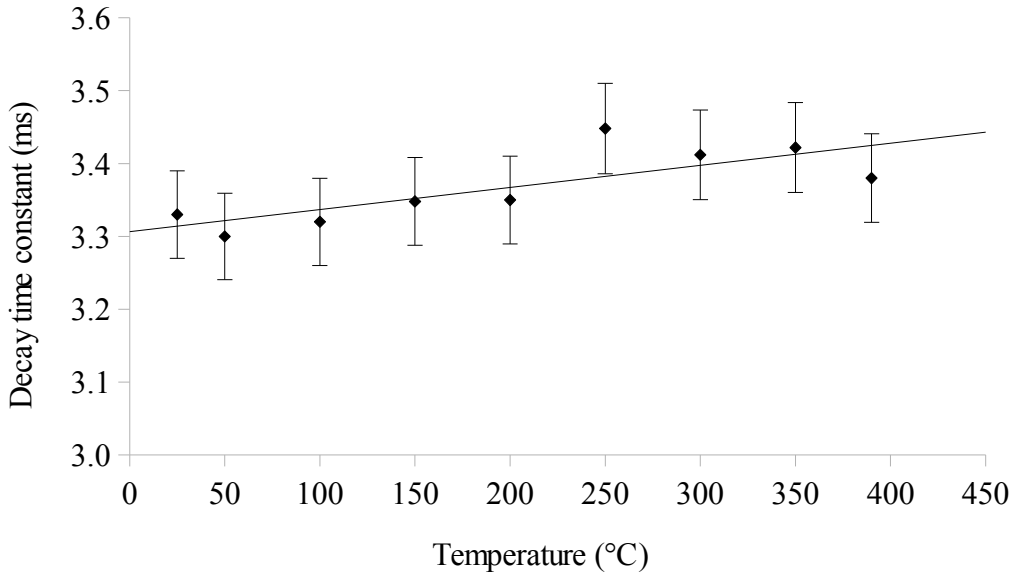

Figure 6.8.9: The dependence of the fluorescence decay time on temperature for the 485nm SPA excited 550 nm emission line.

6.8.4 Conclusion

Like praseodymium, terbium is an excellent dopant choice to showcase the generation of visible light due to two-photon excited fluorescence. The low thermal response at the dopant densities used as well as the rather low two-photon absorption cross-section (100 times less than Pr^{3+} and only 2 times more than ruby) will probably limit its usefulness as a potential dopant for a distributed temperature sensor. As noted above however, thermal response increases strongly with dopant concentration[116] so it may be possible to repeat these experiments with a heavily doped sample with greater success.

6.9. Praseodymium

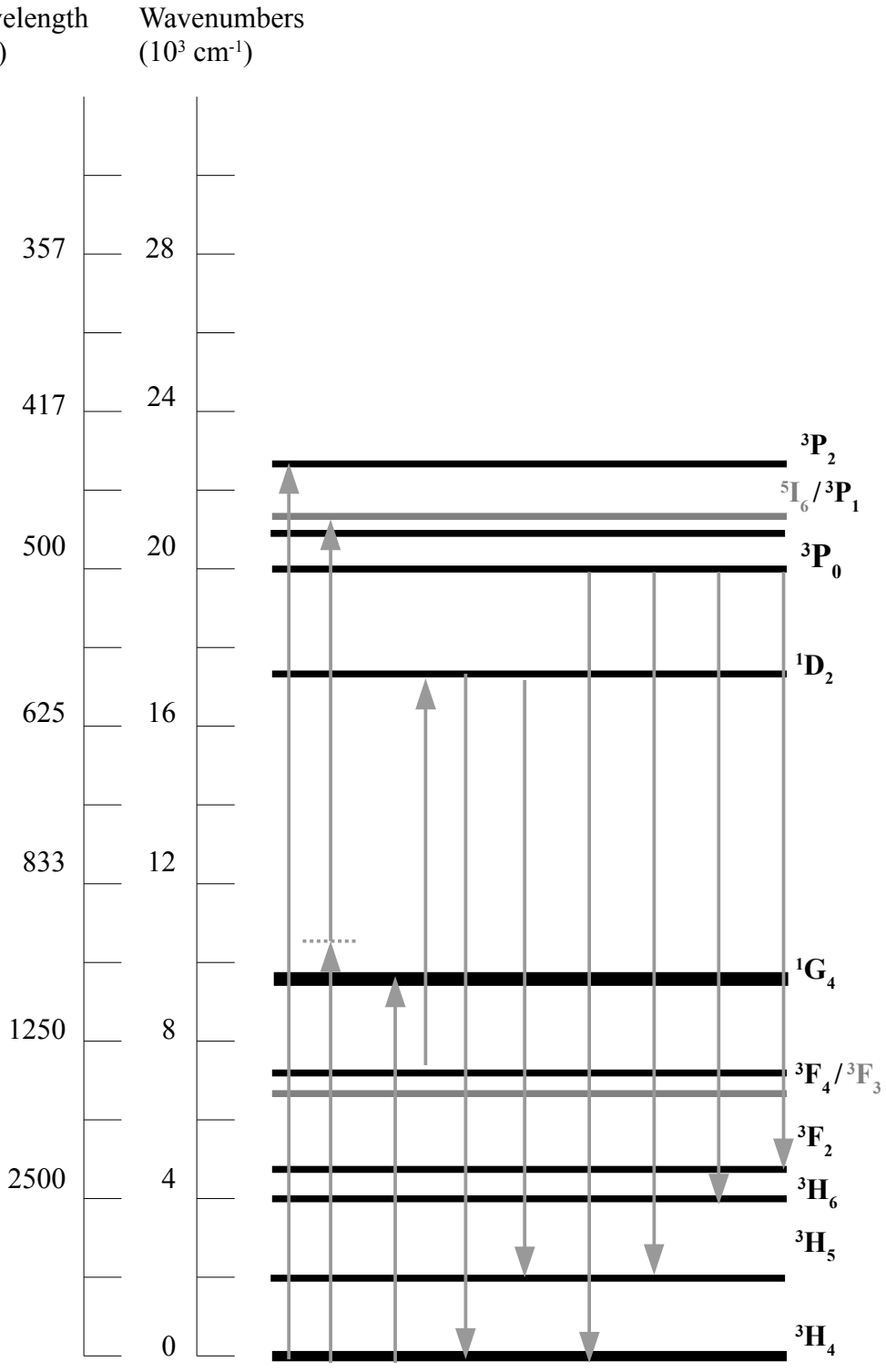

Figure 6.9.1: An energy level diagram of the studied region of Pr^{3+} showing the photon energy required to excited the ion to any given energy level from the ground state in reciprocal cm and the approximate wavelength for an equivalent single-photon excitation.

6.9.1. Excitation and emission

The sample used for this series of experiments, shown below in Figure 6.9.2, was a ZBLAN glass doped with 1% mol weight Pr_2O_3 giving a Pr^{3+} dopant density of approximately $3.4(3)\times10^{20}$ ion cm^{-3}. According to the energy level structure of Pr^{3+}, as measured by Dieke and Crosswhite[100] and shown above in Figure 6.9.1, SPF excitation should occur to the ^3P manifold at around 450 nm to 500 nm. The emission lines were thus located, as shown in Figure 6.9.4, so that the setup could be properly optimised.

This trial emission spectrum, shown in Figure 6.9.3, shows a good correlation with the spectrum found in Pr doped KY_3F_{10} crystals[120] with most of the shifts in wavelength in the peaks attributable to the effects of the host materials and to the difference in temperature between the two cases (300 K in the former, 10 K in the latter).

From this data three lines, 600 nm 715 nm and 960 nm, were selected and the excitation spectra for both SPA and TPA were measured and are shown below in Figure 6.9.4 and Figure 6.9.5 respectively.

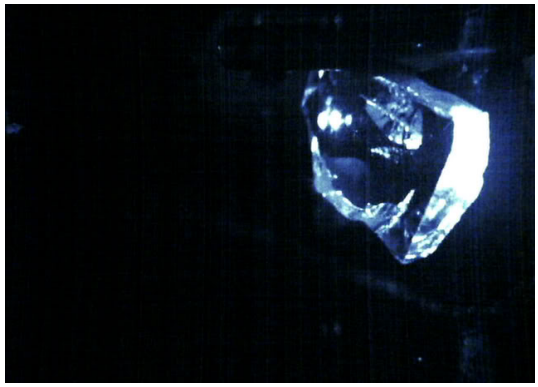

Figure 6.9.2: The sample of Praseodymium examined in this section. The sample is fluorescing under 930nm two-photon excitation.

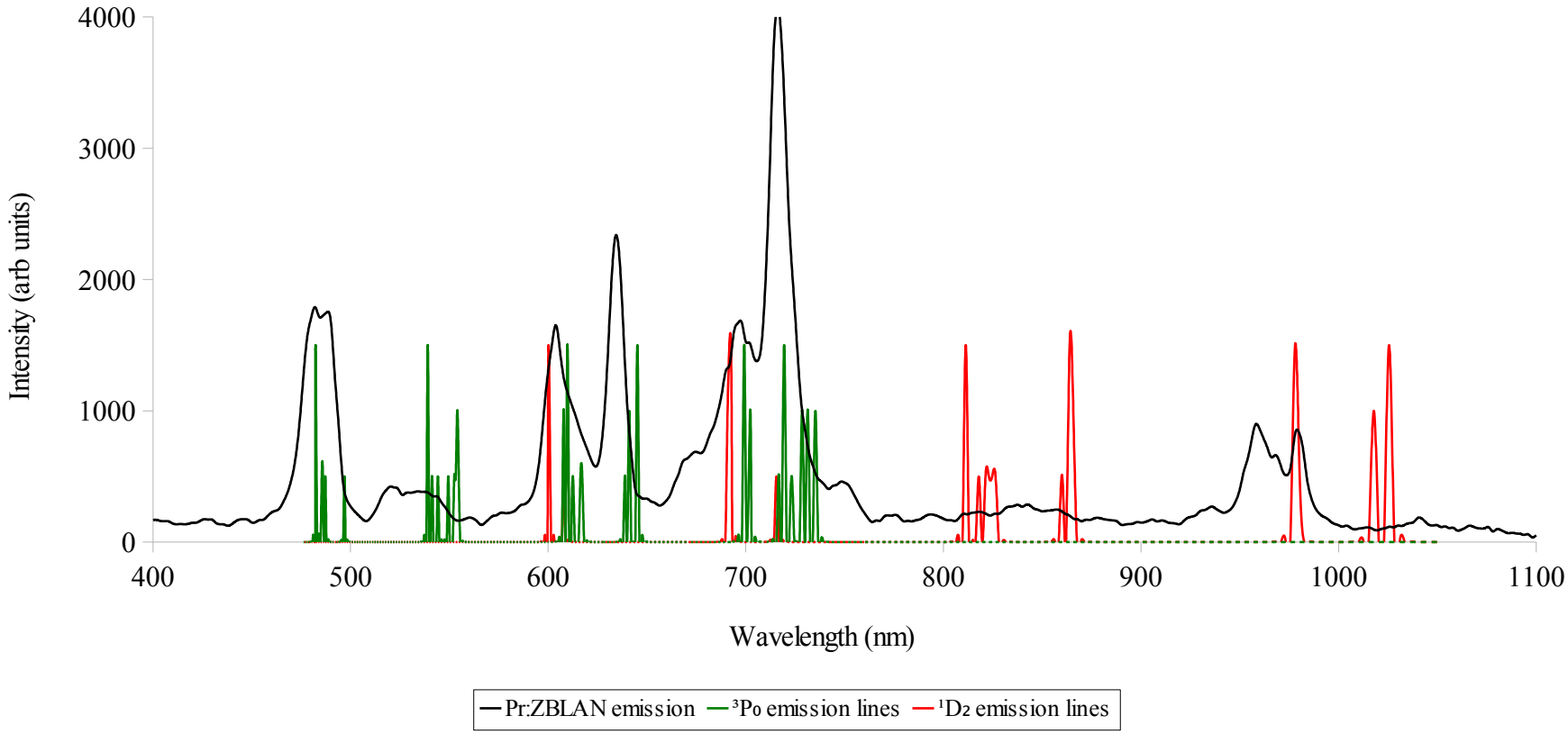

Figure 6.9.3: The first trial emission spectrum of Pr^{3+}:ZBLAN by 490 nm SPA. The position of the emission peaks in Pr^{3+}: KY_3F_{10} are marked by the series of narrow lines. The green lines show emission from the $^3P_0$ level and the red lines emission from the $^1D_2$ level. Only the central positions of these lines are identified. The widths are not to scale and peak magnitudes serve only to indicate a "strong" or "weak" emission.

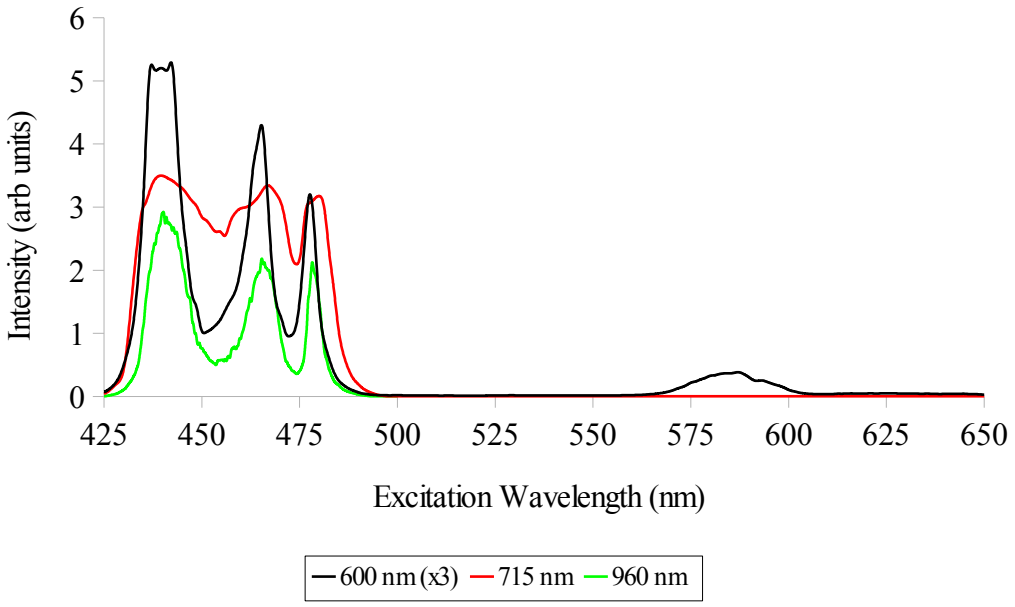

Figure 6.9.4: Single-photon excitation spectra of Pr:ZBLAN in the region representing transitions from the ground state to the $^3P_{0,1,2}$ levels and to the $^1I_6$ level. The excitation spectrum leading to 600 nm emission has been magnified 3 times relative to the other spectra in order to enhance the visibility of the excitation of the $^3H_4 \rightarrow {}^1D_2$ transition at 580 nm.

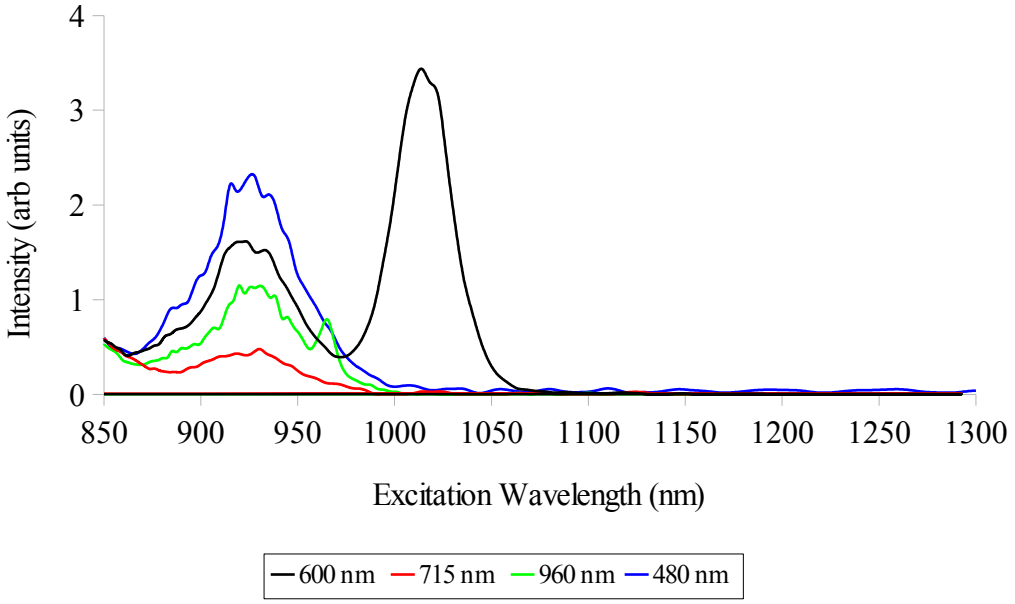

Figure 6.9.5: Two-photon excitation spectra of Pr:ZBLAN. Excitation to the $^3P_{0,1,2}$ levels are absent or greatly suppressed and the majority of the absorption occurs by the $^3H_4 \rightarrow {}^1I_6$ transition. Also visible is an excited state upconversion at 1015 nm to the $^1D_2$ level via a transition from $^3H_4 \rightarrow {}^1G_4$.

The single-photon excitation spectra are well resolved (within the limits of the spectrometer) and show a manifold of three well defined lines, identified as transitions from the $^3H_4$ ground state to the $^3P_{2,1,0}$ levels, and one less well defined line identified as the $^1I_6$ line at 460 nm. Also visible, though only on the 600 nm emission spectrum, is a somewhat weaker excitation at 580 nm of the $^3H_4 \rightarrow {}^1D_2$ transition.

Figure 6.9.5 shows the two-photon excitation of the same emission lines of the Pr:ZBLAN sample and shows several immediate differences from the SPA spectra. The main peak is dominated by only one somewhat broad line with some evidence of two greatly diminished peaks buried in the wings of the main band. A possible interpretation of this result is that, relatively speaking, the $^3H_4 \rightarrow {}^3P_{0,1,2}$ transitions are not as favourable as they are in the equivalent SPA event which would imply that the absorption band is instead dominated by the $^3H_4 \rightarrow {}^1I_6$ transition.

The 600 nm emission line also shows a second excitation peak centred around 1015 nm. This line seems to originate from an excited state upconversion of the $^1G_4$ level which decays down to the $^3F_4$ level before being excited again to $^1D_4$.

In order to complete the picture of the excitation and emission process and so that a complete mapping of the excitation and emission paths could be developed the emission spectra for the 465 nm SPA, 930 nm TPA and 1015 nm ESU peaks were recorded and are shown below in Figure 6.9.6.

Both the SPA and TPA excitations produce a emission spectra similar to the test spectrum in Figure 6.9.3. That the TPF emission lines do not seem to be significantly shifted compared to the SPF spectrum (within the 10 nm resolution of the experiment) indicates that excitation to the region around the $^1I_6$ level also results in non-radiative decay to the $^3P_0$ state from which radiative transitions occur to the various levels down to and including the $^3H_4$ ground state. The 1015 nm excited state upconversion leads to emission at 600 nm and a possible faint emission at 680 nm. This agrees well with the emission lines associated with the $^1D_4$ line. The single-crystal emission spectrum in Figure 6.9.3 shows several emission lines with a wavelength greater than 750 nm. These were not observed in the Pr:ZBLAN due to the limitations of the IP28A photomultiplier. Diagrams summarising these excitation and emission profiles can be found in Figure 6.9.7 and Figure 6.9.8.

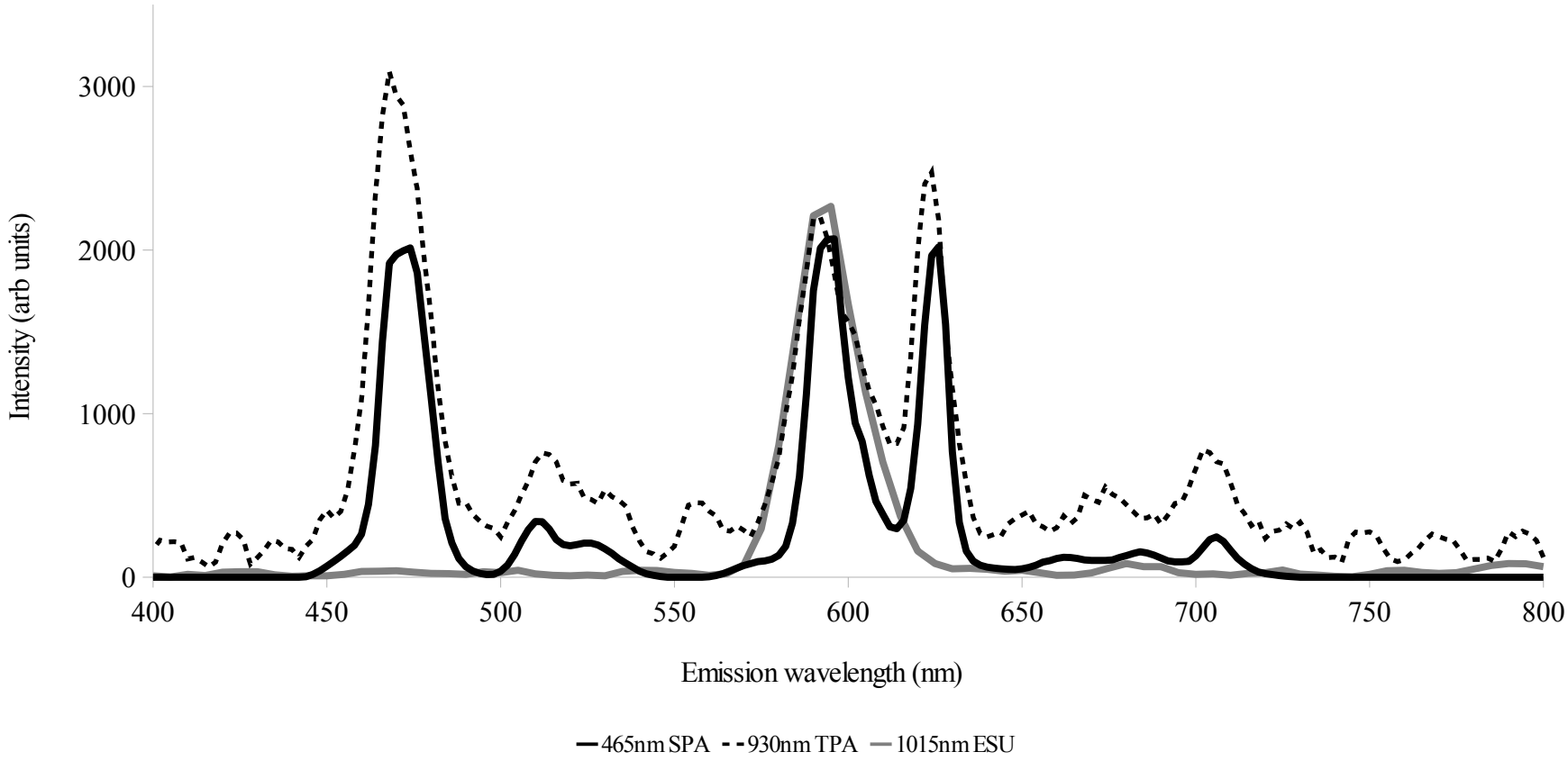

Figure 6.9.6: Three emission spectra for the Pr:ZBLAN sample. Both the 465 nm SPA (solid black line) and the 930 nm TPA (dashed black line) show good agreement with each other displaying primary emission peaks at around 470 nm, 600 nm and 620 nm with secondary groups at 510 nm and 700 nm. The 1015 nm ESU excitation (solid grey line) produces emission only at 600 nm, plus a possible faint signal at 680 nm.

Praseodymium SPA excitation and emission pathways

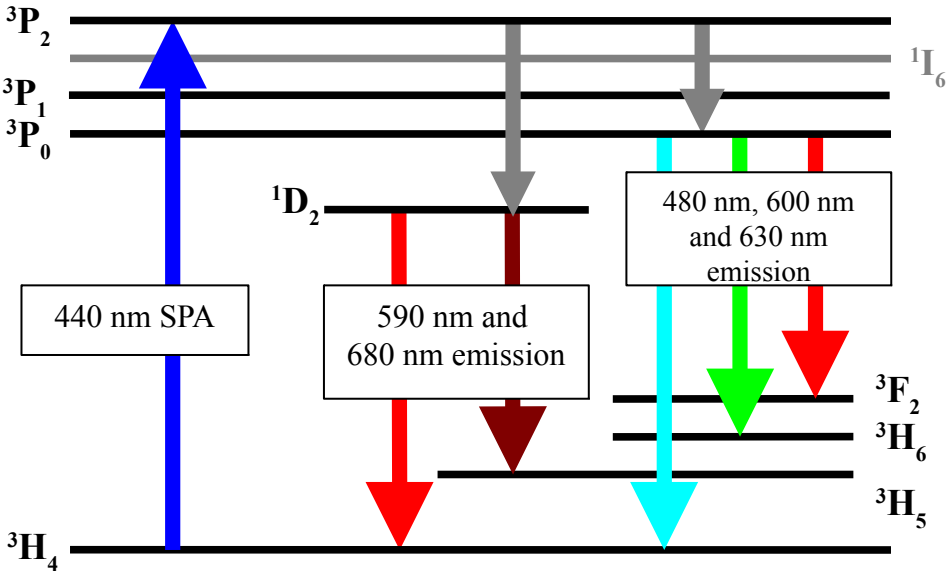

Figure 6.9.7: The first proposed excitation and emission pathways for the sample of Pr:ZBLAN studied. SPA from the ground state to any of the ^3P levels or to the $^1I_6$ level results in a non-radiative decay to the $^3P_0$ level and/or the $^1D_2$ level and from there to the lower levels via radiative decay.

Praseodymium TPA and ESU excitation and emission pathways

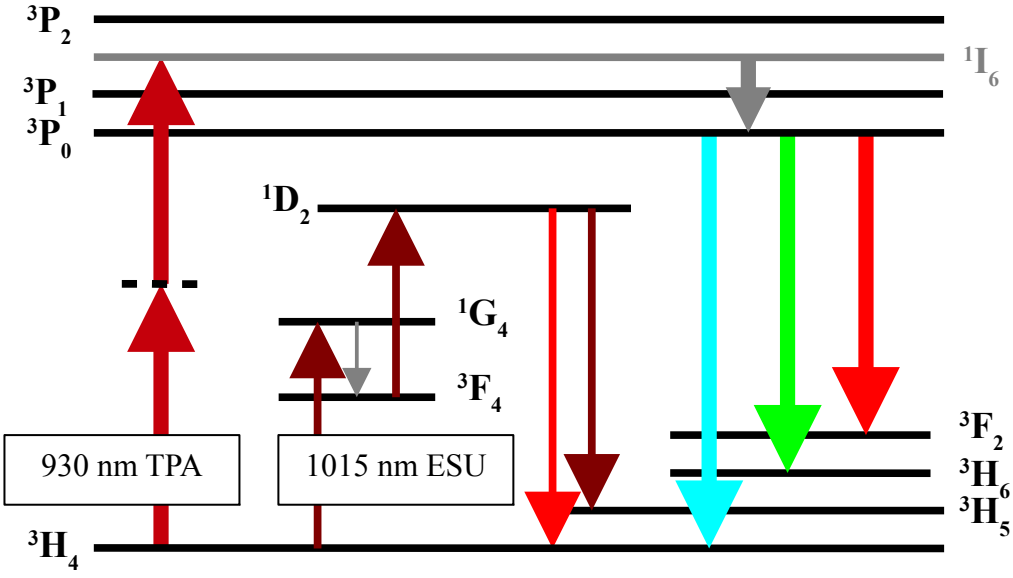

Figure 6.9.8: The second proposed excitation and emission pathway for Pr:ZBLAN. Two-photon excitation to the $^1I_6$ level only which decays to the $^3P_0$ level. Emission from $^1D_2$ can also occur by excited state upconversion of 1015 nm light.

6.9.2. The two-photon excitation cross-section

Unlike the case of the ruby which emits light over a single narrow wavelength band praseodymium's multiple emission lines mean that it is difficult to capture and quantify all of the emission resulting from any given absorption event thus it is not possible to calculate the two-photon absorption cross-section of the material using the method derived in Chapter 4. By selecting any one emission line however and measuring the amount of light emitted it is possible to use this method to calculate the two-photon excitation cross-section for that emission line. If the emission cross-sections for each emission line could be accurately measured then the sum of those cross-sections would be the equivalent of the two-photon absorption cross-section for that excitation wavelength. Alternatively, as it has been established that the emission spectrum of a particular transition is independent of excitation path if the branching ratios (i.e. the fraction of the total emission included in a single line) of one or more emission lines are known that value may be divided into the excitation cross-sections for those lines to calculate the absorption cross-section. It was not possible to calculate the change in quantum efficiency with excitation wavelength as could be done with the ruby in Figure 5.4.4 so a rigorous calculation of the excitation cross-section spectrum could not be made.

If it is assumed though that any change in relative quantum efficiency is negligible then the two-photon excitation spectra of praseodymium for the 600 nm, 715 nm and 960 nm emission lines can be shown as in Figure 6.9.9.

The peak excitation cross-sections for these lines were recorded as 1.6 GM for the 600 nm emission (A combination of $^1D_2 \rightarrow {}^3H_4$ and $^3P_0 \rightarrow {}^3H_6$); 0.3 GM for 715 nm ($^3P_0 \rightarrow {}^3F_4$) and 0.9 GM for 960 nm ($^1D_2 \rightarrow {}^3F_3$). Each of these values has an uncertainty value attached to it of approximately ±24 %, primarily, as with previous cases, dominated by systematic uncertainties in measuring fixed parameters such as the beam area and pulse duration. Details of the recorded parameters for the calculation of the 600 nm excitation cross-section can be found in Table 6.9.1.

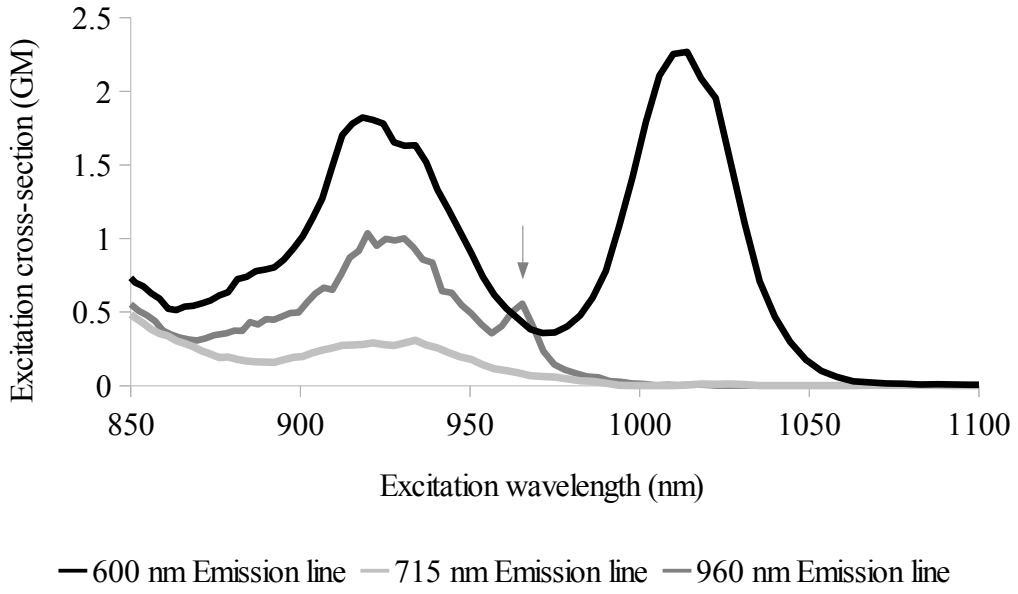

Figure 6.9.9: The two-photon excitation cross-section spectra for three emission lines of Pr^{3+}:ZBLAN. The laser line for the 960 nm excitation is marked by the arrow.

Table 6.9.1. Calculation of δ in Pr^{3+}:ZBLAN			
Parameter	Value	Unit	% Uncertainty
P'(t)	480	mV	3
P”(t)	15.0	mV	3
E'	30	mJ/pulse	8
E”	17	mJ/pulse	8
A”	0.101	cm^2	10
t_p”	10	ns	17
λ'	465	nm	<1
λ”	930	nm	<1
σ_{486nm}	1.20×10^{-19}	cm^2 ion^{-1}	
N_1	3.35×10^{20}	ion cm^{-3}	1
K	0.664	[dimensionless]	n/a
Nd	2.46×10^{-4}	[dimensionless]	2

Table 6.9.1: Data table for the calculation of the two photon excitation cross-section of Pr^{3+}.

6.9.3. The fluorescence decay time constant

With the primary emission lines for the Pr:ZBLAN identified the sample was inserted into a similar experimental arrangement as the ruby was in Section 5.8 so that the effect of temperature on the fluorescence decay time constant could be measured. The principal difference with this version being that the fluoride glass used has a much lower melting point than the ruby and begins to soften and melt at temperatures not far above 150ºC.

The primary emission line studied was the one centred around 635 nm as this minimised the possibility of any confusion between emission from $^3P_0$ and from $^1D_2$. Also if praseodymium were to be chosen as a dopant for a test fibre system any emission caused by a transition to the ground state may cause the same re-absorption problems found in the ruby and should therefore be avoided where possible. The impedance to the instrumentation was set to 5 kΩ giving a minimum resolution of 6 μs.

The fluorescence decay lifetimes shown in Figure 6.9.10 and Figure 6.9.11 are comparable to results found in previous work such as that done by Sun et al[121] with the lower magnitudes of the decay times found here being consistent with the relatively high dopant concentrations (10 000 ppm compared to the 4000 ppm used by Sun et al) as shown below in Figure 6.9.12.

One of the limitations found in trying to calculate the change in τ with temperature was the relatively noisy signals encountered, especially in the two-photon regime where the series of non-linear processes applied to the beam combined with the very low fluorescence intensity resulted in a relatively poor signal-to-noise ratio. Additionally, at the time of this particular experiment the OPO laser was not operating at its optimal performance (something which was corrected shortly afterwards and before the following experiments). This shot-to-shot variation, measured by collecting the deviations of the recorded data from their calculated trend lines and shown in Figure 6.9.13, fits well to a Gaussian envelope with a standard deviation of approximately ±7 % of the full scale reading.

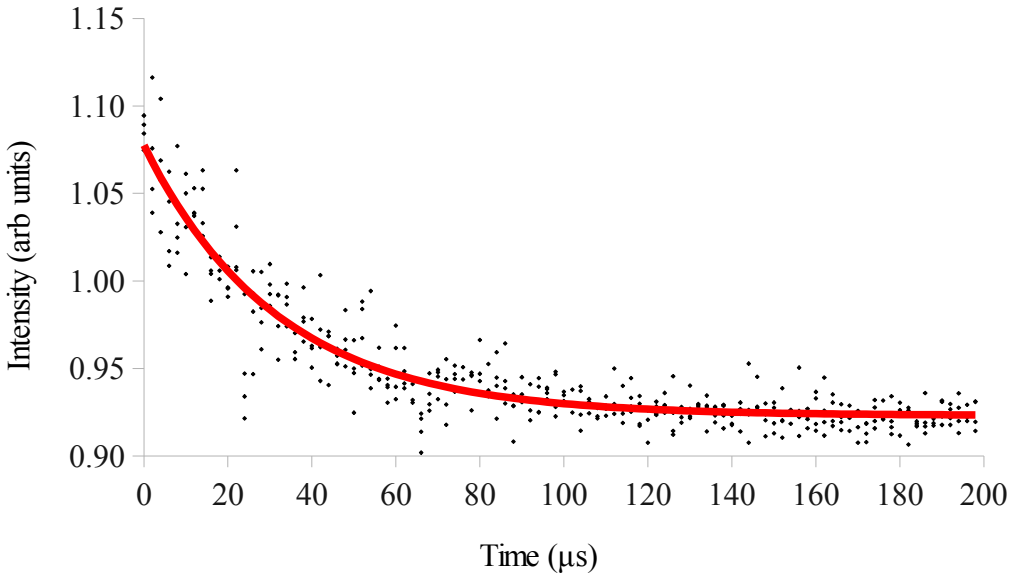

Figure 6.9.10: The decay of 635 nm emission from Pr:ZBLAN excited using 930 nm TPA at a temperature of 50 °C and the best-fit exponential curve from which a value for τ can be measured as 32 µs.

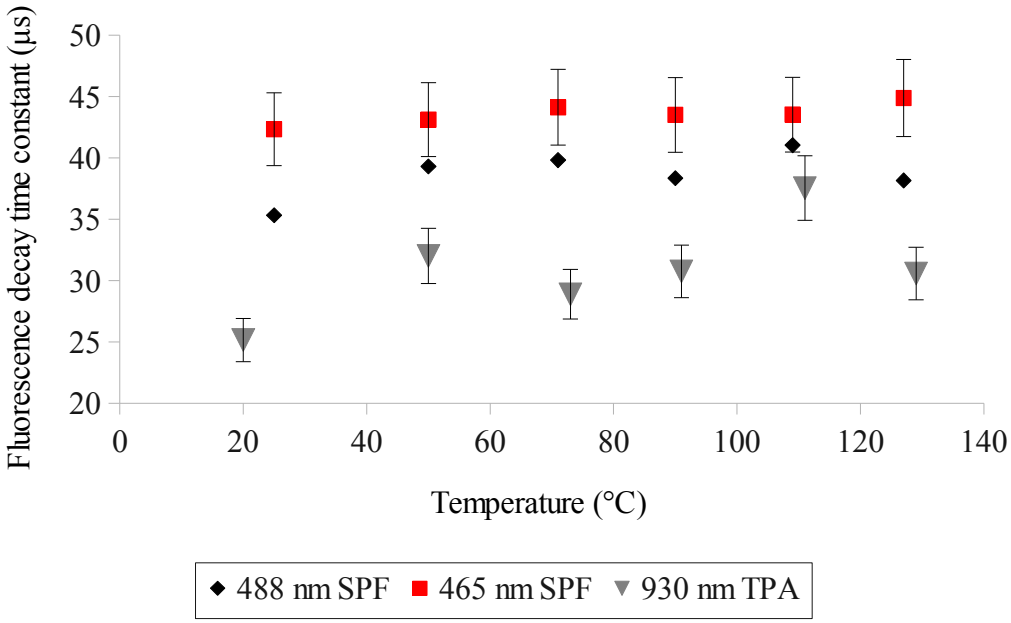

Figure 6.9.11: (grey triangles) The change in the decay time constant for 635 nm emission excited by 930 nm TPA. The average rate of change over this temperature range is approximately +64 ns/°C. Also displayed are the change in decay times for 635 nm excited by 488 nm SPA (black diamonds) and 465 nm SPA (red squares). The average rate of change for these emissions are +27 ns/°C and +19 ns/°C respectively.

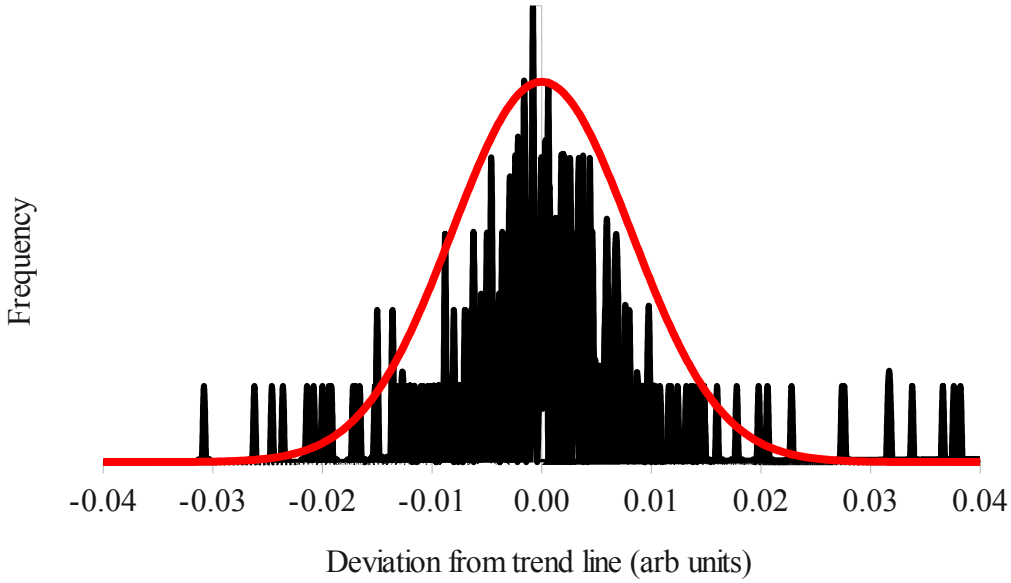

Figure 6.9.13: A histogram showing the combined deviation from the best fit trend line for all TPF emissions shown in Figure 6.8.3.

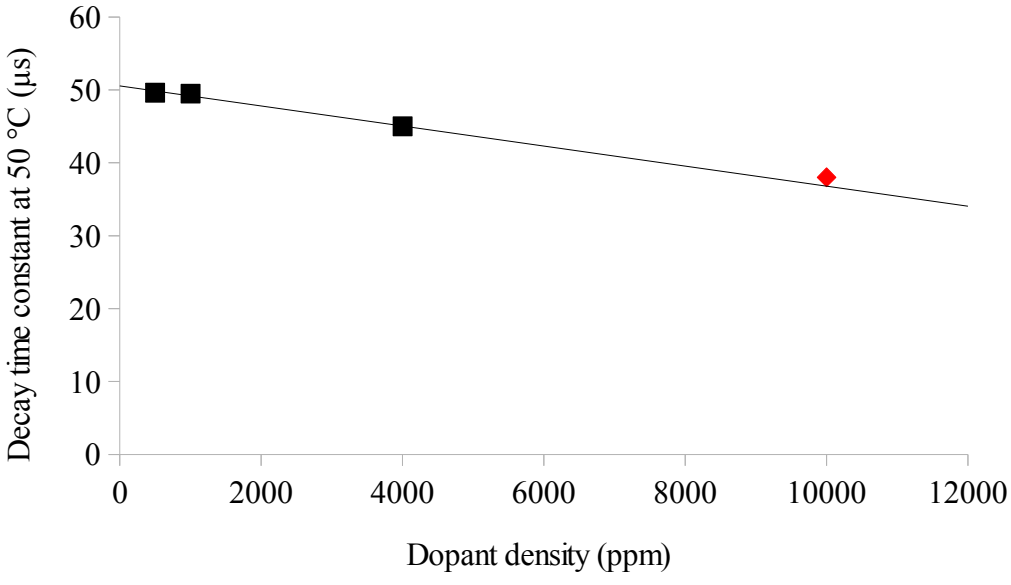

Figure 6.9.12: The change in the 488 nm SPA excited 635 nm fluorescence decay lifetime as a function of dopant concentration. A comparison of the values found by Sun et al[121] (black squares) with the data found in this investigation (red diamond). The trend line is a projection only of Sun's data.

6.9.4. Conclusion

Praseodymium in ZBLAN glass has been shown to demonstrate reliably detectable fluorescent emission resulting from two-photon excitation. The single- and two-photon excitation spectra were recorded and showed some discrepancy between each other. It may be that this is a consequence of the selection rules governing single- and two-photon excitation as it seems that the $^3P_{0,1,2,}$ levels do not strongly excite under TPA relative to the $^1I_6$ level.

Both the two-photon excitation spectrum and the emission spectrum have been measured in detail and a peak value for the two-photon absorption cross-section measured as a very strong (for a rare-earth metal) 1.6 GM at 935 nm (for 630 nm emission). The fluorescence lifetime was found to be long enough to be useful for a practical sensor and the temperature response of the decay time constant was measured reliably and in a repeatable manner.

Praseodymium has therefore been identified as a strong contender for further study as a dopant for a prototype distributed temperature sensor.

6.10. Conclusions

In this chapter a selection of rare-earth metals doped in mainly ZBLAN glasses were investigated for their single- and two-photon characteristics producing several results which have been presented for the first time either here or in peer reviewed journal publications attached to this project.[122],[73],[123],[124] The aim was to find potential dopants which could be useful as part of a distributed temperature sensor.

Successful measurements to a greater or lesser extent of single-photon, two-photon and excited state upconversion events were found in praseodymium, samarium, gadolinium, terbium, dysprosium, holmium and thulium. Doped glasses containing neodymium, europium and erbium were also investigated but various issues with these experiments and inconsistent results preclude publication of these investigations at this time.

The dopants investigated in this chapter have some of their characteristics most relevant for the purpose of an optical fibre sensor summarised below in Table 6.10.1. Many of the dopants suffered issues both experimental and material which, at least within the scope of this study, rule them out as candidates for a fibre sensor.

Of the dopants investigated praseodymium and terbium were found to respond measurably with temperature and exhibited a two-photon excitation cross-section large enough to consider viable as a sensor. Of these two, praseodymium was considered especially suitable as terbium would require to be doped into the fibre at relatively high concentrations for the temperature sensing to be noticeable. Praseodymium was also advantaged by a two-photon absorption cross-section which was high enough to rival some organic dyes. Finally, some suggestion has been made both in the literature and in the results presented here that temperature may be sensed by both measuring the change in fluorescent lifetime and by measuring the ratios of the intensities of several emission lines simultaneously the effect of strain may be isolated without requiring any compensation by special configuration of the installed sensor.[125]

With the most favourable dopant for the fibre sensor identified and a single-mode fibre doped with praseodymium sourced it was possible to construct and begin investigations on the first experimental model of a distributed optical fibre temperature sensor based on two-photon excited fluorescence.

Table 6.10.1. Dopant summary				
Dopant	Peak two-photon excitation cross-section (GM)	Room temperature fluorescence lifetime	Rate of change of lifetime	4-level transitions available?
Thulium	-	48 μs	-	Yes
Gadolinium	-	-	-	Yes
Samarium	-	-	-	Yes
Dysprosium	-	-	-	Yes
Holmium	3.0×10^{-5}	110 μs	-	No
Terbium	1.4×10^{-3}	3.3 ms	+250 ns/°C	Yes
Praseodymium	1.6	25 μs	+64 ns/°C	Yes

Table 6.10.1: A summary of some of the important sensing parameters of the rare-earth dopants studied.

7. Optical fibre sensing

7.1. Introduction

In the previous chapter praseodymium was identified as the primary candidate amongst the samples tested for further investigation as a dopant for a distributed fibre sensor based on two-photon excited fluorescence as it showed considerable promise due to a high two-photon absorption cross section (1.6 GM for 600 nm emission and 935 nm excitation), a detectable dependence of the decay lifetime on temperature and the potential for isolating temperature and strain components via a comparison of emission line intensity ratios.

7.2. Experimental arrangement

The experiments involved in this chapter of the investigation were carried out in a broadly similar manner to many of the previous ones. A single-mode praseodymium doped R31501-Pr fibre sourced from OFS Fitel Denmark I/S, with a core diameter of 3.29 μm and a numerical aperture of 0.24 was cut into a 10 m length and a 1 m length. The 10 m fibre was mounted such that the output of the OPO laser could be coupled into both ends of the fibre simultaneously by means of a beam splitter and that the fluorescence emitted from the ends of the fibre could be combined by the same beam splitter and guided into the spectrometer as shown in Figure 7.2.1. Coupling the laser into the fibre apertures was aided by the same HeNe guide beam propagating alongside the main beam and by visual examination of the beam with the assistance of a CCD camera to roughly align the beam. Fine adjustments were then made by placing a power meter in front of one of the apertures in turn and maximising the transmitted laser power. Also visible in Figure 7.2.1 is the water bath used to warm the fibre during the elevated temperature experiments.

Some of the single-photon excitation experiments were performed using an argon ion laser (emitting at 488 nm) coupled into one aperture only with the other aperture fixed directly onto the input of the spectrometer.

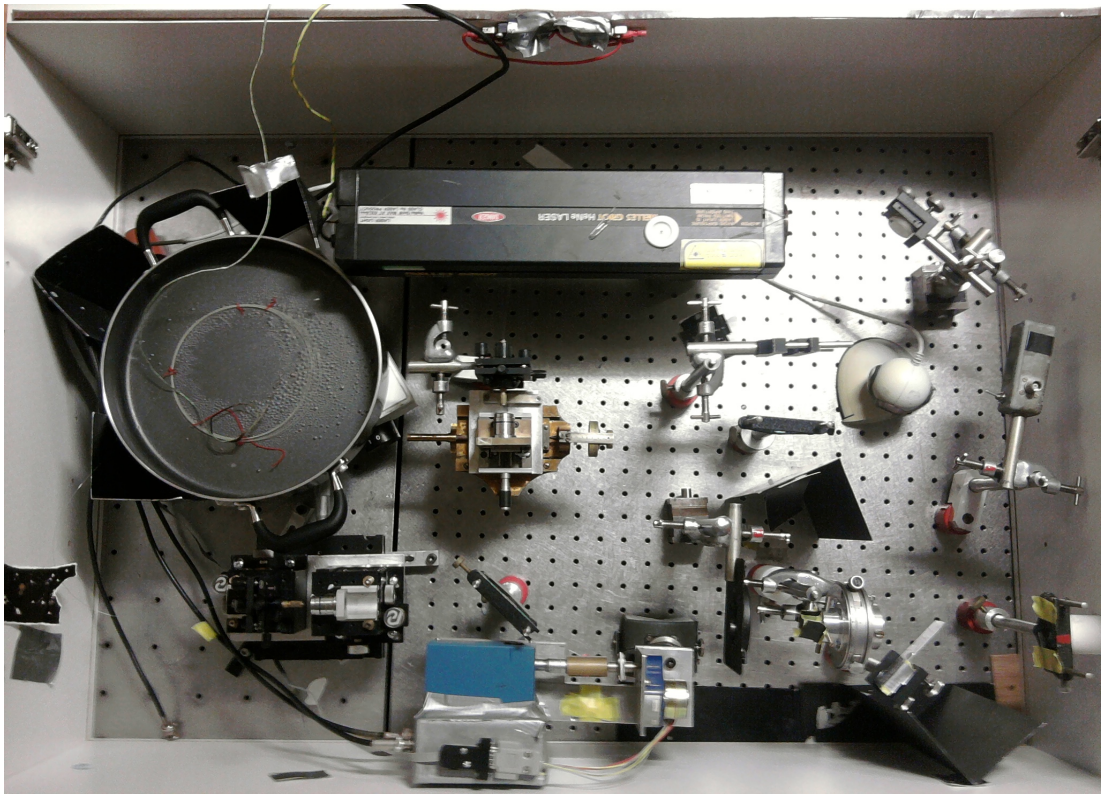

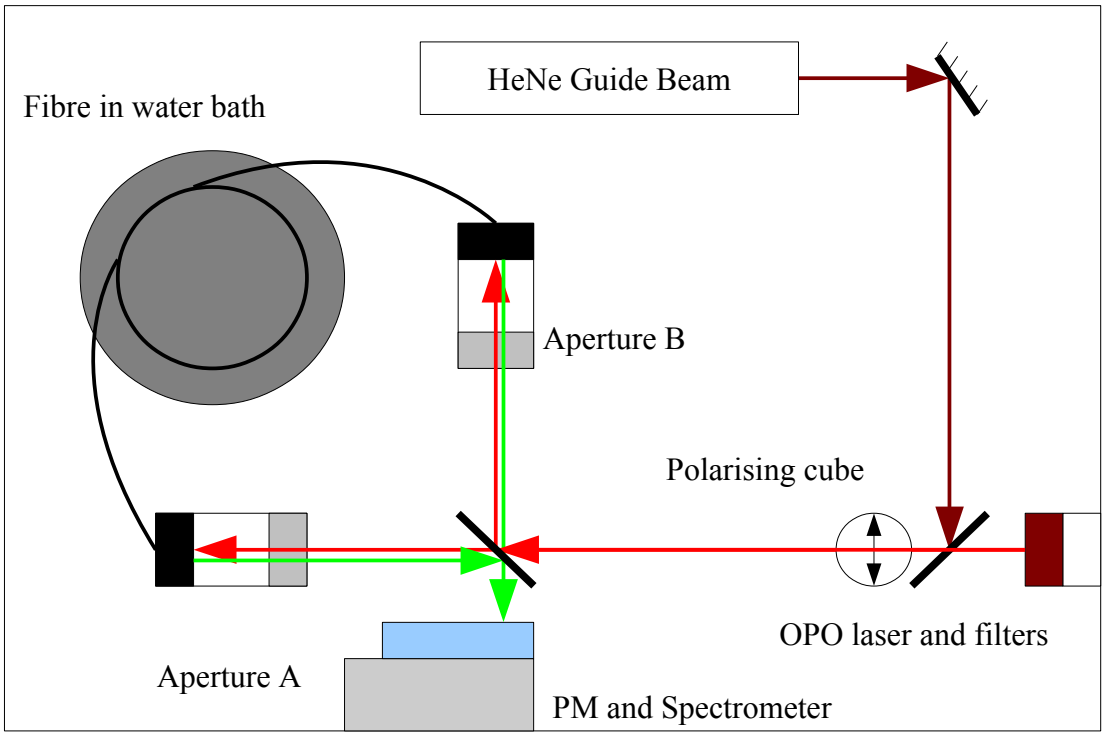

Figure 7.2.1: Experimental arrangement for cross-propagated degenerate excitation of the Pr doped fibre. The excitation pulses (red line) are guided with the aid of the HeNe beam into the apertures of the fibre using the beam splitters. Fluorescent emission (green line) is guided back out either aperture and to the spectrometer. The Polarising cube was used to control beam power.

7.3. Single photon excitation and emission spectra

The first test of the Praseodymium doped fibre was to determine the single-photon emission spectrum by exciting the fibre using the 488 nm output of a cw argon ion laser coupled as described above into one end of the fibre.

The 488 nm light was able to excite the Pr^{3+} ions through the $^3H_4 \rightarrow {}^3P_0$ transition and led to a brightly visible red glow within the fibre, as shown in Figure 7.3.1.

The emission spectrum of the fibre was recorded and compared to the Pr^{3+}ZBLAN sample used previous and excited again here by the same laser. The two emission spectra, shown in Figure 7.3.3, are broadly similar to each other, as should be expected, with a major exception being that in the silica fibre the group of lines centred around 630 nm were broadened with respect to the same group in the ZBLAN and have merged to form one overlapping band rather than the two observed previously. Despite this broadening the position and the shape of the emission band is still in close agreement with the data obtained from the cryogenic analysis of single crystal Pr^{3+}:KY_3F_{10} single crystal hosts[120] (Figure 7.3.2) and the shape of the curve itself closes matches that found by Koziol et al in a similar silica fibre.[126]

Furthermore a comparison of the fluorescence emitted from the end of the 10 m fibre was compared to that from the 1m fibre, shown in Figure 7.3.4, and it was found that the 10 m fibre showed signs of a depression of fluorescence at the short-wavelength end of the band. By overlaying the emission spectrum with the absorption spectrum of the $^3H_4 \rightarrow {}^1D_2$ transition it becomes apparent that there is some overlap of the two and that a degree of self-absorption is taking place which, while low, is significant over lengths above a few metres. As with the case in ruby and holmium this self-absorption has serious implications for the viability of the proposed sensors but unlike the previous examples it should be avoidable in this case as the longer-wavelength end of the emission spectrum (longer than 630 nm) seems unaffected.

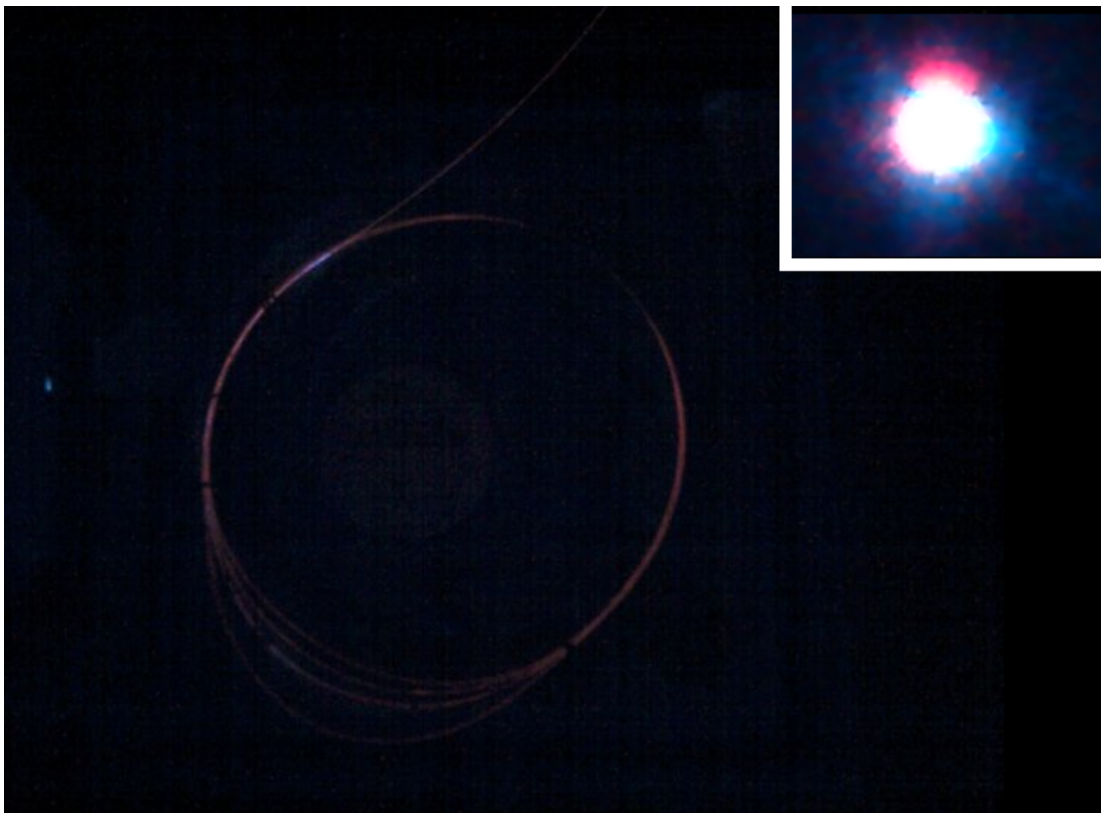

Figure 7.3.1: Visible fluorescence in the praseodymium fibre due to 488 nm SPF. (insert) The light projected from the aperture of the fibre.

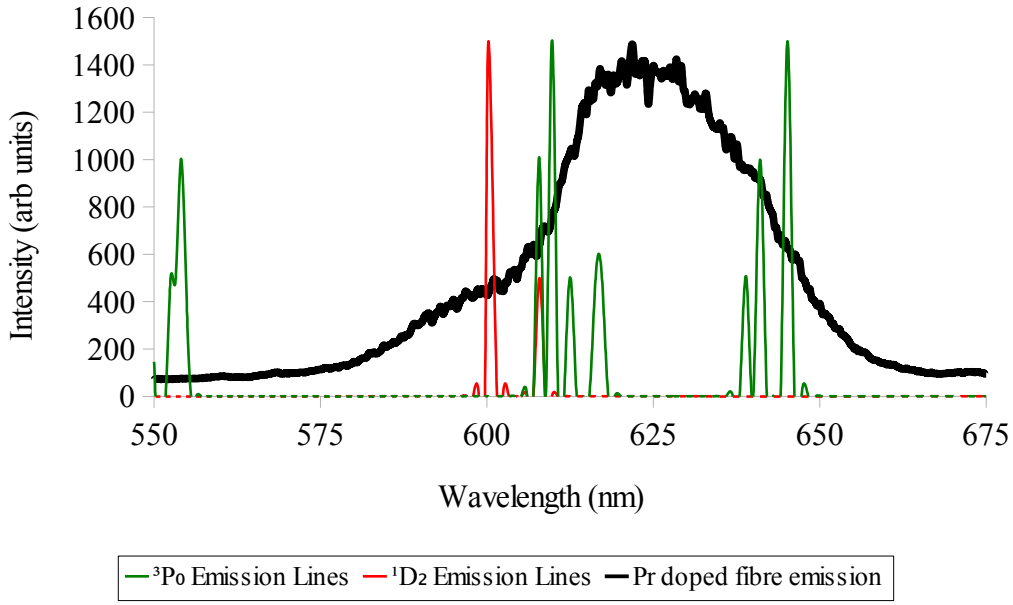

Figure 7.3.2: A comparison of the SPF emission spectrum of the fibre with the positions of the emission lines found in single-crystal Pr^{3+}:KY_3F_{10}.[120] (Intensities of emission lines not to scale)

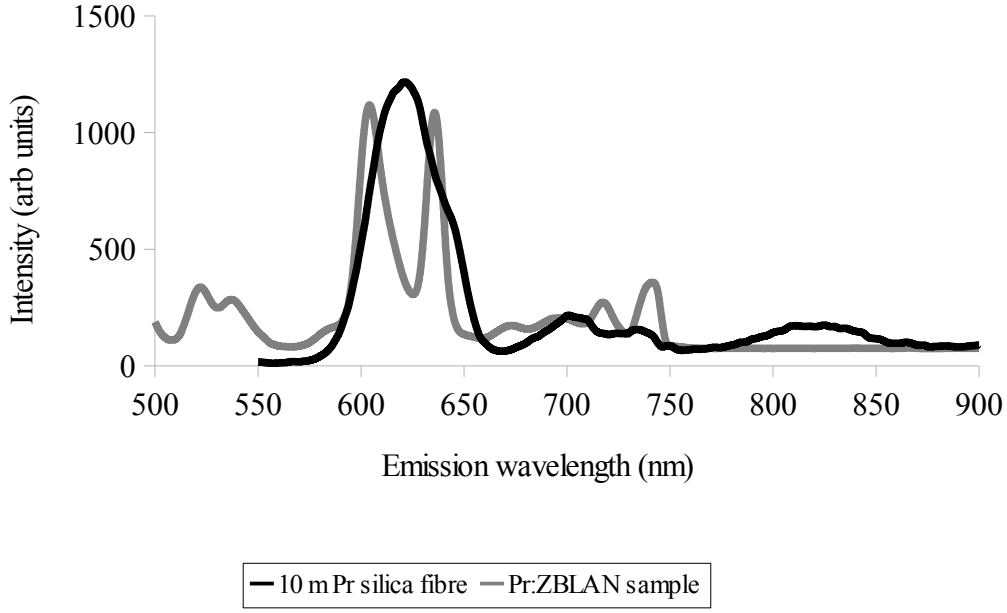

Figure 7.3.3: (black line) the emission spectrum of the praseodymium fibre excited by 488 nm SPA. (grey line) The emission spectrum of the Pr^{3+}:ZBLAN sample from Chapter 6 excited by the same source.

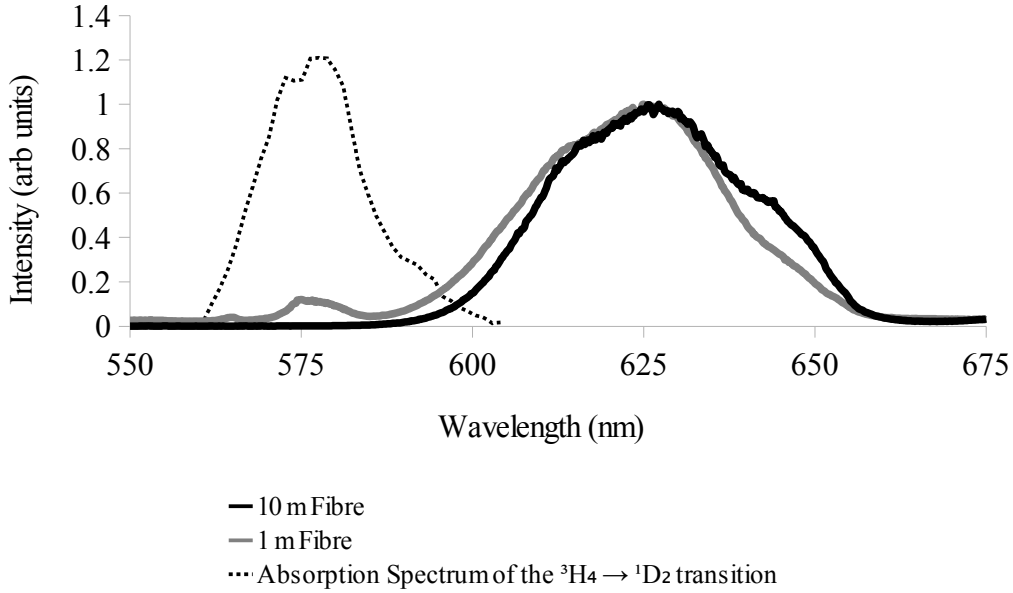

Figure 7.3.4: The SPF emission spectrum from the end of the 10 m Pr^{3+} doped fibre in comparison to that of the 1 m Pr^{3+} doped fibre (intensities are normalised at 625 nm). The 10 m fibre show depressed fluorescence on the short-wavelength side which illustrates the self-absorption nature of self-absorption by the $^3H_4 \rightarrow {}^1D_2$ transition.

The single-photon excitation spectrum was recorded by monitoring emission at 620 nm, near the peak of the primary emission band and away from the self-absorption region. The excitation spectrum, shown in Figure 7.3.5, is essentially identical to that of the Pr:ZBLAN glass tested in Chapter 6 and shows three prominent peaks due to the $^3P_{2,1,0}$ levels at 463 nm, 473 nm and 483 nm respectively. The $^1I_6$ level is mostly obscured by the ^3P levels and the limited resolution of the spectrometer (approximately 7 nm) but is visible as a shoulder on the short-wavelength side of the $^3P_1$ peak and appears to be centred at around 470 nm.

The overall detected signal strength of the emission was somewhat lower than that of the bulk sample mostly due to the increased path length between the fibre and at the detector, around 30 cm compared to the 1-2 cm of that of bulk sample although this is somewhat alleviated by the increased path length of the fibre and by the lenses which act to collimate that fraction of the emission which is collected and guided by the fibre.

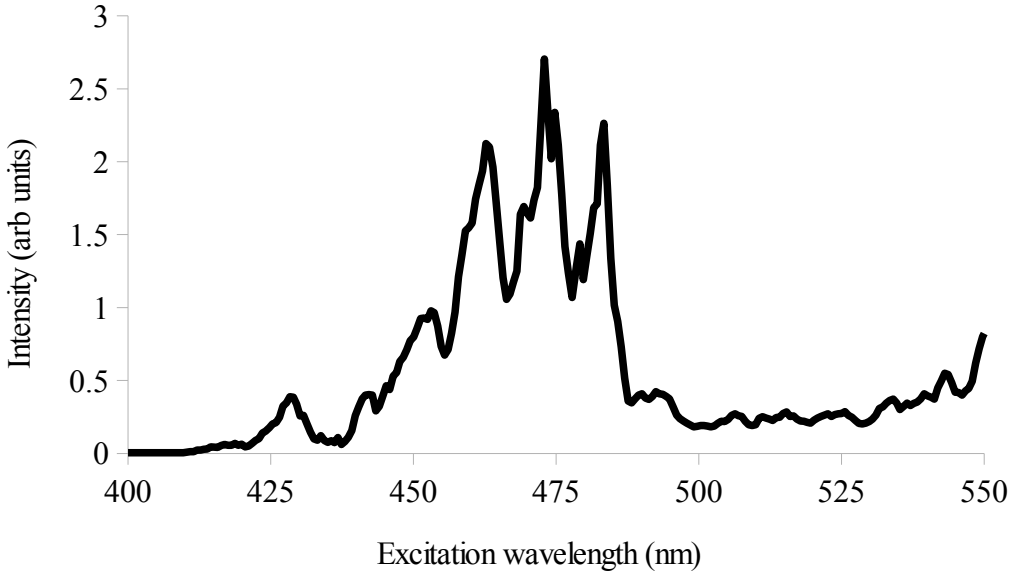

Figure 7.3.5: The single-photon excitation spectrum for the 10 m Pr doped silica fibre emitting at 620 nm. The three prominent peaks due to the $^3P_{2,1,0}$ group are clearly visible.

7.4. Two-photon excitation and emission spectra

Owning to the relatively long path length of the 10 m fibre compared to the 0.5 cm ZBLAN sample it was relatively simple to excite the Pr^{3+} ions by two-photon absorption once the OPO laser was as efficiently coupled into the fibre as could be given the large spot size of the beam relative to the fibre aperture.

As with the ZBLAN sample, the excitation spectrum for the fibre exhibited a single peak centred around 935 nm as can be seen in Figure 7.4.1. The rising signal seen around 840 nm is part of an erroneous background signal and was ignored.

Comparing the TPF and SPF excitation spectra show in Figure 7.4.2, as with the case for Pr^{3+}:ZBLAN, that the TPF excitation spectrum consists of only one well defined peak centred on the energy-equivalent of the $^1I_6$ level and that the ^3P levels are functionally absent.

A notable absence from the fibre excitation spectra compared to the ZBLAN spectra is the absence of the ESU transition via the $^1G_4$ level and which was found to emit at 600 nm. The lack of this transition would later help with attempts at non-degenerate two-photon excitation as it allowed greater confidence that no degenerate excitation would take place if a 1064 nm Nd:YAG laser were to be used.

Despite the clearly detected signals it was not possible to measure the absorption cross section due to the slightly different absorption profiles between SPA and TPA. In the two-photon case the low overall absorption means that the effective absorption length is many times longer than the 10 m fibre length thus the pulse can excite along the full length of the fibre without itself being affected in any significant manner. The relatively higher absorption of SPA means that all significant absorption takes place in the first few centimetres of the fibre thus the beam profile at any particular point within the fibre is significantly more complex. Additionally it was difficult to measure with any precision the amount of laser energy which was actually coupled into the fibre. This may be only about 1 % of the laser power.

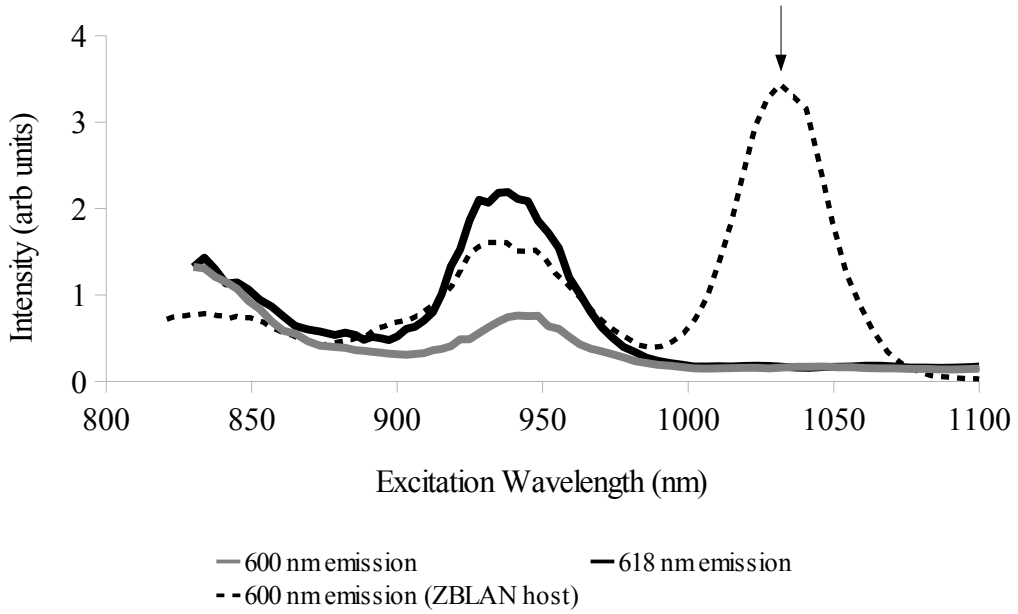

Figure 7.4.1: Two excitation spectra for TPF in Pr doped silica fibre. (grey line) The 600 nm emission primarily from the $^1D_2 \rightarrow {}^3H_4$ transition. (black line) 618 nm emission from the $^3P_0 \rightarrow {}^3F_2$ transition. (dashed line) The TPF excitation spectrum for 600 nm emission in Pr^{3+}:ZBLAN showing the ESU transition (marked by the arrow) which is absent from the silica fibre's emission spectrum.

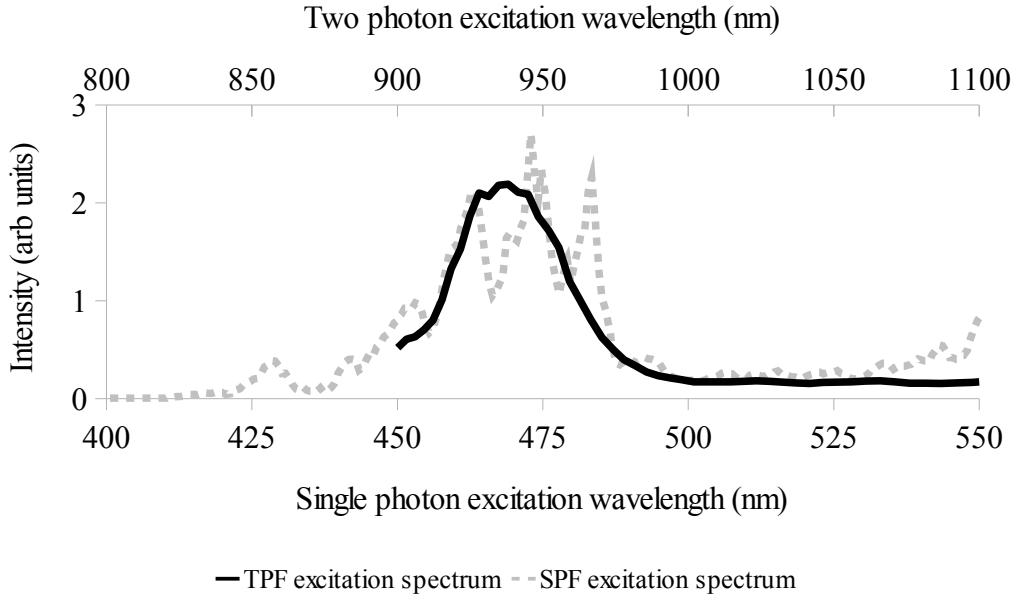

Figure 7.4.2: A comparison of the SPF and TPF excitation spectra. Two photon excitation appears to occur only through the $^3H_4 \rightarrow {}^1I_6$ transition with the $^3H_4 \rightarrow {}^3P_{2,1,0}$ transitions being greatly reduced or absent.

The two-photon excited emission spectrum was tested using the peak excitation wavelength of 930 nm and found a spectrum essentially identical to that of the single-photon excitation. Figure 7.4.3, shows a strong band centred around 620 nm and two smaller bands at 710 nm and 850 nm, thus again agreeing well with the emission from similar silica fibres[126] although it should be noted that the bands found by Koziol et al showed that these longer wavelength bands were much more intense that the 620 nm band and that another even stronger band is located at 1050 nm. The discrepancy here is due to the photomultiplier used which is significantly less sensitive to light of wavelength longer than about 700 nm and cannot sense signals at all beyond around 950 nm.

As the main focus of the investigation was to be on the 620 nm band and that it had been established that multiple emission lines sourced from both the $^3P_0$ level and the $^1D_2$ level were present the band was analysis to try to identify its components by fitting the sum of three Gaussian curves to the band. These three components, shown in Figure 7.4.4 map well to the data and can be identified as belonging to the three strongest transition within the group; $^1D_2 \rightarrow {}^3H_4$ at 595 nm, $^3P_0 \rightarrow {}^3H_6$ at 620 nm and $^3P_0 \rightarrow {}^3F_2$ at 635 nm.

Figure 7.5.1 shows the dependence of the 620 nm emission group's intensity on the peak power of the 935 nm excitation pulses. As the beam power was varied using a polariser the emission intensity, at 620 nm, was found to vary as the square of the beam power thus confirming that a two-photon process is involved in the excitation. As in many of the previous cases, this does not in itself demonstrate a two-photon absorption but the absence of any nearby real energy levels which would suggest an excited state upconversion process true TPA remains the simplest mechanism for the excitation.

The final experiment performed on the emission spectrum was to investigate the effect of elevated temperatures on it by immersing the fibre in the water bath seen in Figure 7.2.1. The temperature was allowed to stabilise at each setting for 30 minutes before the reading was taken and the emission spectrum recorded between a range of 20 ^oC and 55 ^oC.

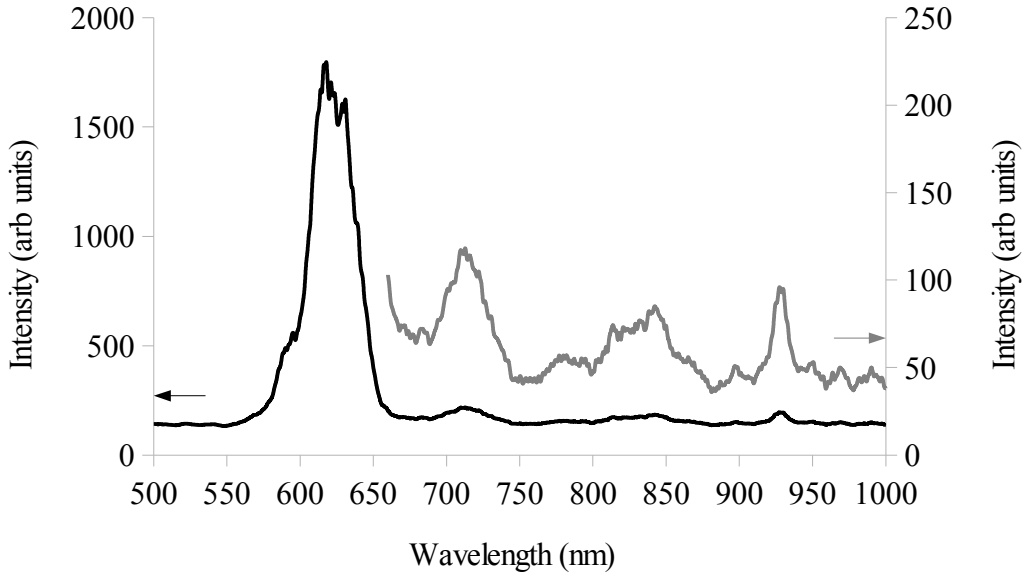

Figure 7.4.3: The emission spectrum of the 10 m Pr doped fibre under 930 nm TPA. The black lines shows the full detected spectrum, in particular the main group at 630 nm. The grey line shows a 5 times magnification of the other detected lines at 710 nm and 850 nm as well as the laser line at 930 nm.

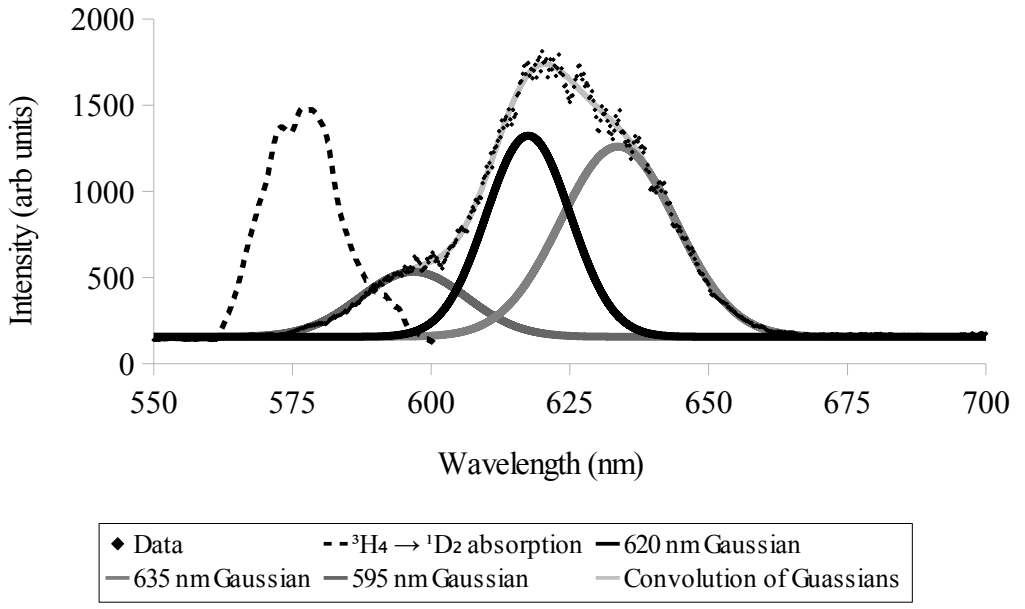

Figure 7.4.4: The deconvolution of the 620 nm emission band revealing the three primary emission lines identified as $^1D_2 \rightarrow {}^3H_4$ at 595 nm, $^3P_0 \rightarrow {}^3H_6$ at 620nm and $^3P_0 \rightarrow {}^3F_2$ at 635 nm. The absorption band due to $^3H_4 \rightarrow {}^1D_2$ is marked by the dashed curve centred at 575 nm.

The peak emission intensity was found to drop rapidly as temperature increased although the rate of decrease appeared to level off as the temperature approached 45 ºC as can be seen in Figure 7.5.2, particularly in the insert.

When the emission spectra at each temperature were normalised to their peak values, as shown in Figure 7.5.3, no significant change in the relative shape of the emission band could be detected in the region around 595 nm which indicates that over this temperature range the absorption spectrum of the $^3H_4 \rightarrow {}^1D_2$ transition is unaffected. Any broadening to that line would cause an increase in self-absorption which would further suppress the short-wavelength edge of the emission curve.

Each of the spectra recorded for Figure 7.5.3 were deconvoluted in the same manner as Figure 7.4.4 and the intensities of the peaks of each of the three emission bands as a function of their relative contribution to the total emission was studied.

The change in the ratio of the emission due to the $^3P_0 \rightarrow {}^3H_6$ transition at 620 nm and the emission due to the $^3P_0 \rightarrow {}^3F_2$ at 635 nm is shown in Figure 7.5.4. There is a clear correlation in the ratio of the intensities of these two emission bands with rising temperature and the rate of change with temperature is great enough that it could be used as a sensing parameter alongside the change in fluorescence lifetime. Furthermore, if it can be shown that, as in other published cases[127][128], that the change in the intensity ratio is dependent only on temperature and not at all on the strain applied to the fibre (unlike the case of the fluorescent lifetime which is dependent on both) then by applying both measurements and subtracting the temperature component from the lifetime data then a simultaneous measurement of both temperature and strain may be made within a single fibre[129]. True strain-free temperature detection would therefore be possible in a distributed sensor for the first time without requiring the use of an installation arrangement where one fibre is coupled to the environment and another left free (thus unaffected by strain).

The temperature of the water bath used in the experiment was not elevated to more than 45 ºC due to the nature of the experimental arrangement. The combination of an open water bath, sealed safety enclosure and exposed optics meant that any temperature sufficient to cause rising steam from the bath also caused condensation on the optical elements which resulted in diffusion of the light as it passed through

the filters and polarisers and reduced coupling efficiency into the fibre.

7.5. The fluorescence decay time constant

With a clear two-photon emission spectrum now identified, the effect of temperature on the fluorescence lifetime of the three emission lines identified within the 620 nm group was investigated. This experiment was carried out using the boxcar integrator to measure the decay of the fluorescent intensity in a manner similar to the experiments described previously. Internal impedance was set to 500 Ω (giving a temporal resolution of 0.6 μs).

One complication in this experiment was that both Figure 7.3.2 and Figure 7.4.4 predicted that there should be a significant overlap between the three emission bands as well as significant sub-structure within them so a single-exponential decay profile would probably be unlikely. If, however, the components were different enough to distinguish then they could be positively identified by scanning the emission at wavelengths near the peak of one of the individual deconvoluted curves where the contribution of that curve would be more intense than the contribution found in emission recorded at a wavelength near the edge of the same curve.

The lifetimes were therefore monitored at 595 nm, 618 nm, 635 nm and 645 nm which allows the analysis and isolation of each of the three emission bands as shown fully in Figure 7.5.5. Each decay consisted of 250 data points each averaged over 10 successive scans and a scan time of just over 4 minutes per wavelength at a laser repetition rate of 10 Hz.

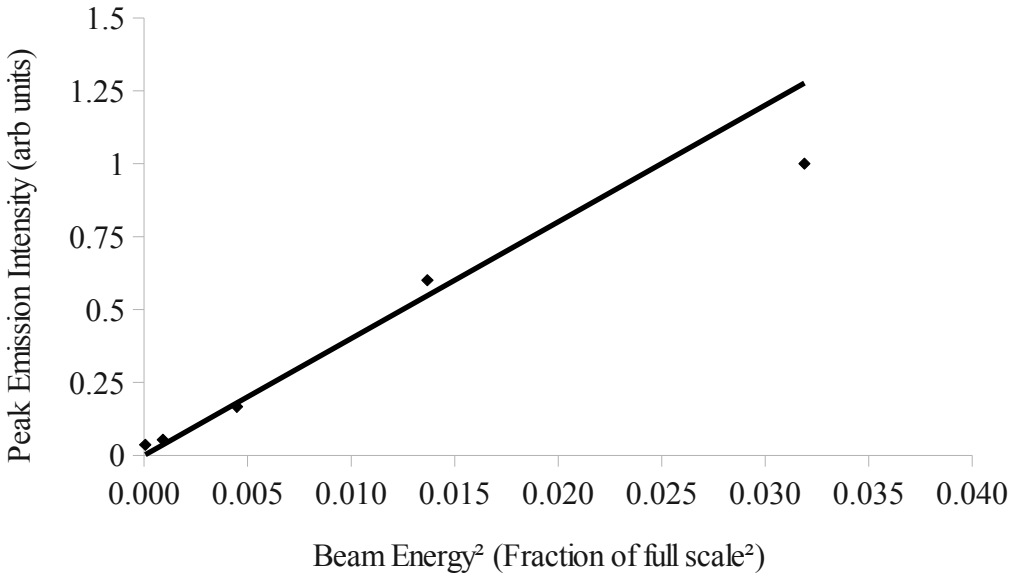

Figure 7.5.1: The relationship between TPF fluorescence emission intensity, P, from the fibre and the excitation power, E. The gradient indicates that $P \propto E^2$ *thus the excitation involves a two-photon process.*

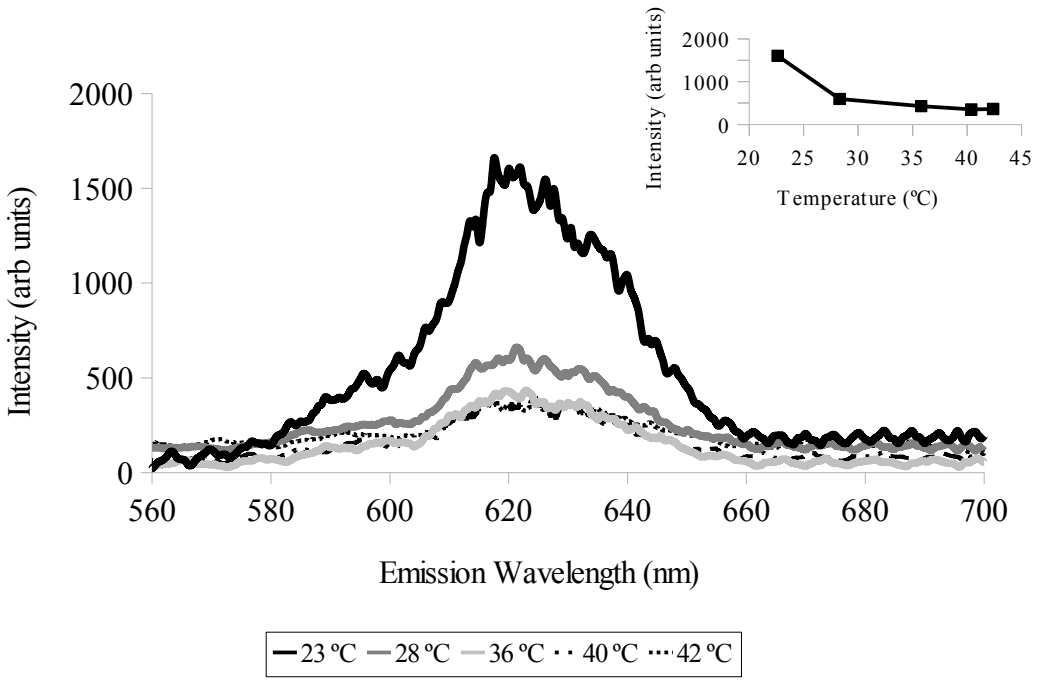

Figure 7.5.2: (main) The change in the emission spectrum with temperature. Emission intensity decreased with increasing temperature. (insert) The change in peak emission intensity with temperature.

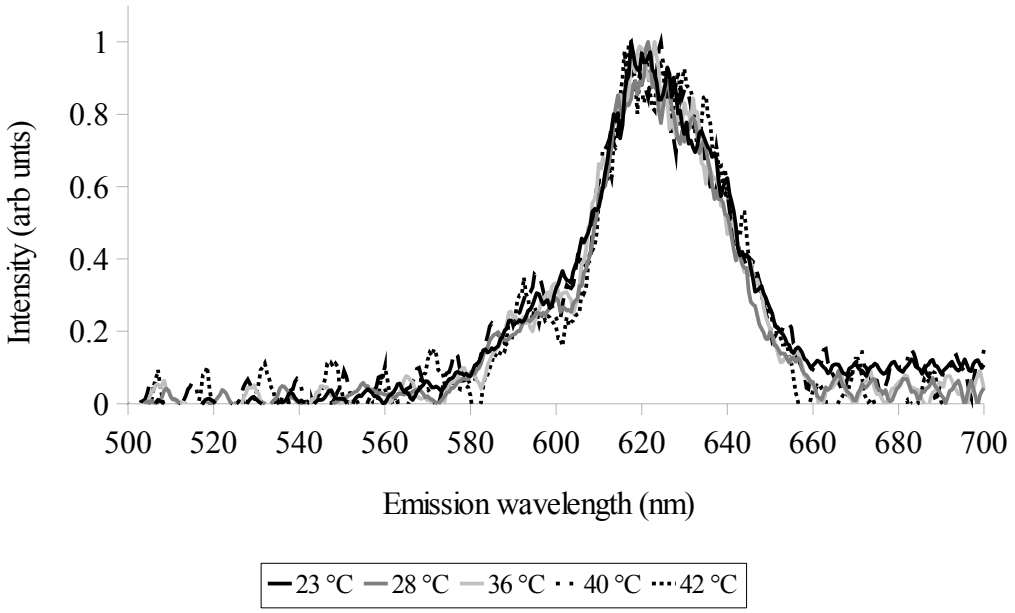

Figure 7.5.3: The emission spectra shown in Figure 7.5.2 normalised to their peak intensities. The emission near 595 nm shows no detectable effects due to self-absorption.

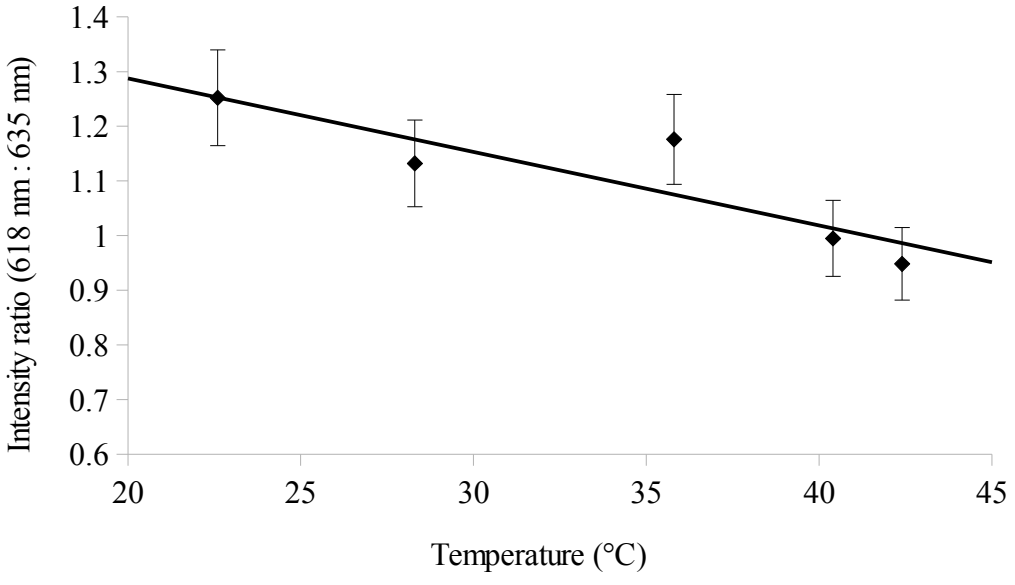

Figure 7.5.4: The ratio of the intensity of the peak of the 618 nm deconvoluted curve and the peak of the 635 nm deconvoluted curve as the fibre is heated. The relative intensity of the 618 nm peak decreases with respect to the 635 nm peak with increasing temperature.

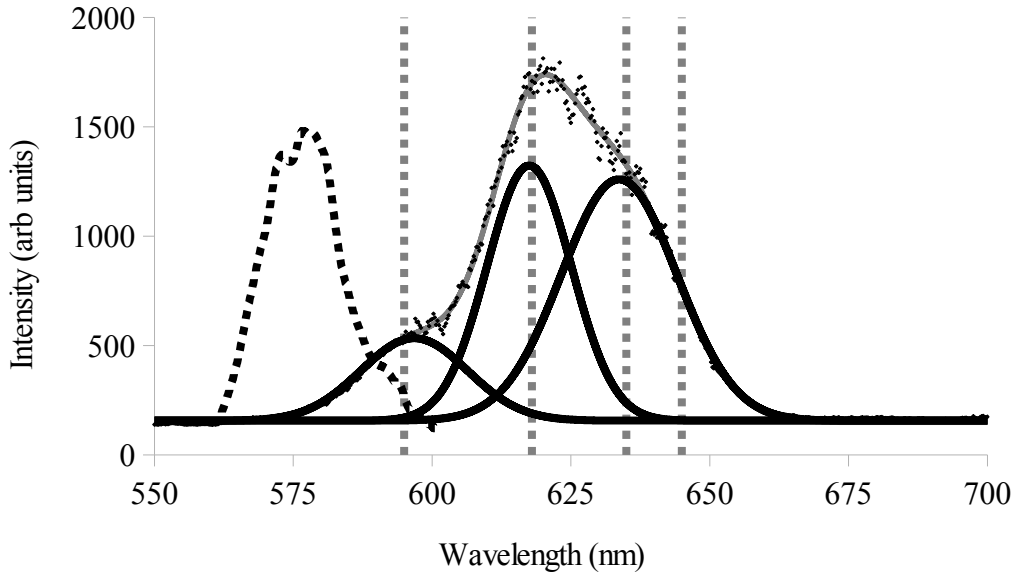

Figure 7.5.5: The emission spectrum of the 620 nm group of the Pr doped silica fibre marked with the wavelengths examined in this section. 595 nm monitors the $^1D_2 \rightarrow {}^3H_4$ transition, 618 nm monitors the peak of the $^3P_0 \rightarrow {}^3H_6$ line and a component of the $^3P_0 \rightarrow {}^3F_2$ line, 635nm monitors the peak of the $^3P_0 \rightarrow {}^3F_2$ line and a component of the $^3P_0 \rightarrow {}^3H_6$ and finally 645 nm monitors the $^3P_0 \rightarrow {}^3F_2$ line only. (dashed line) The absorption spectrum of the $^3H_4 \rightarrow {}^1D_2$ transition for reference.

7.5.1. 595 nm

The emission at 595 nm, the $^1D_2 \rightarrow {}^3H_4$ transition was, as noted previously, likely to be the least useful for sensing purposes due to the presence of self-absorption effects but was examined primarily so that any component of this transition which may appear at other wavelengths could be properly identified.

The fluorescence intensity of the emission recorded at 595 nm, shown in Figure 7.5.6, demonstrated a clear two component exponential function with a fast component lifetime of 14.4 μs and a slow component lifetime of 158 μs at the room temperature of 22.6 ^oC.

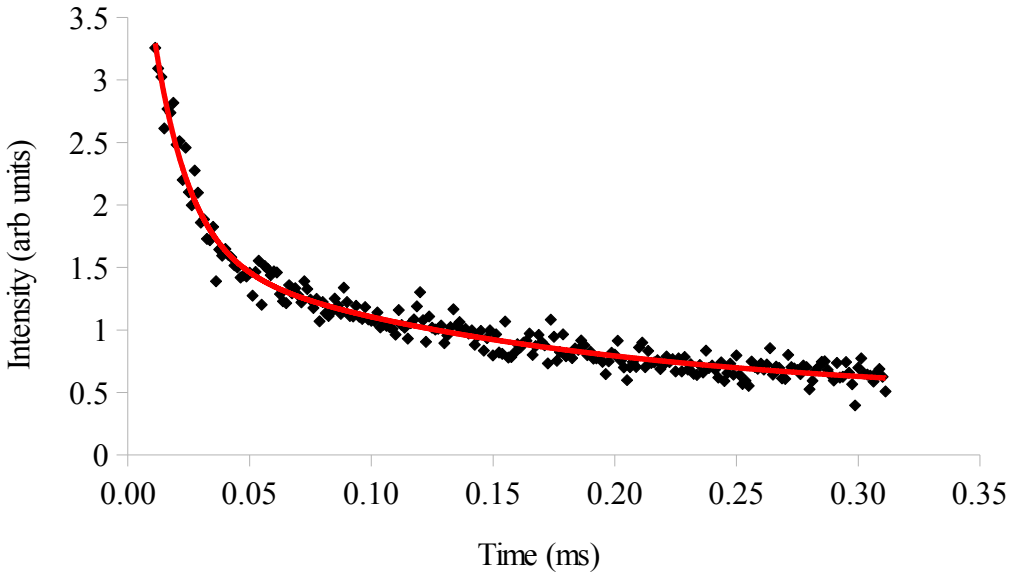

Figure 7.5.6: The decay of the TPF emission recorded at 595 nm at 22.6 °C. The fast component of the decay has a lifetime of 14.4 μs and the slow component a lifetime of 158 μs

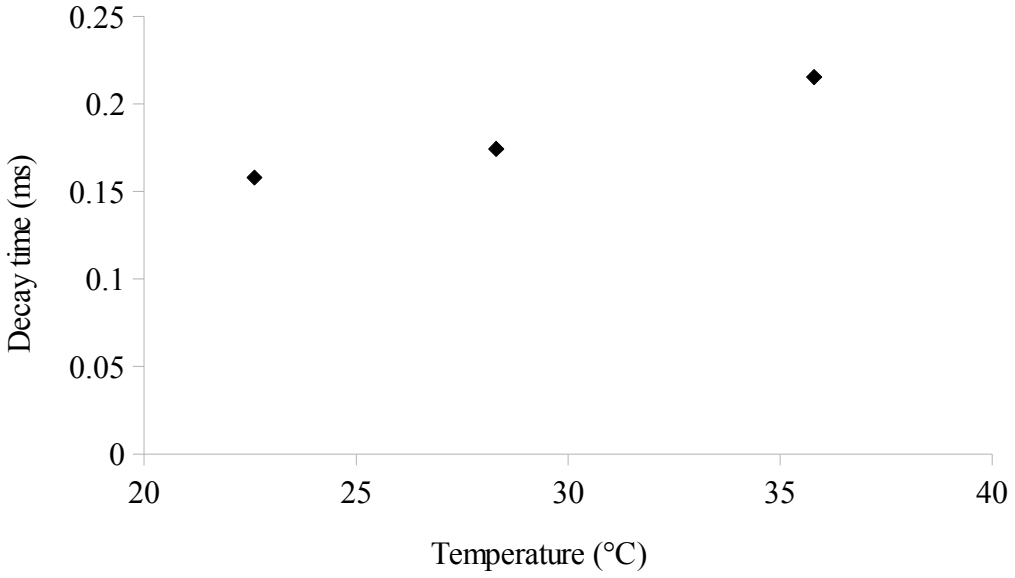

Figure 7.5.7: The change in decay lifetime with temperature for the slow component of the decay measured at 595 nm.

7.5.2. 618 nm

At 618 nm, the peak of the emission from the $^3P_0 \rightarrow {}^3H_6$ transition, the fluorescence decay showed a single-exponential decay with a lifetime of 98.7 μs at the room temperature of 22 °C as shown in Figure 7.5.8.

Figure 7.5.9 shows the change in the fluorescent lifetime with temperature which was found to rise at an average rate of +0.6 μs/°C over the temperature range from 22 °C to 55 °C although the TPF signal was found to be fairly noisy and suffered from uncertainties due to thermal drift and drift in laser power over the several minutes it took to perform each scan. The experiment was ultimately limited thus by the low repetition rate of the OPO laser. It is anticipated that a future follow up study or a fully operational sensor would make use of a high repetition rate diode laser operating at 1 kHz or more which would reduce the time required to make 2500 readings from several minutes to a matter of a few seconds or less.

It should be noted that the maximum repetition rate for a laser will be governed by the decay time as the fluorescence should be allowed to decay almost completely before being re-excited. If this limit is set to 3τ, or about 300 μs in this example, then the maximum repetition rate of the laser would be approximately 3 kHz thus one scan would take place in less than one second.

7.5.3. 635 nm

The emission recorded at 635 nm exhibited a two-component decay, seen in Figure 7.5.10, with the fast component having a lifetime of 13.5 μs while the slow decay was measured at 130 μs at room temperature. As expected from Figure 7.5.5 the 618 nm curve is obviously still present and detectable at 635 nm, especially taking into account the relatively broad 7 nm resolution of the spectrometer.

The slow component of the decay recorded some degree of change as the temperature was elevated between 22 °C and 55 °C with the lifetime dropping on average at a rate of 1.2 μs/°C as shown in Figure 7.5.11.

The fast component of the decay, shown in Figure 7.5.12 did not respond significantly with temperature over the range tested.

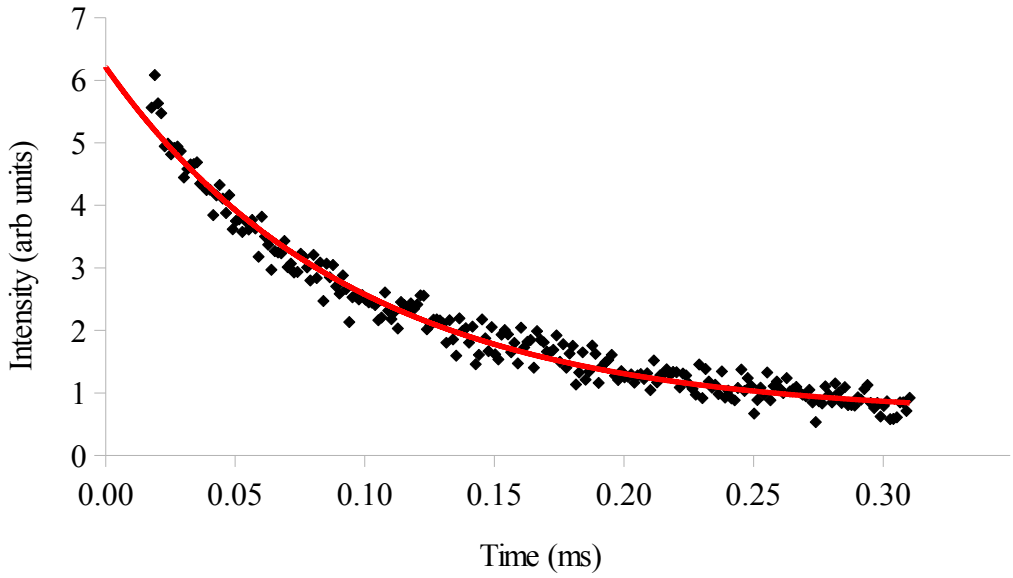

Figure 7.5.8: The decay of the TPF emission recorded at 618 nm at 22.6 °C. Only a single component was recorded and has a lifetime measured at 98.7 µs at this temperature.

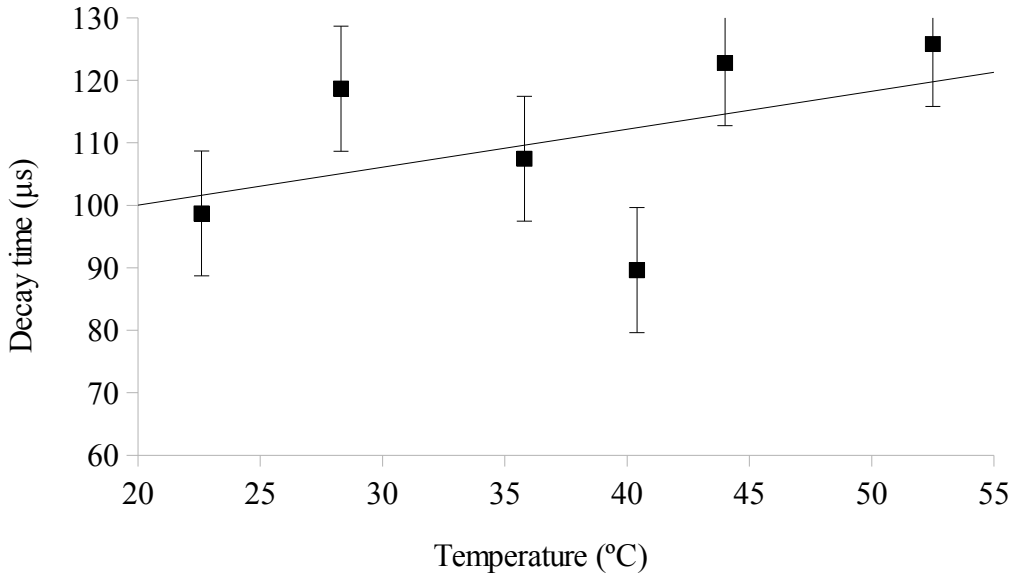

Figure 7.5.9: The change in lifetime at 618 nm with temperature. Some rise in decay lifetime was noted between the temperature range of 22 °C and 55 °C. The average rate of increase was approximately +0.6 µs/°C.

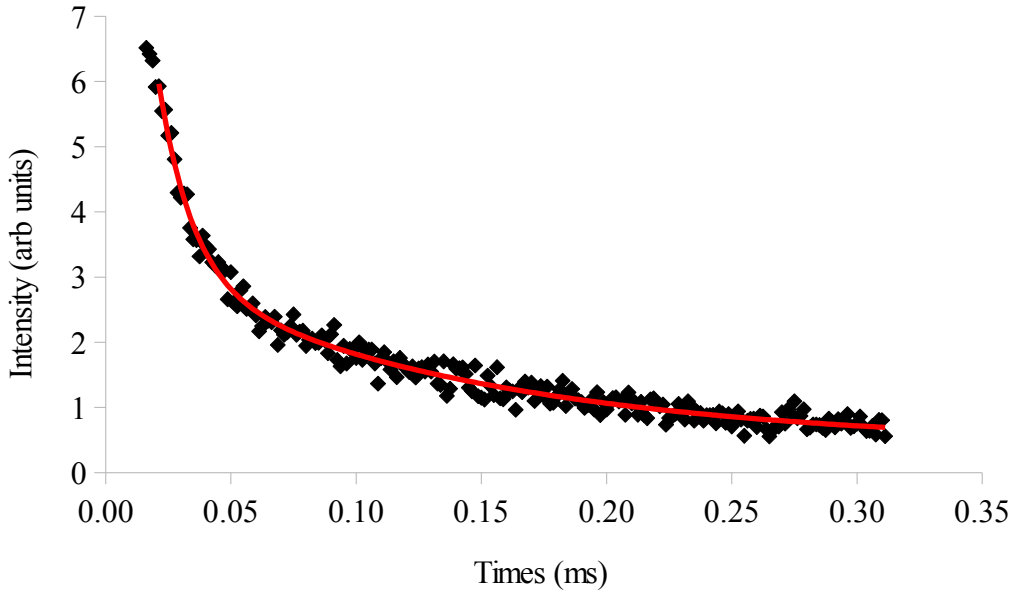

Figure 7.5.10: The room temperature decay of the emission at 635 nm. The fast decay had a lifetime of 13.5 µs while the slow decay was measured at 130 µs

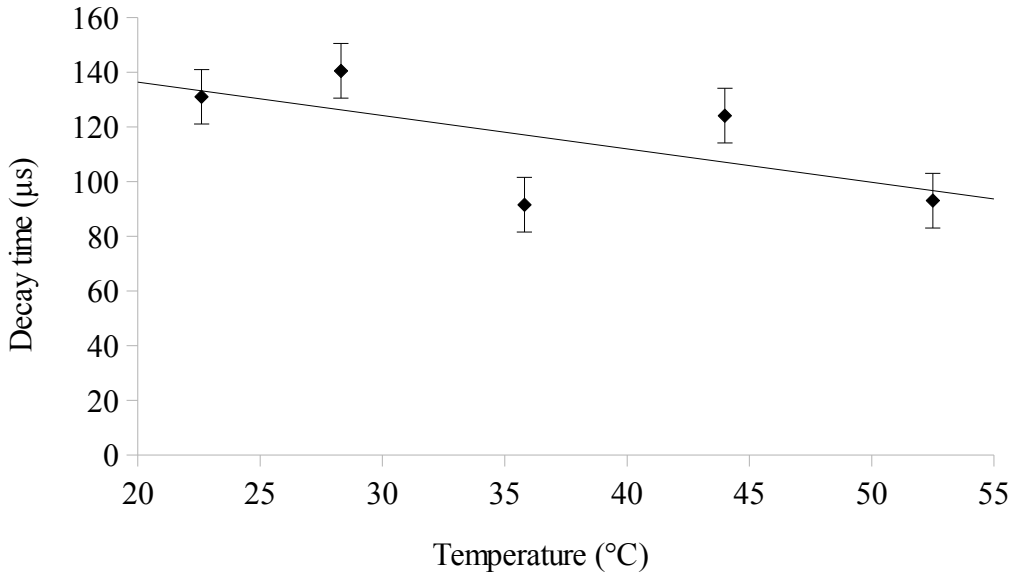

Figure 7.5.11: The change in the slow decay lifetime of the 635 nm emission with temperature. An average change in lifetime with temperature was measured at -1.2 µs/°C.

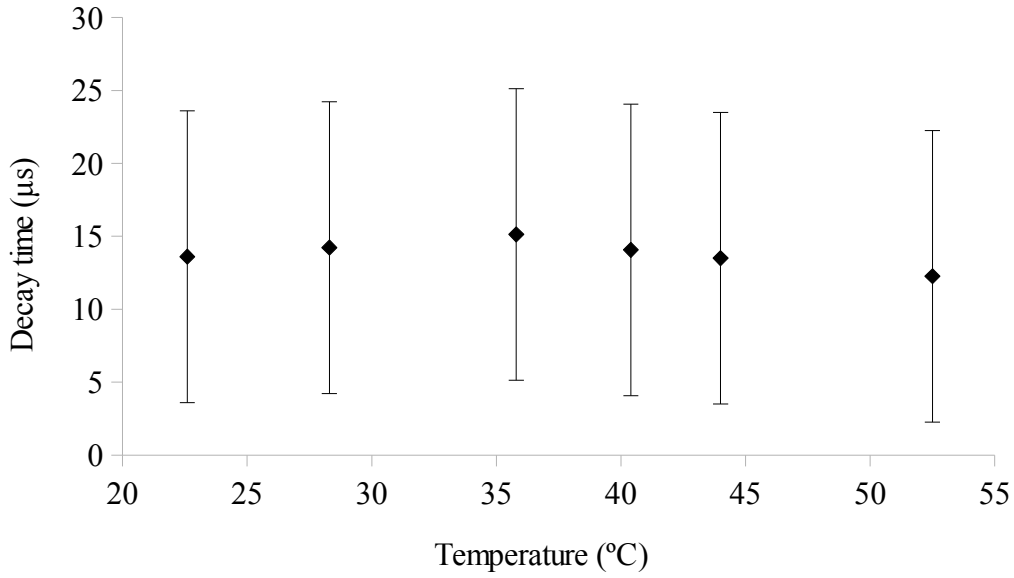

Figure 7.5.12: The change in the fast decay lifetime of the 635 nm emission with temperature.

7.5.4. 645 nm

This wavelength was chosen for testing as it lay well away from the fluorescence generated by the 618nm curve and should only contain the component generated by the 635nm curve.

Indeed Figure 7.5.13 shows that the ratio of the peak intensities of the fast and slow components has changed such that the fast component is much more dominant and the slow component only barely detectable. This strongly suggests that the fast component measured at 635nm and 645nm is the result of the $^3P_0 \rightarrow {}^3F_2$ transition and that the slow component measured throughout the range is due to the $^3P_0 \rightarrow {}^3H_6$ transition.

The slow component was too weak to reliably record the decay lifetime and the change in the fast component with temperature, shown in Figure 7.5.14. The change in the lifetime with temperature was similar to the measurements taken at 635nm showing an average lifetime of approximately 16 μs.

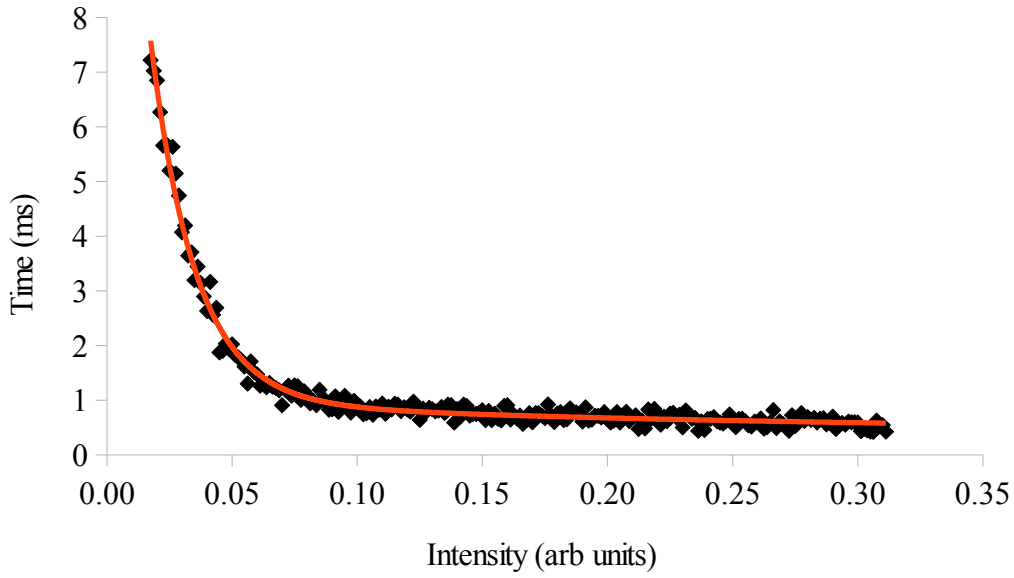

Figure 7.5.13: The room temperature decay of emission recorded at 645nm. Note that the relative intensities of the fast decay and slow decays have shifted compared to the 635nm emission.

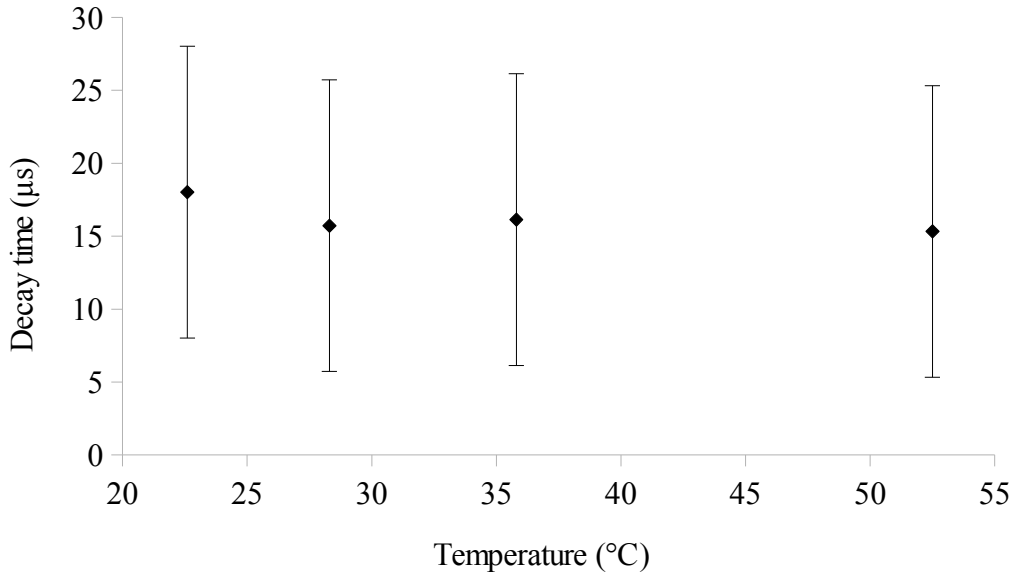

Figure 7.5.14: The change in decay lifetime of the fast component at 645nm.

7.5.5. Conclusions

The decay lifetime characteristics of the Pr doped fibre have been measured for the first time under two-photon excitation and the possibility of extracting temperature related information from the deconvolution of the transition lines which make up that emission band has been demonstrated. Some possible discrepancy was found in the temperature dependence of the slow component of the decays measured due to emission at 618 nm and 635 nm as it was thought that this slow component originated from, therefore should be similar to, the fluorescence recorded at 618 nm. Instead a positive trend with elevating temperature was found at 618 nm while a negative trend was found at 635 nm.

It may be that these apparent changes with temperature, which are somewhat in excess of the degree of change noted by Koziol et al[126] are an artefact of the low number of measurements taken at each temperature due to the comparatively long time required to measure these low two-photon fluorescence signals.

Alternatively it may be that the results presented here are a more accurate representation of the behaviour of the fibre with the rise in decay lifetime with elevating temperature at 618 nm and the drop in the same at 635 nm being averaged out in Koziol's data as that experiment employed a bandpass filter with an acceptance bandwidth covering much of the 620 nm emission band.

Nevertheless, these preliminary results show promise for the use of praseodymium in doped silica fibres for the purposes of temperature monitoring.

The next section will examine the temporal evolution of the decay on the nanosecond scale with the purpose of attempting to determine if any component of the two-photon fluorescence was being generated at the crossing point of the two excitation pulses.

7.6. Fibre emission profiles: confirming simulations and isolating ΔP

In this chapter so far the generation of TPF has been demonstrated within the Pr doped fibre exhibits sufficient signal strength to be used to analyse for the purposes of temperature sensing have been detected. However, due to the degenerate method of excitation TPF is generated at all points within the fibre and the entire length of the fibre was immersed within the heated bath so it was not possible to isolate the signal generated only by ΔP, the crossing point of the two laser pulses.

The relatively intense TPF signals were however strong enough to operate the instrumentation at very low internal impedances which allowed the temporal resolution required to examine the change in signal intensity on a scale of 10's of nanoseconds. This allowed the possibility to attempt to search for ΔP directly by comparing the signal generated by P_A and P_B separately to the sum of these signals generated by P_A and P_B simultaneously.

7.6.1. Simulations

The simulations in Chapter 3 outlined the predicted signal profiles which would be recorded for a distributed fibre sensor consisting of a loop of fibre coupled to a laser at each aperture and a single detector spliced into the fibre at one end. The design used in this chapter however effectively consists of the detector spliced into both apertures of the fibre, shown in Figure 7.2.1 on page 151, thus the model must be adjusted to reflect this.

In this modified model, shown in Figure 7.6.1 and Figure 7.6.2, the laser pulses which enter the fibre apertures are assumed to have identical powers. P_A is the fraction of total emission which is guided counter to the laser propagation direction therefore starts to be detected as soon as the laser pulses enter the fibre (neglecting the time of flight between the fibre aperture and the detector). P_B is the fraction of total emission which is guided in the co-propagating direction with respect to laser pulses. That portion of the emission must travel though the fibre thus a 50 ns delay is introduced before reaching the detector.

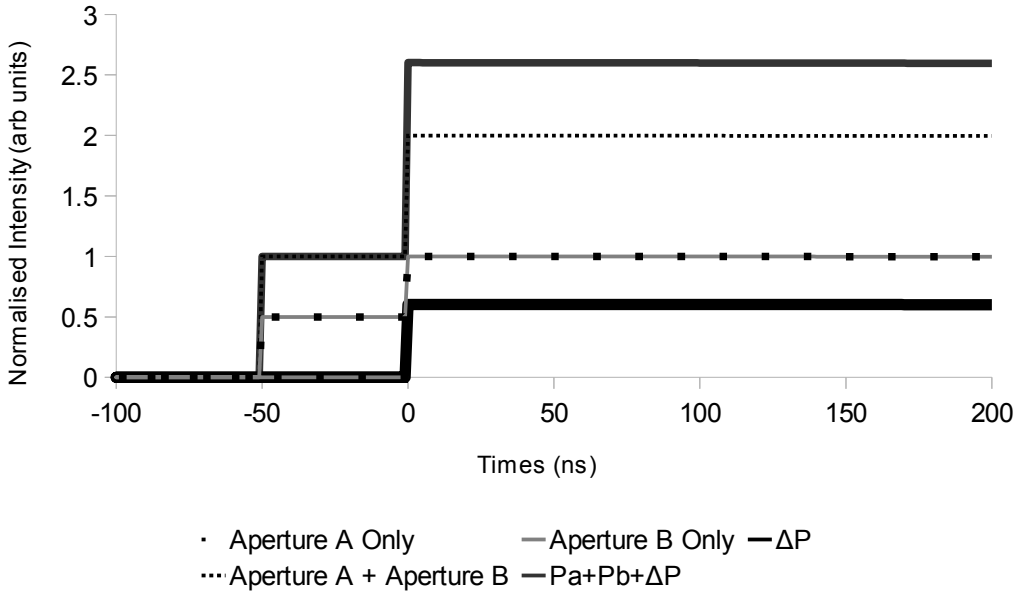

Figure 7.6.1: The simulated emission profile for the 10 m fibre on the nanosecond scale. The time offset T is set to 0 so that the overlap occurs in the middle of the fibre loop (transit time 50 ns). Initial detection begins at t -50 ns when the fluorescence travelling counter to the laser pulses enters the detector. The fluorescence guided in the co-propagating directions travels through the entire length of the fibre before being detected beginning at t +0 ns. ΔP contributes an additional 1/3 over and above the sum of the background emission power.

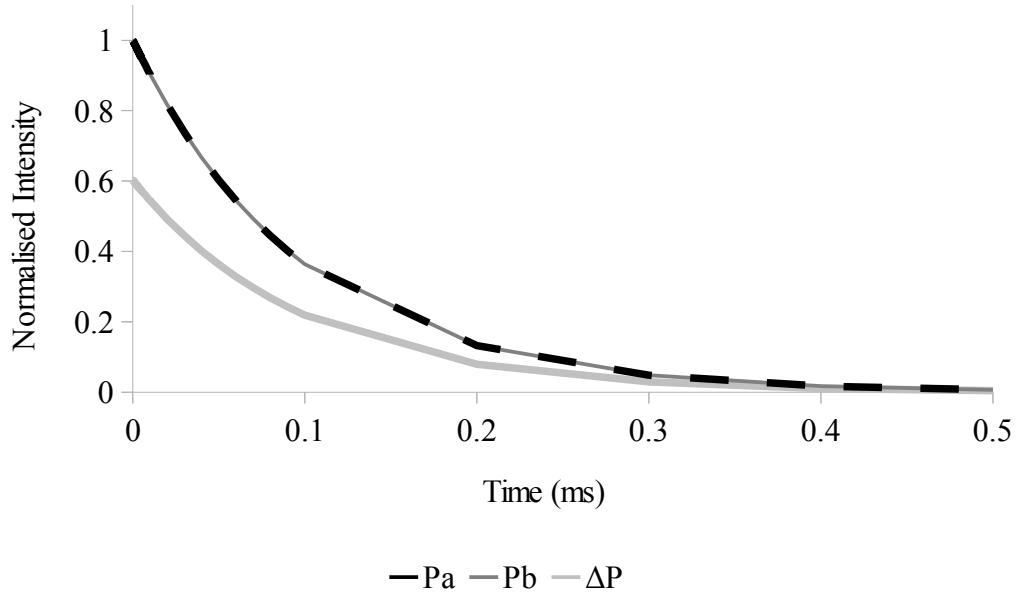

Figure 7.6.2: The simulated emission profile for the 10 m fibre monitoring at 618 nm at room temperature (τ = 98.7 μs). For pulse durations of 10 ns the overlap region has a FWHM of 2.66 m. The total ΔP power from the overlap region is 2/3 that generated by either P_A or P_B over the full 10 m length.

7.6.2. Experimental results.

The effect of ΔP was investigated by inserting a 700 nm short-pass filter into the beam path such that the 935 nm laser light was blocked but that co-propagating 618 nm fluorescence was still transmitted and detectable. By blocking aperture A, taking a reading then blocking aperture B and taking another reading the two could be summed to generate a profile similar to $P_A + P_B$ in Figure 7.6.1. This could be compared to a scan taking without the filter which should reflect the sum of $P_A + P_B + \Delta P$. In the case where both apertures were opened a 400 nm long-pass filter was inserted which allowed both the fluorescence and laser light through but has a similar reflection profile to the 700 nm short-pass thus compensates for any effect that this reflection might have.

Figure 7.6.3 shows the emission profile of the fibre which starts with the detection of scattered light from the laser pulse at -50 ns. From -50 ns to 0 ns the counter-propagating fluorescence light was detected at a low but significant level above the dark current baseline level. At 0 ns a second laser pulse is detected from the laser light travelling through the 10 m fibre. As this second pulse enters into the spectrometer it introduced significant electrical ringing which obscures the fluorescence signal until +25 ns. After this point the co-propagating fluorescence becomes detectable.

The detected co-propagating signal for the case where the B aperture was exposed was lower than that when the A aperture was exposed despite the excitation laser power in each being comparable (and in fact slightly higher in the B case) at 2.3 mJ per pulse and 1.7 mJ per pulse respectively. It was thought that the cause of this was due to the beam splitter used to direct the fluorescence light into the spectrometer. Light co-propagated from A aperture excitation (i.e. exiting from aperture B) had a straight path to the spectrometer while B aperture light had to be reflected by 90 degrees. The beam-splitter was rated as a 50/50 splitter but was optimised for the infra-red region around the laser wavelengths and its reflectivity in the visible region shifted so that only 1/3 of the light emitted from the A aperture was reflected which accounts for the imbalance observed.

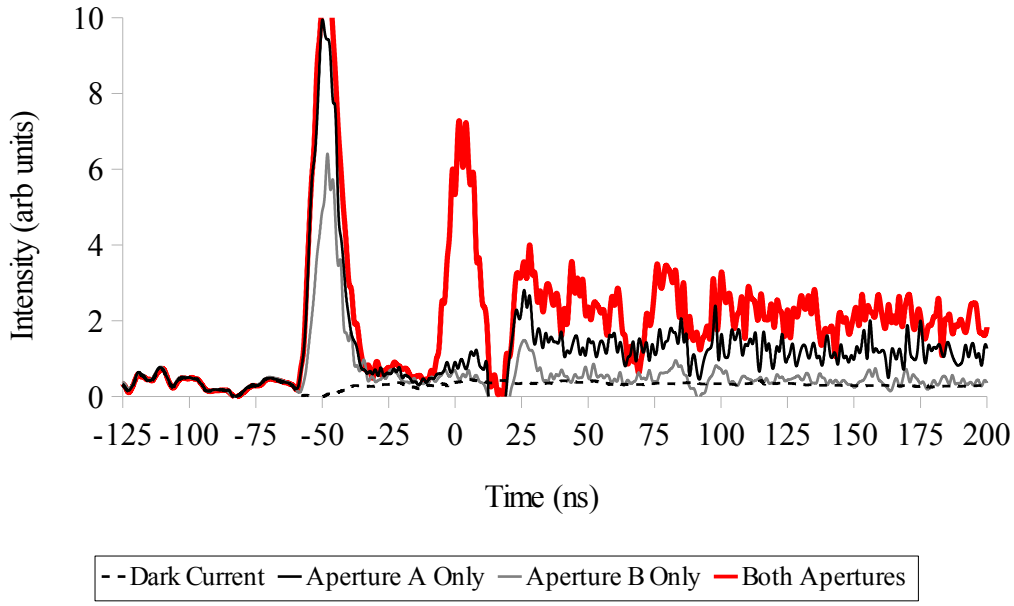

Figure 7.6.3: The first signal detection occurs -50 ns and is marked by scattered laser light entering the spectrometer. The counter-propagating fluorescence is visible in the region up to 0 ns when the laser pulse completes its transit of the fibre. After the electrical ringing had subsided sufficiently the sum of the counter- and co-propagating signals are visible from 25 ns.

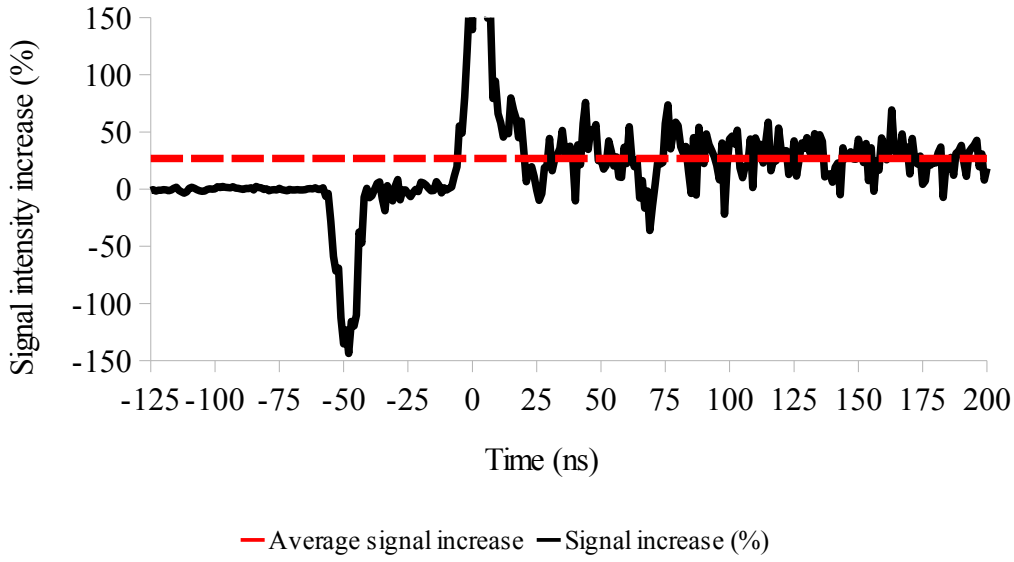

Figure 7.6.4: The additional signal detected when both apertures are open in excess of the background produced by the sum of the individual apertures. No additional signal is found in the counter-propagating region but an increase of 27 % is found in the subsequent total signal region. Only slightly lower than the predicted 33 %.

The total emitted power ($P_A + P_B + \Delta P$) was recorded and the sum of the traces from the signal aperture excitations ($P_A + P_B$) were subtracted from it to give the data shown in Figure 7.6.4.

This shows a clear extra component of the fluorescence signal in the co-propagating light region which is not present in the counter-propagating light region indicating that a signal from the overlap region has been generated. The magnitude of this signal was found to be approximately 27% over and above that generated by the sum of the two background components which is only slightly below the increase of 33% predicted by Figure 3.6.4. The slight under performance was probably due to the same factor which caused a loss of signal from the B aperture readings.

It can be concluded from this that the degenerate two-photon excitation of the Pr doped fibre by cross-propagating pulses has generated additional two-photon fluorescence within the region of overlap of those pulses and that the signal can and has been isolated from the background signals generated by the single-beam degenerate two-photon absorption of the individual pulses.

While this experiment used a relatively short length of fibre and comparatively long laser pulses which meant that the overlap region composed a significant fraction of the overall fibre length these same principles of scanning the background signals and subtracting them from the whole should be feasible in larger models. Additionally, deconvolution factors may be employed to isolate signals based on their decay lifetimes (in the case of elevated temperature measurements) and possibly by time of flight measurements in order better isolate the required ΔP signals.

Obviously however, a far better solution would be to eliminate the background signals entirely and one proposal to do this in this type of sensor is to employ non-degenerate excitation which only produces fluorescence in the overlap region as illustrated in Figure 3.6.5.

7.7. Attempts towards non-degenerated excitation

7.7.1. Experimental arrangement

The experiment outlined in the previous section was modified in order to attempt a non-degenerating excitation of the Pr fibre. To do this the excitation sources had to be considered.

In order to calculate the complementary wavelengths for a non-degenerate excitation the two laser wavelengths are compared to the equivalent wavelength required for the single-photon excitation of the same transition such that:

$$\frac{1}{\lambda'_{SPF}} = \frac{1}{\lambda''_{A}} + \frac{1}{\lambda''_{B}} \tag{66}$$

which, for the $^3H_4 \rightarrow {}^1I_6$ transition in Pr^{3+} gives the curve shown in Figure 7.7.1.

It was decided that the simplest solution for selecting the two laser wavelengths for the excitation was to use the 1064 nm Nd:YAG laser used in Chapter 5, a choice made especially viable due to the lack of absorption at the $^1G_4$ level as shown in Figure 7.4.1, and to select a complementary wavelength suitable to match. This implied that the complimentary wavelength for peak excitation would be 833 nm.

However an exactly matching laser may not be easy to source or that a slightly mismatched laser may be more powerful than one at the peak wavelength. Therefore it was possible to convert the excitation spectrum from Figure 7.4.1 using the same principal to estimate the excitation spectrum for non-degenerate wavelengths assuming that one laser is fixed. In this case, shown in Figure 7.7.2, gave an expected excitation spectrum which not only shows the peak at 833 nm but also reveals that the excitation band is relatively broad with a Full Width, Half Maximum of over 70 nm which suggested that, in this case at least, an exact complementary wavelength match is not a necessary condition for non-degenerate two photon excitation.

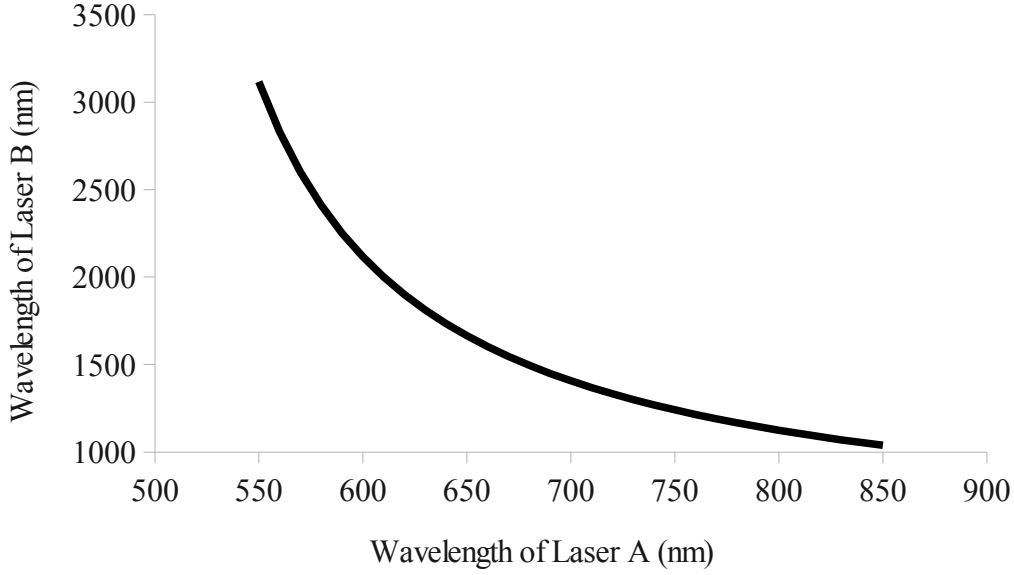

Figure 7.7.1: The complementary wavelength pairs for the non-degenerate two-photon excitation of the $^1I_6$ level of the Pr doped fibre at the equivalent of a 935 nm degenerate excitation. The complementary wavelength if one laser is fixed at 1064 nm is 833 nm.

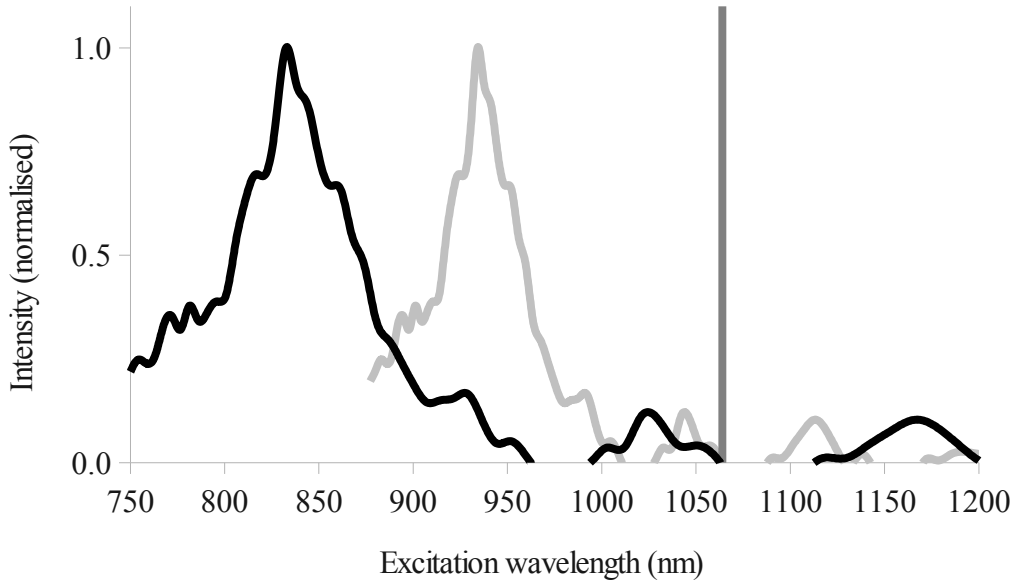

Figure 7.7.2: (grey curve) The degenerate two-photon excitation spectrum for the Pr doped fibre. If laser A is fixed at 1064 nm (vertical line) the expected excitation intensity for a given wavelength for laser B is given by the black spectrum and shows both the maximum intensity at 833 nm and the broad matching range with a FWHM of more than 70 nm.

The laser selected for the experiment was a Hamamatsu L9277-42 cw diode laser with a rated maximum output of 1 W at 830 nm. The beam was analysed by projecting it onto a white paper screen and taking a photograph using a CCD camera. As with the previous beam analyses, the image was converted to a 256-bit grey scale to produce the 3D plot in Figure 7.7.3 and the beam profiles of Figure 7.7.4. The beam was found to be highly asymmetrical, as is common with this type of laser diode, with the vertical axes being so highly divergent that it ran off the top of the screen onto the black matt beam stopper behind it. The different reflective properties of these are the cause of the apparent asymmetry in the vertical axis profile. The overall shape of the profile seemed to be generally Gaussian although a periodic horizontal striping effect was noticeable. The effect of both of these characteristics on the investigation was limited by collecting and collimating the beam by mounting a lens in front of the diode before guiding it into the fibre.

The distance between the screen and the diode was measured at 10.5 cm and the half-width, half maximum for the vertical and horizontal axes were found to be 4.5 cm and 0.4 cm respectively. This allowed an estimation of the divergence of the laser diode to be 0.46 radian (26^o) in the vertical dimension and 0.036 radian (2^o) in the horizontal dimension. This is in accordance with the manufacturer's specifications of 24^o and 8^o respectively.

The output intensity of the diode was found to rise logarithmically with input power up to the maximum tested driving current of 1000 mA though it did not drop to zero when the power supply was set to zero output. This was probably simply due to a mis-calibration of the power supply. The peak wavelength of the diode output was found to shift as the input power was increased with an average rate of +9.29 pm / mW and the rated wavelength of 830 nm was found when the device was supplied with 700 mW as shown in Figure 7.7.5.

The experimental arrangement from the degenerate excitation experiments was modified to accommodate the new lasers. The Q-switched Nd:YAG laser replaced the OPO laser, was aligned in the same manner and was coupled into the A aperture of the fibre. The diode was aligned in front of and coupled into the B aperture as shown in Figure 7.7.6.

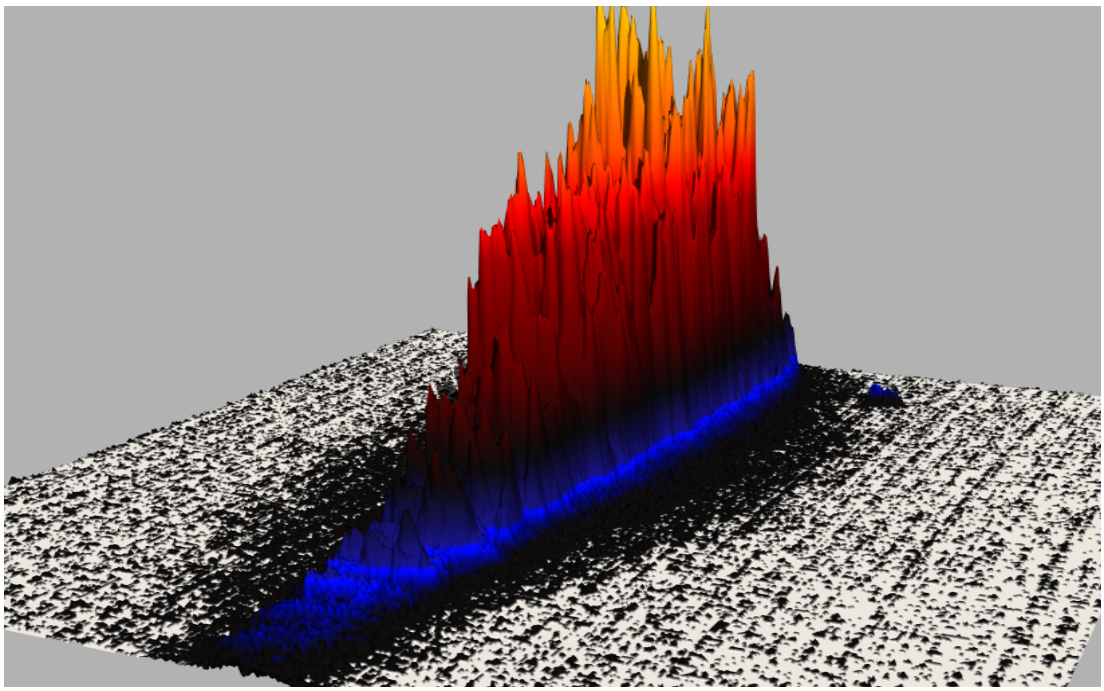

Figure 7.7.3: The intensity map for the projected beam profile for the 830nm diode laser. The profile is highly asymmetrical although both the vertical and horizontal axes have a Gaussian intensity profile.

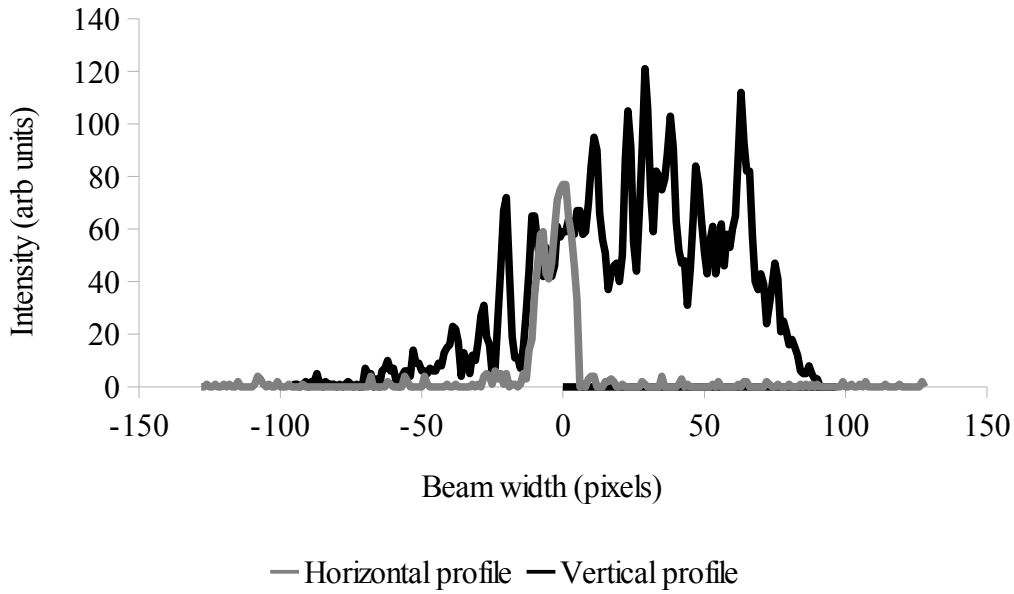

Figure 7.7.4: Intensity profiles for the diode laser taken across the horizontal axis (grey line) and the vertical axis (black line). The apparent asymmetry on the vertical axis was due in part to the beam running off the top edge of the screen that it was projected onto to take the image. On this scale 1 horizontal pixel represents 0.5mm.

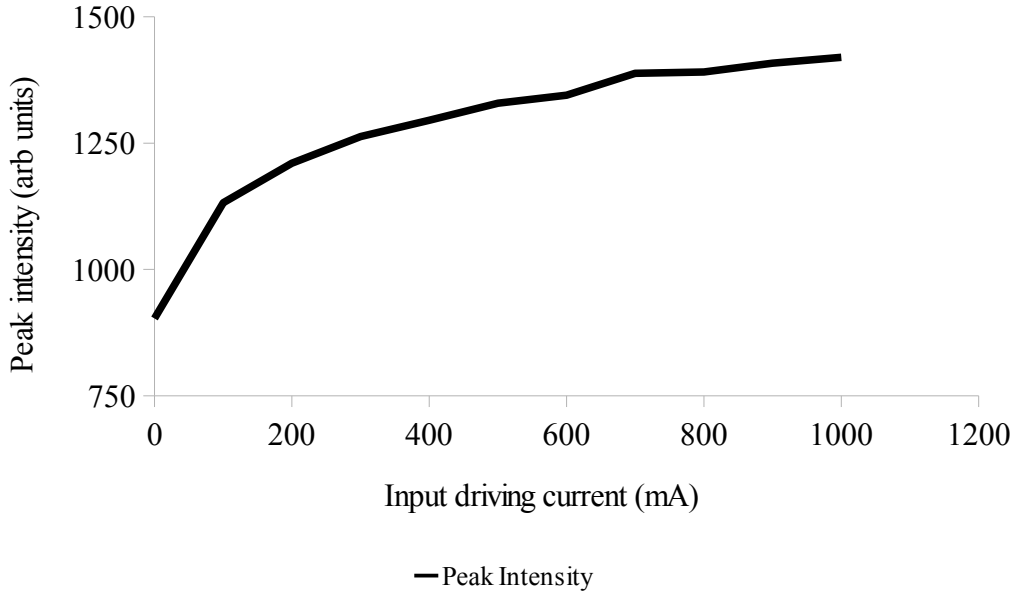

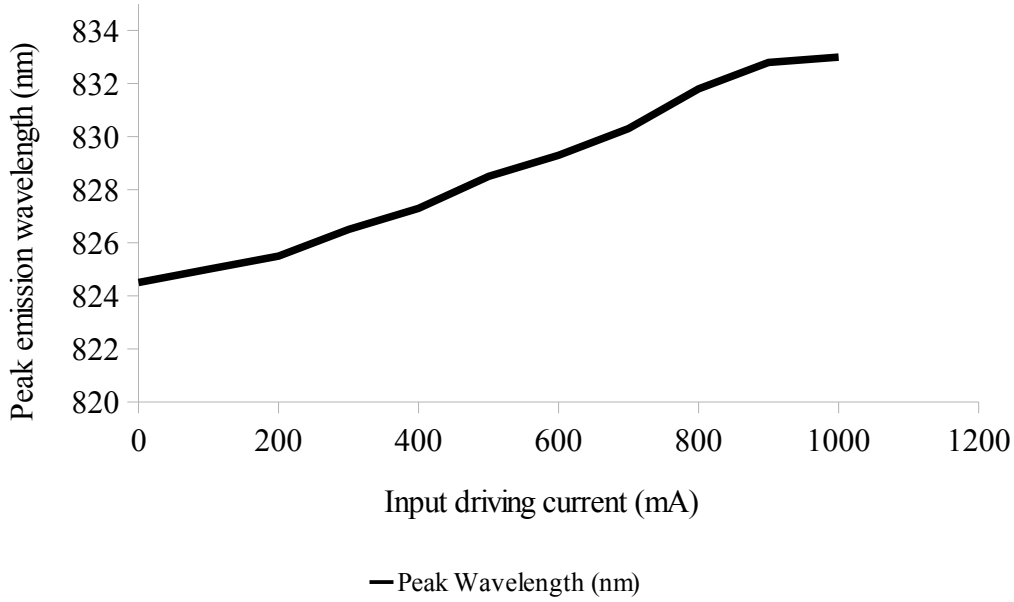

Figure 7.7.5: (top) The peak emission intensity of the diode laser. The non-zero output when the power supply was set to zero was the result of instrumental mis-calibration. (bottom) The shift in peak emission wavelength of the diode. The broad excitation band shown in Figure 7.7.2 indicates that this would have no significant effect.

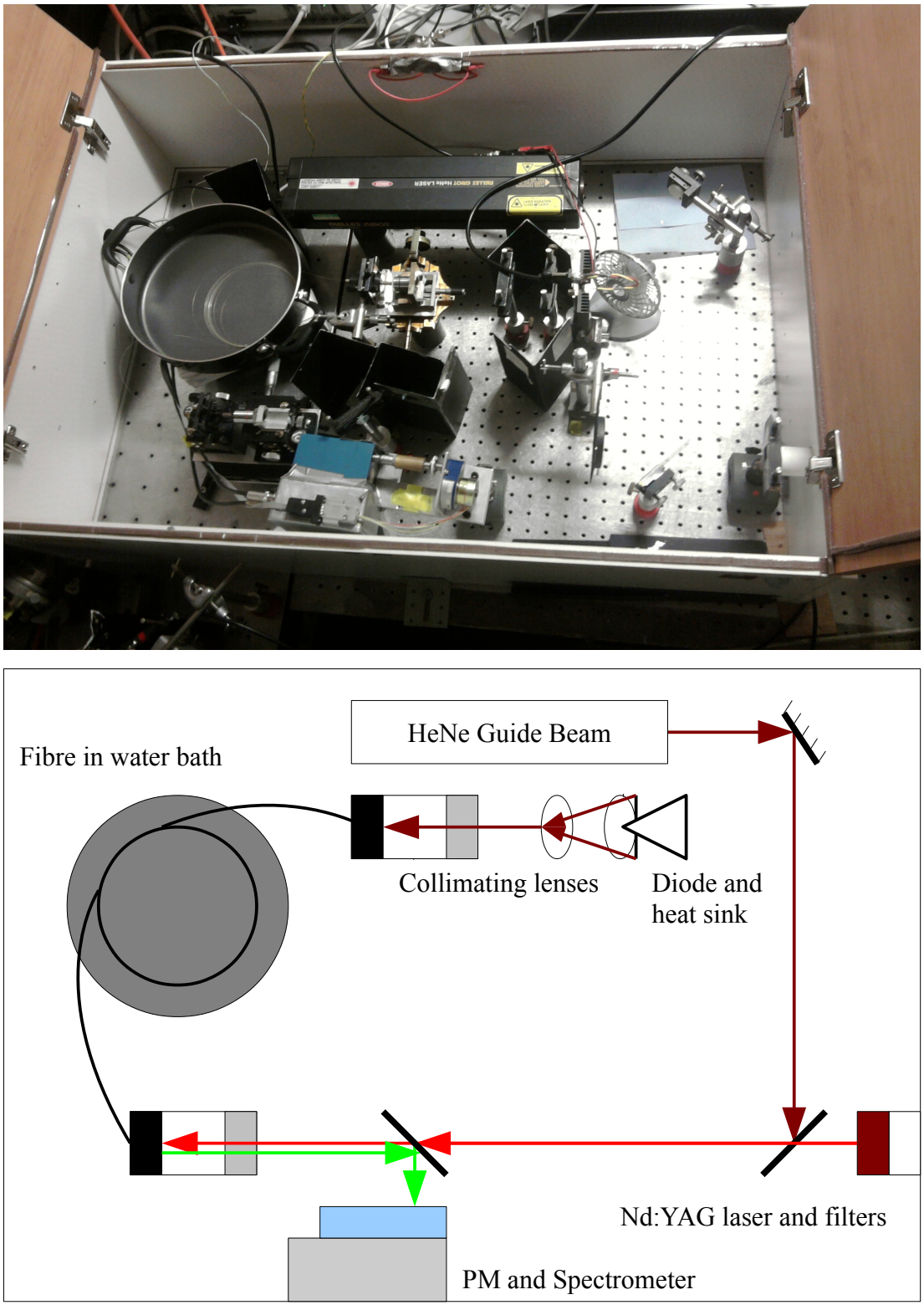

Figure 7.7.6: The experimental arrangement for the non-degenerate excitation experiment. The diode was coupled into the B aperture of the fibre and emission was detected via the reflected light from the beam splitter.

7.7.2. Results

The low power of the diode (compared to the Nd:YAG) and the high divergence of the beam, which meant that efficient coupling of the laser into the fibre was difficult at best, would mean that any two-photon fluorescence would also be difficult to observe. It was also found that because a cw laser was used and it was always running during the course of the readings the lock-in amplifier could not act as a filter to reduce the noise generated when the diode was on. While some repeated scans and manual averaging helped to a degree, as shown in Figure 7.7.7, it was still far from ideal.

As noted in the previous chapter the fluorescence travelling from aperture A seemed to show a reduced signal compared to fluorescence from aperture B due to reduced reflection from the beam-splitter so the experimental arrangement (Figure 7.7.8) was adjusted so that the diode beam was reflected into the fibre and the emission allowed to travel both directions to the spectrometer. The Nd:YAG light was blocked from entering aperture B using a 700nm short-pass filter.

Even in this instance however no evidence of TPF could be demonstrated. It was concluded that the low average power of the diode combined with the inefficient coupling of light into the fibre meant that it was likely that no more than an average power of 10 mW of 830 nm was present in the fibre (assuming a 1% coupling into the fibre which is probably optimistic) and an average energy per pulse from the Nd:YAG laser of 3 mW (again assuming a 1% coupling efficiency) and applying these values to equation (53) which results in only 8×10^{6} fluorescent photons reaching the detector with an average detectable fluorescence power of approximately 36 pW when the Nd:YAG laser was operating at its maximum repetition rate of 15 Hz. This stands in contrast to the approximately 10^{11} photons detectable during the degenerate excitation.

As of the time of writing a follow up experiment was devised replacing the cw 830 nm with a pulsed diode but lack of time prevented this experiment from being performed. Any results forthcoming from this experiment as part of future studies shall be reported as and when they become available.

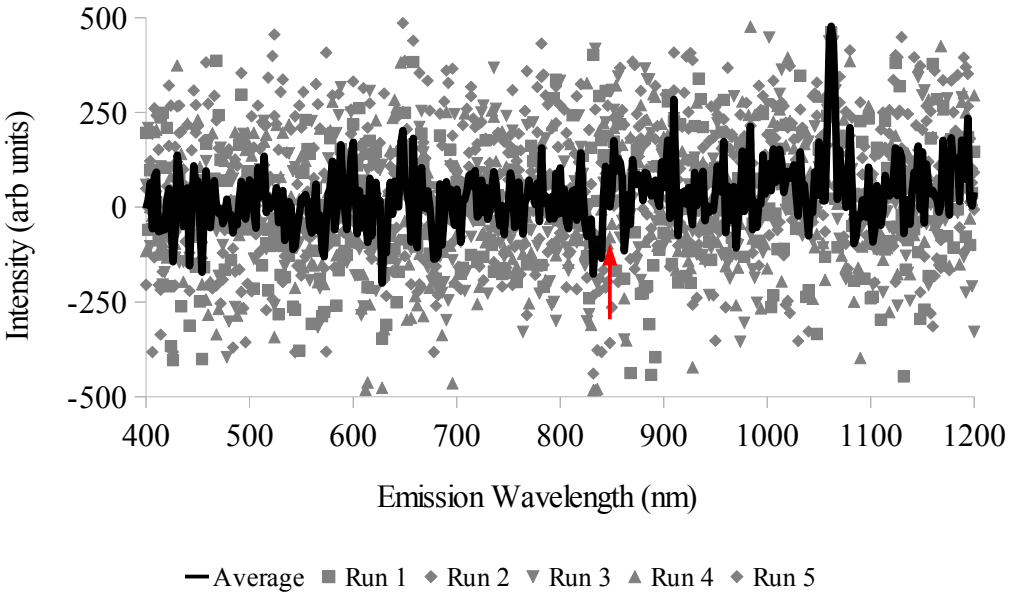

Figure 7.7.7: A scan of the emission spectrum of the fibre excited by both the Nd:YAG and diode lasers. After averaging to reduce the noise caused by the signal the only statistically significant and repeatable features were the two laser spikes at 1064 nm and 830 nm (the ringing feature marked by the arrow)

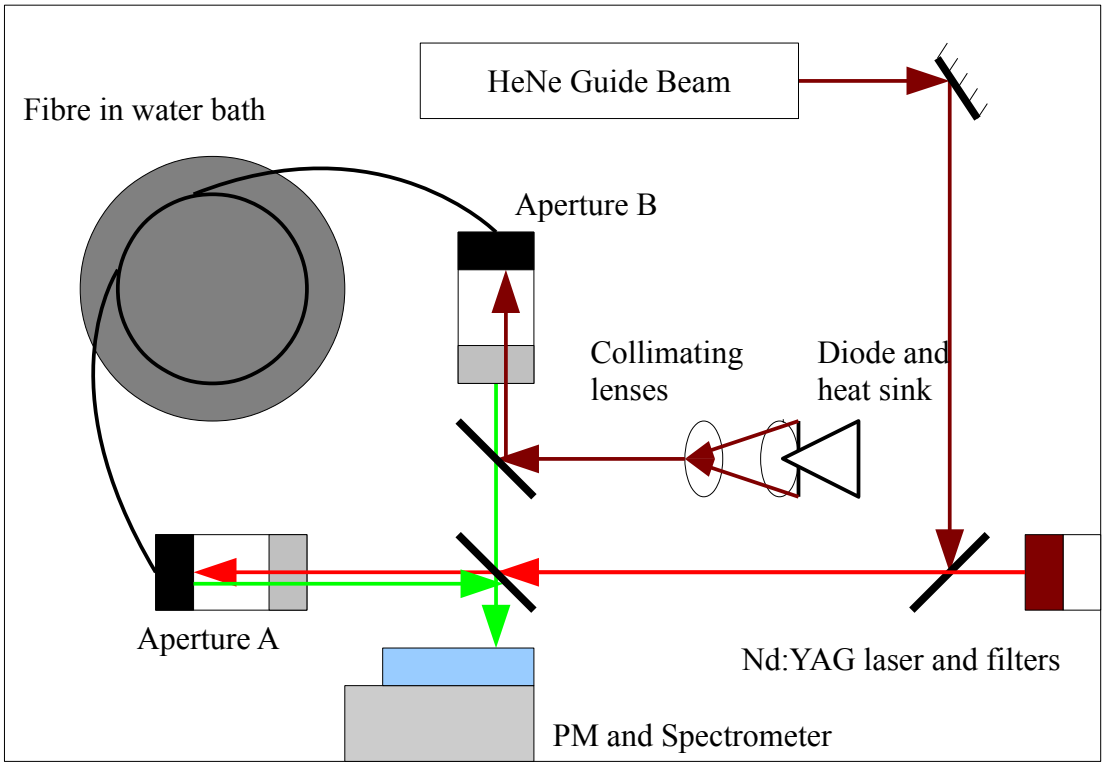

Figure 7.7.8: The modified experimental arrangement for the non-degenerate excitation attempt. Reflected Nd:YAG light was blocked from entering aperture B with a 700 nm short-pass filter.

7.8. Conclusions

This chapter has demonstrated the generation of both single- and two-photon excited fluorescence in a praseodymium doped silica glass fibre. While distinct from the emission spectrum of the Pr:ZBLAN sample from chapter 6 the spectrum was readily identifiable and several emission lines suitable for distributed fibre sensing (i.e. several strongly emitting 4-level transitions) were extracted.

Analysis of such fluorescence shows that it is possible to sense temperature by both analysis of the fluorescent lifetime and by the analysis of the intensity ratio of coupled emission transitions. It has also been shown that an increase in the intensity of the detected fluorescence due to the increased photon flux at the crossing point of the excitation pulses occurs in line with the theoretical predictions.

The temporal profile of the TPF emission revealed that an increase in the intensity of the detected fluorescence due to the increased photon flux at the crossing point of the excitation pulses occurs in line with the theoretical predictions. This prototype therefore is a demonstration of a distributed fluorescence based optical fibre sensor with a spatial resolution of approximately 2 m and a thermal resolution of approximately 10 K. Furthermore it has been shown that an improvement on this performance is a function solely of the performance of the exciting lasers and that spatial resolution in particularly should improved dramatically by the used of pulsed diode lasers with a pulse width of around 100 ps (yielding a theoretical spatial resolution of 2 cm).

The demonstration of non-degenerate TPF would have been a particularly major milestone in this investigation as the elimination of the background fluorescent signals would both significantly ease the detection of the overlap fluorescence but would also completely eliminate the issues surrounding the signal-to-background ratio which may limit the maximum spatial resolution future sensor designs. The null-result of this experiment however is likely to be merely a factor of both the low average power of the cw diode laser used and the poor coupling efficiency into the fibre. A follow-up experiment using a pulse diode arrangement and more refined coupling optics is likely to see greater success.

The non-degenerate excitation experiment is not completely negative however. The discovery that the non-degenerate excitation spectrum is relatively broad is potentially important as it means that the laser wavelengths required do not need to be exactly complementary in order to achieve efficient excitation. This should serve to simplify a future sensor design as a sub-optimal but significantly less expensive or more powerful diode laser may used to greater overall effect.

8. Conclusions and suggestions for future study

8.1. Conclusions

A novel class of distributed optical fibre sensor based on two-photon excited fluorescence has been developed from the foundational theoretical framework through the testing for various candidate dopants for their suitability in a potential prototype sensor. The two-photon spectroscopic properties of these candidate dopants was explored and in particular the two-photon absorption cross-section was measured using it novel method which provides excellent accuracy and a sensitivity capable of measuring cross-sections as low as 10^{-5} GM.

Below is a summary of the main findings from each of the chapters of this thesis and a short discussion of possible avenues for future research.

8.1.1. Theory

The theoretical framework for the sensor has found that, unlike many other non-linear optical phenomena, the sensitivity of the active region of the sensor is not dependent on pulse duration or pulse profile therefore ultrashort pulsed systems are not a necessary requirement for successful operation. Similarly the effects of dispersion within the fibre which will broaden the excitation pulses and reduce the peak excitation power will have no effect on the total fluorescence produced in the overlap region. The use of ultrashort pulses will however govern the spatial resolution of the sensor which is dependent primarily on the excitation pulse duration thus is capable to theoretical resolutions of around 2 cm if relatively inexpensive 100 ps diode laser systems are employed.

8.1.2. The two-photon absorption cross-section

A novel method of measuring the absolute two-photon absorption cross-section of a fluorescent material. This method compares the peak intensity of the fluorescence from an emission line in the material as a factor of the energies of the

excitation pulses as the material undergoes both single- and two-photon absorption. This method was tested using a dilute sample of rhodamine 6G and provided a result of 4.4 GM when excited by 532 nm for the single-photon excitation and 1064 nm for the two-photon excitation.

8.1.3. Ruby

The two photon-absorption cross-section of ruby has been measured for the first time and was found to be 4.53×10^{-4} GM along the o-axis and 2.73×10^{-4} GM along the e-axis when degenerately excited by 1064 nm light. This data was used to measure the two-photon absorption spectrum in the region from 800 nm to 1300 nm. This spectrum was found to be analogous to the single-photon absorption spectrum for the same energy transitions.

The fluorescence decay lifetime was measured at room temperature and at elevated temperatures of up to 600 ºC and was found to be identical to the typical response for the same energy transitions under both single- and two-photon excitation. The temperature response of a particular emission transition is independent of the excitation pathway.

The implications of using ruby as a medium for a distributed optical fibre sensor and by extension the implications of using single crystal fibres for use in extreme environments was discussed.

8.1.4. Rare-earth metals

A number of rare-earth metals doped in fluoride glasses were tested using the methods developed in previous chapters and two-photon excited fluorescence was successfully demonstrated in praseodymium, gadolinium, terbium, dysprosium, holmium and thulium. Absolute values of the two-photon excitation cross section was measured in several of these dopants and a change in the fluorescence lifetime with temperature was identified in praseodymium and terbium. Praseodymium was selected as a candidate dopant of choice for the construction of a functional optical fibre sensor.

8.1.5 Optical fibre sensing

The emission and excitation spectra of the praseodymium doped fibre under both single- and two-photon excitation. The excitation spectra were found to be similar to the spectra found in the fluoride glass host and while the emission spectra were found to be distinct from the fluoride glass they were found to be similar to previous single-photon emission spectra found in silica fibres.

A sensitivity to a change in temperature was found and successfully measured by both monitoring the change in fluorescence lifetime across several emission lines in a band centred around 600 nm and also by monitoring the change in the intensity of emission lines generated by the $^3P_0 \rightarrow {}^3H_6$ and $^3P_0 \rightarrow {}^3F_2$ transitions at 620 nm and 635 nm respectively. It was noted that by combining data from both of these methods it may be possible to construct a sensor which can independently measure both temperature and strain independently of one another without the use of a reference sensor to isolate either effect.

The temporal profile of the intensity of the emission as it emerged from the fibre was recorded and analysed such that it was possible to isolate the background TPF signals generated by the degenerate excitation from each of the laser pulses. The sum of these background signals was compared to the total detected emission and a signal was detected in excess of the sum of these two backgrounds. The intensity and temporal profile of this excess signal was consistent with the contribution expected due to two-photon fluorescence generated in the excitation pulse overlap region within the fibre. This result demonstrated that a fully distributed optical fibre temperature sensor based on praseodymium doped in a silica fibre is viable.

The next potential step forward for the distributed optical fibre sensor could be to construct a prototype suitable for operation in a live environment. Ideally such a sensor would involve the use to pulsed diode lasers operating in a non-degenerate excitation mode. These diodes would be constructed with a pig-tail optical fibre attached to their output aperture such that they could be permanently spliced into the active fibre loop. This should dramatically increase the coupling efficiency of the system leading to much greater fluorescence signal output. Similarly the photo detector would be designed such that it was fixed with a length of fibre and spliced

into the active loop to increase the light collection efficiency. Finally, the only engineering principle not tested within this investigation, namely the delay generator which will allow the sweeping of the sensing region to any point in the fibre, would be applied.

8.2. Suggestions for future study

A prototype model for a distributed optical fibre temperature sensor has been constructed and demonstrated and several avenues for future research have been considered.

Non-degenerate two-photon excitation was attempted but not conclusively demonstrated within the fibre. The successful demonstration of this would eliminate the self-generated background signals and greatly aid the detectability of the overlap signal especially in longer fibres.

The temperature range over which the fibre was monitored in this investigation was relatively small. It would be a logical extension to this investigation to test the fibre over a much broader range of temperatures to ascertain its upper and lower limits as a useful sensor.

The possibility of single-crystal fibres for use in extreme environments is a potentially interesting topic and while ruby has been shown to be sub-optimal as a sensor material due to the energy level structure of the chromium dopants it may be possible to doped rare-earth metals into the sapphire host instead potentially opening up an entire range of applications which require sensors to operate at temperatures in excess of several hundred ^{o}C.

Temperature and strain are not the only measurands to have been studied using fluorescence based techniques. Essentially any of the single-photon fluoresce based point sensors to have been developed to date could, in principle, be turned into a distributed fibre sensor using the two-photon excitation design developed here. For example, it may be possible to investigate a distributed magnetic field strength sensor based on the Zeeman effect.

Appendix I. Derivations of P_A, P_B, and ΔP for other common pulse profiles

The following are a list of derivations for the expressions listed in Table [Table 3.3.2] for each of the common pulse profiles.

Lorentzian

$$n(t)=\frac{n_o}{1+\left(\frac{t}{\Delta t}\right)^2} \tag{67}$$

and

$$\Delta t=\frac{t_p}{2} \tag{68}$$

Applying the standard integral $\int_{-\infty}^{\infty}\frac{a}{a^2+(bx)^2}=\frac{\pi}{b}$ gives

$$\int_{-\infty}^{\infty} n(t)dt=n_o\int_{-\infty}^{\infty}\frac{1}{1+\left(\frac{t}{\Delta t}\right)^2}dt=\pi\ n_o\Delta t=\frac{\pi}{2}n_o t_p \tag{69}$$

$$N=A\int_{-\infty}^{\infty} n(t)dt=A\pi\ n_o\Delta t=\frac{\pi}{2}A\,n_o t_p \tag{70}$$

therefore

$$n_O=\frac{N}{\pi\ A\Delta t}=\frac{2N}{\pi\ A t_p}=\frac{2KN}{A t_p} \tag{71}$$

$$\int_{-\infty}^{\infty} n(t)^2dt=n_o^2\int_{-\infty}^{\infty}\frac{1}{1+\left(\frac{t}{\Delta T}\right)^2}dt=\frac{\pi}{2}n_o^2\Delta t=\frac{\pi}{4}n_o^2 t_p=\frac{4\pi\ N^2 t_p}{4\pi^2A^2t_p^2}=\frac{N^2}{\pi\ A^2 t_p} \tag{72}$$

$$\int_{-\infty}^{\infty} n(t)^2dt=\frac{KN^2}{A^2t_p} \tag{73}$$

$$G(t') = \int_{-\infty}^{\infty} \frac{n_{oA}}{1+\left(\frac{t}{\Delta t}\right)^2} \cdot \frac{n_{oB}}{1+\left(\frac{(t+t')}{\Delta t}\right)^2} \tag{74}$$

$$= n_{oA} n_{oB} \int_{-\infty}^{\infty} \frac{1}{1+\left(\frac{t}{\Delta t}\right)^2} \cdot \frac{1}{1+\left(\frac{(t+t')}{\Delta t}\right)^2} \tag{75}$$

$$= n_{oA} n_{oB} 2\pi \frac{\Delta t^3}{(t'^2 + 4\Delta t^2)} \tag{76}$$

$$= 2\pi\ n_{oA} n_{oB} \frac{\Delta t}{\left(4+\left(\frac{t'}{\Delta t}\right)^2\right)} \tag{77}$$

$$G(t') = \frac{1}{2}\pi\ n_{oA} n_{oB} \frac{\Delta t}{\left[1+\left(\frac{t'}{2\Delta t}\right)^2\right]} \tag{78}$$

$$\int_{\infty}^{\infty} G(t')dt' = \frac{1}{2}\pi\ n_{oA} n_{oB} \Delta t \int_{-\infty}^{\infty} \frac{1}{\left[1+\left(\frac{t'}{2\Delta t}\right)^2\right]} dt' \tag{79}$$

By the standard integral $\int_{-\infty}^{\infty} \frac{a}{a^2+(bx)^2} = \frac{\pi}{b}$ gives

$$\int_{\infty}^{\infty} G(t')dt' = \pi^2 n_{oA} n_{oB} \Delta t^2 \tag{80}$$

Hyperbolic secant

$$n(t) = n_o \operatorname{sech}^2\left(\frac{t}{\Delta t}\right) \tag{81}$$

$$\Delta t = 1.7627\, t_p \tag{82}$$

$$\int_{\infty}^{\infty} n(t)\,dt = \int_{\infty}^{\infty} n_o \operatorname{sech}^2\left(\frac{t}{\Delta t}\right)dt = n_o \Delta t\left[\tanh\left(\frac{t}{\Delta t}\right)\right]_{-\infty}^{\infty} = 2\, n_o \Delta t \tag{83}$$

$$\int_{\infty}^{\infty} n(t)^2 dt = \frac{2}{3} n_o^2 \Delta t\left[\frac{\sinh\left(\frac{t}{\Delta t}\right)}{\cosh\left(\frac{t}{\Delta t}\right)^3} + \frac{2}{3}\tanh\left(\frac{t}{\Delta t}\right)\right] \tag{84}$$

Substitute $\sinh(x) = \tanh(x)\cdot\cosh(x)$ and note that for

$\lim\, t \to \infty : \sinh(\infty) = \infty;\ \cosh(\infty) = \infty;\ \tanh(\infty) = 1$

therefore

$$\int_{\infty}^{\infty} n^2(t)\,dt = \frac{4}{3} n_o^2 \Delta t \tag{85}$$

$$G(t') = n_{oA}\, n_{oB} \int_{-\infty}^{\infty} \operatorname{sech}^2\left(\frac{t}{\Delta t}\right)\operatorname{sech}^2\left(\frac{(t+t')}{\Delta t}\right)dt \tag{86}$$

$$\int_{-\infty}^{\infty} G(t')\,dt' = \frac{4}{3} n_{oA}\, n_{oB} \Delta t\left[\frac{3\left(\left(\frac{t'}{\Delta t}\right)\cosh(t'/\Delta t) - \sinh(t'/\Delta t)\right)}{\sinh^3(t'/\Delta t)}\right] \tag{87}$$

from Sala et al[9] and Diels et al [130]

Rectangular

$$n(t) = n_o \tag{88}$$

For $\sqrt{t^2} \leqslant \delta t$

$$n(t) = 0 \tag{89}$$

elsewhere.

$$\int n(t)\,dt = \int_{-\frac{\Delta t}{2}}^{\frac{\Delta t}{2}} n_o\,dt = n_o \Delta t \tag{90}$$

$$\int_{-\infty}^{\infty} n(t)^2\,dt = \int_{-\frac{\Delta t}{2}}^{\frac{\Delta t}{2}} n_o^2\,dt = n_o^2 \Delta t \tag{91}$$

$$G(t') = n_{oA}\, n_{oB} \int_{-\frac{\Delta t}{2}}^{\frac{\Delta t}{2}} (1 + t') = n_{oA}\, n_{oB} \Delta t \left(1 - \frac{t'}{\Delta t}\right) \tag{92}$$

$$\int_{-\infty}^{\infty} G(t')\,dt' = n_{oA}\, n_{oB} \Delta t \int_{-\infty}^{\infty} \left(1 - \frac{t'}{\Delta t}\right) dt' \tag{93}$$

$$\int_{-\infty}^{\infty} G(t')\,dt' = n_{0A}\, n_{oB} \Delta t^2 \tag{94}$$

Single-sided exponential

$$n(t) = n_o e^{\left(-\frac{t}{\Delta t}\right)} \tag{95}$$

for $t \geqslant 0$

$$n(t) = 0 \tag{96}$$

elsewhere

$$\Delta t = \frac{t_p}{\ln 2} \tag{97}$$

Using the standard integral $\int_0^\infty e^{(a\,x)}dx = \frac{1}{a}\left[e^\infty - e^0\right] = \frac{1}{a}[0-1] = -\frac{1}{a}$

where $a = -\frac{1}{\Delta t}$

$$\int n(t)\,dt = n_o \int_0^\infty e^{\left(\frac{-t}{\Delta t}\right)}dt = -n_o \Delta t[0-1] = n_o \Delta t \tag{98}$$

$$N = A\int_0^\infty n(t)\,dt = A\,n_o \Delta t = \frac{A\,n_o\,t_p}{\ln 2} \tag{99}$$

therefore

$$n_o = \frac{N}{A\,\Delta t} = \frac{N \ln 2}{A\,t_p} = \frac{2\,K\,N}{A\,t_p} \tag{100}$$

$$\int n(t)^2\,dt = n_o^2 \int_0^\infty e^{\left(\frac{-2t}{\Delta t}\right)}dt = \frac{n_o^2 \Delta t}{2} = \frac{n_o^2 t_p}{2\ln 2} = \frac{N^2 \ln 2}{2A^2 t_p} = \frac{K\,N^2}{A^2 t_p} \tag{101}$$

$$G(t') = n_{oA}\,n_{oB}\int_0^\infty e^{\left(\frac{-2t}{\Delta t}\right)} e^{\left(\frac{-t'}{\Delta t}\right)}dt = n_{oA}\,n_{oB}\,e^{\left(\frac{t'}{\Delta t}\right)}\frac{\Delta t}{2} \tag{102}$$

$$\int_{-\infty}^\infty G(t')\,dt' = n_{oA}\,n_{oB}\frac{\Delta t}{2}\int_{-\infty}^\infty e^{\left(\frac{t'}{\Delta t}\right)}dt' \tag{103}$$

$$\int_{-\infty}^\infty G(t')\,dt' = n_{oA}\,n_{oB}\frac{\Delta t}{2}[2\Delta t] \tag{104}$$

$$\int_{-\infty}^\infty G(t')\,dt' = n_{oA}\,n_{oB}\,\Delta t^2 \tag{105}$$

Appendix II. Publications

Journal publications

C.J. Dalzell, T. P. J. Han and I. S. Ruddock,
"Distributed optical fibre sensing of temperature using time-correlated two-photon excited fluorescence: theoretical overview"
Applied Physics B: Lasers and Optics, Volume 93, Issue 2-3, p. 687, (Nov. 2008)
DOI: 10.1007/s00340-008-3195-z,

C. J. Dalzell, T. P. J. Han and I. S. Ruddock
"The two-photon absorption spectrum of ruby and its role in distributed optical fibre sensing"
Applied Physics B: Lasers and Optics, Volume 103, Issue 1, p. 113, (Sept. 2010)
DOI: 10.1007/s00340-008-3195-z,

C.J. Dalzell, T.P.J. Han and I.S. Ruddock,
"Distributed crystal fibre sensing for extreme environments"
IEEE Sensors Journal, **PP**, 99, (Feb. 2011)
DOI: 10.1109/JSEN.2011.2115998

C.J. Dalzell, T.P.J. Han, I.S. Ruddock and D. Hollis,
"Two-photon excited fluorescence in rare-earth doped optical fibre for applications in distributed sensing of temperature",
IEEE Sensors Journal, **PP**, 99, (Mar. 2011)
DOI: 10.1109/JSEN.2011.2132797

Conference proceedings

C. J. Dalzell, T. P. J. Han and I. S. Ruddock, "The two-photon absorption cross-section of ruby and distributed crystal fibre sensing" 20th International Conference on Optical Fibre Sensors, Proc. SPIE Vol 7503, p. 75036L, (Oct 2009), DOI: 10.1117/12.835101

C. J. Dalzell, T. P. J. Han and I. S. Ruddock, "Distributed optical fibre sensing of temperature using time-correlated two-photon excited fluorescence" 20th International Conference on Optical Fibre Sensors, Proc. SPIE Vol 7503, p. 75036K, (Oct 2009), DOI: 10.1117/12.835119

C. J. Dalzell, T. P. J. Han and I. S. Ruddock, "Distributed crystal fibre sensing for extreme environments" Fourth European Workshop on Optical Fibre Sensors, Proc. SPIE Vol 7653, p. 76533E, (Sept 2010), DOI: 10.1117/12.866363

C. J. Dalzell, T. P. J. Han and I. S. Ruddock, “Distributed optical fibre sensing of temperature using time-correlated two-photon excited fluorescence” Fourth European Workshop on Optical Fibre Sensors, Proc. SPIE Vol 7653, 76532Y, (Sept 2010) , DOI: 10.1117/12.866366

Other publications

I.S. Ruddock, C.J. Dalzell and T.P.J. Han, “Nonlinear spectroscopy of doped glass and crystal for applications in distributed fibre sensing” *Central Laser Facility Laser Loans Pool Annual Report*, Lasers for Science Facility – Physics, (2009-2010)

I.S. Ruddock, C.J. Dalzell, T.P.J. Han and D.B. Hollis, “Distributed sensing by time-correlated two-photon excited fluorescence in rare earth doped optical fibres” *Central Laser Facility Laser Loans Pool Annual Report*, Lasers for Science Facility – Physics, (2009-2010)

References

1 K.T.V. Grattan and B.T. Meggit (Eds), "Optical fiber sensor technology" Springer, Ch. 7 p. 133, ISBN-10: 0412844206
2 N. Takahashi et al, "Development of an optical fiber hydrophone with fiber Bragg grating", *Ultrasonics*, **38**, 1-8, p. 581, (2000).
3 Y. Zhang. "Novel Optical Sensors for High Temperature Measurement in Harsh Environments" (PhD Dissertation) Virginia Polytechnic Institute and State University. (2003).
4 T.P.J. Han and I.S. Ruddock, "Temperature sensing", British Patent 0420238,8 (2004).
5 M. Göppert-Mayer, "Über Elementarakte mit zwei Quantensprungen", *Ann. Phys. Lpz.*, **9**, p. 273, (1931)
6 D. Frohlich and M. Sondergeld, "Experimental techniques in two-photon spectroscopy", *Journ. Phys. E.*, **10**, p. 766 (1977)
7 W. Kaiser and C.G.B. Garrett, "Two-photon Excitation in $CaF_2:Eu^{2+}$", *Phys. Lett. Rev.*, **7**, 6, p. 229, (1961)
8 J.A. Giordmaine et al, "Two-photon excitation of fluorescence by picosecond light pulses", *Appl. Phys. Lett.*, **11**, 7, p. 216, (1967)
9 K.L. Sala et al, "CW autocorrelation measurements of picosecond laser pulses", *IEEE Jour. Quan. Elec.,* **QE-16**, 9, p. 990, (1980)
10 W. Denk, J.H. Strickler and W.W. Webb, "Two-photon laser scanning fluorescence microscopy", S*cience*, **248**, 4951, p. 73, (1990)
11 W. Denk, J.H. Strickler and W.W. Webb, "Two-photon laser scanning microscope", Patent No. WO/1991/007651, (1991)
12 K.C. Kao and G.A. Hockam, "Dielectric-fibre surface waveguides for optical frequencies", *Proc. I.E.E.*, **133**, p. 1151, (1966)
13 R. J. Maron and A. D. Kersey, "Multi-parameter fiber optic sensor for use in harsh environments", *US Patent,* Patent No. 5,892,860, (1999)
14 A. Wang, G. Pickrell and R. May, "Single-Crystal Sapphire Optical Fiber Sensor Instrumentation ", *DOE Technical report*, **DE-FC26-99FT40685**, (2002)
15 M. Ott and P. Friedberg, "Technology validation of optical fiber cables for space flight environments", *Proc. SPIE*, **4216**, p. 206, (2001)
16 K.T.V. Grattan and T. Sun, "Fiber optic sensor technology: an overview", *Sensors and Actuators*, **82**, p. 40, (2000)
17 K.T.V. Grattan and A.W. Palmer, "Infrared fluorescence "decay-time" temperature sensor", *Rev. Sci. Instrum.*, **56**, 9, p. 1784, (1985)
18 W. Trettnak, M.J.P. Leiner and O.S. Wolfbeis, "Fibre Optic Glucose Biosensor With an Oxygen Optrode as the Transducer", *Analyst*, **113**, p. 1519, (1988)
19 T.H. Nguyen et al, "A fibre optic chemical sensor for the detection of cocaine", *Proc. of SPIE*, **7653**, p. 76531V, (2010)
20 V. Bhatia et al, "Optical fibre based absolute extrinsic Fabry-Pérot interferometric sensing system", *Meas. Sci. Technol.*, **7**, p. 58, (1996)

21 Y. Zhu and A. Wang, “Miniature fiber-optic pressure sensor”, *IEEE Phot. Tech. Lett.*, **17**, 2, p. 447, (2005)
22 R.O. Claus et al, “Extrinsic Fabry-Perot sensor for strain and crack opening displacement measurements from -200 to 900 ºC”, *Smart Mater. Struct.*, **1**, p. 237, (1992)
23 Q. Shi et al, “A hollow-core photonic crystal fiber cavity based multiplexed Fabry-Pérot interferometric strain sensor system”, *IEEE Phot. Tech. Lett.,* **20**, 15, p. 1329, (2008)
24 S.C. Kaddu, S.F. Collins and D.J. Booth, “Multiplexed intrinsic optical Fabry-Pérot temperature and strain sensors addressed using white-light interferometry”, *Meas. Sci. Technol.*, **10**, 5, p. 416, (1999)
25 Y. Rao, “Recent progress in fiber-optic extrinsic Fabry-Perot interferometric sensors”, *Optical Fiber Technology*, **12**, p. 227, (2006)
26 K.O. Hill et al, “Photosensitivity in optical fiber waveguides: Application to reflection filter fabrication”, *Appl. Phys. Lett.*, **32**, 10, p. 647, (1978)
27 A.D. Kersey, “Demonstration of a hybrid time/wavelength division multiplexed interferometric fibre sensor array”, *Electronics Letters*, **27**, 7, p.554, (1991)
28 A.D. Kersey et al, “Fiber Grating Sensors”, *Journ. Lightwave. Technol.*, **15**, 8, p. 1442, (1997)
29 M.A. Davis et al, “Interrogation of 60 fibre Bragg grating sensors with microstrain resolution capability”, *Electronics Letters*, **32**, 15, p. 1393, (1996)
30 A.J. Rogers, “Polarisation optical time domain reflectometry”, *Electronic Letters*, **16**, 13, p. 489, (1980)
31 J.N. Ross, “Birefringence measurement in optical fibers by polarization-optical time-domain reflectometry”, *Applied Optics*, **21**, 19, p. 3489, (1982)
32 J.P. Dakin et al, “Distributed optical fibre Raman temperature sensor using a semiconductor light source and detector”, *Electronics Letters*, **21**, 13, p. 569, (1985)
33 T. Horiguchi et al, “Development of a distributed sensing technique using Brillouin scattering”, *Journ. Lightwave Technol.*, **13**, 7, p. 1296, (1995)
34 D. Culverhouse et al, “Potential of stimulated Brillouin scattering as sensing mechanism for distributed temperature sensors”, *Electronic Letters*, **25**, 14, p. 913, (1989)
35 T. Kurashima, T. Horiguchi and M. Tateda, “Distributed temperature sensing using stimulated Brillouin scattering in optical silica fibers”, *Optics Letters*, **15**, 18, p. 1038, (1990)
36 T. Horiguchi, T. Kurashima and M. Tateda, “Tensile strain dependence of Brillouin frequency shift in silica optical fibres”, *IEEE Photonics Technol. Lett.,* **1**, 5, p. 1041, (1989)
37 P.C. Wait, T.P. Newson, “Laudau–Placzek ratio applied to distributed fiber sensing”, *Opt. Commun.*, **122**, 4, p. 141, (1996)

38 M.N. Alahbabi, Y.T. Cho and T.P. Newson, “150-km-range distributed temperature sensor based on coherent detection of spontaneous Brillouin backscatter and in-line Raman amplification”, *JOSA B*, **22**, 6, p. 1321, (2005)
39 J.S. Selker et al, “Distributed fiber-optic temperature sensing for hydrologic systems”, *Water Resources Research*, **42**, W12202, (2006)
40 K. Song, Z. He and K. Hotate, “Distributed Strain Measurement with Millimeter-Order Spatial Resolution Based on Brillouin Optical Correlation Domain Analysis and Beat Lock-in Detection Scheme”, *Proc. OFS-18*, ThC2, (2006)
41 F. Göppelsröder, “Ueber eine fluorescirende Substanz aus dem Kubaholze und über Fluorescenzanalyse”, *Fresenius' Journal of Analytical Chemistry*, **7**, 1, p. 195, (1868)
42 J. Wang, X. Qian and J. Cui, “Detecting Hg^{2+} Ions with an ICT Fluorescent Sensor Molecule: Remarkable Emission Spectra Shift and Unique Selectivity”, *J. Org. Chem.*, **71**, p. 4308, (2006)
43 K.T.V. Grattan and A.W. Palmer, “Infrared fluorescence “decay-time” temperature sensor”, *Rev. Sci. Instrum.*, **56**, 9, p. 1784, (1985)
44 T. Sun, Z.Y. Zhang and K.T.V. Grattan, “Erbium/ytterbium fluorescence based fiber optic temperature sensor system”, *Rev. Sci. Instrum.*, **71**, 11, p. 4017, (2000)
45 T. Sun et al, “Intrinsic strain and temperature characteristics of Yb-doped silica-based optical fibers”, *Rev. Sci. Instru.*, **70**, 2, p. 1447, (1999)
46 R.A. Forman et al, “Pressure Measurement Made by the Utilization of Ruby Sharp-Line Luminescence”, *Science*, **176**, 4032, p. 284, (1972)
47 I. Basarab et al, “A fluorescence-based fiber-optic flow sensor – Design considerations”, *Rev. Sci. Instrum.*, **62**, 5, p. 1321, (1991)
48 S. Donati, V. Annovazzi-Lodi and T. Tambosso, “Magneto-optical fibre sensors for electrical industry: analysis of performances”, *IEE Proc*, **135**, Pt. J, No. 5, p. 372, (1988)
49 C.E. Andersen et al. “An algorithm for real-time dosimetry in intensity modulated radiation therapy using the radioluminescence signal from Al_2O_3:C”, *Rad. Prot. Dos.*, **120**, 1, p. 7, (2006)
50 F. Berghmans et al, “An introduction to Radiation Effects on Optical Components and Fiber Optic Sensors”, *Optical Waveguide Sensing and Imaging*, eds W.J. Block, I. Gannot and S. Tanev, **Ch 6**, p. 127, (2006) ISBN 978-1-4020-6950-5
51 S.W. Allison and G.T. Gillies, “Remote thermometry with thermographic phosphors: Instrumentation and applications”, *Rev. Sci. Instrum.*, **68**, 7, p. 2615, (1997)
52 D. Frölich, M. Sondergeld, “Experimental techniques in two-photon spectroscopy”, *Journ. Phys. E.* **10**, p. 766. (1977)
53 X. Qi, T.P.J. Han, H.G. Gallagher, B. Henderson, “Energy upconversion

processes in Er^{3+} and Nd^{3+} doped $RETiNbO_6$ crystals", *Opt. Commun*. **140**, p .65, (1997)
54 I.S. Ruddock, T.P.J. Han, "Continuously distributed sensing via two photon excited fluorescence in doped optical fibre", *J. Phys: Conf. Ser.,* **15**, p. 83 (2005)
55 I.S. Ruddock, T.P.J. Han, "Potential of two-photon-excited fluorescence for distributed fiber sensing", *Opt Lett.* **31***,* p. 891, (2006)
56 A.J. DeMaria, D.A.Stetser and H. Heynau, "Self mode-locking of lasers with saturable absorbers", *Appl. Phys. Lett.*, **8**, 7, p. 174, (1966)
57 J.A. Armstrong, "Measurement of picosecond laser pulse widths", *Appl. Phys. Lett.*, **10**, 1, p. 16, (1967)
58 K. L. Sala, G. A. Kenney-Wallace and G.E. Hall, "CW autocorrelation measurements of picosecond laser pulses", IEEE *Jour. Quan. Elec.*, **QE-16**, 9, (1980)
59 J.A. Buck, "Fundamentals of Optical Fibers", New York: John Wiley & Sons, Inc., (1995)
60 "Corning® 62.5/125 Optical Fiber" Datasheet, (2002)
61 W.A. Gambling, H. Matsumara and C.M. Ragdale, "Zero Total Dispersion in Graded-Index Single-Mode Fibres", *Electronics Letters*, **15**, 15, p. 474, (1979)
62 W. Denk, J.P. Strickler and W.W.Webb, "Two-photon molecular excitation in a laser scanning microscopy", *European patent*, EP0807814, (1990)
63 A. Bhaskar et al, "Investigation of Two-Photon Absorption Properties in Branched Alkene and Alkyne Chromophores", *J. Am. Chem. Soc.*, **128**, p. 11840, (2006)
64 L.A. Padilha et al, "Frequency degenerate and nondegenerate two-photon absorption spectra of semiconductor quantum dots", *Phys. Rev. B,* **75**, 075325, (2007)
65 L.L. Chase and S. A Payne, "Two-photon-absorption cross section of Nd^{3+} in yttrium aluminum garnet and yttrium lithium fluoride near 1.06 μm", *Phys. Rev. B.*, **34**, 12, p. 8883, (1986)
66 P. Sengupta et al, "Senstive measurement of absolute two-photon absorption cross sections", *Journ. Chem. Phys.*, **112**, 21, p. 9201, (2000)
67 V.V. Grabovskii et al, "Measurement of two-photon absorption factors by nonlinear transmission", *Journ. Appl. Spec.*, **63**, 4, p. 491, (1994)
68 M. Sheik-Bahae et al, "Sensitive Measurement of Optical Nonlinearities Using a Single Beam" *IEEE Joun. Quan. Elec.*, **26**, 4, p. 760, (1990)
69 D.H. Auston, "Picosecond Nonlinear Optics", *Ultrashort Light Pulses*, ed S.L Shapiro, C**h. 4**, p. 177, (1977) ISBN 0-387-08103-8
70 C. Xu and W. Webb, "Measurement of two-photon excitation cross sections of molecular fluorophores with data from 690 to 1050 nm", *J. Opt. Soc. Am. B*, **13**, 3, p. 481, (1996)
71 L.S. Rohwer and J.E. Martin, "Measuring the absolute quantum efficiency of luminescent materials", *Journal of Luminescence*, **115**, 3, p. 77, (2005)

72 O. Kim *et al*, “New class of two-photon absorbing chromophores based on dithienothiophene”, *Chem. Mater.* **2000**, 12, p. 284, (1999)
73 C.J. Dalzell, T.P.J. Han and I.S. Ruddock, “The two-photon absorption spectrum of ruby and its role in distributed optical fibre sensing” *Appl.Phys. B*, **103**, 1, p. 113, (2010)
74 D.J. Bradley, M.H.R. Hutchinson and H. Koetser, “Interactions of picosecond laser pulses with organic molecules II. Two-photon absorption cross-sections”, *Proc. R. Soc. Lond. A.,* **329**, p. 105, (1972).
75 K.H. Drexage, “Structure and properties of laser dyes”, *Dye Lasers*, ed. F.P. Shäfer, **Ch 4**, p. 159, (1973), ISBN 0-387-06438-9
76 K.H. Drexage, “Structure and properties of laser dyes”, *Dye Lasers*, ed. F.P. Shäfer, **Ch 4**, p. 169, (1973), ISBN 0-387-06438-9
77 C.J. Dalzell, “Two-photon excited fluorescence and applications in sensing”, Unpublished MSci dissertation, University of Strathclyde, (2007)
78 P.R. Hammond, “Spectra of the Lowest Excited Singlet States of Rhodamine 6G and Rhodamine B”, *IEEE Journ. Quan. Elec.*, **QE-15**, 7, p. 624, (1979)
79 K.H. Drexage, “Structure and properties of laser dyes”, *Dye Lasers*, ed. F.P. Shäfer, **Ch 4**, p. 170, (1973), ISBN 0-387-06438-9
80 F.P. Shäfer, “Principles of Dye Laser Operation”, *Dye Lasers*, ed. F.P. Shäfer, **CH 1**, p. 6, (1973), ISBN 0-387-06438-9
81 T.H. Maiman, “Stimulated optical radiation in ruby”, *Nature*, **187**, p. 493, (1960)
82 R.A. Forman et al, “Pressure measurement made by the utilization of ruby sharp-line luminescence”, *Science*, **176**, 4032, p. 284, (1972)
83 K.T.V. Grattan, R.K. Selli, A.W. Palmer, “Ruby fluorescence wavelength division fiber-optic temperature sensor”, *Rev. Sci. Instru.*, **58**, 7, p. 1231, (1987)
84 Y.L. Hu et al, “Ruby based decay-time thermometry: effect of probe size on extended measurement range (77 – 800K)”, *Sensors and Actuators A*, **63**, p. 85, (1997)
85 K.S. Gibson, “The effect of temperature upon the absorption spectrum of a synthetic ruby”, *Phys. Rev.*, **8**, p. 38, (1916)
86 T.H. Maiman et al, “Stimulated optical emission in fluorescent solids. II. Spectroscopy and stimulated emission in ruby.”, *Phys. Rev.*, **123**, 4, p. 1151, (1961)
87 D.C. Cronemeyer, “Optical absorption characteristics of pink ruby”, *Journ. Opt. Soc. Am.*, **56**, 12, p. 1703, (1966)
88 L. Yang et al, “Upconversion luminescence from ^2E state of Cr^{3+} in Al_2O_3 crystal by infrared femtosecond laser irradiation”, *Optics Express*, **13**, 20, (2005)
89 E. Hecht, “Optics, 4th Ed”, Ch 8 p 360. Addison Wesley, (2002). ISBN 0-321-18878-0.
90 G. Burns and M.I. Nathan, “Quantum efficiency of ruby”, *Journ. Appl. Opt.*, **34**, 3, p. 703, (1963)

91 K.T.V Grattan et al, “Sapphire–ruby single-crystal fibre for application in high temperature optical fibre thermometers: studies at temperatures up to 1500 ◦C ”, *Meas. Sci. Technol.*, **12**, p. 981, (2001)
92 L.S. Rohwer and J.E. Martin, “Measuring the absolute quantum efficiency of luminescent materials”, *Journal of Luminescence*, **129**, 3, p. 329, (2005)
93 Y.L. Hu et al, “Design aspects of a ruby-based fiber optic thermometer probe for use in the cryogenic region (>77K)”, *Rev. Sci. Instrum.*, **67**, 6, p. 2394, (1996)
94 C. Xu et al, “Multiphoton excitation cross-sections of molecular fluorophores”, *Bioimaging*, **4**, p. 198, (1998)
95 B.R. Cho et al, “Two photon absorption properties of 1,3,5-tricyano-2,4,6-tris(styryl)benzene derivatives”, *J. Am. Chem.* **123**, p. 10039, (2001)
96 M. Pawlicki et al, “Two-photon absorption and the design of Two-photon dyes”, *Angew. Chem. Int. Ed.*, **48**, p.3244, (2009)
97 I. Badhrees et al, “Measurement of the two-photon absorption cross-section of liquid Argon with a Time Projection Chamber”, *New J. Phys.*, **12**, 113024, (2010)
98 J.A. Buck, “Fundamentals of Optical Fibers”, New York: John Wiley & Sons, Inc., (1995)
99 J.H. Sharpe, R. Illingworth and I.S. Ruddock, “Graded-index characteristics in single-crystal fibre”, *Opt. Lett.*, **23**, 2, pp. 109, (1998)
100 G.H. Dieke and H.M. Crosswhite, “The spectra of the doubly and triply ionized rare earths”, *Applied Optics*, **2**, 7, p. 675, (1963)
101 D. Hollis, *Private communication*, (2011)
102 P. Williams and H.W. Lam, “Simple boxcar integrator covering a large input frequency range”, *J. Phys. E: Sci. Instru.*, **18**, p. 23, (1985)
103 M. Dagenais et al, “Two-photon absorption as a new test of the Judd-Ofelt theory”, *Phys. Rev. Lett.*, **46**, 8, p. 561, (1981)
104 B.R. Judd and D.R. Pooler, “Two-photon absorption in gadolinium ions”, *J. Phys. C: Solid State Phys.*, **15**, p. 591, (1982)
105 L. Kundu, A.K. Banerjee and M. Chowdhury, “Two-photon absorption spectrum of gadolinium elpasolite”, *Chem. Phys. Lett.*, **181**, 6, p. 569, (1991)
106 K. Annapurna et al, “Fluorescence properties of Sm^{3+}: $ZnCl_2$-$BaCl_2$-LiCl glass”, *Materials Research Bulletin*, **38**, p. 429, (2003)
107 J.R.G. Thorne et al, “Two-photon spectroscopy of samarium(III) in the elpasolite Cs_2NaYCl_6:Sm^{3+}”, *J.Phys. Condens Matter*, **11**, p. 7867, (1999)
108 R. Piramidowicz, M. Klimczak, and M. Malinowski , “Short-wavelength emission analysis in Dy:ZBLAN glasses ”, *Optical Materials*, **30**, p. 707, (2008)
109 S. Kück and I. Sokolska , “The up-conversion of near-infrared excitation radiation in Ho^{3+}-doped $LiYF_4$”, *Chemical Physics Letters*, **325**, p. 257, (2000)
110 A.S. Gouveia-Neto et al, “Intense red upconversion emission in infrared excited holmium-doped PbGeO3–PbF2–CdF2 transparent glass ceramic ”, *Journal of Luminescence*, **110**, p.79, (2004)

111 B.V. Shulgin, K.N.R. Taylor, A. Hoaksey and R.P. Hunt, “Optical characteristics of Tb^{3+} ions in soda glass”, *J. Phys. C: Solid State Physics.*, **5**, p. 1716, (1972)
112 P.R. Selvin and J.E. Hearst, “Luminescence enery transfer using a terbium chelate: Improvements on fluorescence energy transfer”, *Proc. Natl. Acad. Sci. USA*, **91**, p. 10024, (1994)
113 M.V.D. Vermelho et al, “Thermally enhanced cooperative energy-transfer frequency upconversion in terbium and ytterbium doped tellurite glass”, *Journ. of Lumin.*, **102**, p. 762, (2003)
114 M.A. Buñuel et al, “Optical properties of Tb^3-doped Rb_2KInF_6 elpasolite ”, *Optical Materials*, **13**, p. 211, (1999)
115 J.R. Lakowicz et al, “Multiphoton excitation of lanthanides”, *Chem. Phys. Chem.*, **4**, p. 247, (2001)
116 G. Piszczek et al, “Multiphoton ligand-enhanced excitation of lanthanides”, *Journal of Fluorescence*, **11**, 2, p. 101, (2001)
117 M.H.V. Werts, “Action cross-sections of two-photon excited luminescence of some Eu(III) and Tb(III) complexes”, *Photochem. Photobiol. Sci.*, **4**, p. 531, (2005)
118 T. Yamashita and Y. Ohishi, “Concentration and temperature effects on the spectroscopic properties of Tb^{3+} doped borosilicate glasses”, *Journ. Appl. Phys.*, **102**, p. 123107, (2007)
119 G.F White et al, “ Multiphoton-excited luminescence of a lanthanide ion in a protein complex: Tb3+ bound to transferrin”, *Photochem. Photobiol. Sci*, **3**, p. 47, (2004)
120 J.R. Wells et al, “Infrared absorption, laser excitation and crystal-field analysis of the C_{4v} symmetry centre in KY_3F_{10} doped with Pr^{3+}”, *J. Phys.:Condens. Matter*, **12**, p. 5297, (2000)
121 T. Sun et al, “Temperature dependence of the fluorescence lifetime in Pr^{3+}:ZBLAN glass for fiber optic thermometry”, *Rev. Sci. Instrum.*, **68**, 9, p. 3447, (1997)
122 C.J. Dalzell, T.P.J. Han and I.S. Ruddock, “Distributed optical fibre sensing of temperature using time-correlated two-photon excited fluorescence: theoretical overview”, *Appl. Phys B*, **93**, 2, p. 687, (2008)
123 C.J. Dalzell, T.P.J. Han and I.S. Ruddock, “Distributed crystal fibre sensing for extreme environments”, *IEEE Sensors Journal*, **PP**, 99, (2011)
124 C.J. Dalzell, T.P.J. Han, I.S. Ruddock and D. Hollis, “Two-photon excited fluorescence in rare-earth doped optical fibre for applications in distributed sensing of temperature”, *IEEE Sensors Journal*, **PP**, 99, (2011)
125 A. Kerrouche et al, “Design and in-the-field performance evaluation of compact FBG sensor system for structural health monitoring applications”, *Sensors and Actuators A*, **151**, p. 107, (2009)
126 B.G. Koziol, G.W. Baxter and S.F. Collins, “Dependence of fluorescence

lifetime in praseodymium-doped silica optical fibres upon strain and temperature", *J. Opt.*, **12**, 015407, (2010)
127 S.A. Wade, S.F. Collins and G.W. Baxter, "Fluorescence intensity ratio technique for optical fiber point temperature sensing", *J. Appl. Phys.*, **94**, 8, p. 4743, (2003)
128 S.F. Collins et al, "Comparison of fluorescence-based temperature sensor schemes: Theoretical analysis and experimental validation", *J. Appl. Phys*. **84**, p. 4649 (1998)
129 S.A. Wade et al, "Simultaneous strain-temperature measurement using fluorescence from Tb-doped silica fiber", *Rev. Sci. Instru.*, **71**, 6, p. 2267, (2000)
130 J.M. Diels et al, "Control and measurement of ultrashort pulse shapes (in amplitude and phase) with femtosecond accuracy", *Applied Optics*, **24**, 9, p. 1270, (1985)